A Computational Study of Ruthenium Metal Vinylidene Complexes: Novel Mechanisms and Catalysis

David G. Johnson

PhD

University of York,

Department of Chemistry

September 2013

Scientist: How much time do we have professor?
Professor Frink: Well according to my calculations, the robots won't go berserk for at least 24 hours.
(The robots go berserk.)
Professor Frink: Oh, I forgot to er, carry the one.

- The Simpsons: Itchy and Scratchy land

Abstract

A theoretical investigation into several reactions is reported, centred around the chemistry, formation, and reactivity of ruthenium vinylidene complexes. The first reaction discussed involves the formation of a vinylidene ligand through non-innocent ligand-mediated alkyne-vinylidene tautomerization (*via* the LAPS mechanism), where the coordinated acetate group acts as a proton shuttle allowing rapid formation of vinylidene under mild conditions.

The reaction of hydroxy-vinylidene complexes is also studied, where formation of a carbonyl complex and free ethene was shown to involve nucleophilic attack of the vinylidene C_α by an acetate ligand, which then fragments to form the coordinated carbonyl ligand. Several mechanisms are compared for this reaction, such as transesterification, and through allenylidene and cationic intermediates.

The CO-LAPS mechanism is also examined, where differing reactivity is observed with the LAPS mechanism upon coordination of a carbonyl ligand to the metal centre. The system is investigated in terms of not only the differing outcomes to the LAPS-type mechanism, but also with respect to observed experimental Markovnikov and anti-Markovnikov selectivity, showing a good agreement with experiment.

Finally pyridine-alkenylation to form 2-styrylpyridine through a half-sandwich ruthenium complex is also investigated. The mechanism for this process is elucidated, along with a description of the formation of the unexpected experimental deactivation product. Additionally the chemistry and bonding of pyridylidene complexes is also studied.

Contents

List of Figures

List of Tables

List of Accompanying Material

In addition to this document, a supplementary information disc is also present containing geometries and energies of all discussed stationary points, excel spreadsheets containing calculated data, a pdf copy of this thesis, and the endnote library of all references used in this document.

Acknowledgements

Many people have been involved in helping me produce this thesis. Primary credit goes to my academic supervisors, Dr John Slattery and Dr Jason Lynam for their help, guidance, insight and most importantly, patience. I also thank the main experimental collaborators who I've worked with over the last four years – Dr Christine Welby, Dr Neetisha Mistry, Elisabeth Smith and Lucy Milner, who's constant dialogue and expertise were of great value and added to the overall synergy of this thesis. Additional thanks must go out to Dr Robert Thatcher whose contribution, though no longer present in the document, was invaluable and only mildly unnerving. Finally all members of the SLUG group, MChems of days past, as well as various residents in the C, D and E blocks have made my experience at York an incredibly pleasant one.

Significant non-chemistry related support has also been received for many years from Mum, Dad, Katie, Ash and Karin, without whose help, advice, support, peppermint tea and threatened procrastination-related beatings[1] – this document would simply not exist.

Authors Declaration

I declare that, except where explicit reference is made to already published material as well as the contribution of others, this dissertation is the result of my own work and has not been submitted for any other degree at the University of York or any other institution. Additionally, several published studies are associated with this document, and are listed below.

- Insights into the Intramolecular Acetate-Mediated Formation of Ruthenium Vinylidene Complexes: a Ligand-Assisted Proton Shuttle (LAPS) Mechanism, D. G. Johnson, J. M. Lynam, J. M. Slattery and C. E. Welby, *Dalton Trans.*, 2010, **39**, 10432-10441.

- Ruthenium-Mediated C−H Functionalization of Pyridine: The Role of Vinylidene and Pyridylidene Ligands, D. G. Johnson, J. M. Lynam, N. S. Mistry, J. M. Slattery, R. J. Thatcher and A. C. Whitwood, *J. Am. Chem. Soc*., 2013, **135**, 2222-2234.

- Charged Behavior from Neutral Ligands: Synthesis and Properties of N-Heterocyclic Pseudo-amides, R. J. Thatcher, D. G. Johnson, J. M. Slattery and R. E. Douthwaite, *Chem. Eur. J.*, 2012, **18**, 4329-4336.

David Johnson

1. Introduction

This thesis will report *via* the use of theoretical computational chemistry, an investigation into several stoichiometric and catalytic reactions. The area of study is split into two separate areas – the formation, chemistry and reactivity of *bis*-acetate ruthenium vinylidene complexes such as **202**, and the chemistry and mechanism of half-sandwich ruthenium vinylidene complexes such as **503** (Figure 1.1). What these complexes have in common is the presence of metal-vinylidene ligands – stable reactive carbenes which allow for interesting reactive properties in both systems.

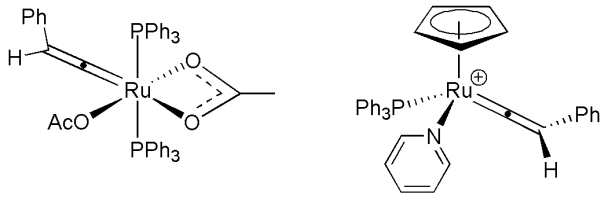

202 **503**

*Figure 1.1 – The two general areas of interest involving complexes such **202** and **503**.*

The *bis*-acetate ruthenium vinylidene complexes such as **202** also possess acetate ligands, which have been shown to engage in C-H activation mechanisms. Here, not only is C-H activation investigated, but a range of additional reactivity is also reported involving the acetates. The half-sandwich ruthenium vinylidene complexes such as **503** will be investigated with respect to their catalytic reactivity as related to direct pyridine alkenylation – a relatively unexplored process.

Collaboration with experimentalists throughout the development of the theoretical study allowed not only a comparison with real empirical values, but provided a significant symbiotic advance in the understanding of these systems.

The introduction begins with a brief description of the theoretical methods used, as well as their applicability to real experimental systems. After identifying the main areas of chemistry which will be explored within this document, the focus will be turned to an investigation of the *bis*-acetate vinylidene complexes in chapters 2-4, with the half sandwich vinylidene complexes being further investigated in chapter 5.

1.1 Computational Methods

1.1.1 Introduction

This thesis focusses upon the use of theoretical computational chemistry methods, in particular density functional theory (DFT), to describe the structure and chemistry of several 'real world' experimental systems. Computational chemistry itself can be divided into two categories - semi-empirical and ab-initio methods. The former relies on empirical observations in order to produce information for a system, and shall not be detailed here. The latter involves describing properties such as the energy of a molecule from first principles – i.e. modelling a system using the basic laws of nature (although it should be noted that the DFT functionals presented in this thesis are parameterised, so do possess some semi-empirical character).[2]

In order to properly describe DFT a brief (yet by no means comprehensive) development of the methods leading from physical experiments through quantum mechanics and the Schrödinger equation, Hartree-Fock theory, the Thomas Fermi model and DFT itself shall be detailed here.[3, 4]

1.1.2 Particles, Waves and Quanta

One of the earliest foundations of quantum theory was the notion of the particle/wave duality of matter which arose from several experiments in the early 20th century. The photoelectric effect, where a metal surface is subjected to UV radiation ejecting photoelectrons, was shown by Millikan to depend on the frequency of the incident radiation.[5] A minimum threshold was needed below which no electrons were omitted, and indeed the kinetic energy of the electrons depended on the frequency and not the amplitude of the radiation, contrary to the classical interpretation of waves.[6]

This verified an earlier theory in 1905 by A. Einstein, which stated that the radiant energy was focussed in discrete packets - called photons. Here the energy (*E*) was related to the frequency (ν) by Planck's constant (*h*) (Equation 1.1).[7]

$$E = h\nu \qquad \textit{Equation 1.1}$$

Additionally, experiments performed by Davisson and Germer as well as Thomson in 1927 showed that electrons could be diffracted by a crystal – an intrinsic feature of waves.[8, 9] This as well as other diffraction experiments with neutrons showed that all matter possessed wave-like properties.

One year earlier, de Broglie hypothesised this result by proposing that all matter and radiation possessed properties of both a particle *and* a wave. This would mean a relation of the momentum (*p*) (Equation 1.2, where *m* is the mass and *v* is the velocity) to the wavelength (λ) resulting in the de Broglie equation (Equation 1.3). This equation states that a shorter wavelength relates to a larger momentum.[10]

$$p = mv \qquad \textit{Equation 1.2}$$

$$\lambda = \frac{h}{p} \qquad \textit{Equation 1.3}$$

Another fundamental concept is that of the quantisation of energy, which began to be understood through the emission spectrum of hydrogen. Here an electrical charge is passed through a volume of hydrogen gas, emitting light which can be diffracted *via* a prism to display the spectrum. This can be observed through detection on a suitable collection medium (such as photographic film for visible light, shown in Figure 1.2).[11]

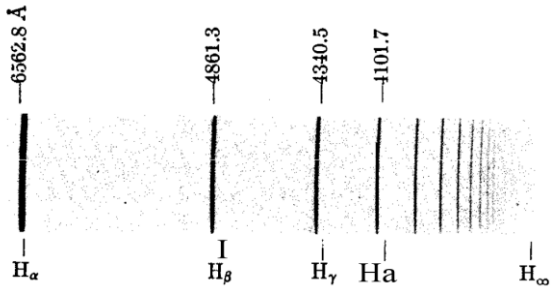

Figure 1.2 – Visible spectrum of hydrogen gas.[11]

The reasoning behind the splitting pattern seen for the visible, infra-red and ultraviolet spectrum of hydrogen was explained with the Rydberg formula - an overall equation for the splitting pattern of hydrogen, presented in 1888 (Equation 1.4). Here n_1 and n_2 are integers ($n_1<n_2$) and R is the Rydberg constant. While able to predict the bands within a spectrum, the theory behind the empirical observation was not well understood.

$$\nu = R\frac{1}{n_1^2} - \frac{1}{n_2^2} \qquad \textit{Equation 1.4}$$

Progress toward understanding the nature of the Rydberg formula began with Rutherford's model of the atom in 1911. An experiment where deflection of a small quantity of α-particles was observed when the beam was directed towards a thin gold film, suggested to Rutherford that a concentrated charge was present in the gold atoms – the nucleus, with electrons being located in orbit around it (Figure 1.3).[12]

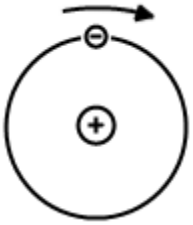

Figure 1.3 – Depiction of the Rutherford model.

However the model had some associated problems, most notably that the classical attraction between the two oppositely charged components would see the orbit of the electron decay and fall into the nucleus, much like the orbit of satellites around Earth. The work of Bohr expanded the model by first simply assuming that the orbit of the electron did not decay, and that there were stable orbits where the electron could remain indefinitely without losing energy and falling into the nucleus.

It was also proposed that an orbiting electron could transition to a higher energy stable orbit by being excited by a packet of energy such as a photon, with energy being released upon the electron transitioning to a lower energy stable orbit (Figure 1.4). The energy of the photons obeys the relation seen in Equation 1.1, explaining the discrete amount of observed frequencies in the hydrogen spectrum in Figure 1.2.

Figure 1.4 – Energy being absorbed and released by the excitation of electrons.

The model assumed that the centripetal force of the electron and the attraction between the nucleus and electron were equal, allowing the electron to remain in a stable orbit. This is represented in Equation 1.5, where the energy of the electron orbit is equal to the kinetic (*T*) and potential (*V*) energy of the electron.

$$E = T + V \qquad \textit{Equation 1.5}$$

Bohr also calculated that the angular momentum (*L*) of the allowed stable orbits were equal to integers of $\hbar$ (Equation 1.6), and calculated the smallest allowed radius (*r*) in Equation 1.7 for an electron, where ε_0 = permittivity of a vacuum, *n* = integer representing a given orbit, m_e = mass of an electron and *e* = charge of an electron. For hydrogen where *n* = 1 - *r* = 52.92 pm and is named the Bohr radius (a_0). Additionally Bohr managed to derive the Rydberg constant (*R*) from the model, with the formula being used to predict the entire experimental hydrogen atom spectrum.[13-15]

$$L = n\frac{h}{2\pi} = n\hbar \qquad \textit{Equation 1.6}$$

$$r_n = \frac{\varepsilon_0 h^2 n^2}{\pi m_e e^2} \qquad \textit{Equation 1.7}$$

While Bohr's theory successfully modelled the hydrogen atom, it could not be applied to larger atoms and was superseded by other methods. However the quantisation of electron orbits as well as the nature of wave-particle duality would lead to the development of modern quantum mechanics such as the Schrödinger equation.

1.1.3 The Schrödinger Equation – Introduction, Description and Limits

As previously shown with the de Broglie relation in Equation 1.3, an electron possesses wave-like properties. As this takes the form of a standing wave, an electron in orbit around a nucleus must contain a whole number of wavelengths (Equation 1.8), meaning there are only certain discrete orbits around the nucleus - similar to Bohr's quantisation of angular momentum seen previously in Equation 1.6.[10]

$$n\lambda = 2\pi r \qquad \textit{Equation 1.8}$$

This allows the definition of the angular wavenumber (k – wavelength per unit distance of 2π - Equation 1.9) and the angular frequency (ω – frequency per unit distance of 2π - Equation 1.10), and applying the angular wavenumber to the de Broglie relation in Equation 1.3 gives an alternate form of the momentum in Equation 1.11.

$$k = \frac{2\pi}{\lambda} \qquad \textit{Equation 1.9}$$

$$\omega = 2\pi\nu \qquad \textit{Equation 1.10}$$

$$p = \frac{h}{\lambda} = \hbar k \qquad \textit{Equation 1.11}$$

Inspired by the wave-nature of matter, Schrodinger sought to describe atoms by the use of a modified wave equation.[16] In one dimension, the second order derivative of a wave function (ψ - e.g. e^{ikx} where x is the displacement of the wave along the x-axis and i is $\sqrt{-1}$) takes the form of ψ multiplied by a constant (Equation 1.12), with ψ being classed as an eigenfunction.

$$\frac{d^2\psi}{dx^2} = -k^2\psi \qquad \textit{Equation 1.12}$$

The integral of the momentum (p) in Equation 1.2 gives the kinetic energy (T) of a particle (Equation 1.13). This can then be related to the angular wavenumber through the de Broglie relation to give Equation 1.14.

$$T = \frac{1}{2}mv^2 = \frac{p^2}{2m} \qquad \textit{Equation 1.13}$$

$$T = \frac{(\hbar k)^2}{2m} \qquad \textit{Equation 1.14}$$

Rewriting Equation 1.12 to take into account the kinetic energy leads to Equation 1.15, which can further be rearranged to Equation 1.16. The total energy of the wavefunction can be obtained by the addition of a potential energy (*V*) term to Equation 1.16 to form Equation 1.17. For example, the potential energy term for a hydrogenic system is described in Equation 1.18, where ε_0 is the permittivity of a vacuum, and *Z* is the nuclear charge.

$$\frac{d^2\psi}{dx^2} = \frac{2mT\psi}{\hbar^2} \qquad \textit{Equation 1.15}$$

$$\frac{\hbar^2}{2m}\left(\frac{d^2\psi}{dx^2}\right) = T_x\psi \qquad \textit{Equation 1.16}$$

$$\frac{\hbar^2}{2m}\left(\frac{d^2\psi}{dx^2}\right) + V_x\psi = E_x\psi \qquad \textit{Equation 1.17}$$

$$-\frac{Z^2}{4\pi\varepsilon_0 r} \qquad \textit{Equation 1.18}$$

The one-dimensional Schrödinger equation can be expanded into three dimensions by the inclusion of the Laplacian operator (∇), which can be expressed in terms of Cartesian coordinates (Equation 1.19) or in spherical coordinates (Equation 1.20), with *r* being the radius of the sphere, and Λ being shorthand notation for Equation 1.21, with θ and ϕ being the spherical angles of *r* (Figure 1.5).

$$\nabla^2 = \frac{d^2}{dx^2} + \frac{d^2}{dy^2} + \frac{d^2}{dz^2}$$ *Equation 1.19*

$$\nabla^2 = \frac{1}{r^2}\left[\frac{d}{dr}\left(r^2\frac{d}{dr}\right) + \Lambda^2\right]$$ *Equation 1.20*

$$\Lambda^2 = \frac{1}{\sin\theta}\frac{d}{d\theta}\left(\sin\theta\frac{d}{d\theta}\right) + \frac{1}{\sin^2\theta}\frac{1}{d\phi^2}$$ *Equation 1.21*

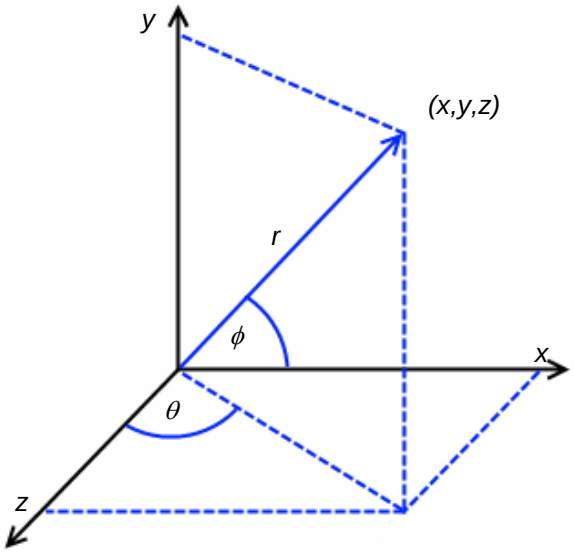

Figure 1.5 – Depiction of the spherical coordinate variables (r), (θ) and (ϕ).

The equation can be further simplified into the popular notation for the Schrödinger equation in Equation 1.22, where $\hat{H}$ is the Hamiltonian differential operator containing kinetic and potential energy terms.

$$\hat{H}\psi = E\psi$$ *Equation 1.22*

Additionally in 1926, Born provided a description of the wavefunction in terms of the probability. The wavefunction itself contains information about the particle such as the location; however the square of the wavefunction (Equation 1.23) gives the probability of finding the electron within a set space. For example the probability of finding a particle in a sphere of volume *dxdydz* is proportional to Equation 1.24.[17] As the probability of finding the particle within the sphere described in Equation 1.24 must be equal to 1, a normalisation constant can be applied to the wavefunction in order to achieve this.

$$|\psi|^2 = \psi^* \psi \geq 0 \qquad \textit{Equation 1.23}$$

$$|\psi|^2 dxdydz \qquad \textit{Equation 1.24}$$

The Schrödinger equation can be used successfully to calculate single electron, mono-atomic atoms such as H, He^+ and Li^{2+} as well as the particle in a box and harmonic oscillator models.[18] However the Schrödinger equation encounters problems upon application to many electron systems such as H_2 and beyond. These multiple electron wavefunctions can be dealt with through the use of several approximations, which will be covered in the next section.

1.1.4 Many Electron Wavefunctions – Hartree Theory

While the Schrödinger equation for hydrogenic-like systems contained an operator for the kinetic energy of the electron (T_e) and a potential energy operator for the nuclear-electron interaction (V_{Ne}), three additional terms must be included for many electron systems. The first is the kinetic energy of the nuclear components (T_N), and potential energy operators for both the nuclear-nuclear interaction (V_{NN}) and the electron-electron interaction (V_{ee}), with the total formula for the Hamiltonian shown in Equation 1.25. Here *A* and *B* refer to the nuclei, with *i* and *j* referring to the electrons.

$$\hat{H} = -\frac{\hbar^2}{2}\sum_A \frac{1}{m_A}\nabla_A^2 - \frac{\hbar^2}{2m_e}\sum_i \nabla_i^2 + \sum_A \sum_{A>B} \frac{Z_A Z_B e^2}{r_{AB}} - \sum_A \sum_i \frac{Z_A e^2}{r_{iA}} + \sum_j \sum_{i>j} \frac{e^2}{r_{ij}}$$

$$\hat{T}_N \qquad \hat{T}_e \qquad \hat{V}_{NN} \qquad \hat{V}_{Ne} \qquad \hat{V}_{ee}$$

Equation 1.25

The first simplification to the many electron wavefunction is the Born-Oppenheimer clamped-nuclei approximation.[19] Here, the relative speed of the electron compared with that of the nucleus allows the assumption that the nucleus of an atom remains stationary while the electrons remain mobile, allowing the Schrödinger equation to be separated into nuclear and electronic components. The simplified electronic Schrödinger Hamiltonian is shown in Equation 1.26.

$$\hat{H}_{elec} = -\frac{\hbar^2}{2m_e}\sum_i \nabla_i^2 - \sum_A \sum_i \frac{Z_A e^2}{r_{iA}} + \sum_j \sum_{i>j} \frac{e^2}{r_{ij}} \qquad \textit{Equation 1.26}$$

$$\hat{T}_e \qquad \hat{V}_{Ne} \qquad \hat{V}_{ee}$$

However the electron-electron potential energy term (V_{ee}) poses some difficulty with respect to the complexity of the calculation. A solution to the Schrödinger equation for a one electron system consists of a wavefunction of 3 variables relating to the *x*, *y* and *z* coordinates (Equation 1.27). However a two electron wavefunction now has the *x*, *y* and *z* coordinates of both electron one and electron 2 to consider simultaneously (Equation 1.28). This differential equation is much more complex to compute, and increases in complexity exponentially with larger systems.

$$\psi_{(x_1 y_1 z_1)} \qquad \textit{Equation 1.27}$$

$$\psi_{(x_1 y_1 z_1 x_2 y_2 z_2)} \qquad \textit{Equation 1.28}$$

The Hartree-Fock method (HF) was the first major attempt to obtain a reasonable approximation for a many-electron wavefunction, with it being the basis for methods still used in quantum chemical calculations to this day. Initial work on the method began with Hartree a year after the publication of the Schrödinger equation in 1928,[20] and consists of several important approximations and methods.

One major component of the Hartree method is the independent electron approximation. Here, the wavefunction of electrons r_i and r_j (where *r* represents the degrees of freedom of the electron) are separated into one electron wavefunctions (ϕ), known as the Hartree product (Equation 1.29)

$$\psi(r_1 r_2) = \phi(r_1)\phi(r_2) \qquad \textit{Equation 1.29}$$

Hartree proposed to solve these one electron wavefunctions through the self-consistent field (SCF) method. This involves an approximate one electron wave equation for the i^{th} electron, which is solved for each of the electrons in the system (Equation 1.30), where V is the potential energy term giving the overall energy (E_i) for the one electron equation.

$$\left[-\frac{\hbar^2}{2m_e}\nabla_i^2 + V(r_i)\right]\phi_i = E_i\phi_i \qquad \textit{Equation 1.30}$$

This potential energy term contains the nuclear-electron interaction term (V_{Ne}) as well as a mean field term describing the interaction with the electrons with all other electrons (V_{ee} Equation 1.31). Here, r_j is described as a field of probability, averaged over the distance between r_i and r_j – essentially treating the electron interaction with the other electrons as a mean-field interaction.

$$\sum_{i\neq j}^{n} e^2 \int d^3 r_j \frac{\sum_j \left|\phi_j\left(r_j\right)\right|^2}{\left|r_i - r_j\right|} \qquad \textit{Equation 1.31}$$

As can be seen in Equation 1.31, the potential energy term (V) is required to calculate the one electron Schrödinger equation, but this requires the solution of all the other one dimensional Schrödinger equations, which also require the potential energy term (V). Hartree proposed a way around this problem with the SCF method, by first estimating the one electron wavefunctions and adding them to the potential energy term Equation 1.30. This improved version of the wavefunction is then used for all subsequent electrons, repeating until the change in energy is below a certain threshold, with the SCF calculation said to have converged at this point.

When solving the Schrödinger equation, the ideal wavefunction would be one that minimises the energy to the ground state (E_0). However the exact wavefunction is difficult to locate analytically. A starting point is the use of a trial wavefunction (ψ_{trial}), however calculation of this wavefunction may not lead to the ground state energy, giving an eigenvalue that is higher in energy than E_0. Because of this uncertainty, an average of the total energy is obtained from a large number of measurements ($\langle E \rangle$). Termed the expectation value of the energy it can be found through Equation 1.32.

$$\langle E \rangle = \frac{\int \psi_{trial}^{*} \hat{H} \psi_{trial} dxdydz}{\int \psi_{trial}^{*} \psi_{trial} dxdydz} \qquad \textit{Equation 1.32}$$

The variational principle states that for ψ_{trial}, the expectation value of the energy can never be less than the ground state (Equation 1.33). In practical terms, this means searching through all acceptable N-electron wavefunctions to find the ground state energy, and is a key component in solving many-electron wavefunction equations.

$$E_0 \leq \frac{\int \psi_{trial}^{*} \hat{H} \psi_{trial} dxdydz}{\int \psi_{trial}^{*} \psi_{trial} dxdydz} \qquad \textit{Equation 1.33}$$

While a useful way of estimating the total wavefunction, the Hartree method suffered from certain shortfalls such as not accounting for electron spin. This was fixed with the use of Slater determinants, which along with their implications and additional methods for describing the orbitals are discussed in the next few sections.

1.1.5 Many Electron Wavefunctions - Accounting for Spin

In 1922 Stern and Gerlach performed the Stern-Gerlach experiment where a magnetic field was applied to a beam silver atoms before heading into a detector. It was observed that the beam was split in two, due to spin of the electron possessing a magnetic moment which was affected by the applied magnetic field (Figure 1.6).[21]

Figure 1.6 – Depiction of the Stern-Gerlach experiment.

Electron spin (*s*) is a quantum number which possesses the value ½. The spin can be clockwise or anti-clockwise, which is given the spin magnetic quantum number (m_s), which can have the values of either +½ or -½, also written as α and β.

While the theory presented here so far has not assumed electrons have spin, a vast majority of considered systems will have more than one electron. This leads to significant problems when considering how to treat the electrons. The Pauli exclusion principle states that no electron can have the same four quantum numbers – for example in the case of helium the electrons would have the same principle (n), angular (l) and magnetic (m_l) quantum numbers representing the 1s orbital, but the electrons must possess opposite spins (m_s).

Due to the Pauli exclusion and the Aufbau principle (where electrons fill the lowest lying orbitals first), the helium atom must have two electrons of opposite spins – α and β. Therefore, electron 1 and 2 must be in one of two arrangements (Equation 1.34 and Equation 1.35). However with electrons being indistinguishable due to the Heisenberg uncertainty principle,[22] it is impossible to say which configuration is true - meaning both possibilities have an equal probability of existing.

$$\alpha(1)\beta(2) \qquad \textit{Equation 1.34}$$

$$\alpha(2)\beta(1) \qquad \textit{Equation 1.35}$$

This probability can be represented by a linear combination of the spin functions shown in Equation 1.36 and Equation 1.37, with a normalisation factor of $1/\sqrt{2}$. The interchange of the coordinates of any two electrons within a wavefunction must equal the negative of the wavefunction – i.e. the wavefunction must obey an antisymmetry principle. The exchange of electrons in Equation 1.36 gives an equivalent result in the form of Equation 1.38, violating the aforementioned principle. Performing the same operation on Equation 1.37 to form Equation 1.39 creates the negative of Equation 1.37, satisfying the antisymmetry principle, therefore, the true two electron wavefunction can be written as shown in Equation 1.40.

$$\frac{1}{\sqrt{2}}\left[\alpha(1)\beta(2)+\alpha(2)\beta(1)\right] \qquad \textit{Equation 1.36}$$

$$\frac{1}{\sqrt{2}}\left[\alpha(1)\beta(2)-\alpha(2)\beta(1)\right] \qquad \textit{Equation 1.37}$$

$$\frac{1}{\sqrt{2}}\left[\alpha(2)\beta(1)+\alpha(1)\beta(2)\right] \qquad \textit{Equation 1.38}$$

$$\frac{1}{\sqrt{2}}\left[\alpha(2)\beta(1)-\alpha(1)\beta(2)\right] \qquad \textit{Equation 1.39}$$

$$\psi(1,2)=\psi_{1s}(1)\psi_{1s}(2)\frac{1}{\sqrt{2}}\left[\alpha(1)\beta(2)-\alpha(2)\beta(1)\right] \qquad \textit{Equation 1.40}$$

A different way of writing Equation 1.40 is can be performed with the use of a Slater determinant (an example for Helium is shown in Equation 1.41), developed by Slater in 1929.[23] The determinant consists of a set of N non-interacting electrons, and each term within the determinant consists of an electron orbital multiplied by a spin function, referred to as a spin orbital.

$$\psi(1,2) = \frac{1}{\sqrt{2}}\begin{vmatrix} \psi_{1s}(1)\alpha(1) & \psi_{1s}(1)\beta(1) \\ \psi_{1s}(2)\alpha(2) & \psi_{1s}(2)\beta(2) \end{vmatrix} \qquad \textit{Equation 1.41}$$

1.1.6 Many Electron Wavefunctions – Orbitals and Basis Sets

In order to deal with molecular structures as opposed to single atoms, the wavefunction must be described in terms of molecular orbitals (MO's). The form of a molecular orbital is complex and difficult to elucidate, therefore the molecular orbital is approximated through the linear combination of atomic orbitals (LCAO) method, where atomic orbitals are combined in order to be applied to the entire molecule. For example, the wavefunctions of two atoms *A* and *B* can be combined along with an orbital coefficient (*c*) in Equation 1.42 to form an LCAO-MO.

$$\psi = c_A\psi_A \pm c_B\psi_B \qquad \textit{Equation 1.42}$$

Two hydrogen atoms (with the function for the 1s orbitals shown in Equation 1.43 and Equation 1.44), combine positively in Figure 1.7, and negatively in Figure 1.8. The probability of finding an electron, and indeed the overall 'shape' of the molecular orbital is obtained upon squaring the product of the two wavefunctions (Figure 1.9).

$$\psi_A = \frac{1}{\sqrt{\pi a_0^3}} e^{\frac{-r_A}{a_0}} \qquad \textit{Equation 1.43}$$

$$\psi_B = \frac{1}{\sqrt{\pi a_0^3}} e^{\frac{-r_B}{a_0}} \qquad \textit{Equation 1.44}$$

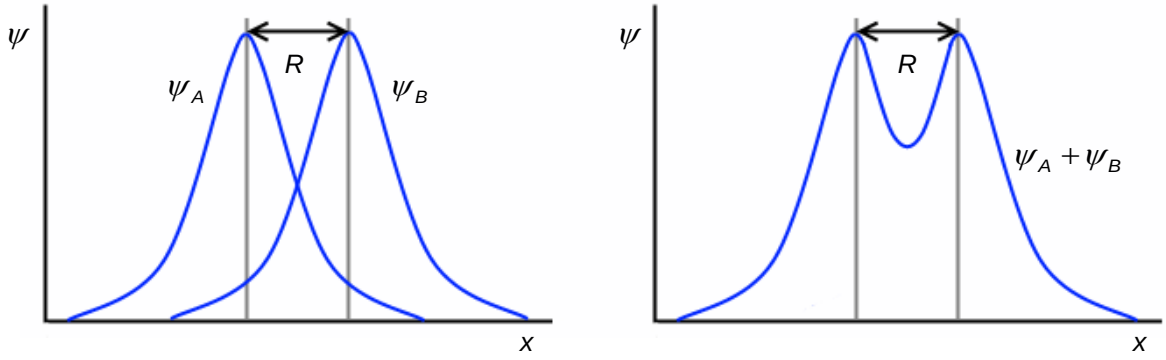

Figure 1.7 – Representation of positive wavefunction addition.

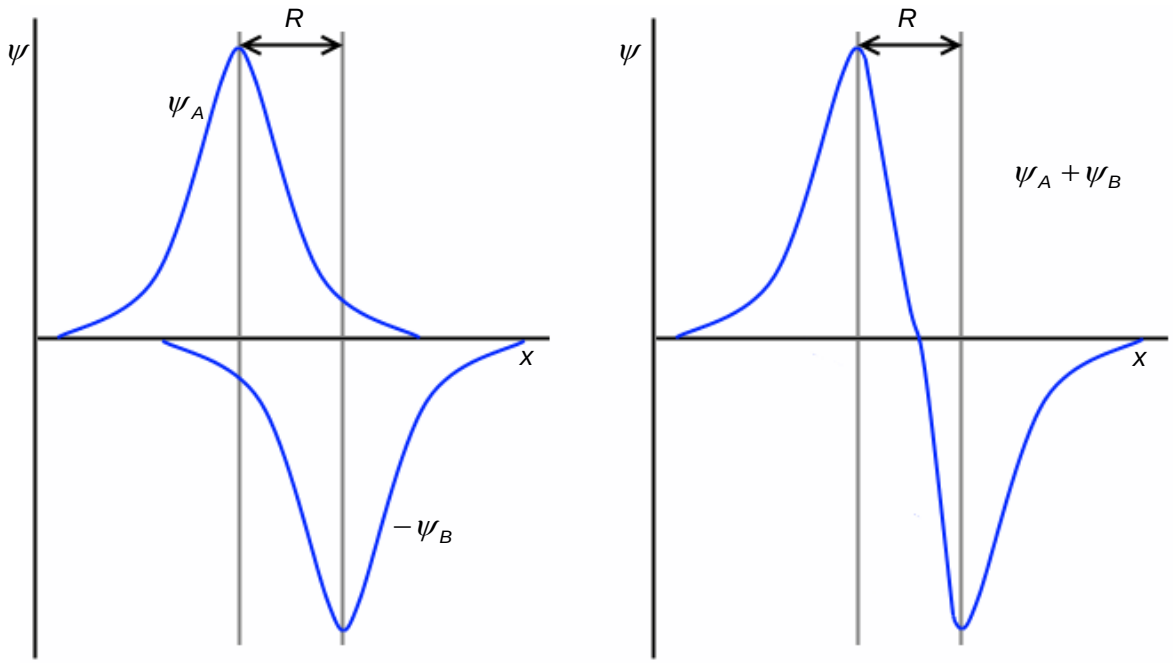

Figure 1.8 – Representation of negative wavefunction addition.

The probability of the positive and negative combinations of the atomic wavefunctions lead to the bonding σ and the antibonding σ^* orbitals, with electron density and a node located in each combination respectively.

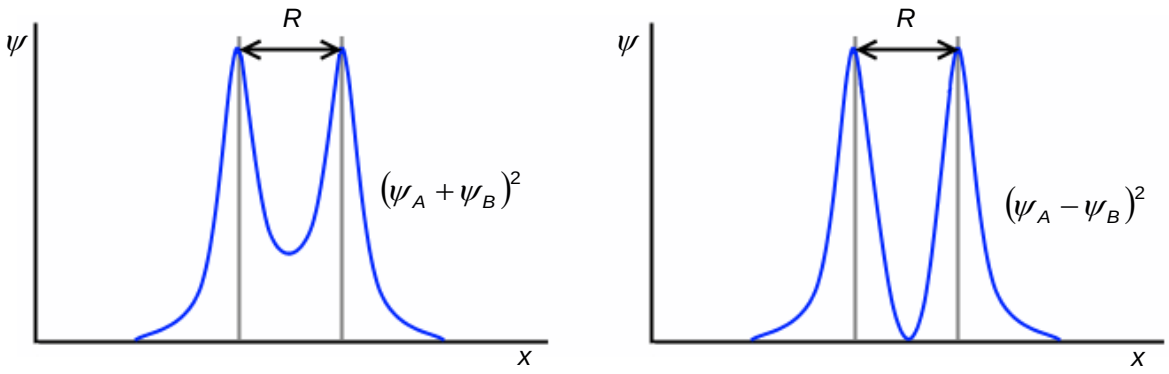

Figure 1.9 – Square of the wavefunctions, bonding (left) and antibonding (right).

A total molecular orbital is the sum of all coefficients (*c*) and atomic orbital functions (ψ_f) (Equation 1.45), with the functions being known as a basis set. The basis set can employ Slater- or Gaussian-type orbitals to describe the atomic orbital functions.

$$\psi = \sum c\psi_f \qquad \textit{Equation 1.45}$$

First proposed by Slater in 1930,[24] Slater type orbitals (STO's) take the general form seen in Equation 1.46. Here, *N* is a normalisation constant, *n* is the principal quantum number, *r* is the position, ζ is the effective charge of the nucleus, dictating the size of the orbital, with Y_{lm} describing the angular part of the wavefunction which determines the shape of the orbital.

$$\psi_f^{STO} = Nr^{n-1}e^{-\zeta r}Y_{lm}(\Theta,\phi) \qquad \textit{Equation 1.46}$$

However STO's are difficult to compute when used in many-centre integrals. As a result, much more computationally efficient methods were developed with the use of Gaussian-type orbitals (GTO's),[25] with the general formula shown in Equation 1.47. Here a Cartesian-type GTO is shown as opposed to a spherical-harmonic orbital shown in Equation 1.46, with *x*, *y* and *z* being the coordinates and *l*, *m* and *n* being integers (with (l+m+n=0) for an s orbital, (l+m+n=1) for a p orbital etc.).

$$\psi_f^{GTO} = Nx^l y^m z^n e^{-\zeta r} Y_{lm}(\Theta, \phi)$$ *Equation 1.47*

While less computational efficient, STO's more closely mirror the behaviour of the hydrogen atom, with a correct discontinuous slope at the cusp when r → 0 and more realistic exponential decay at the boundary of the function (Figure 1.10).

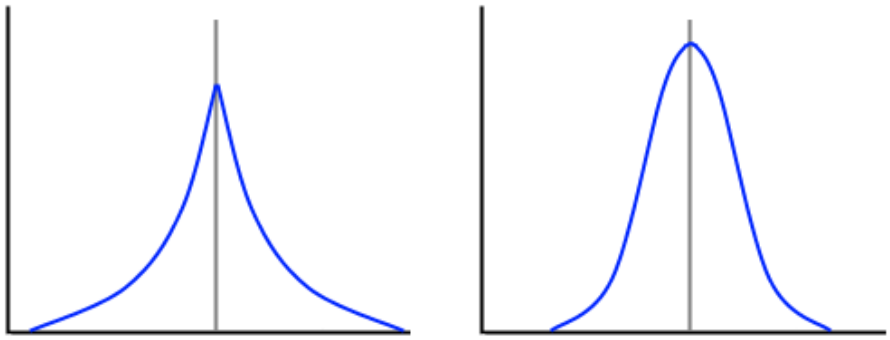

Figure 1.10 – Simple depiction of Slater- (left) and Gaussian- (right) type function.

As a result, many GTO's are used in conjunction with one another in order to better mimic the behaviour of STO's, with contracted GTO basis sets being combined to form a single contracted Gaussian function (Figure 1.11).

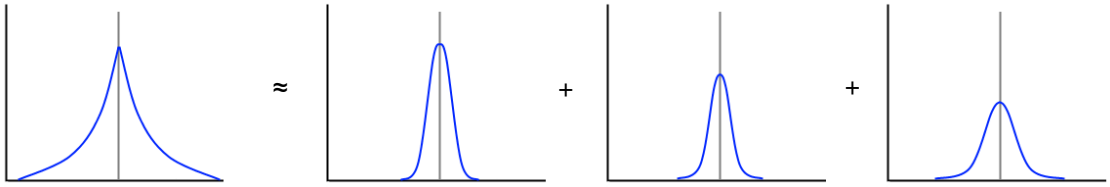

Figure 1.11 – Simple depiction of a contracted GTO basis function.

Basis sets can be classified by the number of functions per orbital within an atom. A minimal basis set has one function per orbital of an atom, with this over-simplistic model no longer generally used. Double-ζ and triple-ζ functions possess two and three functions per orbital respectively, with split-valence basis sets having one basis function for the core orbitals, and two basis functions for the valence orbital. More basis functions allow for a more accurate description of molecular orbitals, taking into account changes in orbital shape between bonded and non-bonded atoms.

Additionally basis sets can possess polarization functions, where orbital functions for higher angular momentum than those 'naturally' found at a particular element are added – for example a d-orbital is added to all heavy non-hydrogen atoms and a p-orbital to hydrogen atoms. This allows atoms to be polarized away from the nucleus, thus giving a more realistic portrayal of bonding in molecules.

1.1.7 Many Electron Wavefunctions –Hartree-Fock Theory

With the introduction of Slater determinants Hartree theory was modified by Fock in 1930, providing a corrected formalism of the one-electron orbital many electron wavefunction. The wavefunction, described as a Slater determinant (Φ_{SD} – Equation 1.48) is simplified in terms of one electron spin orbitals, composed of a spatial orbital ($\vec{x}_n$) and a spin function (χ_n).

$$\psi_0 \approx \Phi_{SD} = \frac{1}{\sqrt{N!}} \begin{vmatrix} \chi_1(\vec{x}_1) & \chi_2(\vec{x}_1) & \cdots & \chi_N(\vec{x}_1) \\ \chi_1(\vec{x}_2) & \chi_2(\vec{x}_2) & \cdots & \chi_N(\vec{x}_2) \\ \vdots & \vdots & & \\ \chi_1(\vec{x}_N) & \chi_2(\vec{x}_N) & \cdots & \chi_N(\vec{x}_N) \end{vmatrix} \qquad \textit{Equation 1.48}$$

Here, the Fock operator (*F*) (Equation 1.49) is described in terms of the one electron operator (*h*) containing electron kinetic and nuclear-electron potential terms, and the Hartree-Fock potential (V_{HF}) acting upon the Slater determinant.

$$\hat{F}_i = \hat{h} + V_{HF} \qquad \textit{Equation 1.49}$$

While similar to the Hartree equation, the (V_{HF}) term handles electron-electron coulombic interaction in a similar manner, only with extra terms to take into account the antisymmetry provided by the use of a Slater determinant. (V_{HF}) can be split into coulombic (*J*) and exchange (*K*) terms shown in Equation 1.50 and Equation 1.51 respectively.

$$J = \sum_{i<j}^{n} e^2 d^3 r_i d^3 r_j \int \frac{|\chi_i(x_i)|^2 |\chi_j(x_j)|^2}{|r_i - r_j|} \qquad \textit{Equation 1.50}$$

$$K = \sum_{i<j}^{n} e^2 d^3 r_i d^3 r_j \int \frac{\chi_i(x_i)\chi_j(x_j)\chi_i(x_j)\chi_j(x_i)}{|r_i - r_j|} \qquad \textit{Equation 1.51}$$

The coulombic potential term (*J*) is identical to the electron-electron potential term seen in the Hartree equation. However the exchange term (*K*) exists purely as a result of the spin functions present within the Slater determinant, with the electrons in the spin orbitals χ_i and χ_j being exchanged. This term describes the interaction of electrons of parallel spins (antiparallel spins would cancel), with the result being that two electrons with parallel spins repel one another.

The equations and methods discussed here and in previous sections briefly represent what occurs in the Hartree-Fock (HF) equation, which was the first tractable solution to a many electron wavefunction. However HF theory has several significant issues, which lead to the development and use of DFT.

One of the largest issues with HF theory is the lack of a description for electron correlation, which is the difference between the exact energy and the HF energy (Equation 1.52). HF theory treats electron interaction with all other electrons in an averaged way, rather than an instantaneous interaction which would occur in the real system. This leads to not only a difference in energy, but a failure to describe physical effects such as dispersion. Attempts at correcting for the correlation energy include post-HF methods such as the Møller–Plesset and configuration interaction methods, as well as with DFT.

$$E_C = E_{exact} - E_{HF} \qquad \textit{Equation 1.52}$$

A final issue is the associated computational cost of solving a many-electron wavefunction such as HF theory, where expense increases exponentially with the number of electrons within the system. For example HF scales with N^4, with MP2 scaling as N^5 (where N = the number of basis functions - i.e. the number of electrons/size of the system). This becomes prohibitive when dealing with large systems such as the organometallic complexes studied here, and is another reason for the use of DFT in this thesis. However this does not make HF theory irrelevant, in fact many of the key concepts discussed in the preceding sections are also used within DFT itself.

1.1.8 Density Functional Theory – Beginnings and Hohenberg-Kohn Theory

The key concept of density functional theory is the electron density of the molecule. This is a physically measurable phenomena of an atom or molecule, and is related to the square of the wavefunction ($|\psi|^2$) which gives the probability of finding an electron. Here, the multiple integral over all spin coordinates and spatial variables ($\vec{x}_n$) of the square of the wavefunction will give the number of electrons (*n*) (Equation 1.53). Performing the same multiple integral operation over all spin coordinates and all but one spatial variable ($\vec{r}_n$) gives what is termed the electron density (Equation 1.54).

$$n = N\int\cdots\int|\psi(\vec{x}_n)|d\vec{x}_1 d\vec{x}_2\ldots d\vec{x}_n \qquad \textit{Equation 1.53}$$

$$\rho(\vec{r}) = N\int\cdots\int|\psi(\vec{x}_n)|ds_1 d\vec{x}_2\ldots d\vec{x}_n \qquad \textit{Equation 1.54}$$

The electron density ($\rho(\vec{r})$), is the probability of finding any of the electrons (as electrons are indistinguishable from one another and $\vec{r}$ possesses no spin component) within a volume $d\vec{r}$. As this represents just one electron, the probability of finding any electron at this position is simply the number of electrons (*n*) multiplied by the probability.

An ancestor to DFT is the Thomas-Fermi model developed in 1927,[26, 27] which gave the energy of a system purely through the use of the electron density. The general formula of the Thomas-Fermi model is shown in Equation 1.55, and consists of a kinetic energy component (T_{TF}) and classical electron-nuclear (U_{eN}) and electron-electron (U_{ee}) potential energy components. The kinetic energy component is an approximation, built upon the uniform electron gas (UEG) model, where the density is represented by an evenly distributed electron cloud.

$$E_{TF} = T_{TF} + U_{eN} + U_{ee} \qquad \textit{Equation 1.55}$$

However the approximation for the kinetic energy is poor and completely ignores exchange and correlation effects. It was found to only be useful with atomic systems, with the model being unable to describe molecular bonding.

DFT itself began in 1964 with the Hohenberg–Kohn theorems developed by Hohenberg and Kohn,[28] and consists of two main themes – the proof of existence, and use of the variational principle to find the ground state energy. The first theorem states that the electron density of a system determines the Hamiltonian operator and therefore the entire system. This relation of the density to the Hamiltonian exists by way of the nuclear electron potential (V_{Ne}), (referred to hereon as the external potential (V_{ext}) – Equation 1.56), and consists of the coulombic nuclear-electron interaction for *M* nuclei.

$$V_{ext} = \sum_{A}^{M} \sum_{i}^{N} \frac{Z_A e^2}{r_{iA}} \qquad \textit{Equation 1.56}$$

The electronic Hamiltonian (Equation 1.57) is contains V_{ext}, but also the electron kinetic energy (T) and electron-electron interaction potential (V_{ee}). While T and V_{ee} are static with respect to the position of the atoms within the molecule, (V_{ext}) directly depends upon the status of the system, and it is this term which allows the identification of the wavefunction, and therefore the total energy of the entire system.

$$\hat{H} = \hat{T} + \hat{V}_{ee} + \hat{V}_{ext} \qquad \textit{Equation 1.57}$$

This hypothesis was proven by Hohenberg and Kohn with the use of a contradictory proof. The proof begins by considering two different external potentials V_{ext} and V'_{ext}, which give the same electron density. As shown above, the external potential dictates the form of the Hamiltonian, which in turn dictates the form of the wavefunction and finally the electron density.

Therefore each external potential will have a distinct Hamiltonian *H* and *H′* and wavefunction ψ and ψ' associated with it. ψ' can be used as a trial wavefunction with *H* as well as *H′*, with the expectation value of *H* being higher than with *H′* (Equation 1.58). The two expectation values can be equated by the addition of the difference in the Hamiltonians (Equation 1.59), with the difference expanded in Equation 1.60.

$$E_0 < \left\langle \psi' \middle| \hat{H} \middle| \psi' \right\rangle > \left\langle \psi' \middle| \hat{H}' \middle| \psi' \right\rangle \qquad \textit{Equation 1.58}$$

$$E_0 < \left\langle \psi' \middle| \hat{H} \middle| \psi' \right\rangle = \left\langle \psi' \middle| \hat{H}' \middle| \psi' \right\rangle + \left\langle \psi' \middle| \hat{H} - \hat{H}' \middle| \psi' \right\rangle \qquad \textit{Equation 1.59}$$

$$E_0 < E'_0 + \left\langle \psi' \middle| \hat{T} + \hat{V}_{ee} + \hat{V}_{ext} - \hat{T} - \hat{V}_{ee} - \hat{V}'_{ext} \middle| \psi' \right\rangle \qquad \textit{Equation 1.60}$$

As *T* and V_{ee} are independent of V_{ext}, they are equivalent and cancel one another in each side of the equation. Expansion of the bra-ket notation then gives Equation 1.61. Similarly, the process can be repeated by exchanging the variables in Equation 1.59 to give Equation 1.62. Addition of Equation 1.61 and Equation 1.62 finally gives Equation 1.63.

$$E_0 < E'_0 + \int \rho(\vec{r}) \{ \hat{V}_{ext} - \hat{V}'_{ext} \} d\vec{r} \qquad \textit{Equation 1.61}$$

$$E'_0 < E_0 - \int \rho(\vec{r}) \{ \hat{V}_{ext} - \hat{V}'_{ext} \} d\vec{r} \qquad \textit{Equation 1.62}$$

$$E_0 + E'_0 < E'_0 + E_0 \qquad \textit{Equation 1.63}$$

Clearly Equation 1.63 cannot be correct - therefore the electron density is proven to be directly related to the external potential. As the Hamiltonian and the energy are directly obtainable from the electron density, a new expression can be written in Equation 1.64, where E_{ee} and E_{Ne} are electron-electron and nuclear-electron terms. Separation of the V_{ext} independent values T and E_{ee} into the Hohenberg-Kohn functional (F_{HK}) gives Equation 1.65, which would allow for the computation of the exact Schrödinger equation to give the energy of the system - however there is no way to know what the form of the Hohenberg-Kohn functional is.

$$E[\rho] = T[\rho] + E_{ee}[\rho] + E_{Ne}[\rho] \qquad \textit{Equation 1.64}$$

$$E[\rho] = \int \rho(\vec{r})\hat{V}_{ext}d\vec{r} + F_{HK}[\rho] \qquad \textit{Equation 1.65}$$

The second Hohenberg-Kohn theorem relates to the variational principle (shown previously in section 1.1.4), and states that any trial electron density (ρ_{trial}) will always be equal to or higher than the ground state density (Equation 1.66).

$$E_0 \leq E[\rho_{trial}] = \int \rho_{trial}(\vec{r})\hat{V}_{Ne}d\vec{r} + F_{HK}[\rho_{trial}] \qquad \textit{Equation 1.66}$$

While the Hohenberg-Kohn theorems are a proof of concept, the actual workings of the equation (such as the identity of F_{HK}) are not known. This was and remains a continuing area of study in the development of DFT, with further approaches being detailed below.

1.1.9 Density Functional Theory – Kohn-Sham Theory

A year after publication of the Hohenberg-Kohn theorem, Kohn and Sham produced the Kohn-Sham (KS) equations – a method which attempted to identify the nature of the functional shown in the Hohenberg-Kohn proof.[29] The method took advantage of tools seen with the development of HF theory, and consists of two major approximations.

The first approximation is to assume that the electrons exist as a fictitious system of non-interacting electrons in an averaged potential of all the other electrons. It is also assumed that this non-interacting system possesses the exact same density as a system where the electrons do interact. This can be represented exactly as a Slater determinant (Θ_S) (Equation 1.67), which consists of a series of electrons ($\vec{x}_N$) and spin orbitals (φ), termed Kohn-Sham orbitals. The electrons can then be dealt with in a similar fashion to that of HF theory with one-electron orbitals here combining to give the total density of the system.

$$\Theta_S = \frac{1}{\sqrt{N!}} \begin{vmatrix} \varphi_1(\vec{x}_1) & \varphi_2(\vec{x}_1) & \cdots & \varphi_N(\vec{x}_1) \\ \varphi_1(\vec{x}_2) & \varphi_2(\vec{x}_2) & \cdots & \varphi_N(\vec{x}_2) \\ \vdots & \vdots & & \\ \varphi_1(\vec{x}_N) & \varphi_2(\vec{x}_N) & \cdots & \varphi_N(\vec{x}_N) \end{vmatrix} \qquad \textit{Equation 1.67}$$

The second major approximation was a rearrangement of terms in such a way that all of the unknown variables were collated in a single element. The HK functional seen in Equation 1.66 can be divided as per Equation 1.68.

$$F[\rho] = T_S[\rho] + J[\rho] + E_{XC}[\rho] \qquad \textit{Equation 1.68}$$

Here, J is the coulombic electron-electron interaction, described in the same way as in HF theory, with an electron interacting with a mean field of the remaining electrons. T_s is the sum of all of the single electron kinetic energy terms (Equation 1.69), with E_{XC} being known as the exchange and correlation energy, which contains all of the remaining instantaneous electron-electron interaction terms.

The true kinetic energy (T) of the real system is equal to the one electron kinetic energy term (T_s) together with an unknown quantity (T_c) which adds to the full kinetic energy. Additionally the true energy of electron-electron interaction (E_{ee}) is equal to (J) plus the non-classical contribution (E_{ncl}). The full E_{XC} term contains this unknown quantity, and is displayed in Equation 1.70.

$$T_S = \sum_i^N -\frac{\hbar^2}{2m_e}\left\langle \varphi_i \middle| \nabla^2 \middle| \varphi_i \right\rangle \qquad \textit{Equation 1.69}$$

$$E_{XC}[\rho] \equiv (T[\rho] - T_S[\rho]) + (E_{ee}[\rho] - J[\rho] = T_C[\rho] + E_{ncl}[\rho] \qquad \textit{Equation 1.70}$$

The exact form of E_{XC} is unknown, with methods for approximating it constituting a significant effort in DFT development. These methods will be discussed in the next section.

1.1.10 Exchange-Correlation Functionals

The accuracy of DFT methods is based upon the identity of the exchange-correlation functional (E_{XC}), however as there is no systematic way to identify the exact nature of it an approximation must be used. Three methods of calculating E_{XC} shall be presented here – the local density approximation (LDA), the generalized gradient approximation (GGA) and finally hybrid functionals. The two functionals used in this thesis are GGA (BP86[30, 31]) and hybrid (PBE0[32-35]) functionals.

The local density approximation has the central principle of a uniform electron gas (mentioned previously in section 1.1.8), where the electrons are assumed to be averaged evenly over space. The LDA form of E_{XC} can be written as Equation 1.71, with $\varepsilon_{XC}(\rho(\vec{r}))$ being the exchange correlation energy per particle in a uniform electron gas of density ($\rho(\vec{r})$).

$$E_{XC}^{LDA}[\rho] = \int \rho(\vec{r})\varepsilon_{XC}(\rho(\vec{r}))d\vec{r} \qquad \textit{Equation 1.71}$$

$\varepsilon_{XC}(\rho(\vec{r}))$ can be further split into both the exchange (ε_X) and correlation (ε_C) components (Equation 1.72). A form of (ε_X) for a local homogenous electron density is shown in Equation 1.73, and was first proposed as a simple approximation to the exact-exchange component in HF theory.[36]

$$\varepsilon_{XC}(\rho(\vec{r})) = \varepsilon_X(\rho(\vec{r})) + \varepsilon_C(\rho(\vec{r})) \qquad \textit{Equation 1.72}$$

$$\varepsilon_X = -\frac{3}{4}\sqrt[3]{\frac{3\rho(\vec{r})}{\pi}} \qquad \textit{Equation 1.73}$$

Unlike the ε_X term, no explicit expression exists for ε_C, but several approximations are known. Based on highly accurate Monte-Carlo simulations, several different analytical models have been proposed which interpolate between different known densities. Additionally the LDA can be modified to include spin through the local spin density approximation (Equation 1.74).

$$E_{XC}^{LSDA}[\rho_\alpha, \rho_\beta] = \int \rho(\vec{r})\varepsilon_{XC}(\rho_\alpha(\vec{r}), \rho_\beta(\vec{r}))d\vec{r} \qquad \textit{Equation 1.74}$$

While the LDA approximation models systems such as ionic salts or metal bonding well, the model fails for systems which do not resemble a uniform electron density. This can be solved with the use of GGA functionals, where it models the change in density ($\nabla\rho$) to more closely resemble the real system (Equation 1.75). Usually the gradient correction is applied to LDA-type functionals, along with cut-off parameters to better model long-range interactions.

$$E_{XC}^{GGA}[\rho_\alpha, \rho_\beta] = \int f(\rho_\alpha(\vec{r}), \rho_\beta(\vec{r}), \nabla\rho_\alpha, \nabla\rho_\beta)d\vec{r} \qquad \textit{Equation 1.75}$$

The aforementioned BP86 functional employs Becke's 1988 exchange and Perdew's 1986 correlation components. The former is given by Equation 1.76, where σ denotes spin, S_σ is a local inhomogeneity parameter, and β is an empirical parameter which was found to fit the exact exchange energies of several noble gasses. The latter (in a simplified form) is given in Equation 1.77, with the correlation energy from the uniform electron gas (first integral) modified to form the GGA correlation functional. This also contains empirical parameters, fitted to the correlation of the neon atom.

$$E_X^{GGA} = E_X^{LDA} - \beta \sum_\sigma \int \rho_\sigma^{\frac{4}{3}} \frac{s_\sigma^2}{(1 + 6\beta s_\sigma \sinh^{-1} s_\sigma)} d\vec{r} \qquad \textit{Equation 1.76}$$

$$E_{XC}^{GGA}[\rho_\alpha, \rho_\beta] = \int d\vec{r} \rho \varepsilon_C(\rho_\alpha, \rho_\beta) + \int d\vec{r} d^{-1} e^{-\Phi} C(n) s_\sigma^2 \qquad \textit{Equation 1.77}$$

The final type of functional mentioned here is the hybrid functional, which uses the exact exchange energy from the KS orbitals as opposed to an approximation. The approximated correlation energy is then added to make up the full electron-correlation term, with many functionals employing weighting ratios to better parameterize the functional.

The PBE0 functional is one such functional, with the general formula given below in Equation 1.78. The PBE functional itself contains a simplified modification of the non-empirical PW91 exchange and correlation functionals,[37] with the hybrid PBE0 functional using 25% exact HF exchange.

$$E_{XC}^{PBE0} = E_{XC}^{PBE} + 0.25(E_X^{HF} - E_X^{PBE}) \qquad \textit{Equation 1.78}$$

1.1.11 General DFT Procedure

While the basic machinery of DFT has been described above, the general procedure for running a typical calculation has not. The KS equation was summarised in Equation 1.68, with a one electron kinetic, electron-electron coulombic, and exchange-correlation terms. Analogous to the HF one electron operator in Equation 1.30, the KS operator ($\hat{f}^{KS}$) can interact with the one electron orbitals of the Slater determinant (φ_i) to give the one electron energy (ε_i) in Equation 1.79, and expanded in Equation 1.80. Here (V_{XC}) is the functional derivative of (E_{XC}) (Equation 1.81),

$$\hat{f}^{KS}\varphi_i = \varepsilon_i\varphi_i \qquad \textit{Equation 1.79}$$

$$\left(-\frac{\hbar^2}{2m_e}\nabla^2 + \left[\sum_j^N \int \frac{\left|\varphi_j(\vec{r}_2)\right|^2}{r_{12}} d\vec{r}_2 + V_{XC}(\vec{r}_1) - \sum_A^M \frac{Z_A}{r_{1A}}\right]\right)\varphi_i = \varepsilon_i\varphi_i \qquad \textit{Equation 1.80}$$

$$V_{XC}(r) \equiv \frac{\delta E_{XC}[\rho(r)]}{\delta\rho(r)} \qquad \textit{Equation 1.81}$$

Equation 1.80 will give the KS molecular orbitals which will in turn provide the ground-state electron density for a specific exchange-correlation functional, as the exact ground state density depends on knowing the exact form of V_{XC}. Much like in HF theory, the KS orbitals are defined using the LCAO method, which linearly expands the KS orbital using a number (L) of basis functions (η_u) and coefficients (c) (Equation 1.82). The basis functions are described with basis sets, again much like HF theory. While modern basis sets are often parameterised for DFT, the use of HF-specific basis sets are often comparable to their DFT counterparts.[38]

$$\varphi_i = \sum_{\mu=1}^{L} c_{\mu i}\eta_u \qquad \textit{Equation 1.82}$$

Equation 1.79 can now be written as Equation 1.83, and gives *L* equations when multiplied by an arbitrary basis function (η_v) and integrated over space (Equation 1.84).

$$\hat{f}^{KS}(\vec{r}_1)\sum_{\mu=1}^{L} c_{\mu i}\eta_u(\vec{r}_1) = \varepsilon_i \sum_{\mu=1}^{L} c_{\mu i}\eta_u(\vec{r}_1) \qquad \textit{Equation 1.83}$$

$$\sum_{\mu=1}^{L} c_{\mu i}\int \eta_v(\vec{r}_1)\hat{f}^{KS}(\vec{r}_1)\eta_u(\vec{r}_1)d\vec{r}_1 = \varepsilon_i \sum_{\mu=1}^{L} c_{\mu i}\int \eta_v(\vec{r}_1)\eta_u(\vec{r}_1)d\vec{r}_1 \qquad \textit{Equation 1.84}$$

The integrals on the left and right hand side of the equation both define an *L* by *L* dimensional matrix, known as the Kohn-Sham (***F*^{KS}**) and overlap matrix (***S***) respectively. Additionally the expansion coefficients (*c*) and the orbital energies (ε_i) can also be described by an *L* dimensional matrix ***C*** and $\boldsymbol{\varepsilon}$ respectively, giving a matrix equation (Equation 1.85).

$$\boldsymbol{F^{Ks}C = SC\varepsilon} \qquad \textit{Equation 1.85}$$

The electron-electron coulombic term (*J*) in the KS equation requires the electron density (ρ) which can be expressed in terms of expansion coefficients and basis functions (Equation 1.86), with the coefficients often collected together in a density matrix (***P***). The coulombic term can then be expressed as Equation 1.87

$$\rho(\vec{r}) = \sum_{i}^{N}\left|\varphi_i(\vec{r})\right|^2 = \sum_{i}^{N}\sum_{\mu}^{L}\sum_{\nu}^{L} c_{\mu i}c_{\nu i}\eta_\mu(\vec{r})\eta_\nu(\vec{r}) \qquad \textit{Equation 1.86}$$

$$J = \sum_{\lambda}^{L}\sum_{\sigma}^{L} P_{\lambda\sigma}\int\int \eta_\nu(\vec{r}_1)\eta_\mu(\vec{r}_1)\frac{1}{r_{12}}\eta_\lambda(\vec{r}_2)\eta_\sigma(\vec{r}_2)d\vec{r}_1 d\vec{r}_2 \qquad \textit{Equation 1.87}$$

The calculation of *J* requires the calculation of L^4 integrals, which is a significant number. In HF theory the calculation of *J* was tied to the calculation of the exchange component, whereas here they are no longer connected allowing for a more efficient calculation of the electron-electron coulombic interaction through the use of atom-centred auxiliary basis sets. As the coefficients and functions of λ and σ are equivalent to the electron density with respect to ($\vec{r}_2$), Equation 1.87 can be rewritten as Equation 1.88. Now an approximate density ($\tilde{\rho}$) can be calculated *via* the use of Equation 1.89, allowing the coulombic term to be expressed as Equation 1.90. This term now requires only L^2K integrals as opposed to L^4. This simplification is provided in the TURBOMOLE program as the RI-J method, incorporating the resolution of the identity approximation in the calculation of *J*.[39]

$$J = \eta_\nu(\vec{r}_1)\eta_\mu(\vec{r}_1)\frac{\rho(\vec{r}_2)}{r_{12}}d\vec{r}_1 d\vec{r}_2 \qquad \textit{Equation 1.88}$$

$$\rho(\vec{r}) \approx \tilde{\rho}(\vec{r}) = \sum_{\kappa}^{K} c_\kappa \omega_\kappa(\vec{r}) \qquad \textit{Equation 1.89}$$

$$J = \sum_{\kappa}^{K} \iint \frac{\eta_\nu(\vec{r}_1)\eta_\mu(\vec{r}_1)\omega_\kappa(\vec{r}_2)}{r_{12}}d\vec{r}_1 d\vec{r}_2 \qquad \textit{Equation 1.90}$$

Quasi-relativistic effective core potentials (ECP's) are used to describe the non-valence core electron density of large atoms such as transition metals as a static pseudo-potential. While reducing the overall computational cost significantly, the use of ECP's with calculations of transition metal complexes has been shown to produce very similar results to that of expensive all-electron methods such as the zero-order regular approximation (ZORA).[38]

A simplified schematic of a typical DFT calculation is shown in Figure 1.12.

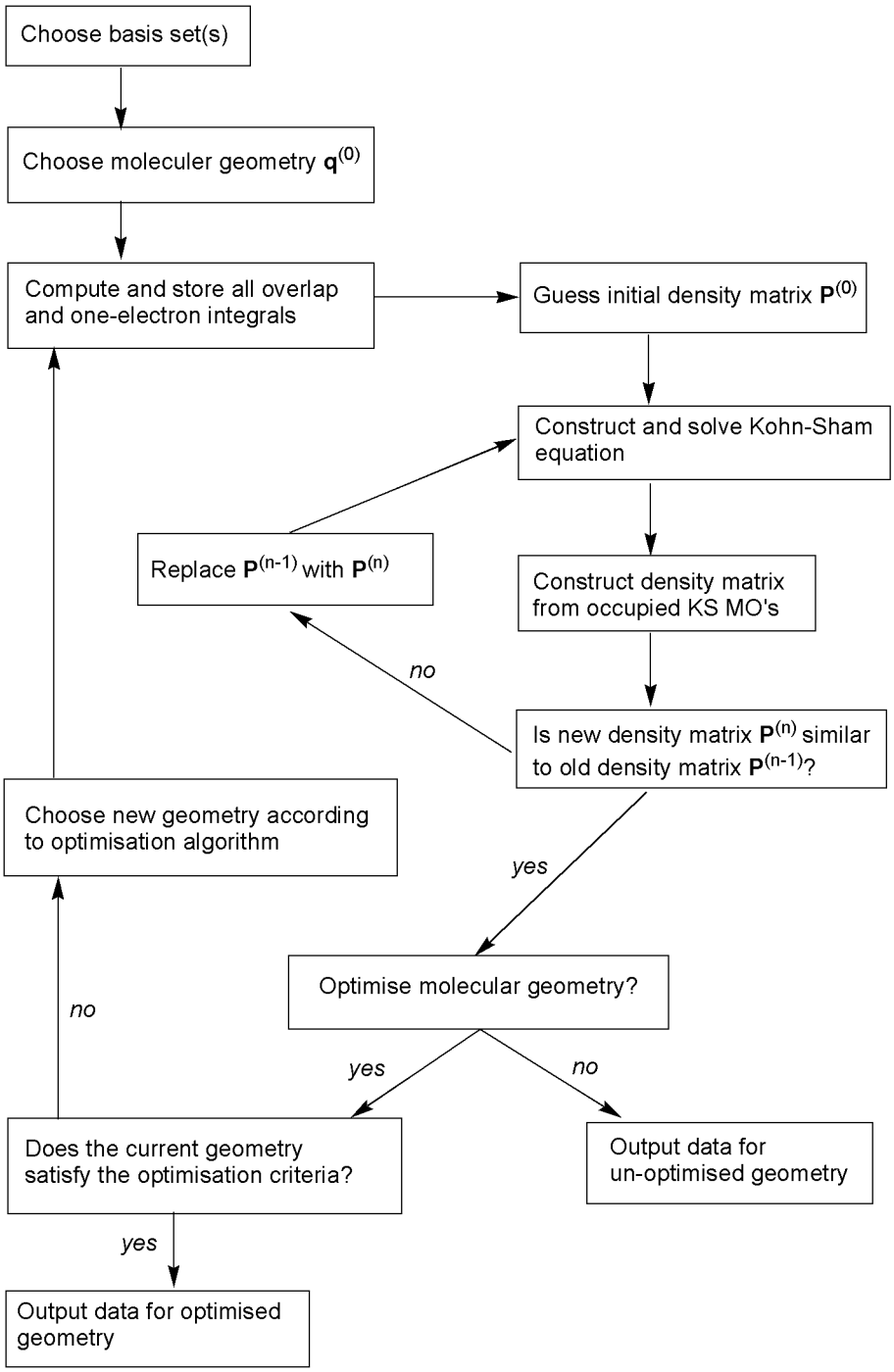

Figure 1.12 – Typical DFT calculation procedure.[3]

The KS calculations are then performed in a similar manner to that used in the HF SCF method. Here, while the density is determined from a solution of the KS orbitals, the density itself is needed to determine the nature of the orbitals themselves. Therefore KS equations are solved using an approximate density, which is then compared to the last iteration of the density matrix. If the change in energy of the iteration is below a certain threshold then the SCF is once again classed as having converged.

Once the SCF is converged, the geometry of the structure can be modified by the use of an optimisation algorithm, which is used to alter the atomic coordinates of a structure to lower the energy until no further change is observed, at which point the optimisation is also said to have converged, thus completing the calculation.

1.1.12 Vibrational Spectrum, Zero Point Energy, Thermodynamic and Entropic Corrections

Calculating the electronic energy of a molecule is still a significant theoretical distance away from the real empirical system where reactions are monitored using enthalpies and Gibbs free energy. Therefore the theoretical model must incorporate thermal and entropic corrections, which will be detailed in this section. Additionally a vibrational spectrum is desirable in order to identify whether or not a molecular geometry is a transition state, or simply to compare it to experimental data. The whole process initially begins with calculation of the vibrational frequency with the use of the aoforce[40] module of the TURBOMOLE program.

In the example of a simple diatomic molecule (Figure 1.13), the potential energy increases and decreases with respect to the distance (R) between the two nuclei. As R decreases from the equilibrium distance (R_e), the potential energy also increases. This is also true when R is increased, but levels out as the nuclei no longer interact with one another. The shape of the potential energy curve and position of R_e is defined by the force constant (k), in a similar manner to the flexibility of a spring. The diatomic molecule also vibrates, with the vibrational energy levels also shown in the diagram.

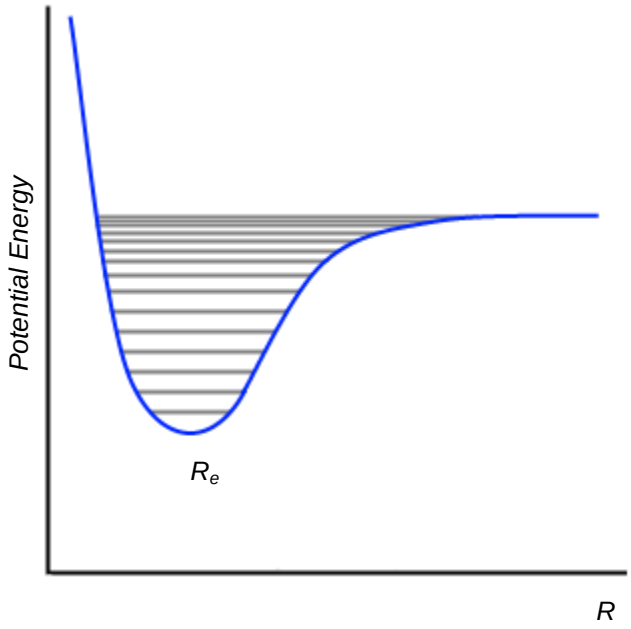

Figure 1.13 – Schematic of a potential energy of a diatomic molecule, showing vibrational energy levels (grey lines).

The model above represents what is known as an anharmonic oscillator. However to simplify the vibrational spectrum calculation, the harmonic oscillator approximation is employed, where instead of an asymmetric curve an even parabola is used – with vibrational energy levels equally spaced to infinity (Figure 1.14).

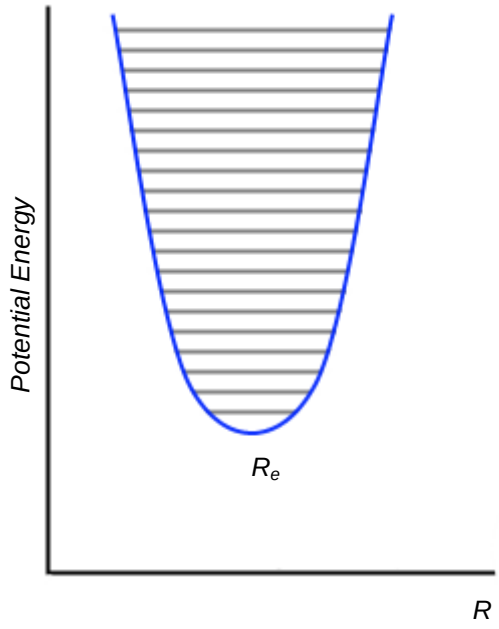

Figure 1.14 – Harmonic oscillator and vibrational energy levels (grey lines).

The vibrational energy levels are given by Equation 1.91, with *v* being the vibrational quantum number (*v* = 0,1,2 etc) and ν given in Equation 1.92 where μ is the effective mass of the two nuclei. The lowest vibrational energy level where *v* = 0 is the minimum amount of energy that a molecule can have, and the difference between it and the energy at (R_e) – the lowest point on the potential energy surface is known as the zero point energy (ZPE).

$$E_v = \left(v + \frac{1}{2}\right) h\nu \qquad \textit{Equation 1.91}$$

$$\nu = \frac{1}{2\pi}\left(\frac{k}{\mu}\right)^{\frac{1}{2}} \qquad \textit{Equation 1.92}$$

TURBOMOLE calculates the vibrational spectrum through the use of a Hessian matrix, whose elements consist of second derivatives of the total energy with respect to the Cartesian coordinates. The hessian matrix is then mass weighted, with the diagonalization of this matrix giving $(k/\mu)^{½}$. This is then used to calculate the vibrational spectrum with the use of the harmonic oscillator approximation.

To obtain thermodynamic functions, the ensemble partition function Q, is reduced to a molecular partition function q using the ideal gas assumption. The molecular energy can then be expressed as separable electronic (q_{elec}), translational (q_{trans}), rotational (q_{rot}) and vibrational (q_{vib}) elements, with (q_{vib}) using the calculated vibrational energy levels obtained from the Hessian matrix. These elements are further used to calculate the chemical potential, using Equation 1.93. The chemical potential is then added to the electronic SCF energy in order to obtain the absolute Gibbs free energy of the molecule.[3]

$$Chem.pot. = ZPE - RT.\ln(q_{trans}.q_{rot}q_{vib}) \qquad \textit{Equation 1.93}$$

1.1.13 Solvation Models with the Conductor-Like Screening Model (COSMO)

All methods discussed so far have been described in the gas phase, without consideration of interactions with solvent molecules. For neutral and intramolecular reactions the gas phase approximation is often sufficient. However when modelling reactions involving charged or heavily polarised molecules, calculations in the gas phase no longer accurately describe the modelled system. Therefore the effect of solvation must be included through a solvent correction to the gas phase energy either during or post SCF calculations.

Two general methods can be employed (Figure 1.15). The first involves an explicit solvent 'cage', where solvent molecules are calculated along with the target structure. This is often used in semi-empirical methods where the computational cost of modelling multiple solvent molecules is not prohibitively expensive.[41] However with ab-initio calculations the cost of this method is often too great, therefore the effects of solvation are implicitly stated with the use of a continuum solvation model (CSM), where the reaction is modelled in a 'cavity' (which can be a sphere, oval or tailored to the solute through the use of Van der Waals radii) representing the solvent interaction.[42]

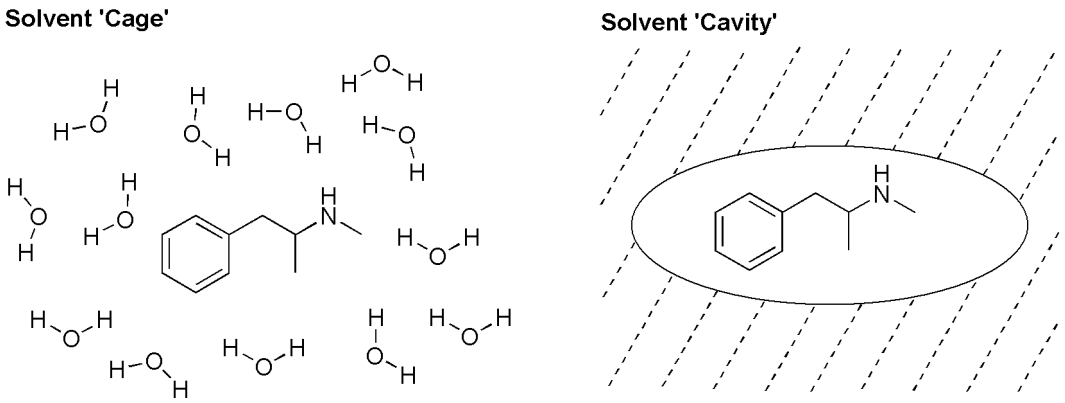

Figure 1.15 – Two methods of solvation. The solvent 'cage' (left) and the solvent continuum 'cavity' (right).

Several continuum solvation methods exist, most notably the polarizable continuum model (PCM) used in the Gaussian program.[43] The TURBOMOLE program however uses the conductor-like screening model (COSMO), the features of which will be briefly mentioned here.[44, 45]

The COSMO method has the solute centred in a molecular cavity surrounded by a dielectric continuum of permittivity (ε). However it differs from other CSM methods with generation of the cavity surface being based on the screening found with conductors. Instead of calculating the rather complicated boundary conditions of the cavity with the use of a dielectric,[39] COSMO uses the vanishing electrostatic potential for an ideal dielectric medium where $\varepsilon = \infty$ (i.e. a conductor). This approximation is accurate for solvents with high permittivity such as water (ε = 80.4 at 293 K)[46], but can be modified for solvents with finite dielectric constants with the use of a scaling factor.

The surface of the cavity itself is a polygonal construction, which begins by generating spheres on each of the atoms with a radius taking into account the Van der Waals and solvent interaction radii. Hexagonal, pentagonal and triangular polygons are then mapped over this to produce the cavity surface.

1.1.14 Applicability of Theoretical Methods

DFT and indeed computational chemistry in general exists as an augmentation to empirical experimental evidence, providing insight into reactions, mechanisms and electronic structure which may not be available with 'real world' methods. As a result, accuracy in comparison with empirical evidence is prized in computational chemistry, with several points to consider before employing DFT calculations.

The foremost point to be considered is the choice of functional. As was stated previously, the energy is related as a function of the electron density of the molecule, and it is the identification of this function, in particular the identification of the exchange/correlation term which is key – with improvements in DFT approximations having famously been compared to Jacob's ladder.[47, 48] Until the 'perfect' DFT functional has been obtained, care must be taken in choosing the correct tool for the job, which can be identified by surveying the literature for applicable functions and most importantly – benchmarking against known experimental results. The former is by no means an easy task, with the most frequently used functionals (such as the immensely popular hybrid B3LYP functional[49]) not always being the best choice for all systems. The methods used in this thesis are the GGA functional BP86 for optimisation of geometries, and the hybrid functional PBE0 for single point energies on the optimised structures. With respect to BP86, arguments have been made for and against the functional with respect to optimised M-C bond lengths.[50] The functional also has been shown to agree with experiment with respect to the structure of metal-agostic complexes.[51] Assessment of the PBE0 functional has also been favourable,[35] with both methods showing reasonable agreement with experiment in recent comparative reviews.[52, 53]

However a definitive answer of functional applicability can never truly be provided; the latter method involving testing of computational methods can therefore provide more concrete answers. In an investigation published in 2008, calculations were performed by Dr John Slattery on a rhodium alkyne-vinylidene tautomerization mechanism.[54] In the study activation barriers calculated with the (RI-)BP86/SV(P)//(RI-)PBE0/def2-TZVPP method showed favourable agreement with those calculated experimentally.

Additionally, functional and basis set testing were also performed on a precursor to the LAPS mechanism (chapter 2), which investigated several functional and basis set combinations, in particular the use of the dispersion-corrected functional B97-D developed by Grimme.[55] It was shown that the energies of the B97-D/def2-TZVPP minima and transition states were very similar in energy to that of the BP86/SV(P) and BP86/def2-TZVPP stationary points, with ca. 8 kJ mol^{-1} for the BP86/SV(P) transition states and BP86/def2-TZVPP minima, suggesting that dispersion effects with the B97-D functional are not essential in the description of the model.

The choice of basis set is very much as important as choosing a correct functional. As was shown in section 1.1.6, additional basis functions from a larger basis set can improve the description of calculated structures, often with increased computational expense. One important consideration when choosing a basis set is basis set superposition error (BSSE). This error manifests during calculation of fragments and complete systems (for example an ligand entering the sphere of a transition metal and coordinating to the metal centre), where basis functions used to describe other parts of the system interact with the fragment when in close range, artificially lowering the energy of the overall system compared with the completely separate systems. The use of a larger basis set often negates the effect of BSSE, once again with the side-effect of increased computational expense.

The final consideration when performing calculations is to match the experimental conditions as much as possible with the use of thermal and entropic corrections obtained from the calculated vibrational spectrum (discussed in section 1.1.12) as well as solvation corrections for heavily polarized and charged structures (discussed in section 1.1.13).

ZPE, entropic and thermodynamic corrections allow for a more realistic determination of the system than just the electronic energies. The energies reported in potential energy surfaces in this document are SCF + ZPE ($E_{SCF+ZPE}$) corrected and Gibbs free energies (G), however all energies, barriers and energetic spans found in the text exclusively use $E_{SCF+ZPE}$, and not G. While $E_{SCF+ZPE}$ is approximate to the enthalpy of a system, it is missing important entropic and thermal contributions to the system found with G.

However the calculation of *G* in the gas phase is problematic, with calculations requiring the use of approximations such as harmonic potentials and ideal-gas expressions.[56] More importantly the calculation of entropy in bimolecular systems (e.g. loss of a ligand, or a single molecule breaking into two fragments) is often overestimated when calculating in the gas phase and comparing the results to solution phase reactions. The translational and rotational portions of the entropy see large increases upon the advent of a bimolecular reaction, due to the two fragments being able to move independently. This however would not be the case in the experimental system due to the presence of solvent molecules, meaning the total entropy and Gibbs free energy changes are overestimated. As a result, $E_{SCF+ZPE}$ has been used despite limitations.[57]

The level of accuracy reported for optimised geometries is reported at 2 and 1 decimal places for all bond distances and angles respectively. When obtaining geometries a close model to what exists experimentally is always desired, however with calculations being performed in the gas phase and experimental parameters being obtained from solid crystal structures – a significant level of disparity between the two results is unavoidable.

While modelling structures with crystal packing effects taken into account has shown good agreement with obtained crystal structures,[58] this is of little help when comparing structures within this document. However it should be noted that all computed geometries presented here are within the gas phase, so comparisons with one another (e.g. section 5.2.4 and 5.2.13) will be subject to the same overarching error.

While noted previously in this section that geometries obtained with BP86 often show good agreement experimentally, it can be seen in section 5.2.4 that the comparison to computed and crystal structures is very close, being accurate to 1 decimal place. Therefore it can be assumed that to 1 decimal place is a fairly reliable number, decreasing in certainty at 2. The reader is therefore asked to keep this in mind during the course of this thesis.

1.1.15 The Natural Bond Orbital (NBO) Program

Calculation of molecules with the use of DFT will reveal information about the structure, energy and secondary information such as the vibrational spectrum. In terms of the description of the bonding however, information is limited to bond length, qualitative orbital shapes or a population analysis of charges. Another way of analysing the bonding within a structure is through the use of the Natural Bond Orbital (NBO) program,[59-61] which is used within this thesis.

The NBO program models use Lewis-based methods[62] to describe the electronic structure of a molecule, which is achieved by the use of natural bond orbitals. The program can also quantify donor-acceptor interactions with the use of perturbation theory, as well as examine delocalisation through resonance structures.

Natural bond orbitals themselves are localized orbitals that represent the Lewis-based electron model in terms of occupation and bonding. They are part of a sequence of natural orbitals (Figure 1.16) which originate from the atomic orbital (AO) density matrix, which is transformed into the natural atomic orbital (NAO) *via* a matrix transformation. NAO's have two key differences to AO's, the first of which is that the spatially-diffuse characteristic of the orbital is directly influenced by the effective atomic charge, allowing a change in density depending on the nature of the local charge, which is difficult to achieve in AO's. The second difference relates to the orthogonal nature of the orbital, which is created by specifying inner and outer nodes at the atomic core and between the local density and the density present on other atoms.[61]

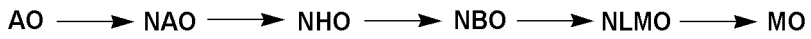

Figure 1.16 – Orbital transformations from atomic orbitals through to natural orbitals.[60]

A further set of matrix transformations leads to the natural hybrid orbital (NHO) and NBO's. The NBO's themselves are described (for atoms A and B) in Equation 1.94 for the bonding interaction, and Equation 1.95 for the anti-bonding interaction.

$$\sigma_{AB} = c_A.h_A + c_B.h_B \qquad \textit{Equation 1.94}$$

$$\sigma^*_{AB} = c_A.h_A - c_B.h_B \qquad \textit{Equation 1.95}$$

These equations consist of NHO's for A and B (h_A and h_B) and polarization constants (c_A and c_B). The orbitals are of the Lewis (bonding) and non-Lewis (anti-bonding) type, with occupation numbers near 2 and 0 respectively.[60]

An analysis of a typical calculation output can provide a significant amount of information about the electronic structure and bonding of a molecule. Analysis of the NBO's reveals information on the orbital nature (e.g. core, bonding or lone pair), occupation and hybridization (e.g. percentage of s-and p-orbital character).

However even further insight into the bonding occurs with the results of the second-order perturbation analysis. This lists all of the major donor-acceptor interactions within the structure, showing amount of donated electron density as well as the stabilising energy of this interaction. This is achieved by a calculation of all possible donor-acceptor interactions, with only notable interactions (above 20 kJ mol^{-1}) being listed.

Other useful information can be obtained from an NBO calculation, such as Wiberg bond indices, analysis of NHO directionality and 'bond bending', as well as visualisations of the orbitals themselves. Additionally an analysis of the delocalisation present within the electron structure can be performed using the Natural Resonance Theory (NRT)[63-65] module, and was attempted for several structures in section 5.2.13. However as the NRT module of NBO 5.9 was unable to be applied to the system, a further discussion of this feature will not be included here.

1.1.16 Computational Summary

This section has summarised the basis of the theoretical methods used within this thesis. Density functional theory is shown to have a historical relation to the Schrödinger equation and Hartree-Fock method, with many of the typical procedures carried over into DFT. The electronic energy of the calculated structures is supplemented with corrections from a calculated vibrational spectrum of the molecule, giving results that are more realistic to those observed empirically.

DFT in general, as well as the functional and basis set combinations used, have been shown to be good approximations when used to model organometallic systems. Constant vigilance must be maintained during studies to ensure that the calculations are representative of reality. While this section has detailed the acquisition of the absolute energies of a molecule, it is the comparison between molecules that allows reaction mechanisms to be understood. This will be the basis of the next section.

1.2 Modelling Reaction Mechanisms

1.2.1 Transition State Theory

Transition state theory is an overarching method employing several theoretical principles to follow and understand what is occurring in a reaction in terms of energy change. First proposed by Eyring, Evans and Polanyi in 1935, it was an amalgam of thermodynamic, kinetic and statistical-mechanical methods. A precursor to transition state theory is the Arrhenius equation (Equation 1.96), which relates the rate constant (k) to the activation energy (E_a), with A being a pre-exponential factor, and is a direct successor to the Van't Hoff equation.[66] The equation was determined empirically, with efforts to further understand the equation and determine the basis for A and E_a leading to the development of transition state theory.

$$k = Ae^{-Ea/(RT)} \qquad \textit{Equation 1.96}$$

Further developments involving kinetic-theory treatments were proposed with the use of collision theory to calculate the rate constant, which showed good agreement with some experimental results such as the reaction of hydrogen iodide to form hydrogen and iodine.[67] A statistical treatment was proposed by Marcelin,[68] which sought to describe a chemical reaction as a motion of a point in phase-space – essentially representing the progress of a reaction from reactants to products in the form of a potential energy surface (PES).[69] This led to the development of transition state theory, and to the Eyring-Polanyi equation (Equation 1.101).

In the reaction of molecules A and B (Equation 1.97, with a depiction of the PES shown in Figure 1.17) the reaction is shown to proceed through the activated transition state complex $AB^{‡}$ to the product P. As formation of the product from the complex is assumed to be slower than formation of $AB^{‡}$ from A and B, the reactants are said to be in quasi-equilibrium with complex $AB^{‡}$.

$$A + B \rightleftharpoons AB^{\ddagger} \rightarrow P$$ *Equation 1.97*

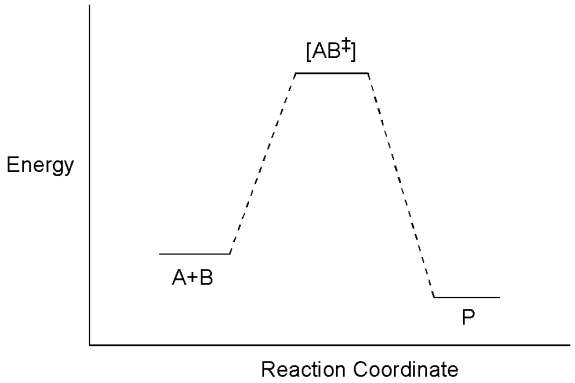

Figure 1.17 – Depiction of PES of A+B → P.

The concentration of $AB^{\ddagger}$ can then be calculated as the concentration of A and B, with an equilibrium constant for the quasi-equilibrium shown in Equation 1.98.

$$K^{\ddagger} = \frac{[AB]^{\ddagger}}{[A][B]}$$ *Equation 1.98*

This quasi-equilibrium and transition state decomposition can be related to the overall rate through Equation 1.99 (k_{obs} = observed rate constant, and $k^{\ddagger}$ = transition state complex decomposition rate constant) and Equation 1.100 (k_B = Boltzmann constant).

$$rate = k^{\ddagger}[AB^{\ddagger}] = k^{\ddagger}K^{\ddagger}[A][B] = k_{obs}[A][B]$$ *Equation 1.99*

$$k_{obs} = \frac{k_B T}{h} K^{\ddagger}$$ *Equation 1.100*

As $\Delta G = -RT\ lnK$, the Gibbs free energy of activation, temperature and rate constant can be related through the Eyring-Polanyi in Equation 1.101.[69, 70]

$$k_{obs} = K^{\ddagger}k^{\ddagger} = \frac{k_B T}{h} e^{-\frac{\Delta G^{\ddagger}}{RT}} \qquad \textit{Equation 1.101}$$

This allows for the assessment of the barriers of a reaction, allowing direct comparison with the magnitude of the rate, reaction temperatures, and barriers to formation of the products. Crucially it also allows for comparison with the computationally calculated energies of minima and transition states, allowing for a validation of theoretical methods. However for more complex systems as well as catalysts, this model requires further expansion and will be detailed in the next section.

1.2.2 The Energetic Span Model

As has been shown previously, the use of transition state theory and the Eyring equation translates between experimental and theoretical methodologies allowing for a direct comparison between the experimental rate and computed potential energy surface (PES).

However, several studies by Kozuch, Shaik *et al*. on the catalytic mechanism of palladium cross coupling showed that the transition state barriers alone were not sufficient in describing the turnover frequency (TOF) of the system. Two potential energy surfaces were calculated using bi-dentate ligands with differing chain lengths. While one mechanism had lower energy transition states, it also possessed lower energy intermediates, giving no indication of which complex was the better catalyst.[71, 72]

This lack of information can be particularly problematic when analysing competing pathways within the mechanism itself or upon the effect of substituents. To this end, Kozuch and Shaik proposed to conceptualise catalytic cycles *via* the use of the 'Energetic Span Model', a way to tie the fundamental measure of catalytic efficiency – the turnover frequency (TOF) to Eyring's transition state theory.[73, 74]

The authors sought a way of joining the 'languages' of the experimental and theoretical chemistry, and began by looking at the Amatore-Jutland equation (Equation 1.102) which is based on the Arrhenius equation. This connected the rate of the reaction to the energetic span (δE) – the difference between the lowest and highest points on the PES (Figure 1.18). However this model is only accurate when the difference in energy between C_0 and the end state P (ΔG_r) approaches zero, as opposed to exergonic formation of P. This is due to the 'Ouroboros-like' cyclical nature of the catalytic cycle, where formation of the end state P begins a new catalytic cycle from C_0.

$$r = [C_0]Ae^{-\frac{Ea+\Delta E}{RT}}$$ *Equation 1.102*

(Where $E_a + \Delta E = \delta E$)

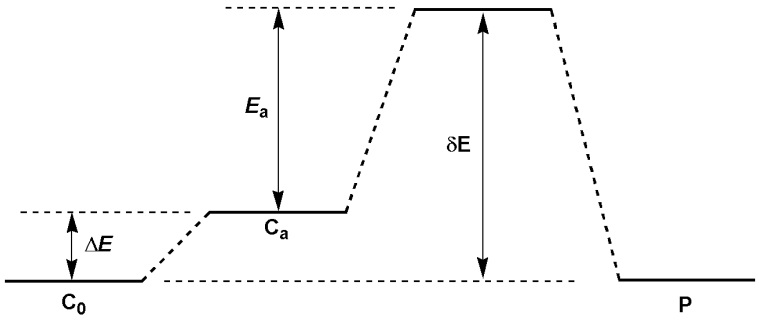

Figure 1.18 – Amatore-Jutland equation and representation of the energetic span.

In order to better describe the cyclical nature of a catalytic mechanism, attempts were made to modify the Eyring equation and a rate-constant *k*-formulation by Christiansen, producing Equation 1.103 below. T_a and I_b are the Gibbs energies of each transition state or intermediate and ΔG_r^o is the Gibbs energy of reaction for a complete cycle.

$$TOF = \frac{k_B T}{h} \cdot \frac{e^{-\frac{\Delta G_r^o}{RT}} - 1}{\sum_{a,b=1}^{N} e^{(T_a - I_b - \delta G'_{a,b})/RT}}$$ *Equation 1.103*

$$(\delta G'_{a,b} = \Delta G_r^o \text{ if } a \geq b, 0 \text{ if } a \leq b)$$

While comprehensive, a significantly accurate approximation to the full equation can be used instead, termed the energetic span approximation (Equation 1.104). Here the TOF is calculated with the use of only two states, the TDI (turnover determining intermediate) and the TDTS (turnover determining transition state).

$$TOF = \frac{k_B T}{h} . e^{-\frac{\delta E}{RT}}$$ *Equation 1.104*

$$\text{Where } \delta E = \begin{cases} T_{TDTS} - I_{TDI} & \text{if TDTS appears after TDI} \\ T_{TDTS} - I_{TDI} + \Delta G_r & \text{if TDTS appears before TDI} \end{cases}$$

The TDTS and TDI are the transition state and intermediate that creates the largest energetic span within a PES, and not necessarily the transition state which has the highest energy globally (Figure 1.19). A PES with a larger energetic span will have a slower rate than with a smaller energetic span, allowing the direct comparison of competing mechanisms and pathways.

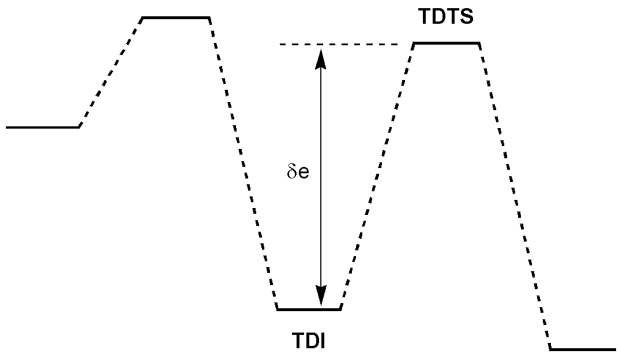

Figure 1.19 – Depiction of the TDI and TDTS of a PES.

The concept of the energetic span is used throughout this thesis to determine the viability of several mechanisms. The energetic span is measured and used 'semi-qualitatively' – without the calculation of the TOF – to compare the potential energy surfaces. This is primarily done due to the use of ZPE corrected SCF energies throughout the text instead of Gibbs free energies. These energies have primarily been chosen due to the over-estimation of entropic effects seen when calculating the Gibbs free energies, which is explained in more detail in section 1.1.14.

Additionally, while the energetic span model is primarily used to describe catalytic systems, the model has been applied to stoichiometric reactions seen in chapter 2 and 3. The energetic span model has been shown to be effective in describing stoichiometric reactions,[74, 75] and to avoid confusion the turnover determining states have been labelled S-TDTS and S-TDI.

Overall, the energetic span method has been demonstrated to be an accurate model of mechanistic viability with respect to turnover frequencies, with many examples showing agreement with experiment.[74] As such, this method has been used throughout the thesis.

1.3 General Organometallic Introduction – C-H Activation

C-H activation is the process of cleaving a carbon-hydrogen bond by activating the inert and strong (435 kJ mol^{-1} for methyl) C-H σ bond. This is primarily used as a precursor to functionalise alkane and arene groups, with activation traditionally occurring *via* the use of organometallic complexes, but examples with organocatalysis[76] and frustrated Lewis pairs[77] are known in the literature.

Due to C-H activation with organometallic complexes being featured to some extent in every chapter of this thesis, a limited introduction to the topic is necessary which will be split into two parts – firstly with a brief overview of transition metal mediated activation and secondly with activation by the use of coordinated ligands.

1.3.1 Transition Metal Mediated C-H Activation

The topic of transition metal mediated C-H activation is an expansive one, with many articles and reviews concerning the subject.[78-81] Transition metal C-H activation is known to occur *via* several methods (Figure 1.20), of which the primary method is oxidative addition where the C-H bond binds to the metal centre through an agostic interaction. The metal centre is normally a low-valent electron-rich late transition metal (such as ruthenium,[82] rhodium and iridium[83]) which can be promoted to a higher oxidation state in order for the bond cleavage to occur.

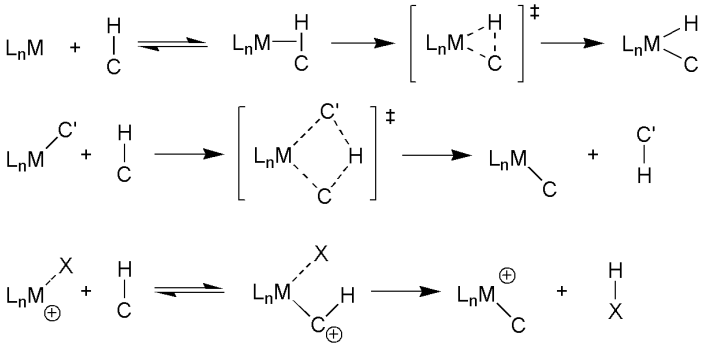

Figure 1.20 – Selected methods of C-H activation, showing agostic (top), σ-bond metathesis (middle) and electrophilic addition (bottom).

For earlier transition metals C-H activation can occur through a σ-bond metathesis mechanism, where C-H bonds are cleaved and formed in a concerted manner. A further example of activation is by electrophilic addition into the C-H bond, normally by a late or post-transition metal such as Pt^{2+} or Pd^{2+}.[81]

The area of C-H activation with metallic complexes predominantly began in the 1960s, with Chatt and Davidson reporting in 1965 the cyclometalation of phosphine ligands and napthalene through oxidative addition of a C-H bond to a ruthenium centre (Figure 1.21).[84]

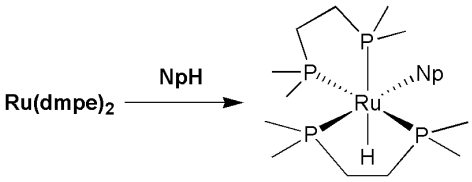

Figure 1.21 – Napthalene C-H oxidative addition.

Research into the field continued through the 1970s and 80s, with notable developments coming from the groups of Shilov with a Pt(IV) complex $[PtCl_4]^{-2}$ used to chlorinate methane groups through oxidation of a C-H bond,[78, 85, 86] and Bergman in 1982 with the stoichiometric formation of alkyl metal hydrides from simple alkanes and an Ir(I) complex which was formed from the photo-extrusion of hydrogen from $[Cp^*IrH_2(PMe_3)]$.[87, 88]

While transition metal mediated C-H activation is well studied in organometallic chemistry, C-H activation involving ligands is comparatively unexplored, and will be discussed in detail *vide infra*.

1.3.2 Ligand-Mediated C-H Activation and Proton Transfer

Increasing numbers of examples of C-H activation and deprotonation aided by secondary ligands within the coordination sphere of the metal have been proposed on the basis of both theoretical and experimental studies, with many reviews concerning the subject.[89-92] The ligands that have been identified as taking part in the C-H activation mechanism range from acetate to carbonate groups to hydroxy ligands.[93] Ligand-assisted C-H activations have also been observed in many different systems (as well as biological systems such as acetylene hydratase[94]).

While several different acronyms for these processes exist, this section shall focus briefly on three that are most relevant to the system under study here due to their involvement of carboxylate ligands – The ambiphilic metal ligand activation mechanism (AMLA), the concerted metalation deprotonation mechanism (CMD), and a mercury-based deprotonation/protonation of a phenyl substituent.

The investigation into the AMLA mechanism began with a system studied by Ryabov *et al.*[95, 96] where the reaction of $[Pd_3(O_2CMe)_6]$ with an excess of dimethylbenzylamine forms a palladium metallacycle (Figure 1.22).

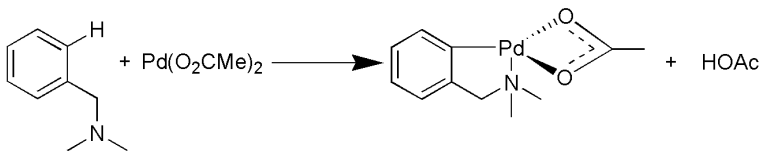

Figure 1.22 – Formation of a palladium metallacycle with $[Pd_3(O_2CMe)_6]$ and an excess of dimethylbenzylamine.

The original study of this system suggested that a Wheland-type intermediate (where the aromaticity is broken and the phenyl group is positively charged - Figure 1.23) is involved in the transformation. The acetate can be shown stabilising the proton through a hydrogen bond, and the acetate ligand is then presumed to deprotonate the arenium group in order to form the cyclometalated product.

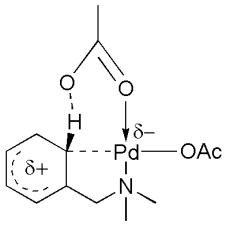

Figure 1.23 – Originally suggested Wheland-type intermediate.

Several years later, this reaction was investigated by Davies and Macgregor *et al.* who undertook a theoretical study in order to establish the mechanism of cyclometalation and the validity of the Wheland-type intermediate.[97, 98] Literature presented by Davies seemed to suggest that a C-H agostic intermediate and transition state were more likely to be involved in the mechanism[99] with a crystal structure of such an agostic structure being shown in a publication by Milstein *et al.*.[100]

The study by Davies and Macgregor focussed on the role of the acetate ligands *via* the use of DFT, and their results are summarised in the PES shown in Figure 1.24. Starting from a square planar complex with one κ^1 and one κ^2 acetate ligand, a C-H agostic structure is shown at +54.4 kJ mol^{-1}. This agostic complex has an activated proton which is removed by the κ^1 acetate to form the cyclometalated product at -55 kJ mol^{-1}, with the acetic acid formed during this process initially remaining coordinated to the metal with additional stabilisation provided by the second acetate ligand. This mechanism had a significantly lower kinetic barrier than that of oxidative addition of the C-H bond followed by reductive elimination of acetic acid.

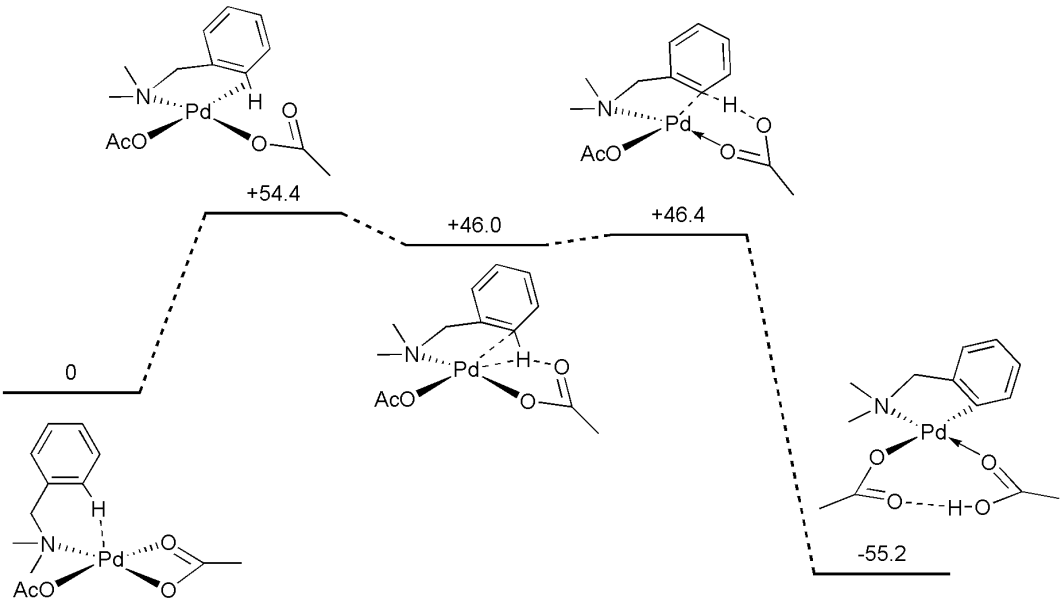

Figure 1.24 – Acetate-assisted PES for the cyclometalation of dimethylbenzylamine. All energies are zero-point corrected SCF energies in kJ mol^{-1}. [97]

These results demonstrated not only the likelihood of an agostic intermediate being stabilised by an acetate group, but seemed to show a mechanism where C-H activation occurs with an electrophilic metal agostic C-H interaction being deprotonated by the lone pair of an internal base. This ambiphilic duality lead to the mechanism being termed the ambiphilic metal ligand activation (AMLA) process.[92]

Additionally it was shown that mechanisms of this type could proceed *via* a 4-membered transition state where the oxygen atom of the assisting acetate which is bound to the metal acts as the intramolecular base, as opposed to a 6-membered transition state where the non-bound oxygen instead acts as the base.[101, 102] The alternative 4-membered AMLA mechanism was also studied with DFT and compared with the 6-membered mechanism (Figure 1.24) which showed a far higher barrier height of 143.5 kJ mol^{-1} compared to 54.4 kJ mol^{-1} for the 6-membered mechanism. This indicated that either a more sterically strained transition state was involved or that the coordinated oxygen atom of the 4-membered mechanism was less basic due to donation of electron density to the palladium centre and less able to assist in the C-H activation process. The 6 and 4-membered AMLA mechanism were termed the AMLA(6) and AMLA(4) processes respectively.[92]

This study was followed by an investigation into ruthenium, rhodium and iridium half-sandwich complexes that also undergo acetate-assisted cyclometalation with dimethylbenzylamine.[103, 104] It was shown once again in DFT studies on the iridium system that the AMLA mechanism occurs here also, with electrophilic activation of the C-H bond followed by deprotonation by the internal base, with the acetate stabilising and then deprotonating the agostic C-H bond. These results showed that the [Cp*Ir] fragment is capable of electrophilic activation of C-H bonds as well as oxidative addition, which is normally observed for complexes of this type.

As in the palladium system the transition state for the AMLA(6) mechanism was lower in energy compared with the constrained AMLA(4) process. The AMLA mechanism was also corroborated by a mechanistic study on $[Cp^*RhCl_2]_2$ or $[Cp^*IrCl_2]_2$ with sodium acetate, which again showed an acetate group activating and deprotonating a phenyl C-H bond.[105] The research groups of Davies and Macgregor have also shown AMLA-type mechanisms in reactions of 2-substituted pyridines,[106] ethene hydroarylation[107] and other cyclometalation reactions.[108]

Substantial experimental and theoretical studies have also been performed (primarily by the Fagnou research group) into the activating and deprotonating properties of ancillary oxygen-based ligands. Although possessing similar mechanistic features to the AMLA process, a different acronym – CMD (concerted metalation deprotonation mechanism) has become popular based on this work.

An early investigation by Fagnou *et al.* on the direct arylation of electron deficient benzenes (Figure 1.25),[109] suggested that rather than arene nucleophilicity, arene reactivity depended on the acidity of the phenyl C-H bond.

.

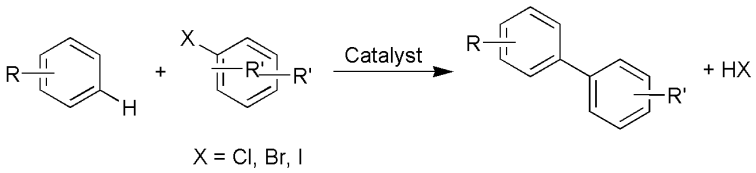

Figure 1.25 – Catalytic direct arylation of benzene.

Here, the reaction of 4-bromotoluene and pentafluorobenzene was studied with the reaction conditions seen in Figure 1.26, where 5 mol% of a [Pd(P^tBu_2Me)] catalyst (generated in situ with [$Pd(OAc)_2$] and HBF_4 salt of di-tertbutylmethylphosphine) and 1.1 equivalents of potassium carbonate formed a 98% yield of the cross-coupled arylation product after 3 hours.

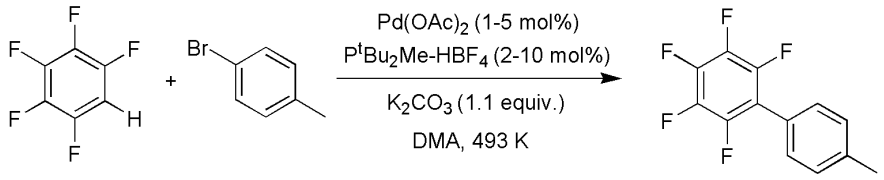

Figure 1.26 – Initial study of the reaction of 4-bromotoluene and pentafluorobenzene.

A brief computational study was reported, where three different mechanisms were studied: oxidative addition of the C-H bond to the metal, electrophilic aromatic substitution, and metalation with activation and deprotonation by the ancillary ligands. Of these mechanisms, it was reported that no suitable stationary points were located for either the oxidative addition or electrophilic substitution mechanisms. For the ancillary ligand mechanism, it was shown that coordinated bromide and intermolecular palladium-carbonate assisted deprotonation are too high in energy or could not be located on the PES. Instead it was postulated that a carbonate ligand substituted for bromide, activates and deprotonates the aryl group (a transition state can be seen below in Figure 1.27) which shows the lowest barrier height on the PES of 41 kJ mol^{-1}, consistent with experimental data.

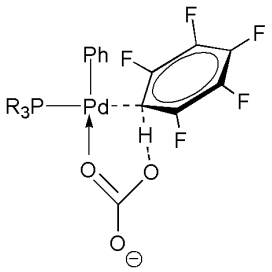

Figure 1.27 – Transition state for the deprotonation of C_6F_5H by a coordinated carbonate ligand.

This study was followed by a subsequent investigation[110] where pivalic and acetic acid was used as a 'proton shuttle', instead of a carbonate group. It was shown once again experimentally and theoretically that the carboxylate is instrumental in activating the phenyl C-H bond, lowering the energy of the bond cleavage as well as acting as a proton shuttle to the free potassium carbonate.

At a similar juncture, studies were published by Maseras and Echavarren[111-114] which also looked at the mechanism of palladium catalyzed arylation. With the use of DFT they too confirmed the supporting role the carboxylate ligand played in bond activation and cleavage of the phenyl C-H bond. Deprotonation by bromine was once again shown to be too high in energy, with the basicity of the halogen speculated to be the cause of the high energy barriers.

Within the Fagnou group, a significant amount of evidence was provided that validated the CMD mechanism, including examples of acetates,[115, 116] pivalates,[117, 118] activation of pyridine N-oxides and other heterocycles,[119-124] and ring closing reactions.[125-127]

In addition to various substituent effects observed when changing the nature of the carboxylate used in the above studies, Fagnou and co-workers showed that substituents on the activated phenyl also play a role in determining the kinetics of the C-H activation reaction of the type shown in Figure 1.25. The main effect that is described is that more electron withdrawing groups on the fluoroarene substrate lowers the energy barrier for C-H activation, suggesting that an electron deficient C-H bond is key to reactivity. This effect is perhaps most notable in one study where non-fluorinated arenes were found to have a barrier to C-H activation that is 43.1 kJ mol^{-1} higher than for a fluorinated arene.

While the majority of work on CMD- and AMLA-type C-H activation processes has been reported in the last ten years, there is precedence for this type of carboxylate-assisted C-H activation in much earlier literature. An early example of protonation by an acetate group (the reverse of the CMD/AMLA mechanism) was shown with a mercury-based system and published by Winstein and Traylor in 1955.[128] This publication showed free acetic acid protonating a mercurial phenyl group in order to form benzene and an acetate-coordinated mercurial compound, shown below in Figure 1.28.

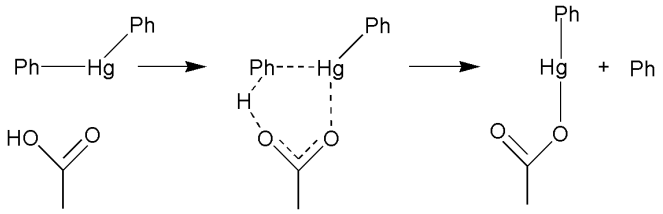

Figure 1.28 – Acetic acid protonation of a mercury-bound phenyl ligand.

Conversely in phenyl mercuration studies, a *bis*-trifluoroacetate mercury complex was shown to deprotonate a phenyl group in a similar mechanism to that shown with the acetic acid based phenyl extraction, showing that the direction of the reaction can be changed depending on the substituents on the acetate group.[129]

In summary acetate and other bi-dentate oxygen ligands have been shown to not only activate C-H bonds, but also act as an intramolecular base in the AMLA and CMD mechanisms - deprotonating substrates and leading to further reactivity. Additionally it is shown that different reactions can occur through modification of the acetate groups. These factors shall come in to play later on within the thesis.

1.4 General Organometallic Introduction – Vinylidenes and Allenylidenes

1.4.1 Vinylidenes – General Background

A vinylidene is a high energy unsaturated carbene tautomer of an alkyne, where a group based on the terminal end of the alkyne such as a proton, migrates over the triple bond *via* 1,2-hydrogen shift, leaving unsaturated valence electrons at the proton's former location (Figure 1.29). As can be expected the vinylidene conformation is +188 kJ mol^{-1} higher in energy than the alkyne analogue,[130] with the free vinylidene showing an experimental lifetime of 10^{-10} s.[131]

Figure 1.29 – Alkyne and vinylidene.

Metal vinylidene complexes meanwhile are far more common, with the first known vinylidene complex, the $[Fe_2(\mu\text{-}C{=}CPh_2)(CO)_8]$ dimer reported in 1966 by Mills and Redhouse.[132, 133] The first terminal vinylidene complex – $[CpMoCl(PPh_3)_2(=C=C(CN)_2)]$ was reported six years later by King and Saran.[134-136] Of particular note to this thesis, the first terminal ruthenium complex $[CpRu(PPh_3)_2(=C=CHPh)]$ was isolated by Bruce and Wallis in 1979 from $[CpRuCl(PPh_3)_2]$.[137] Research into the field progressed significantly over the next few years, with a large amount of metal vinylidene complexes known to exist.[138]

Vinylidenes themselves can be considered carbenes – often short-lived neutral organic molecules, with an unsaturated carbon atom possessing two unpaired valence electrons.[139] These electrons can be arranged in either a singlet or triplet arrangement in their non-coordinated form, with the electrons contained in an sp^2 orbital in the singlet case, and the sp^2 and *p* orbitals in the triplet form (Figure 1.30).[140]

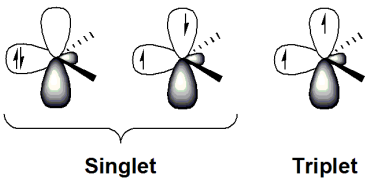

Figure 1.30 – Carbene example showing both singlet and triplet forms.

While examples of persistent non-coordinated carbenes exist,[141, 142] the discovery and synthesis of transition metal carbenes allowed for stable longer-lived carbenes to be accessed.[143, 144] This had wide ranging implications in chemistry – some of the most notable examples being Grubbs[145-148] and Schrock[149-152] catalysts[153] as well as N-heterocyclic carbenes.[154-157]

Transition metal carbenes can be classed as either Fischer or Schrock carbenes (Figure 1.31). Fischer carbenes are electrophilic at C_α, possess π-donating R groups, are typically found with middle and late transition metals with low oxidation states, with the unpaired electrons in a singlet occupation donating to an empty metal orbital *via* a σ-bond. Conversely Schrock carbenes are nucleophilic at C_α, possess alkyl or hydrogen R groups and are formed with early transition metals in high oxidation states. The unpaired electrons in this instance are normally in a triplet occupation, with bonds being formed between the carbene and a similarly triplet-occupied metal centre.

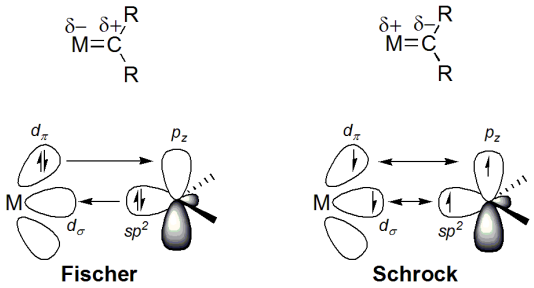

Figure 1.31 – Depiction of Fischer and Schrock type orbital interactions.

In the Fischer case, the sp^2 orbital of the carbene donates into the d_σ of the of the metal, while a d_π orbital donates into the empty carbene p_z orbital. In Schrock carbenes, a covalent bond is formed between the sp^2 and the d_σ orbitals as well as between the d_π and p_z orbital.

The nature of the electrophilic and nucleophilic carbon centres is produced from the relative heights of the metal d_π orbitals relative to the carbene. In the Fischer case the metal *d* orbitals are lower in energy and are therefore closer to the highest occupied molecular orbital (HOMO) of the metal carbene structure, leaving the unfilled lowest unoccupied molecular orbital (LUMO) to have more carbene p_z character, giving a formally positive charge on the C_α. In the Schrock carbene case higher energy *d* orbitals mean the LUMO is now more metallic in character, with the HOMO having more influence from the carbene orbitals leaving a formal negative charge on the carbon.[158]

Transition metal vinylidenes are similar to carbenes, with the addition of a double bond from the carbene centre to an additional carbon. Much like their carbene counterparts, they can be classes as Fischer and Schrock carbenes, with an electrophilic and nucleophilic C_α respectively (Figure 1.32). This thesis will be dealing with ruthenium(II) vinylidenes, which are exclusively Fischer in character.

Figure 1.32 – Fischer and Schrock vinylidene representations.

In the case of a Fischer vinylidene complex, the electrophilic nature of the C_α can be explained once again by an orbital interaction diagram reproduced below in Figure 1.33.[138] As in the carbene case, the C_α *p*-orbital contributes most to the LUMO orbital $\pi 4$. The HOMO $\pi 3$ orbital contains an antibonding interaction between the metal centre and the C_α *p* orbital, meaning the electron density is concentrated on the metal centre and C_β. As a result the C_α is electrophilic in character.

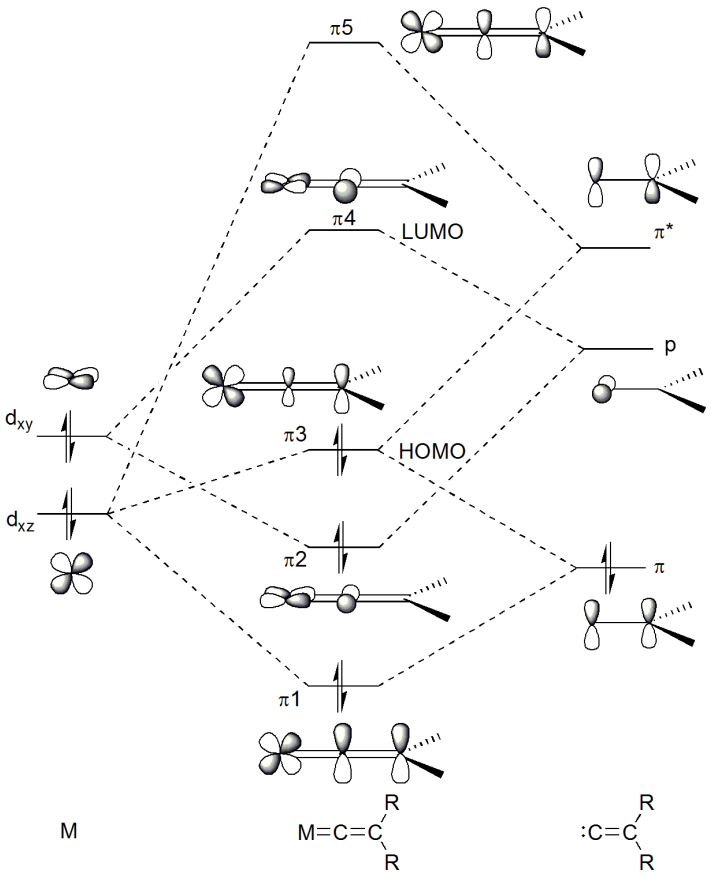

Figure 1.33 – π-orbital interaction diagram for a Fischer vinylidene complexes.[138]

For Schrock vinylidenes, the metal *d* orbitals are higher in energy, meaning that in a similar way to carbenes, the LUMO is more metallic in character creating a positive charge on the metal and C_β.

In summary, vinylidenes are highly reactive short-lived molecules which can be stabilised upon coordination to a metal centre. Furthermore with the Fischer-type vinylidenes orbital interactions between the vinylidene group and the metal, induce an electrophilic C_α and nucleophilic C_β, with great implications for further reactivity and catalysis. This shall be explored in more detail *vide infra*, as well as with the research presented within this thesis.

1.4.2 Alkyne-Vinylidene Tautomerization

Vinylidenes are typically formed from an alkyne precursor through a range of potential mechanisms. What all mechanisms have in common is the migration of a group (usually a proton or other substituent such as SMe,[159] $SiMe_3$[160] or I[161]) from one end of the carbon-carbon triple bond to the other.

Free acetylene-vinylidene tautomerization has been shown to be significantly kinetically unfavourable, with a barrier of ca. 185 kJ mol^{-1} seen in both experimental,[162, 163] and theoretical studies.[164, 165] Transition metal-based acetylene-vinylidene tautomerization is significantly more accessible, with a range of possible alkyne-vinylidene tautomerization mechanisms summarised below in Figure 1.34.

The first and arguably the simplest mechanism is a direct 1,2-hydrogen shift from an η^2-bound alkyne. The second mechanism involves the formation of a C-H 'σ-complex' where the metal can either donate or accept electron density in an interaction with the terminal C-H bond *via* an agostic interaction, weakening it to allow a 1,2-hydrogen shift. Thirdly a metal hydride can be formed by oxidative addition of the C-H bond of a σ-complex to the metal, whereupon the hydride can then migrate to the C_β of the intermediate acetylide via 1,3-hydrogen shift.

Finally mechanistic possibilities exist where an additional proton can come from a source other than the initial alkyne, which typically could be from an existing metal hydride, or from an external proton source. In the example in Figure 1.34, hydride migration from the metal to a coordinated alkyne forms a vinyl complex, which can then undergo a subsequent hydrogen migration to form the vinylidene.[166]

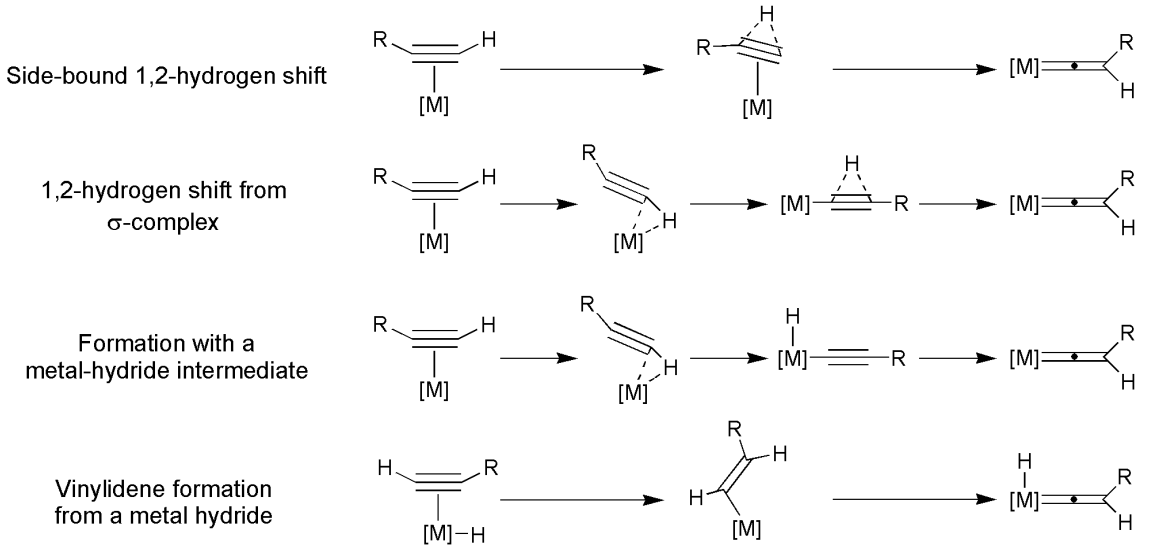

Figure 1.34 – Selected mechanisms for alkyne-vinylidene tautomerization involving hydrogen migration.

Many theoretical investigations into alkyne-vinylidene tautomerization have been reported,[138, 167, 168] with the 1,2-hydrogen shift starting from the σ-complex being shown repeatedly to be the lowest energy mechanism when compared with competing pathways. The first theoretical study reported by Silvestre and Hoffmann in 1985 used extended Hückel calculations on a mononuclear manganese complex.[169] It was shown that the direct 1,2-hydrogen shift starting from the σ-complex is the most favourable in energy of the mechanisms calculated when compared to the side-bond 1,2-hydrogen shift or through a metal hydride intermediate.

Angelis and Sgamellotti later studied the tautomerization mechanism involving the same complex as Silvestre and Hoffmann with DFT ((VWN-LDA/BPW91)/6-311G**).[170] Agreeing with the findings of the initial study, the σ-complex 1,2-hydrogen shift mechanism has the lowest barrier of 114 kJ mol^{-1}, compared with ca. 190 kJ mol^{-1} for the side-bound and hydride intermediate mechanisms.

A combined experimental and theoretical study ((RI-)BP86/SV(P)//(RI-)PBE0/def2-TZVPP) was performed by Lynam *et al.* (mentioned previously in section 1.1.14),[54] for the alkyne-vinylidene tautomerization mechanism involving a rhodium complex. The mechanism involving formation of the hydride intermediate followed by a 1,2-hydrogen shift had the lowest energy barrier, which compares favourably to experimentally observed free energy activation barriers obtained through kinetic studies.[54] This observation was also reported in a theoretical study by Grotjahn *et al.* (BLYP/DQZ).[171]

One particular alkyne-vinylidene tautomerization of relevance to systems discussed in chapter 2 was published by Wakatsuki and co-workers in 1994.[172] In this paper the authors reacted $RuX_2(PPh_3)_3$ (where X = Cl, Br) with 3,3-Dimethyl-1-butyne to form its vinylidene tautomer. As can be seen in Figure 1.35, the initial complex is stabilised by an agostic phenyl C-H from one of the three triphenylphosphine ligands.[173, 174] This ligand is then lost, creating a free coordination site at the metal centre where the alkyne coordinates. Once coordinated, tautomerization occurs to form the vinylidene, after which the complex rearranges to form a product with the triphenylphosphine ligands *trans* to one another. In terms of experimental conditions, the reaction time was sizeable, taking 24 h to reach completion at room temperature.

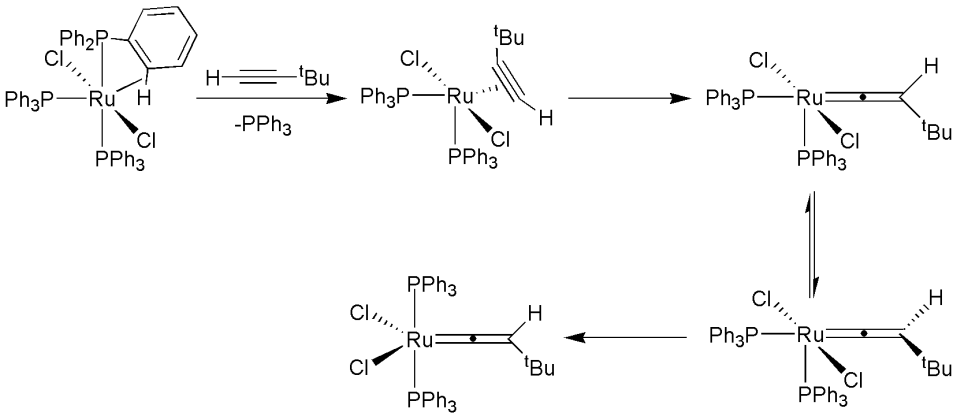

Figure 1.35 – Mechanistic proposal for the reaction of $RuX_2(PPh_3)_3$ with an Alkyne.[172]

The authors undertook a computational study at the MP2/6-31G* level and constructed a PES, which showed the lowest energy pathway involves the formation of a C-H σ-complex, followed by a 1,2-hydrogen shift to form the vinylidene. A stationary point associated with formation of a metal hydride intermediate was shown to be 282 kJ mol^{-1} higher in energy than the transition state for the 1,2-hydrogen shift.

In summary, internal alkyne-vinylidene tautomerization mechanisms favour the 1,2-hydrogen shift either from a coordinated alkyne σ-complex or from a oxidatively added hydride intermediate. Additionally it was shown that a 1,2-hydrogen shift from a side-bound η^2-alkyne structure is generally unfavourable in energy when compared to the σ-complex hydrogen shift mechanism.

1.4.3 Vinylidenes – Role in Catalysis and Oxygen-based Nucleophilic Attack

With Fischer-type metal vinylidene complexes possessing a stabilised electron deficient carbon centre, the vinylidene C_α can be attacked by a large range of nucleophiles. As such, vinylidenes have been used in an enormous array of catalytic and stoichiometric transformations, including pericyclic reactions,[175, 176] dimerization of terminal alkynes,[177, 178] synthesis of furans[179, 180] and other heterocycles,[181, 182] formation of unsaturated ketones with allylic alcohols,[183, 184] hydration,[185] alkene-alkyne coupling,[186] and chiral synthesis.[187]

With more examples known than are able to be listed here,[138, 188, 189] this section shall attempt to describe transformations pertinent to this thesis, specifically the use of oxygen as a nucleophile in anti-Markovnikov type additions.[138, 190]

Markovnikov's rule refers to the addition of nucleophiles to unsaturated bonds. Addition is said to obey the Markovnikov rule when H-X (where X = nucleophile) adds to the unsaturated bond in such a way as to have X form a bond with the most substituted carbon, with hydrogen forming a bond with the least substituted carbon. This is due to the cation formed during addition of the proton being stabilised by the more substituted carbon group. A reaction is said to be adding in an anti-Markovnikov fashion when the reverse is true, i.e. when the nucleophile adds to the least substituted carbon present over the unsaturated bond (Figure 1.36).[191, 192]

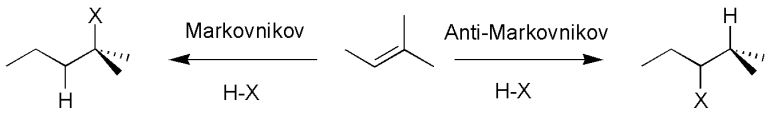

Figure 1.36 – Example of Markovnikov and anti-Markovnikov addition.

Metal alkyne complexes are known to undergo Markovnikov-type addition *via* a Lewis acid-type activation of triple bonds.[193, 194] An example, shown below in Figure 1.37 shows the Markovnikov addition to a terminal alkyne with formic acid acting as a nucleophile.[195]

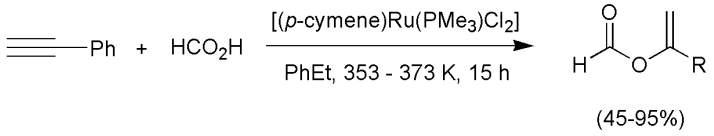

Figure 1.37 – Example of Markovnikov addition to a terminal alkyne.

However due to the stabilised electrophilic C_α of the Fischer-type metal vinylidenes, anti-Markovnikov addition is also viable, with the more substituted C_β no longer the preferred nucleophilic attack site.

One of the first examples of a catalytic system *via* a metal vinylidene complex was proposed in 1986 by Mahé and Dixneuf with the formation of vinyl carbamates with a $RuCl_3.3H_2O$ catalyst through an anti-Markovnikov addition. The reaction involved a terminal alkyne reacting with an amine in a one-step reaction, contrary to the existing multi-step formation of vinyl carbamates.[196]

Dixneuf also investigated the formation of enol esters in reactions of terminal alkynes with carboxylic acid (Figure 1.38).[197]

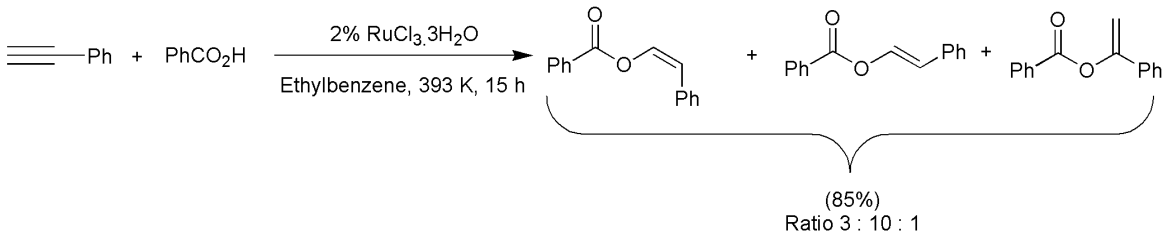

Figure 1.38 – Addition of carboxylate to phenylacetylene with $RuCl_3.3H_2O$.

Reaction of the alkyne produced significant quantities of the anti-Markovnikov product, with small quantities of the Markovnikov product due to competing nucleophilic addition to the alkyne after undergoing electrophilic activation at the metal centre. Of the anti-Markovnikov products, a stereoisomerization ratio of 10:3 selective for the *E*-isomer was obtained.

In a subsequent study [Ru(methallyl)$_2$dppb] was used in place of the ruthenium trichloride catalyst, and as well as significantly higher yields of enol formation, selectivity for the *Z*-isomer was observed (Figure 1.39).[198] Changing the alkyne to *n*-hexyne additionally formed a small quantity of the *E*-isomer (2%),[199] with a change in Markovnikov to anti-Markovnikov product ratios also reportedly being achieved by variation of the ligand and base,[200] as well as with solvent effects.

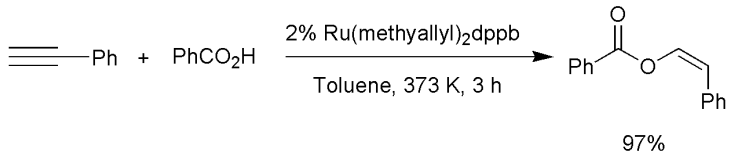

Figure 1.39 – Addition of carboxylate to phenylacetylene with [Ru(methallyl)$_2$dppb].

It was observed in the study by Yi and Gao,[201] that the addition of an alkyne and carboxylic acid in the presence of (PCy$_3$)$_2$(CO)RuHCl showed a preference for the Markovnikov product in dichloromethane (DCM), and the anti-Markovnikov product in toluene when varying the alkyne to include a range of electron donating and withdrawing ligands. In varying the carboxylic acids, the same solvent dependence was largely observed once again. However, more electron withdrawing groups on the carboxylic acid in toluene instead showed small amounts of Markovnikov product, contrary to the general trend for anti-Markovnikov addition in toluene (Table 1.1)

Table 1.1 – Depiction of Markovnikov anti-Markovnikov selectivity with varied substituents and solvents

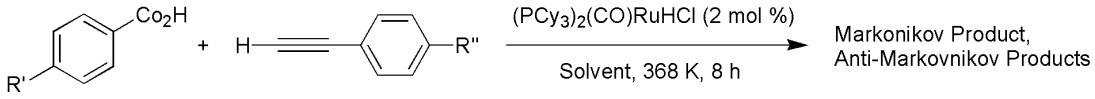

		Solvent = THF	***Solvent = DCM***
R'	***R''***	***Product Ratio (Markovnikov:anti-Markovnikov)***	***Product Ratio (Markovnikov:anti-Markovnikov)***
H	OMe	100:0	0:100
H	Me	100:0	0:100
H	H	100:0	0:100
H	Br	100:0	0:100
H	CF_3	100:0	0:100
H	F	100:0	0:100
OMe	H	100:0	0:100
Me	H	100:0	0:100
Br	H	100:0	0:100
CN	H	100:0	3:97
CF_3	H	100:0	8:81

From these examples, it is clear that addition of oxygen-based nucleophiles is a diverse field. With respect to Markovnikov and anti-Markovnikov addition, it is shown particularly with the contribution by Yi and Gao that changes in solvents and substituents can change the overall preference of the reaction, demonstrating the potential for a tunable catalytic reaction. This subject shall be explored further in chapter 4.

1.4.4 Allenylidenes: Chemistry and Formation

Allenylidenes have similar chemistry to that of carbenes and vinylidenes, with a double bond on either side of the $C_{\beta,}$ and with an unsaturated pair of valence electrons once again at the terminal end of the chain (Figure 1.40).[138, 202] Free allenylidene molecules are reactive and short lived, but examples have been observed trapped in a cold matrix or used as intermediates in trapping reactions,[203] with Bertrand *et al.* reporting the formation of lithium allenylidenes.[204]

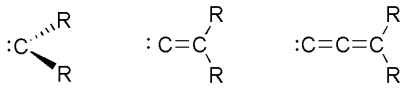

Figure 1.40 – Free carbene, vinylidene and allenylidene molecules.

Much like carbenes and vinylidenes, metal allylidene complexes are stable, and can be classed as either Fischer or Schrock allenylidene complexes. A π-orbital interaction diagram (similar to that seen in Figure 1.33) for Fischer allenylidene complexes is displayed below in Figure 1.41. Once again the LUMO ($\pi 4$) is mainly localised on the C_α and C_γ, allowing nucleophilic attack to occur at these positions.[138]

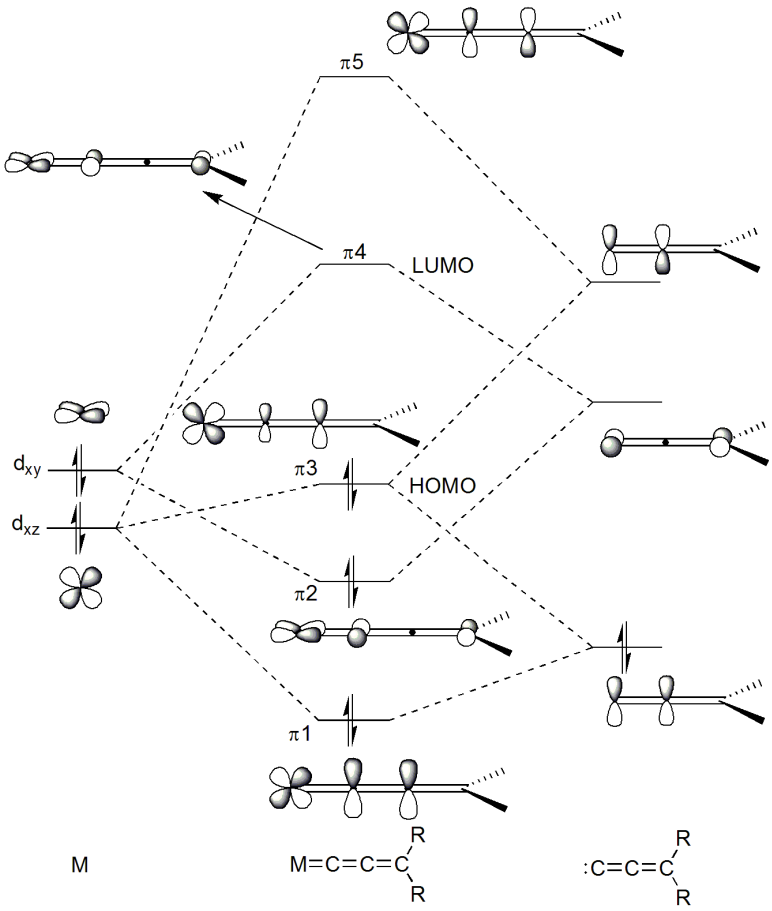

Figure 1.41 – Simplified π-orbital interaction diagram for Fischer-type metal allenylidene complexes.[138]

Historically, the first examples of metal allenylidene complexes were reported in 1976 by Fischer *et al.* and Berke,[205, 206] with $[M(=C=C=CPh(NEt_2))(CO)_5]$ (where M = Cr, W) and $[MnCp(=C=C=Ct Bu_2)(CO)_2]$. In 1982 Selegue first introduced what is now the most common route to allenylidene formation, with the reaction of the $[RuCpCl(PMe_3)_2]$ complex with a propargyl alcohol (Figure 1.42).[207] This initially forms a hydroxy vinylidene at room temperature, but after 27 hours an allenylidene was isolated and identified by single-crystal X-ray crystallography.

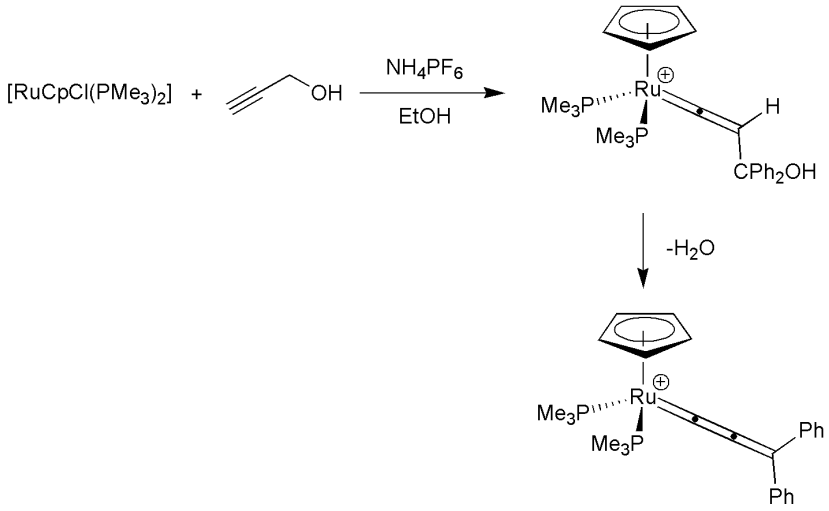

Figure 1.42 – Formation of allenylidene reported by Selegue.[207]

While formation of the vinylidene followed a mechanism of alkyne-vinylidene tautomerization to that seen in section 1.4.2, allenylidene formation proceeded through dehydration of the hydroxy-vinylidene complex.

One particular dehydration mechanism which will become relevant in chapter 3 was reported by Bustelo and Dixneuf in 2004.[208] The study investigated direct heterocycle propargylation with mononuclear ruthenium catalysts and propargylic alcohol. During the reaction one equivalent of water is released indicating a dehydration mechanism such as the one in Figure 1.42.

In a reaction outlined in Figure 1.43, alkynol HC≡CCHPhOH was added to the complex [(p-cymeme)RuCl(PCy_3)][$B(Ar_F)_4$], which was monitored by low-temperature NMR at 213 K. Two complexes were identified, the allenylidene [(p-cymene)RuCl(PCy_3)(=C=C=CHPh)][$B(ArF)_4$] and alkenyl-hydroxycarbene complex [(p-cymene)RuCl(PCy_3)(=C(OH)CH=CHPh)][$B(ArF)_4$]. Upon warming to room temperature, peaks associated with the allenylidene disappeared, leaving only the alkenyl-hydroxycarbene compex. Upon warming to 323 K over 4 hours, this complex reacted further to produce the carbonyl complex [(p-cymene)-RuCl(PCy_3)(CO)][$B(ArF)_4$] and free ethene. This reaction indicated not only allenylidene formation *via* the established route of dehydration, but that water is involved in the further reaction to ultimately produce a carbonyl complex and free ethene.

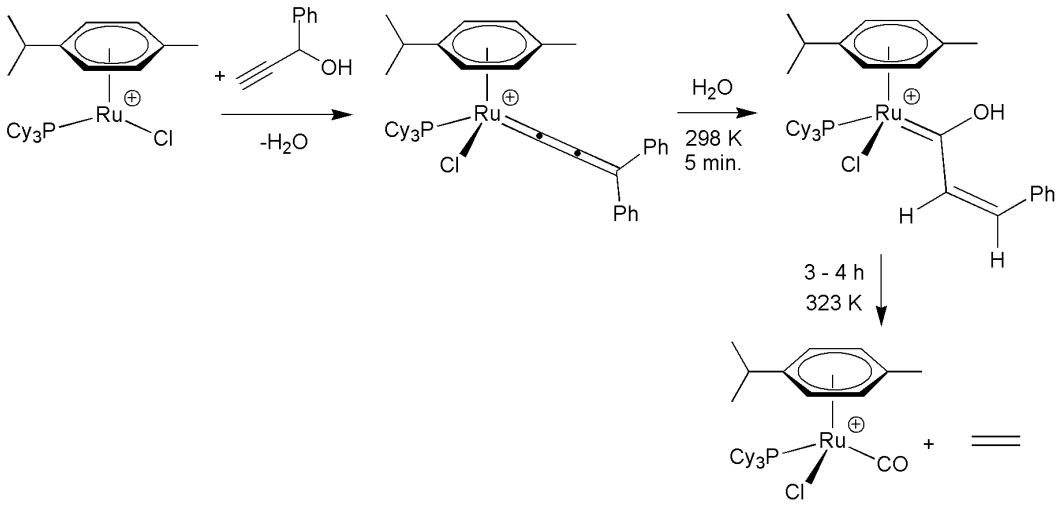

Figure 1.43 – Reaction of HC≡CCHPhOH with complex [(p-cymeme)RuCl(PCy$_3$)][B(Ar$_F$)$_4$].

A similar reaction involving an allenylidene intermediate achieved *via* Lewis-acid mediated hydroxy elimination to form an alkene and free carbon monoxide was also reported by Liu *et al.* in 2003.[209] ^{18}O labelling of the hydroxy group showed that this is the source of the carbon-monoxide oxygen atom, which attacked the allenylidene C_α.

Much like vinylidenes, metal allenylidene complexes have been employed in a range of catalytic applications,[138, 190] primarily due to the stabilisation and accessibility of the δ+ charge located on the C_α and C_γ, allowing allenylidenes to be susceptible to nucleophilic attack. Catalytic reactions such as intramolecular attack to form heterocyclic unsaturated ketones,[210] isomerisation of propargyl alcohols,[211] and ring closing mechanisms[212] are just some of the many examples studied. This reactivity is one of the major reasons for the study of allenylidenes and in particular their formation within this thesis. Indeed, a unique mechanism contrary to that seen with the work by Bustelo and Dixneuf will be shown later in chapter 3.

2. Investigation into a Ruthenium *bis*-Acetate Mediated Alkyne-Vinylidene Tautomerization: Elucidation of the Ligand Assisted Proton Shuttle (LAPS) Mechanism

2.1 Introduction

This chapter will focus on an unusual alkyne-vinylidene tautomerization mechanism involving a *bis*-acetate complex **201** (Figure 2.1) and phenylacetylene.

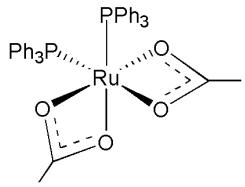

*Figure 2.1 – **201**.*

An alkyne-vinylidene tautomerization can occur through several methods involving the migration of a proton or other small group to the opposite side of the triple bond (see section 1.4.2). However the presence of coordinated acetate ligands presents the possibility of an AMLA/CMD type mechanism (section 1.3.2, Figure 2.2).

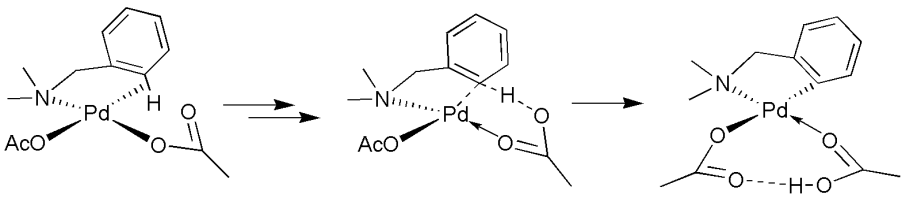

Figure 2.2 – AMLA mechanism.

In the majority of these systems once the assisting ligand is protonated it leaves the coordination sphere of the metal, whereas if the acetate group is facilitating the alkyne-vinylidene tautomerization here, the ligand may also be acting as a Brønsted base. Therefore this chapter shall investigate and present the alkyne-vinylidene tautomerization mechanism with **201**, comparing classical mechanisms with those of a ligand assisted method.

2.1.1 Experimental Observations

The initial basis for this chapter relies on experimental work carried out by Dr Christine Welby, which can be found in several publications,[213, 214] as well as within her published thesis.[215] Preliminary investigations involved a ruthenium *bis*-acetate complex **201**,[216, 217] which can be seen in Figure 2.3. Complex **201** had never been verified as either possessing a *cis* or *trans*-phosphine geometry, and to that end attempts were made to verify the structure. A crystal structure was then obtained during experimental studies which verified the *cis*-phosphine orientation.[213]

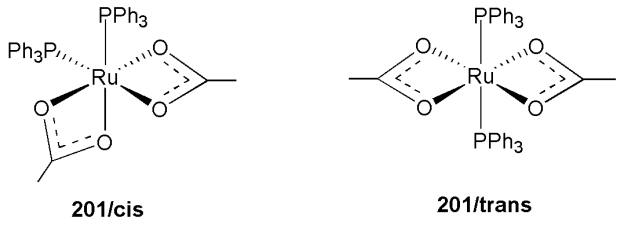

*Figure 2.3 – Two orientations of **201**, cis and trans.*

Once **201** was prepared, this complex was reacted with 1 equivalent of phenylacetylene at room temperature in DCM for one hour which formed complex **202** (Figure 2.4). ^{1}H NMR showed evidence of a vinylidene proton, which was also confirmed by characteristic C_α and C_β resonances in the ^{13}C NMR spectrum. All ancillary ligands were also shown to be present, with ^{31}P and ^{13}C NMR showing that the triphenylphosphine ligands were magnetically equivalent, suggesting a *trans* orientation. In terms of the acetate ligands, IR analysis showed evidence for both κ^1 and κ^2 binding modes.

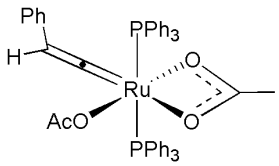

*Figure 2.4 – **202/trans**.*

Further evidence for the formation of **202** was obtained in the form of a single-crystal X-ray structure, of which an ORTEP diagram is shown in Figure 2.5, with a table of bond lengths and angles shown in Table 2.1. Evidence is once again shown for the vinylidene, the *trans* triphenylphosphine groups, as well as the two different binding modes for the acetate ligands. It should be noted that because of a relatively acute O(1)-Ru(1)-O(2) angle (59.08^{o}) due to the κ^2-acetate group, **202/trans** has a distorted octahedral structure.

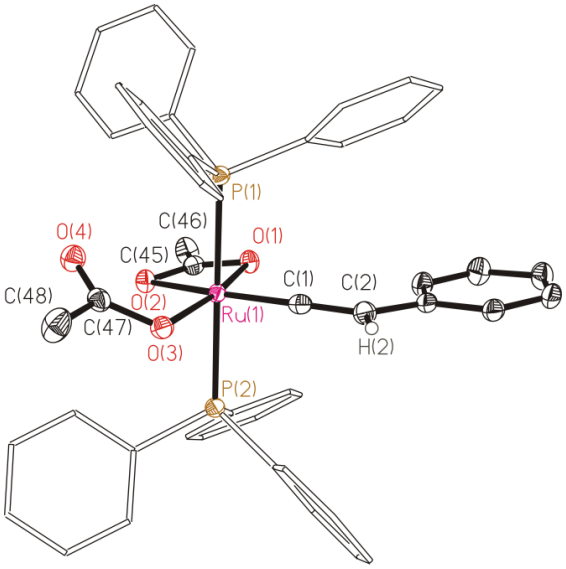

*Figure 2.5 – ORTEP diagram of **202/trans**, thermal ellipsoids, where shown, at the 50 % probability level. Hydrogen atoms, except for H(6), and two molecules of dichloromethane of crystallization omitted for clarity.*[215]

*Table 2.1 – Selected bond lengths and angles for **202/trans**[215]*

Bond	Bond Length (Å)	Angle	Bond Angle (°)
Ru – P(1)	2.385 (7)	P(1) – Ru – P(2)	178.89(3)
Ru – P(2)	2.391 (7)	P(1) – Ru – O(1)	89.08(5)
Ru – O(1)	2.114(2)	P(1) – Ru – O(2)	98.59(5)
Ru – O(2)	2.286 (2)	P(1) – Ru – O(3)	93.06(5)
Ru – O(3)	2.070(2)	O(1) – Ru – O(2)	59.08(6)
Ru – C(5)	1.786(3)	O(1) – Ru – O(3)	168.17(7)
C(5) – C(6)	1.318(4)	O(2) – Ru – O(3)	109.09(7)
		P(1) – Ru – C(5)	87.77(8)
		P(2) – Ru – C(5)	91.58(8)
		O(1) – Ru – C(5)	97.81(9)
		O(2) – Ru – C(5)	155.65(9)
		O(3) – Ru – C(5)	93.90(9)
		Ru – C(5) – C(6)	176.50(2)

The rate of formation of **202** at room temperature is also contrary to the system studied by Wakatsuki *et al.*[172] (Figure 2.6, discussed previously in section 1.4.2). Here the formation of a vinylidene complex from the reaction of an alkyne and $[RuCl_2(PPh_3)_3]$ at room temperature requires 24 hours - contrary to the near instantaneous reaction with **201** and phenylacetylene. Additionally the system investigated by Wakatsuki ultimately forms a *trans*-phosphine vinylidene complex, parallel to the observation of **202/trans**.

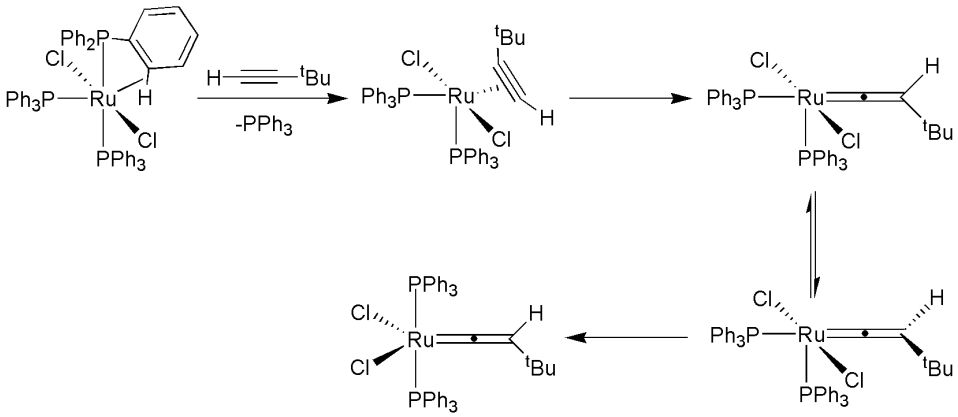

Figure 2.6 – System studied by Wakatsuki.[172]

For the alkyne to coordinate to **201**, an acetate ligand must change its binding mode from κ^2 to κ^1. As shown previously in section 1.3.2 a κ^1-acetate is involved in C-H activation and deprotonation (AMLA/CMD mechanism), with the possibility here being that the acetate is involved in a similar deprotonation mechanism followed by a proton transfer to form the vinylidene, explaining the difference in rates between this system and the one studied by Wakatsuki. However the difference in reactivity between the two systems could also be explained by a change in the electronic properties of the ligands when changing from a halogen to an acetate group, so the assumption is by no means conclusive.

In order to further understand the tautomerization mechanism, an attempt was made to observe the progress of the alkyne-vinylidene tautomerization reaction through *in situ* NMR spectroscopy at room temperature. However the large rate of formation meant the reaction had concluded before the first spectrum could be recorded. An *in situ* low temperature NMR spectroscopic study was then performed in an attempt to observe intermediates during the reaction. The NMR spectrometer was initially cooled to 205 K, with a NMR tube prepared which contained a solution of **201** and deuterated DCM which had previously been frozen in liquid nitrogen. Phenylacetylene was then introduced to the NMR sample of **201**, where the tube was immediately added to the spectrometer upon thawing of the reaction mixture.

Initial observations at 205 K showed that **201** was the main component of the mixture, with small traces of **202** also observed. Warming the mixture to 245 K showed a significant increase in the amount of **202** present, with an additional species – **203** (Figure 2.7) also being observed. The $^{31}P(^{1}H)$ spectrum contained two doublet resonances (at δ_P 66.6 and 30.7 ppm with a mutual coupling constant of $^{2}J_{PP}$ = 17.1 Hz) that suggested **203** contained *cis*-phosphine ligands. The ^{1}H NMR spectra contained a proton resonance (at δ_H 5.94 ppm) that was not consistent with the presence of either a vinylidene or alkyne group in **203**. Upon warming of the reaction mixture to 255 K, ^{1}H and $^{31}P(^{1}H)$ resonances associated with **203** rapidly decreased in intensity, with the singlet of **202** increasing. Cooling a solution of **202** to 220 K did not result in the reformation of **203**.

When this low temperature reaction was repeated using ^{13}C-labelled phenylacetylene (at the terminal position), a large $^{2}J_{PC}$ coupling in the $^{31}P(^{1}H)$ spectrum ($^{2}J_{PP} \approx {}^{2}J_{PC} \approx$ 16.7 Hz at δ_P 66.7 and $^{2}J_{PP}$ = 16.8 Hz, $^{2}J_{PC}$ = 94.5 Hz at δ_P 30.8) indicated that the labelled carbon is *trans* to one of the phosphine groups.

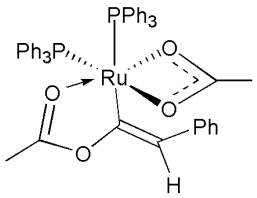

*Figure 2.7 – **203/cis"**.*

These observations and the comparison with experimental data for similar systems mentioned later in the thesis (e.g. the reaction of **302** with phenylacetylene described in chapter 3) suggested the presence of the metallo-enol ester **203** in the reaction mixture at 245 K. This species presumably forms from nucleophilic attack of the uncoordinated oxygen atom of the κ^1-acetate at the electrophilic α-carbon of the vinylidene. Unfortunately the stereochemistry of the vinyl group in **203** could not be determined experimentally during this study.

From these results it was clear that while no proton-transfer intermediates could be observed experimentally, a mechanism of hydrogen migration by 'non-innocent' ligands could not be ruled out. It was also clear that contrary to the ruthenium chloride analogue by Wakatsuki[172] seen in section 1.4.2, the vinylidene was formed very rapidly.

Additionally it appeared that the phosphine groups were rearranging to become *trans* to one another from their initial *cis* orientation during the course of vinylidene formation. The observation of intermediate **203** at 245 K, which converted to the final product **202** on warming to 255 K, could be a precursor for a Berry pseudorotational rearrangement,[218] much like the system investigated by Wakatsuki.

In order to further probe the nature of the isomerisation, the effect of bi-dentate phosphine groups on reactivity toward alkynes was investigated by Elizabeth Smith, with the use of 1,2-*bis*(diphenylphosphino)ethane (DPPE) and 1,2-*bis*(diphenylphosphino)butane (DPPB). These ligands formed the corresponding ruthenium complexes [$Ru(OAc)_2$(DPPE)] (**204**) and [$Ru(OAc)_2$(DPPB)] (**205**) . A single-crystal X-ray structure of **204** is depicted in Figure 2.8 with bond lengths and angles shown in Table 2.2.

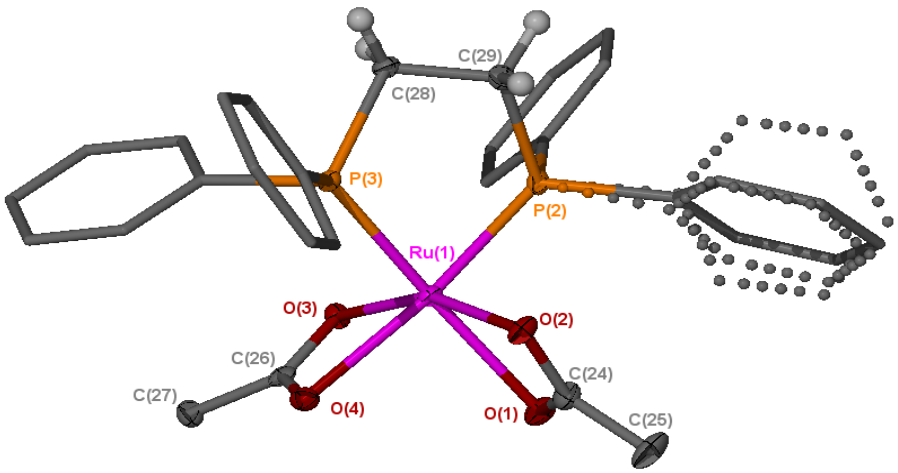

*Figure 2.8 – ORTEP representation of **204**. Thermal ellipsoids, where shown, are at 50% probability, hydrogen stoms have been omitted for clarity (except those on the DPPE backbone). The disordered phenyl ring on the DPPE ligand is shown with dotted lines.*[219]

*Table 2.2 – Selected bond lengths and angles for **204**[219]*

Bond	Bond Length (Å)	Angle	Bond Angle (°)
P(2) – Ru(1)	2.216(6)	P(2) – Ru(1) – P(3)	84.23(2)
P(3) – Ru(1)	2.226 (6)	P(2) – Ru(1) – O(1)	97.12(5)
O(1) – Ru(1)	2.212 (2)	P(2) – Ru(1) – O(2)	88.97(5)
O(2) – Ru(1)	2.121(2)	P(2) – Ru(1) – O(3)	107.12(4)
O(3) – Ru(1)	2.110(2)	P(2) – Ru(1) – O(4)	167.37(4)
O(4) – Ru(1)	2.221 (2)	P(3) – Ru(1) – O(1)	165.81(5)
		P(3) – Ru(1) – O(2)	105.53(4)
		P(3) – Ru(1) – O(3)	90.72(4)
		P(3) – Ru(1) – O(4)	92.76(4)
		O(1) – Ru(1) – O(2)	60.46(6)
		O(1) – Ru(1) – O(3)	102.29(6)
		O(1) – Ru(1) – O(4)	88.81(6)
		O(2) – Ru(1) – O(3)	158.36(6)
		O(2) – Ru(1) – O(4)	103.65(6)
		O(3) – Ru(1) – O(4)	60.56(6)

Unfortunately upon reaction with phenylacetylene complexes **204** and **205** were not able to produce a metal vinylidene complex as easily as **201**, instead forming a complex mixture of products, such as alkyne dimers. Reaction of **204** and **205** with 4-ethynyl-*α,α,α*-trifluorotoluene produced similar results. These results indicate that alkyne to vinylidene tautomerization either does not occur as readily with the *cis*-phosphine orientation, or that mono-dentate phosphine groups are required.

In summary reaction of **201** with phenylacetylene rapidly affords the metal vinylidene complex **202** at room temperature. Intermediates for the reaction were not observable, with the exception of the metallo-enol ester complex **203** - seen in low temperature NMR experiments at 220 K. Additionally *cis*/*trans* phosphine isomerisation is occurring along with formation of the vinylidene complex, with the geometry of the potential intermediate **203** possessing *cis*-phosphine groups. Attempts at vinylidene tautomerization with complexes **204** and **205** proved unsuccessful, suggesting that the bi-dentate *cis*-phosphine groups obstruct the alkyne-vinylidene tautomerization.

2.2 Results and Discussion

2.2.1 Computational Preamble

The reaction of **201** and phenylacetylene proceeds to form the vinylidene complex tautomer **202** near instantaneously, contrary to a similar system observed by Wakatsuki.[172] Due to the speed of reaction no intermediates were observable apart from the metallo-enol ester complex **203** at 245 K (Figure 2.9). Additionally complex **201** possessed *cis*-phopshines, however in **202** the phosphines have become *trans* to one another. This is especially interesting due to the formation of the *cis*-phosphine intermediate **203**. The presence of acetate ligands also present the possibility of an AMLA/CMD type mechanism occurring.

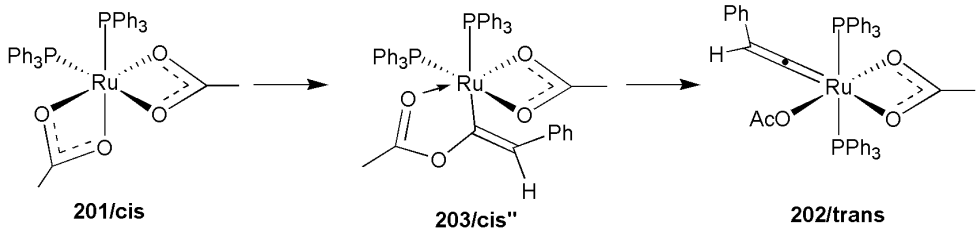

Figure 2.9 – Overview of the tautomerization mechanism intermediates.

In order to provide more information on the nature of the alkyne-vinylidene tautomerization mechanism, a computational investigation was performed and is presented here. As the tautomerization mechanism was not elucidated experimentally, the classical methods of vinylidene tautomerization such as through a 1,2-hydrogen shift or *via* a hydride intermediate shall be studied, along with the possibility of an AMLA/CMD type mechanism being involved. The *cis*/*trans* phosphine isomerisation from **201** to **202** shall also be investigated in order to identify the location and mechanism of the isomerisation.

Potential energy surfaces were generated with the use of DFT. The general methodology used for these studies is outlined in section 7.1 with DRC analyses performed on all transition states as per section 7.2. Due to the intramolecular nature of the tautomerization mechanism and lack of charged intermediates and fragments which would be strongly affected by the solvent in solution, solvation corrections were not applied to the gas-phase energies determined during this study. All energies reported in the text are ZPE corrected SCF energies.

Due to the ambiguous location of phosphine rearrangement, three separate PESs were created for each mechanism that was investigated. The first involved the *trans* phosphine complex (**trans**) and the second and third involved the two different isomers where the phosphine groups were *cis* to one another (**cis'** and **cis"**) (Figure 2.10).

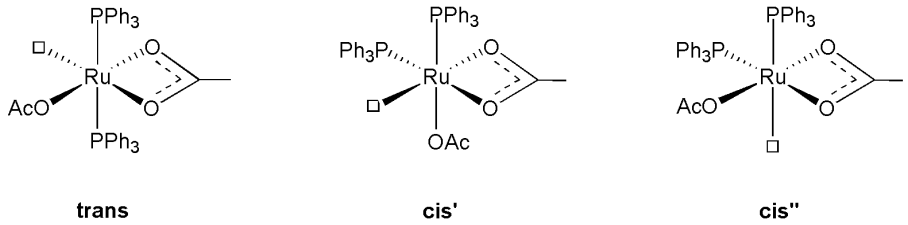

Figure 2.10 – Different isomers of the ruthenium complexes modelled in this study.

2.2.2 Classical Alkyne-Vinylidene Tautomerization

In order to establish the feasibility of the 'classical' mechanisms, the alkyne-vinylidene tautomerization at the ruthenium centre was studied. These mechanisms consisted of a direct 1,2-hyrdogen shift (from either a side-bound or C-H agostic alkyne complex) or by oxidative addition of the alkyne C-H bond to the metal to give a hydride intermediate, which subsequently undergoes 1,3-hydrogen migration (Figure 2.11).

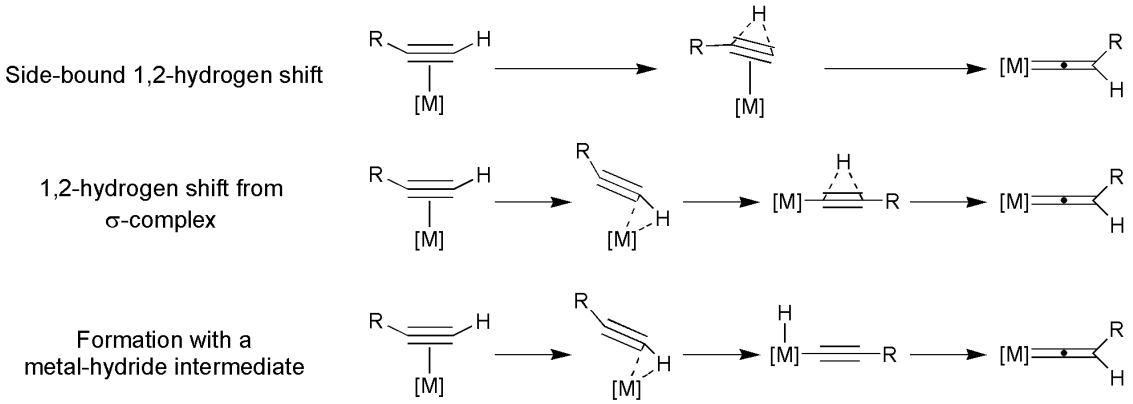

Figure 2.11 – Methods of classical alkyne-vinylidene tautomerization.

All mechanisms begin by an acetate ligand in complex **201** changing its binding mode from κ^1 to κ^2 to form **A1**. Hemi-labile oxygen-based ligands at ruthenium is a common occurrence in the literature - an example being the Grubbs-Hoveyda catalysts, where oxygen ceases to coordinate to the metal centre in order to free a coordination site for further reaction.[147, 220] Once formed, the alkyne would coordinate in an η^2 fashion - forming **A2**. These steps are shown in Figure 2.12 (for simplicity all stationary points are shown as the **trans** isomers, but both **cis'** and **cis''** were also calculated).

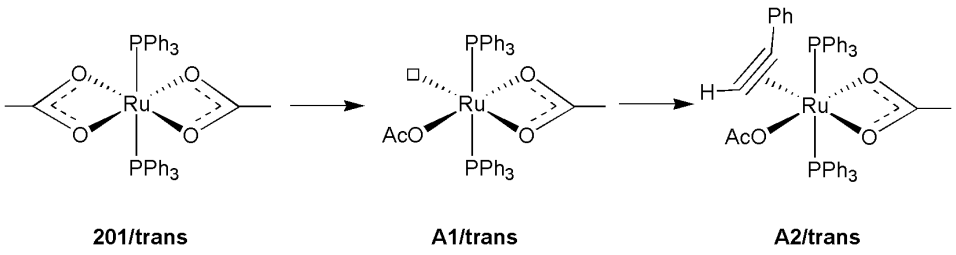

*Figure 2.12 – Formation of **A2** from **201**.*

The first alkyne-vinylidene tautomerization mechanism to be considered in this system involves a direct 1,2-hydrogen shift from the side-bound alkyne to directly form complex **A2**, which can be seen in Figure 2.13. This mechanism proceeds through the transition state $\mathbf{TS_{A2\text{-}202}}$, where a distorted η^2-alkyne simultaneously undergoes proton migration while adjusting its orientation towards the metal to form **202**.

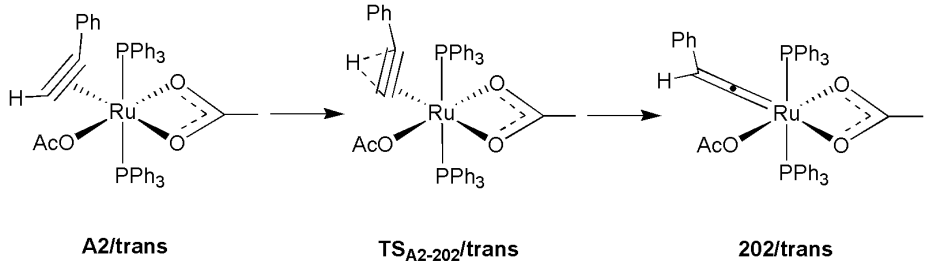

*Figure 2.13 – Mechanism of direct 1,2-hydrogen shift from **A2** through $\mathbf{TS_{A2\text{-}202}}$.*

The second pathway initially involves the rearrangement of the alkyne complex **A2** to complex **A3** – a C-H agostic alkyne 'σ-complex'. Once formed the σ-complex forms **202** through a direct 1,2-hydrogen shift *via* transition state $\mathbf{TS_{A3\text{-}202}}$, shown below in Figure 2.14.

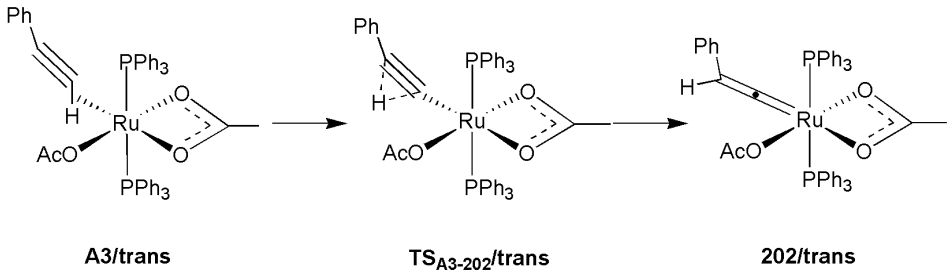

*Figure 2.14 – Mechanism of direct 1,2-hydrogen shift from **A3** through $\mathbf{TS_{A3\text{-}202}}$.*

Finally a pathway through the hydride intermediate **A4** was also considered. As in the mechanism above, this pathway initially proceeds through the σ-complex **A3**, which undergoes oxidative addition to the metal to form the hydride complex **A4**. A 1,3-hydride migration from the metal to the β-carbon of the acetylide ligand in **A4** then results in the formation of the vinylidene complex **202** (shown below in Figure 2.15). Due to the relatively high energy of **A4/trans** (see below), no attempt was made to optimise the structures of the transition states $\mathbf{TS_{A3\text{-}A4}}$ and $\mathbf{TS_{A4\text{-}202}}$.

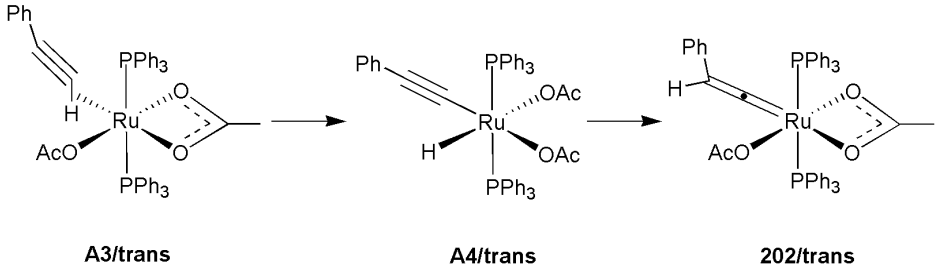

*Figure 2.15 – Formation of **202** through the hydride intermediate **A4**.*

The PES showing all classical alkyne-vinylidene tautomerization mechanisms described above is presented in Figure 2.16.

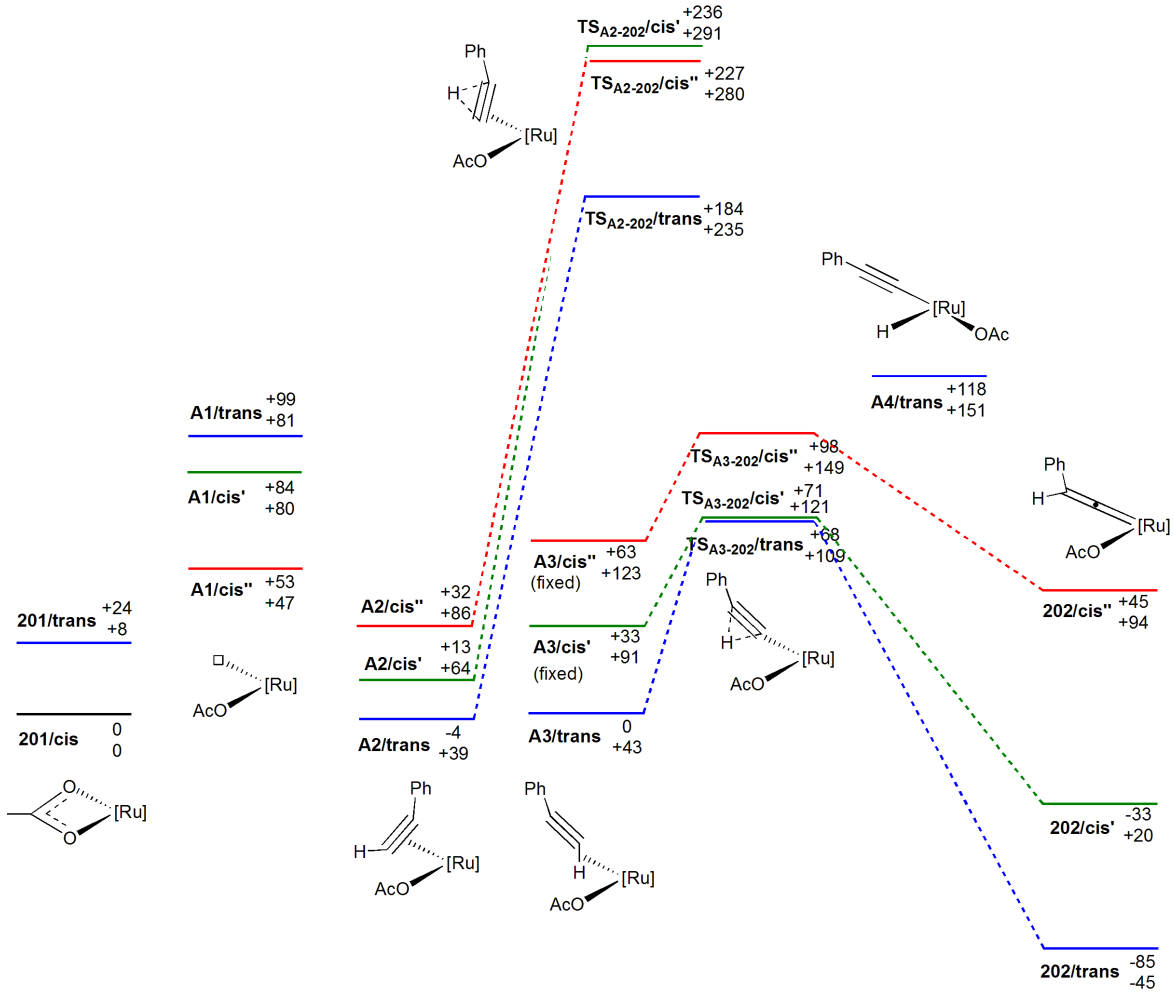

*Figure 2.16 – Classical alkyne-vinylidene tautomerization. Energies are ZPE corrected SCF (top) and Gibbs free (bottom) energies in kJ mol^{-1}, relative to **201/trans**. The **trans**, **cis'** and **cis"** pathways are shown in blue, green and red respectively. [Ru] = [Ru(OAc)(PPh$_3$)$_2$].*

For the starting complex **201** a difference in energy between the *trans* and *cis* isomers (24 kJ mol^{-1}) was found, with **201/cis** being the lowest in energy - consistent with the exclusive observation of the *cis* isomer experimentally.

The κ^1-acetate complexes **A1** are shown to be significantly higher in energy than the κ^2-acetate starting complexes **201**, being between +53 and +99 kJ mol^{-1} higher in energy than the reference point (**201/cis**). Here, the ruthenium centre in **A1** is now coordinatively unsaturated, which in the real system would have been accompanied by coordination of a solvent molecule. Because this can only be effectively modelled with the use of explicit solvation, these barriers will be artificially higher in energy than would be expected in reality. With respect to the phosphine geometry, the formation of **A1/cis''** from **201/cis** was found to be the lowest energy isomer of **A1**.

For the geometry of **A1/trans** and **A1/cis** (Figure 2.17), the structure may not represent the most heavily populated isomer in solution as only the **b** isomers were able to be optimised. In these isomers, the free oxygen atom is forced to rotate 180° away from the free coordination site in order to prevent formation of a Ru-O bond during geometry optimisation and hence the reformation of **201**. This has the effect of changing the geometry of **A1/trans** to that of a trigonal bipyramidal structure, when in reality the free coordination sites of both isomers would be occupied with either the alkyne or a solvent molecule.

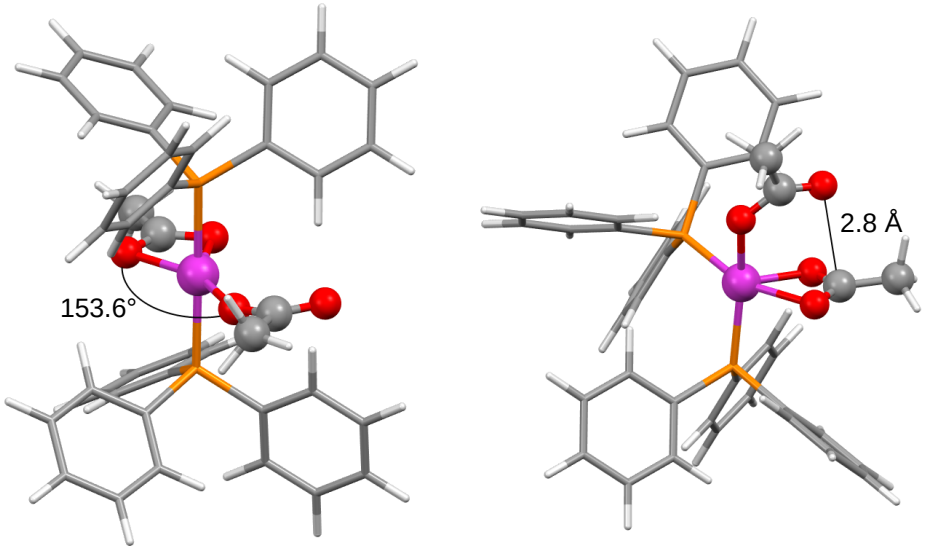

*Figure 2.17 – Optimised geometries of **A1/trans** (left) and **A1/cis'** (right).*

The η^2 bound alkyne complexes **A2** are found to be between -4 and +32 kJ mol^{-1} higher in energy than the starting complexes of **201**, with the **cis''** isomer now being highest in energy and the **trans** isomer now lowest. The **a/x** geometry of the **cis'** and **cis''** isomers of **A3** could not be optimised, instead the structures optimised to the geometry of **A5** (see section 2.2.3). Geometries for the **a/x** isomers for **A2/cis'** and **A2/cis''** were obtained by fixing the C-H bond distance to that of a previously observed σ-complex. The σ-complex of **A3** is shown to be at similar energies to that of **A2** for the **trans** isomer, with the **cis'** and **cis''** isomers higher in energy relative to their η^2-alkyne isomers (+20 and +31 kJ mol^{-1} respectively). Additionally isomers **A3** (Figure 2.18) and **A2** have a short hydrogen bond between the acetate group and the terminal proton of the alkyne, which explains not only the energetic stability of the stationary points but also the deprotonation to form **A5** from **A3**.

The stability of the **trans** pathway compared with the **cis'** and **cis''** for **A2** and **A3** is due to the steric clash involved with orientation of the phosphine groups. As can be seen in Figure 2.18, **A3/trans** is less sterically strained due to the bulky phosphine groups being furthest away from each other. However this is not the case in **A3/cis'**, where the phosphine groups interact with both the κ^1-acetate and alkyne groups. The angle between phosphine atoms is shown to increase by 5.2° from **201/cis** to **A3/cis'** due to a rearrangement of the phenyl groups in order to accommodate an alkyne and κ^1-acetate.

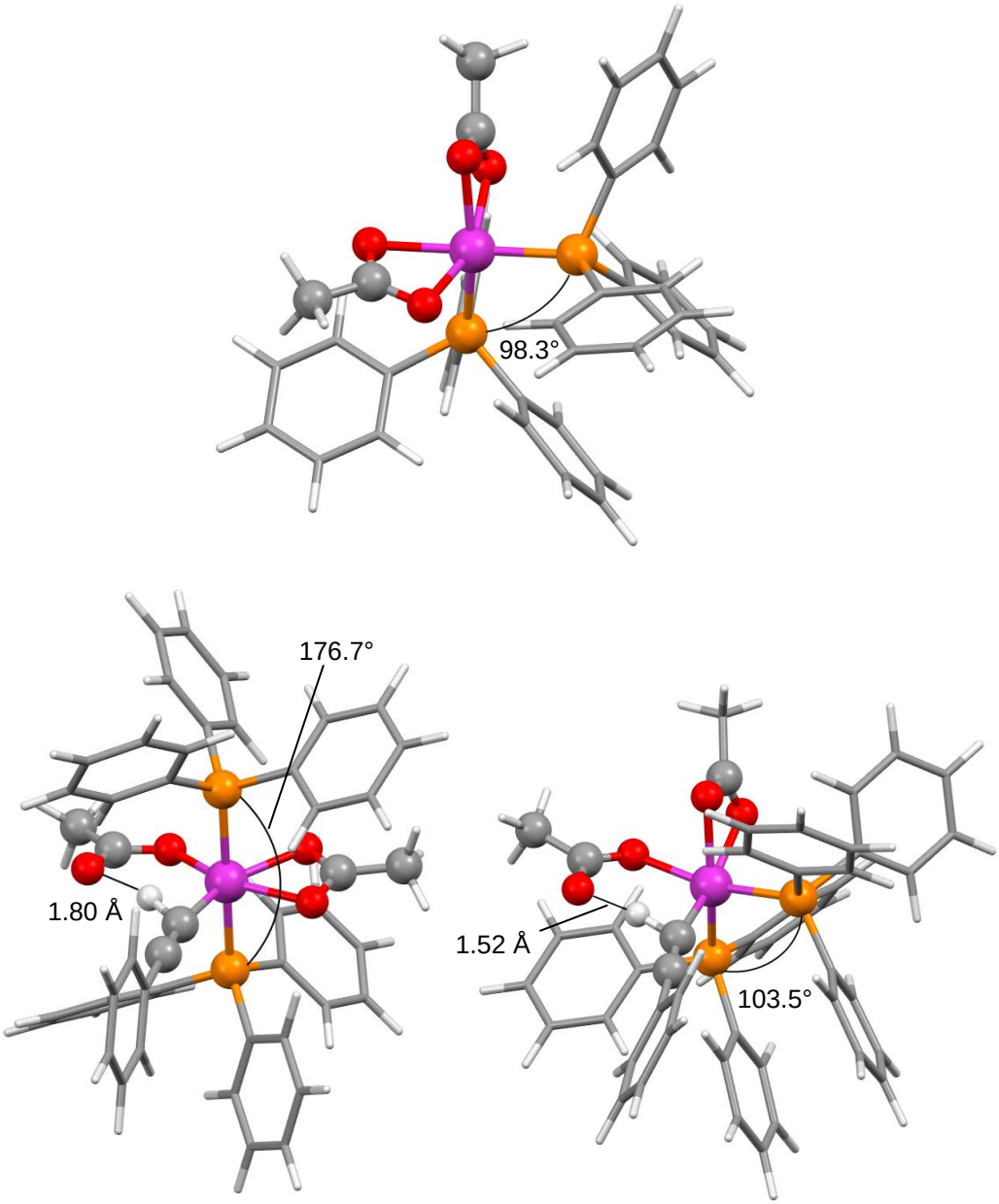

*Figure 2.18 – Optimised geometry of **201/cis** (top), **A3/trans/a/x** (bottom left) and **A3/cis'/a/x** (bottom right).*

The vinylidene **202** is -45 +20 and +94 kJ mol^{-1} for the **trans**, **cis'** and **cis''** isomers respectively, relative to the starting complex **201**. The thermodynamic stability of **202/trans** relative to **201/cis** agreed with the experimental observation that the *trans*-phosphine isomer of vinylidene complex **202** is the overall product of the reaction.

The transition state for the 1,2-hydrogen shift pathway from the η^2-bound alkyne (**$TS_{A2\text{-}202}$**) is too high in energy for all phosphine isomers for the mechanism to be feasible for the observed reaction conditions (298 K, 1 s), with the lowest energy transition state being found at +184 kJ mol^{-1} for **$TS_{A2\text{-}202}$/trans**. This agreed with the study by Angelis and Sgamellotti that showed the η^2-bound 1,2-hydrogen shift to be much higher in energy than the σ-complex mechanism.[170]

The metal hydride intermediate **A4/trans** is +118 kJ mol^{-1} relative to **201**, which is also too high in energy to be considered for the observed experimental conditions. The high barrier of the hydride intermediate agrees with the study by Wakatsuki, which showed a 76 kJ mol^{-1} difference between the hydride and 1,2-hydrogen shift transition state.[172] Additionally, no other isomers of **A4** could be located on the PES.

Based on these investigations, the 1,2-hydrogen shift mechanism from the C-H agostic alkyne σ-complex (**$TS_{A3\text{-}202}$**) appears to be the most likely classical alkyne-vinylidene tautomerization mechanism for this system, which concurs with the study by Angelis and Sgamellotti, but most importantly with the study by Wakatsuki into the analogous ruthenium system. The 1,2-hydrogen shift mechanism from the σ-complex has an energetic span (ignoring stationary point **A1**) of 72 kJ mol^{-1} for the **trans** pathway (S-TDI=**A2**) and 71 and 98 kJ mol^{-1} for the **cis'** and **cis''** pathways respectively (S-TDI = **201/cis**).

2.2.3 Acetate-Ligand Assisted Mechanism

After investigation of the classical alkyne-vinylidene tautomerization pathways, a possible acetate ligand-assisted mechanism was investigated and is presented here. Beginning in a similar manner to the mechanisms described above, an η^2-alkyne complex (**A2**) is formed from the starting complex **201**. The alkyne can then change its coordination mode to form the C-H agostic complex **A3**, with a short O-H bond distance between the alkyne σ-bond and the acetate (1.8 Å for **A3/trans/a/x**). This is similar to the AMLA and CMD mechanisms (see section 1.3.2.) where an agostic bond was also stabilised by an acetate ligand.

This has the effect of pre-organising the structure to allow the facile deprotonation by the acetate group. This can be achieved *via* the η^2 or σ-complex alkyne (**A2** and **A3** respectively) through the transition states $\mathbf{TS_{A2\text{-}A5}}$ and $\mathbf{TS_{A3\text{-}A5}}$. This deprotonation leads to complex **A5** - a ruthenium acetylide complex with an acetic acid ligand coordinated to Ru, which can be seen below in Figure 2.19. The acetate ligand is therefore acting as an intramolecular base to assist in the C-H activation step which is also seen with the AMLA and CMD mechanisms.

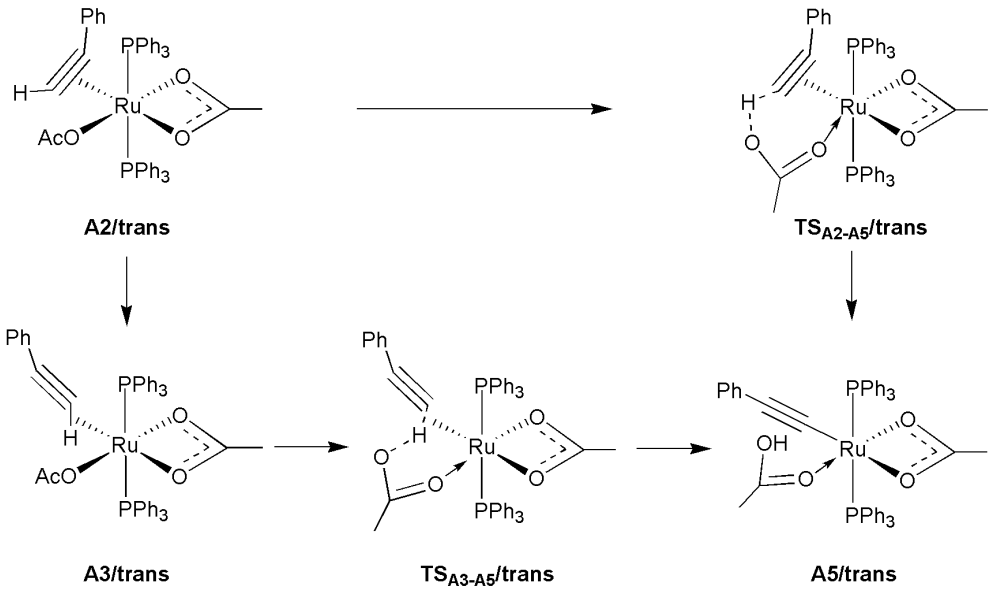

*Figure 2.19 – Deprotonation mechanism to form acetylide **A5**.*

Once formed, the Ru-bound acetic acid can then act as an intramolecular Brønsted acid to protonate the C_β position of the acetylide ligand through transition state **$TS_{A5\text{-}202}$** to form the vinylidene complex **202** (Figure 2.20).

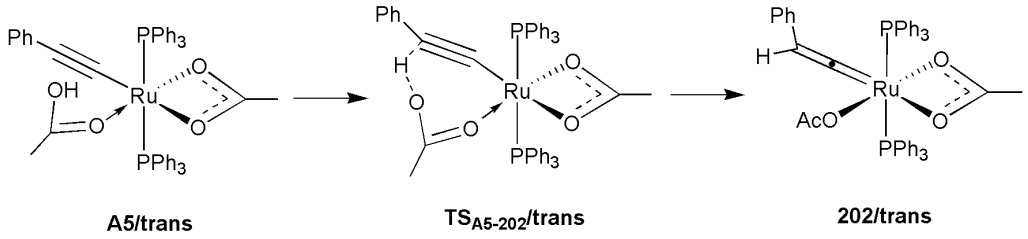

*Figure 2.20 – Formation of the vinylidene complex **202** through protonation of C_β.*

A ligand-assisted alkyne-vinylidene tautomerization was also shown in a study performed by Carmona *et al.* where a pyridyl ligand was instrumental in vinylidene formation. The mechanism shown in Figure 2.21, was investigated theoretically, and showed a facile rearrangement with a small barrier of only 51 kJ mol^{-1} for the ligand-assisted mechanism.[221]

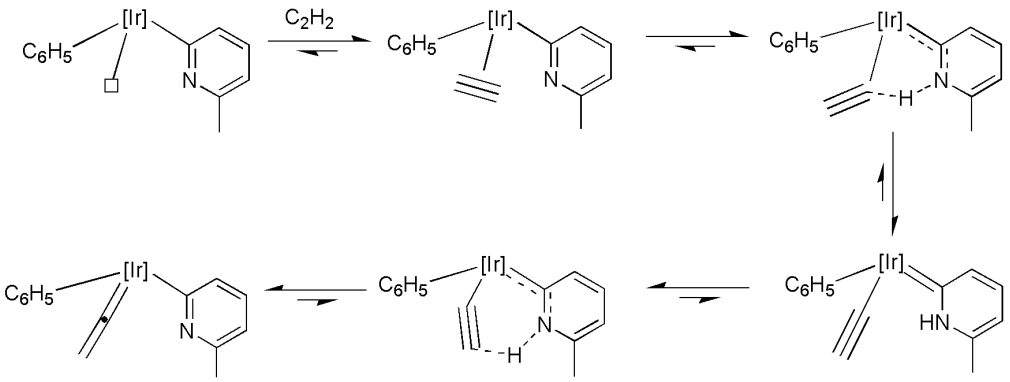

Figure 2.21 – Ligand assisted alkyne-vinylidene tautomerization mechanism with acetylene.[221]

While the use of acetate ligands to engage in C-H activation is by no means unique, this proposed mechanism has the unusual and potentially synthetically very useful possibility that the acetate ligand is acting as both an intramolecular base and acid at different points in the mechanism, 'shuttling' the proton from C_α to C_β in a similar mechanism to the one reported by Carmona and co-workers. Due to the dual base-acid nature of the acetate ligand in forming the vinylidene, this mechanism was termed the ligand assisted proton shuttle mechanism (LAPS). The PES for this mechanism is shown in Figure 2.22.

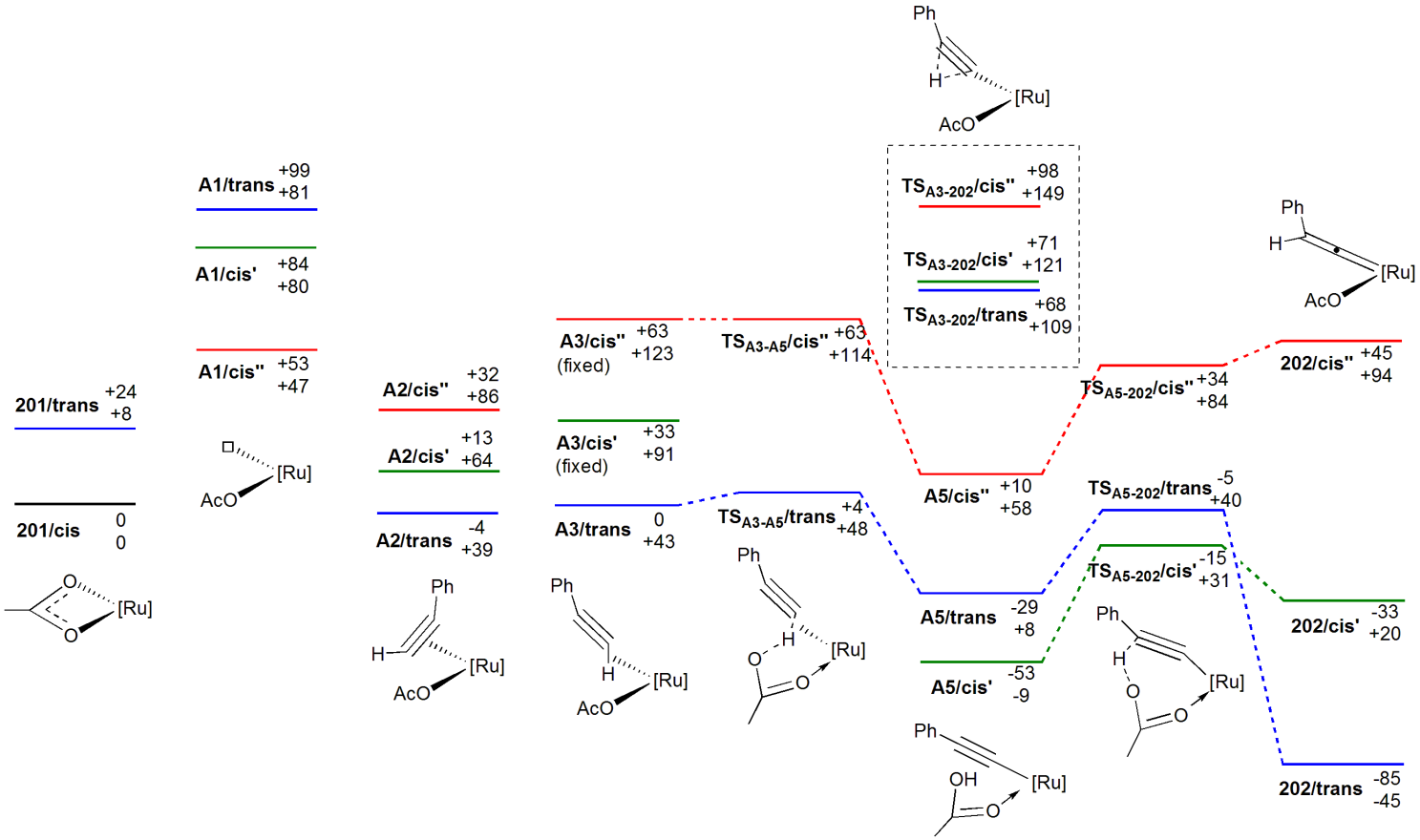

*Figure 2.22 – Acetate-assisted alkyne-vinylidene tautomerization mechanism with lowest classical tautomerization barrier for comparison. Energies are ZPE corrected SCF (top) and Gibbs free (bottom) energies in kJ mol^{-1}, relative to **201/cis**. The **trans**, **cis'** and **cis"** pathways are shown in blue, green and red respectively. [Ru] = [Ru(OAc)(PPh$_3$)$_2$].*

The transition state $\mathbf{TS_{A3\text{-}A5}}$ was shown to be similar in energy to the σ-complex **A3**, for example it is only 5 kJ mol^{-1} higher in energy than **A3** for the **trans** isomer. The transition state $\mathbf{TS_{A3\text{-}A5}}$**/cis'** could not be located using the standard transition state search methodology described in section 7.1, neither was it possible to locate this state using linear transit approaches. In addition it was not possible to locate stationary points corresponding to the transition state for direct deprotonation of the η^2-alkyne complex ($\mathbf{TS_{A2\text{-}A5}}$).

The small barrier to C-H activation in this system is unusual and is likely to be related to the small O-H distance seen in structures **A2** and **A3** (1.80 Å for **A3/trans** – see Figure 2.18) effectively pre-ordering the geometry for a facile deprotonation by the acetate group. This is very similar to the agostic structure seen in the AMLA mechanism, with the palladium and iridium systems showing O-H bond lengths of approximately 2 Å.[97, 98]

As mentioned previously the **cis'/a/x** and **cis''/a/x** isomers of **A3** were optimised with a fixed C_α-H distance, as both isomers consistently optimised to structure **A5** during normal optimisation. This may be due to the small energy difference that the proton transfer has to overcome to undergo a ~70 kJ mol^{-1} drop in energy to form **A5**.

Formation of **A5** is significantly exothermic for both the **cis'** and **trans** pathways, being -53 and -29 kJ mol^{-1} relative to **201/cis**. Despite being the highest in energy of the three isomers, **A5/cis''** is only +10 kJ mol^{-1} relative to **201/cis**, and is still exothermic in comparison with $\mathbf{TS_{A3\text{-}A5}}$**/cis''**.

Protonation of the C_β *via* $\mathbf{TS_{A5\text{-}202}}$ for the **cis'** and **trans** isomers was +38 and +24 kJ mol^{-1} higher in energy than **A5**, and -15 and -5 kJ mol^{-1} relative to **201/cis**. While once again the highest of the three isomers, $\mathbf{TS_{A5\text{-}202}}$**/cis'** is only +34 kJ mol^{-1} relative to **201/cis**. The energy of the transition states show that protonation of the acetylide by acetic acid has a low barrier (ca. 20-30 kJ mol^{-1} from **A5**), and is consistent with the fast kinetics observed experimentally at 298 K.

The optimised geometry of $\mathbf{TS_{A5\text{-}202}}$ (an example is shown in Figure 2.23) shows a slight change in the linearity of the acetylide group, with the C_β bent toward the proton of the acetic acid ligand.

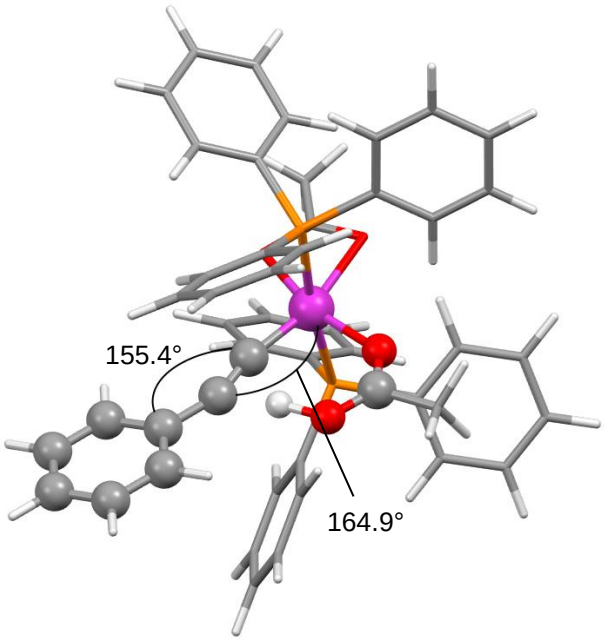

Figure 2.23 – Optimised geometry of ***$TS_{A5\text{-}202}$/trans****.*

The energetic span for the LAPS mechanism for the **trans** and **cis'** isomers is 24 and 38 kJ mol^{-1} (S-TDI = **A5**, S-TDTS = $\mathbf{TS_{A5\text{-}202}}$) respectively and 63 kJ mol^{-1} for the **cis"** isomer (S-TDI = **201/cis**, S-TDTS = $\mathbf{TS_{A3\text{-}A5}}$) this compares with 72, 71 and 98 kJ mol^{-1} for the **trans**, **cis'** and **cis"** isomers of the 1,2-hydrogen shift mechanism. These results suggest that the acetate-assisted LAPS mechanism is the most likely alkyne-vinylidene tautomerization mechanism in this system when compared to classical mechanisms.

It has been shown for the AMLA mechanism that it is possible for the acetate ligand to activate a C-H bond *via* the oxygen atom that is coordinated to the metal through a four-membered transition state as well as through the previously discussed six-membered transition state. In the AMLA system this is denoted as AMLA(4) to distinguish it from the 'standard' AMLA(6) mechanism. In analogy to the AMLA mechanism, a four-membered version of LAPS – **LAPS(4)** – was compared to the regular six-membered LAPS mechanism.

In order to proceed along the **LAPS(4)** mechanism, the κ^1-acetate group of **A3** would initially need to be facing away (isomer **b/x**) from the alkyne ligand (Figure 2.24). This has the additional effect of losing the energetic stability afforded by the acetate-alkyne hydrogen bond, with the O-H bond distance to the terminal alkyne proton being larger (2.2 Å for **A3/trans/b/x** compared with 1.8 Å for **A3/trans/a/x**).

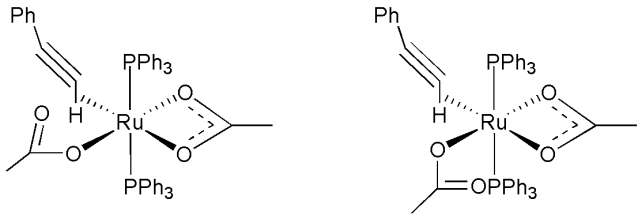

A3/trans/a/x **A3/trans/b/x**

Figure 2.24 – ***A3/trans/a/x*** *and* ***A3/trans/b/x****.*

The alkyne is then deprotonated by the acetate *via* $\mathbf{TS_{A3\text{-}A5}}$ to form **A5**. To complete the LAPS mechanism, the acetic acid group can then protonate the C_β of the acetylide group *via* $\mathbf{TS_{A5\text{-}202}}$ (Figure 2.25).

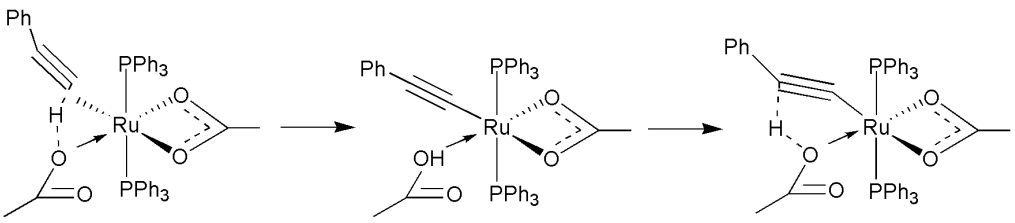

$\mathbf{TS_{A3\text{-}A5}}$**/LAPS-4/trans** **A5/LAPS-4/trans** $\mathbf{TS_{A5\text{-}202}}$**/LAPS-4/trans**

Figure 2.25 – ***LAPS(4)*** *stationary points.*

As can be seen from the PES in Figure 2.26, the **LAPS-4** isomers are generally higher in energy than the standard LAPS stationary points, potentially due to steric strain or a lack of electron density on the coordinated oxygen, making it a poorer hydrogen-bond acceptor and base. Additionally the **b** isomers of **A3** are found to be higher in energy by 30-40 kJ mol^{-1} due to the loss of the stabilising acetate-alkyne hydrogen bond.

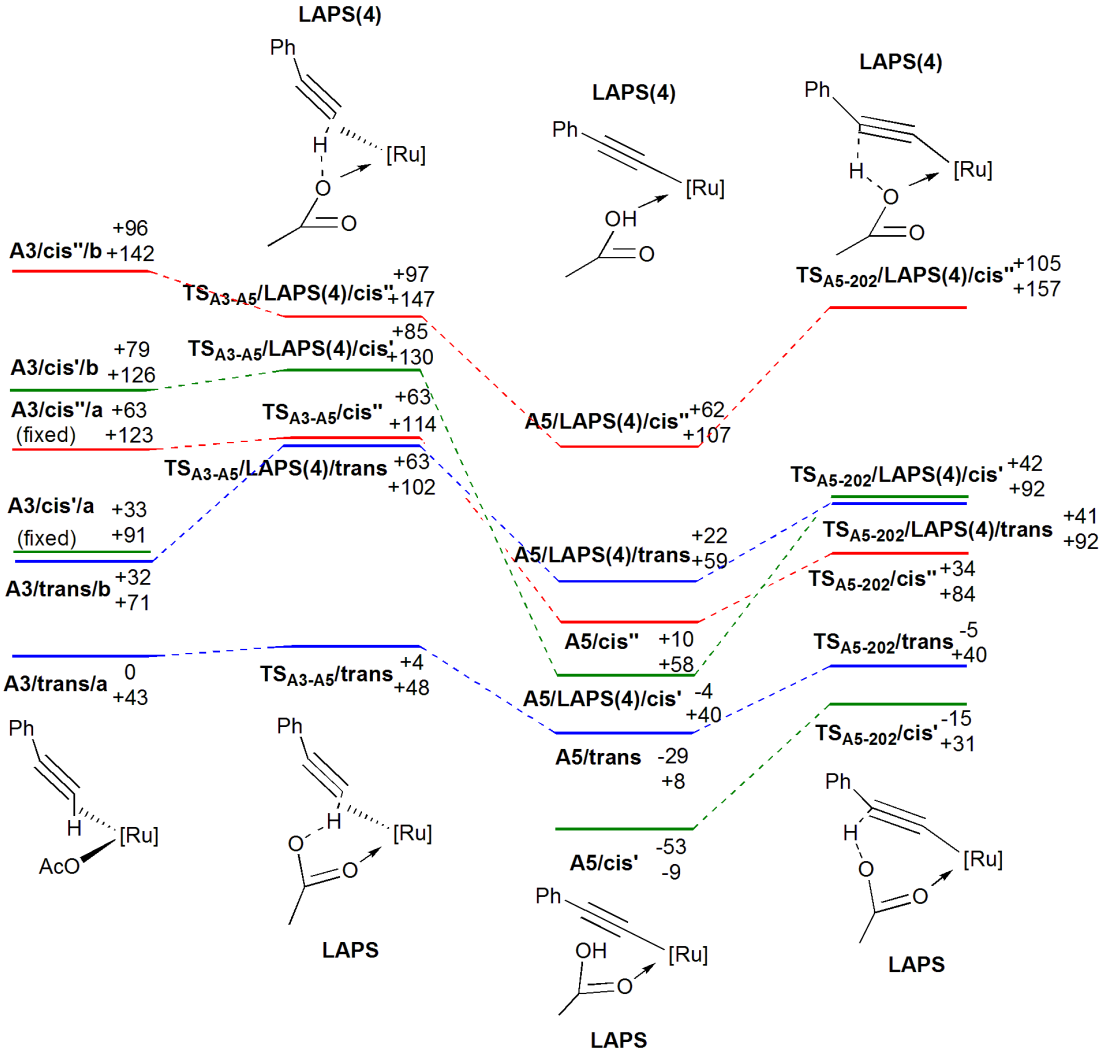

*Figure 2.26 – Comparison of **LAPS(4)** energies. Energies are ZPE corrected SCF (top) and Gibbs free (bottom) energies in kJ mol^{-1}, relative to **201/cis**. The **trans**, **cis'** and **cis''** pathways are shown in blue, green and red respectively. [Ru] = [Ru(OAc)(PPh$_3$)$_2$].*

Due to the distance between the bound oxygen and the C_β of the acetylide, the optimised geometry of **$TS_{A5\text{-}202}$/LAPS(4)** (Figure 2.27) shows considerably more distortion of the acetylide structure than the **LAPS(6)** analogue.

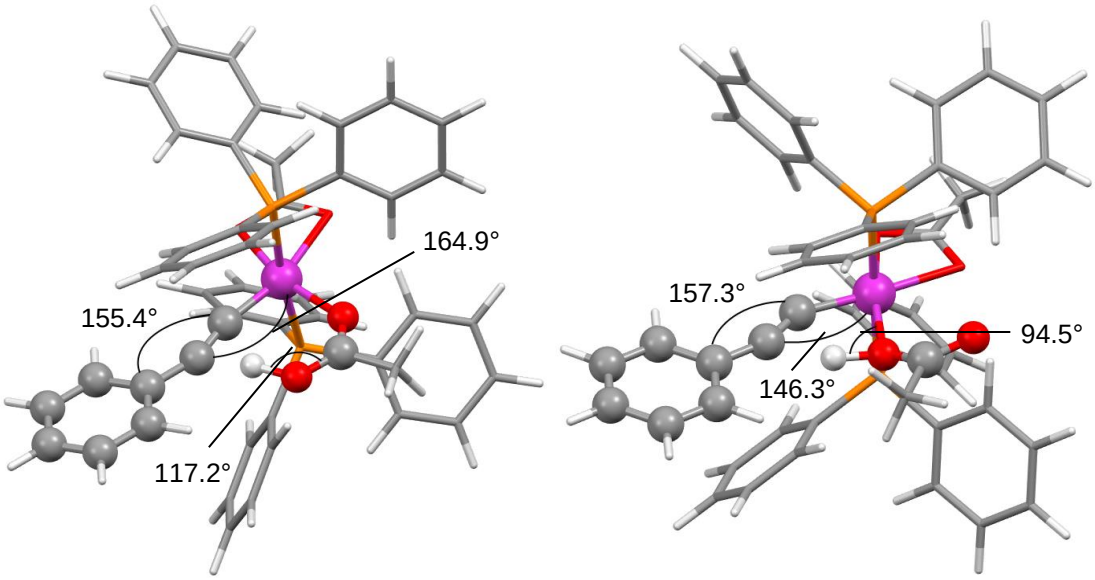

*Figure 2.27 – Optimised geometry of **$TS_{A5\text{-}202}$/LAPS(4)** (left), with **$TS_{A5\text{-}202}$** (right) for comparison.*

The energetic span for the **LAPS(4)** system was 65, 83 and 97 kJ mol^{-1} for the **trans**, **cis'** and **cis"** isomers, compared with 24, 38 and 63 kJ mol^{-1} for the **LAPS(6)** mechanism. These results indicate that much like the AMLA mechanism, deprotonation and protonation by the acetate occurs with the non-bound oxygen atom of the acetate ligand.

2.2.4 Investigation of Metallo-Enol Ester Complexes

During the theoretical investigation two significant metallo-enol ester structures were located on the PES: complex **203** - which was seen in low temperature NMR studies (mentioned earlier in section 2.1.1) and complex **A6** - a product of the nucleophilic attack of the κ^1-acetate on the η^2-alkyne in **A2,** both of which are shown in Figure 2.28. Stationary points could be located for all three isomers of **203** and **A6**, and their relative energies are shown in Figure 2.29.

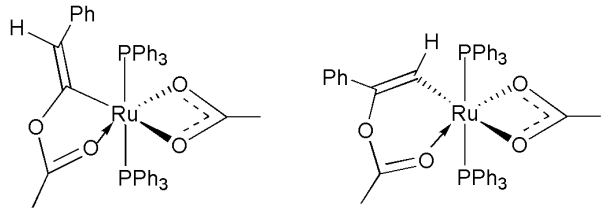

203/trans **A6/trans**

*Figure 2.28 – The structures of the metallo-enol ester **203** and **A6**.*

The C=C bond in **203** was shown experimentally to be *trans* to a phosphine ligand which corresponds to the **cis"** isomer in the computational studies, however it is the **trans** isomer which is the lowest energy isomer of **203** and not the **cis"**, with a difference of 39 kJ mol^{-1}.

As the formation of **203** during low temperature NMR studies occurred before formation of **202** and was not reformed upon re-cooling of **202** to 220 K, it was suggested that **203** is an intermediate in the phosphine *cis*/*trans* isomerisation. As **203/trans** is significantly lower in energy than the experimentally observed **203/cis"**, it is possible that **203/cis"** isomerises to form **203/trans** *via* loss of one oxygen ligand to form a 5-coordinate intermediate that can undergo a Berry pseudorotation.[218] Afterwards **203/trans** can then form the thermodynamic product **202/trans**.

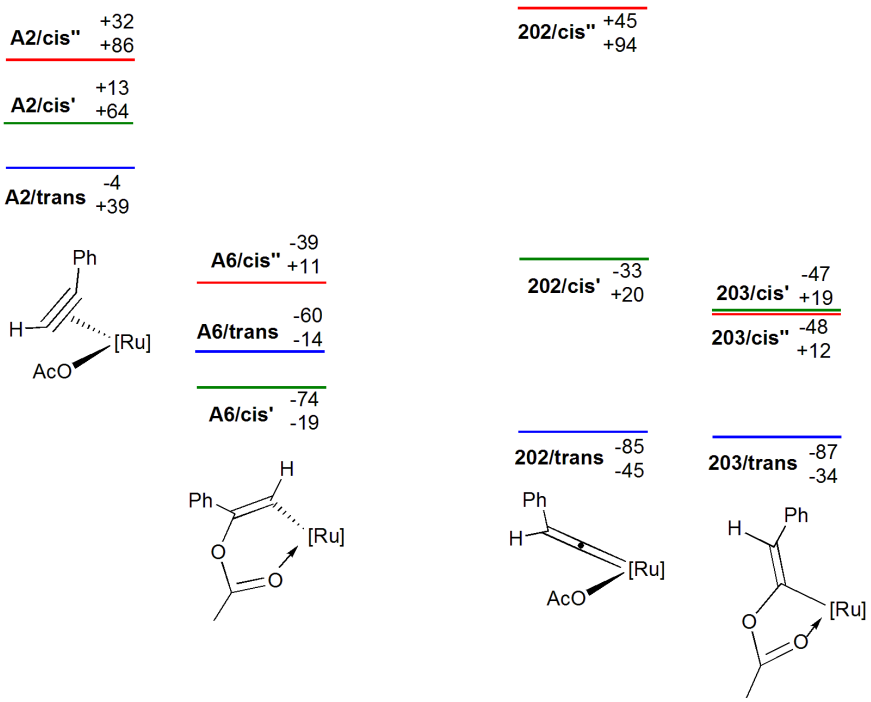

*Figure 2.29 – Energies of the various isomers of **203** and **A6**. For comparison the vinylidene and η^2 alkyne states (**202** and **A2**) are also displayed. Energies are ZPE corrected SCF (top) and Gibbs free (bottom) energies in kJ mol-1, relative to **201/cis**. The **trans**, **cis'** and **cis''** pathways are shown in blue, green and red respectively. [Ru] = [Ru(OAc)(PPh$_3$)$_2$].*

Interestingly the three isomers of **A6** were all lower in energy than **A2**, with a difference between **A6/trans** and **A2/trans** of 70 kJ mol^{-1}. Only one orientation of the alkyne could be found, with nucleophilic attack occurring at the substituted C_β. It is likely that attack at the C_α is prohibited due to either the competing LAPS mechanism, or steric strain in the resulting metallo-enol ester. An optimised geometry of **A6** is shown below in Figure 2.30, showing a C_β-O length of 1.4 Å.

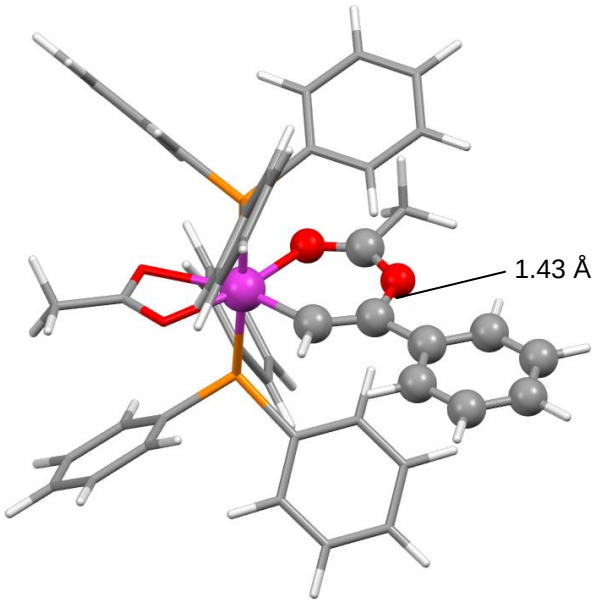

*Figure 2.30 – Optimised structure of **A6/trans**.*

As none of the isomers of **A6** were observed in the experimental studies it is unclear whether or not these complexes are relevant to the alkyne-vinylidene tautomerization reactions discussed above. It is possible that isomers of **A6** are formed as short lived resting states during the reaction and are not observable experimentally. Alternatively there may be a significant energetic barrier to the formation of **A6**, which prevents formation under the reaction conditions. However this structure will become relevant later in chapter 4 with the reaction of **302** with phenylacetylene.

2.2.5 Effects of a Smaller Model System

During the initial stages of investigation a model system was used with simplified substituents in order to reduce computational cost. Triphenylphosphine groups were replaced by phosphine, with methylacetylene being used in placed of phenylacetylene. Key states of this system can be seen below in Figure 2.31, with a PES being shown in Figure 2.32.

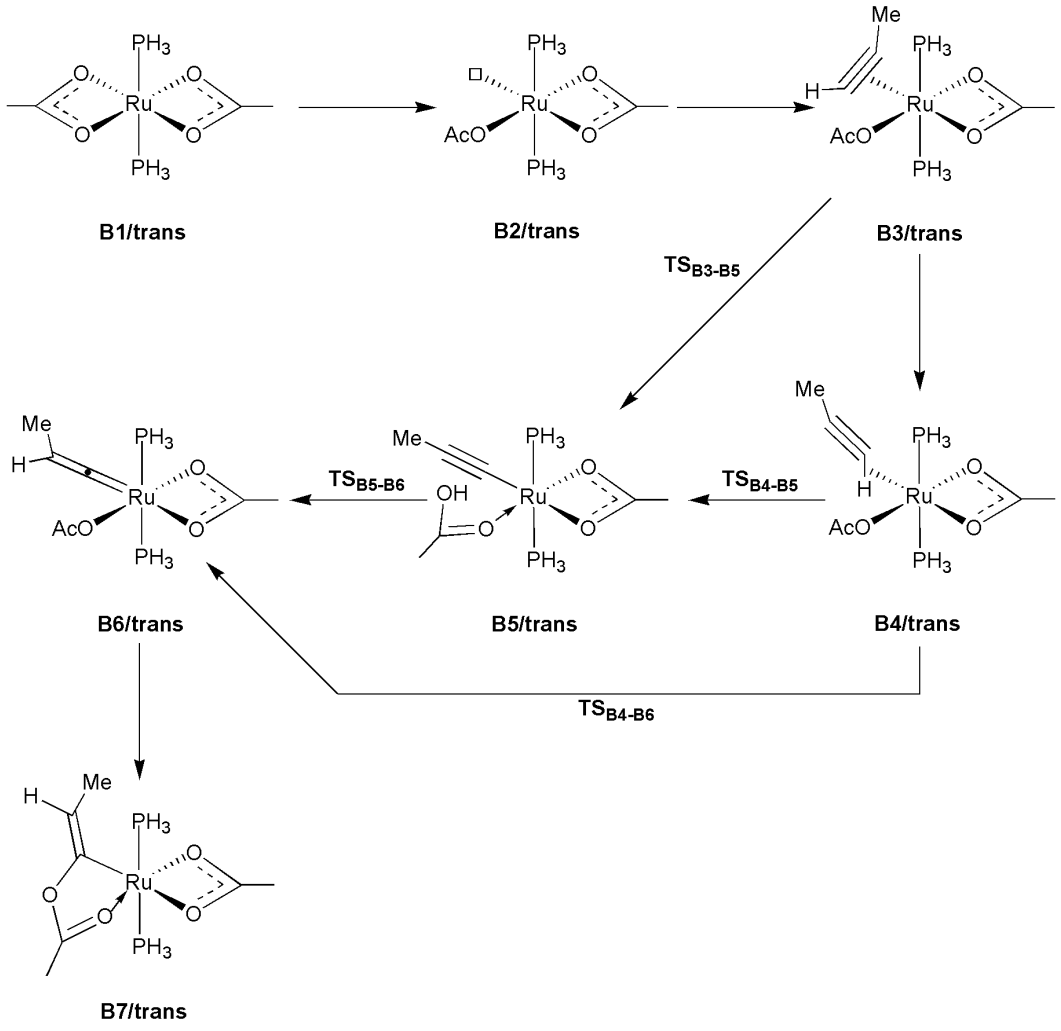

*Figure 2.31 – Key stationary points of the smaller system - **B**. For simplicity only the **trans** isomers are shown.*

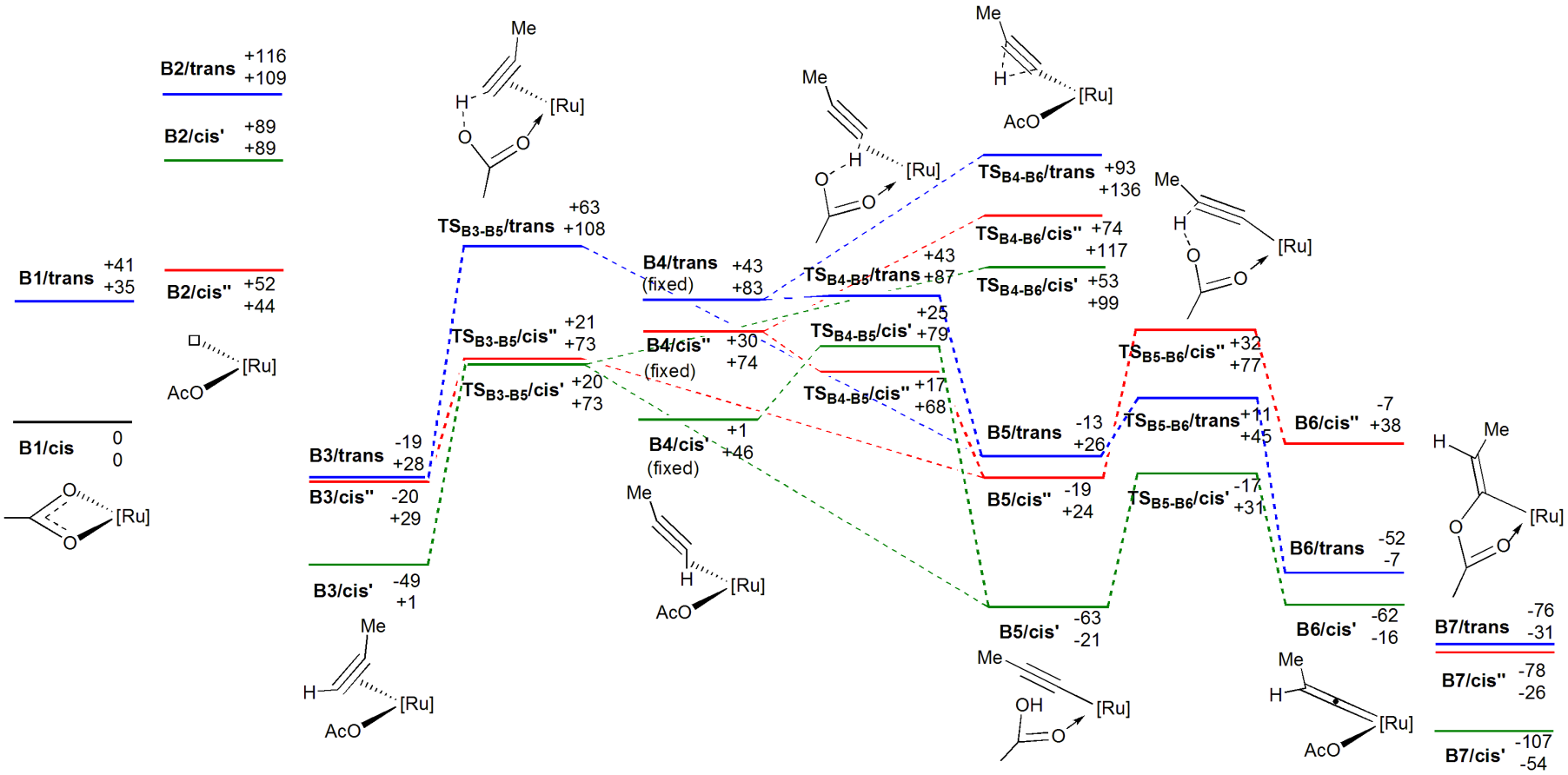

*Figure 2.32 – PES of system **B**. Energies are ZPE corrected SCF (top) and Gibbs free (bottom) energies in kJ mol^{-1}, relative to **B1/cis**.*

*The **trans**, **cis'** and **cis"** pathways are shown in blue, green and red respectively. [Ru] = [Ru(OAc)(PMe$_3$)$_2$].*

System **B** has several similarities to the larger System **A** discussed previously. Firstly **B1/cis** is the lowest energy isomer of **B1** by 41 kJ mol^{-1}, agreeing with experiment and System **A**. Secondly the LAPS mechanism is the lowest energy pathway to vinylidene formation, with the energetic span for the LAPS mechanism being 62 kJ mol^{-1} for the **trans** pathway (S-TDI = **B3**, S-TDTS = $\mathbf{TS_{B4\text{-}B5}}$), 69 kJ mol^{-1} for the **cis'** pathway (S-TDI = **B3**, S-TDTS = $\mathbf{TS_{B3\text{-}B5}}$) and 52 kJ mol^{-1} for the **cis''** pathway (S-TDI = **B3**, S-TDTS = $\mathbf{TS_{B5\text{-}B6}}$), compared with 112, 102 and 94 kJ mol^{-1} for the 1,2-hydrogen shift mechanism (S-TDI = **B3**, S-TDTS = $\mathbf{TS_{B3\text{-}B6}}$).

However the energetic span for the LAPS mechanism for System **A** is 24 38 and 63 kJ mol^{-1} for the **trans**, **cis'** and **cis''** isomers, showing a significant difference compared to the smaller model system. This difference is potentially due to the low energy of the η^2-alkyne **B3**, being ca. 40 kJ mol^{-1} lower in energy than in System **A**. An additional difference is that instead of being the lowest energy pathway, the **trans** manifold is now consistently the highest energy of all three isomers for a wide array of stationary points.

These differences are potentially explained by the sterically unencumbered phosphine ligands. For example in the optimised geometry of **B3/cis'/b/x** (Figure 2.33), the alkyne and acetate ligand are now perpendicular to one another with the acetate group interacting with the phosphorous atom (P-O distance = 2.45 Å). This differs with **A3/cis'/a/x**, where the bulkier triphenylphosphine positions the acetate and alkyne proton to interact with one another.

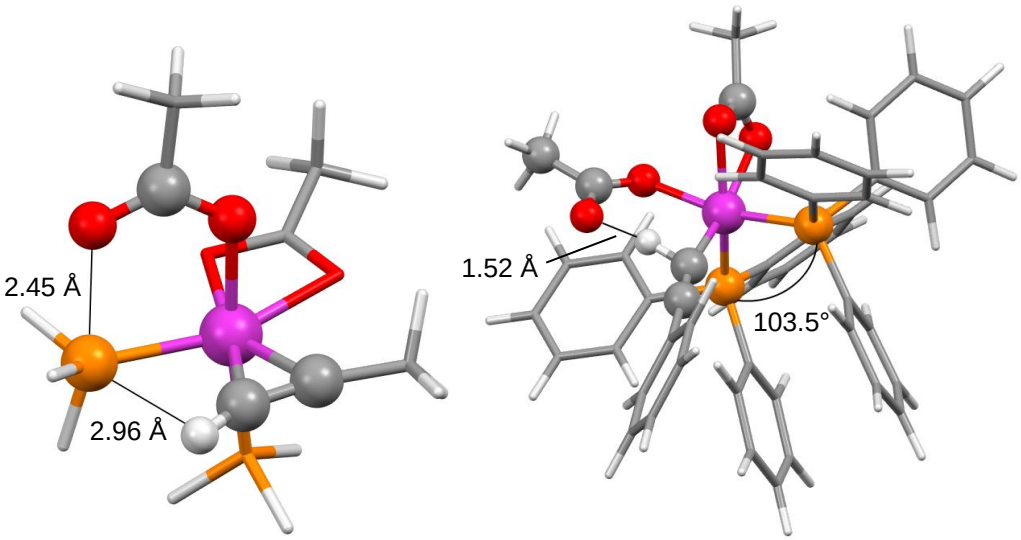

*Figure 2.33 – Optimised geometry of **B3/cis'/b/x** (left) and **A3/cis'/a/x** (right) for comparison.*

Another key difference is complex **B6** where the **cis'** isomer is 10 kJ mol^{-1} more stable than the **trans** isomer - contrary to experimental results. Additionally the metallo-enol ester **B7** is the overall thermodynamic minimum of the surface with the lowest energy isomer **B7/cis'** found at -107 kJ mol^{-1} relative to **B1/cis**, which is ca. 40 kJ mol^{-1} lower in energy than the vinylidene **B6**. The energy of the vinylidene complex as well as the acetate-phosphine interaction suggest that System **B** is not a proficient model of the experimental system. While certain key trends are maintained with the large and small model systems, the high energy of the **trans** phosphine isomers for many stationary points in System **B** is unlikely with the bulkier triphenylphosphine ligands used experimentally.

2.2.6 Investigation into Phosphine Cis/Trans Isomerisation During the LAPS Mechanism in Ruthenium Complexes of 1,2-bis(diphenylphosphino)butane

In order to determine the point of phosphine *cis*/*trans* isomerisation an experimental investigation was performed using bi-dentate phosphine ligands *bis*(diphenylphosphino)ethane (DPPE) and 1,2- *bis*(diphenylphosphino)butane (DPPB) to enforce the *cis*-phosphine orientation during the LAPS mechanism (see section 2.1.1). However the reaction did not proceed to completion, with an unidentified mixture of products detected.

To investigate the reasons for this and to possible identify the location of the *cis*/*trans* a PES was constructed for the LAPS mechanism with the DPPB ligand (System **C**). The entire PES and a key can be located in the appendix section A.1, with the most important points taken and presented below.

Firstly, the **cis'** phosphine isomer is consistently the lowest in energy, similar to system **A**. Secondly, several significant stationary points could not be located on the PES, most notably the alkyne deprotonation transition state. Geometry optimisation of these transition states repeatedly optimised to the acetylide/acetic acid complex **C4** rather than the TS, which suggests a shallow saddle point on the PES. Thirdly and most importantly, the vinylidene complex **C5** is not the global minimum on the PES, with the **cis'** and **cis''** isomers of **C6** being the thermodynamic product at -81 and -48 kJ mol^{-1} relative to the starting product **205**. Additionally stationary point **C4/cis'** is also lower in energy than the vinylidene **C5/cis'** by 36 kJ mol^{-1} (Figure 2.34).

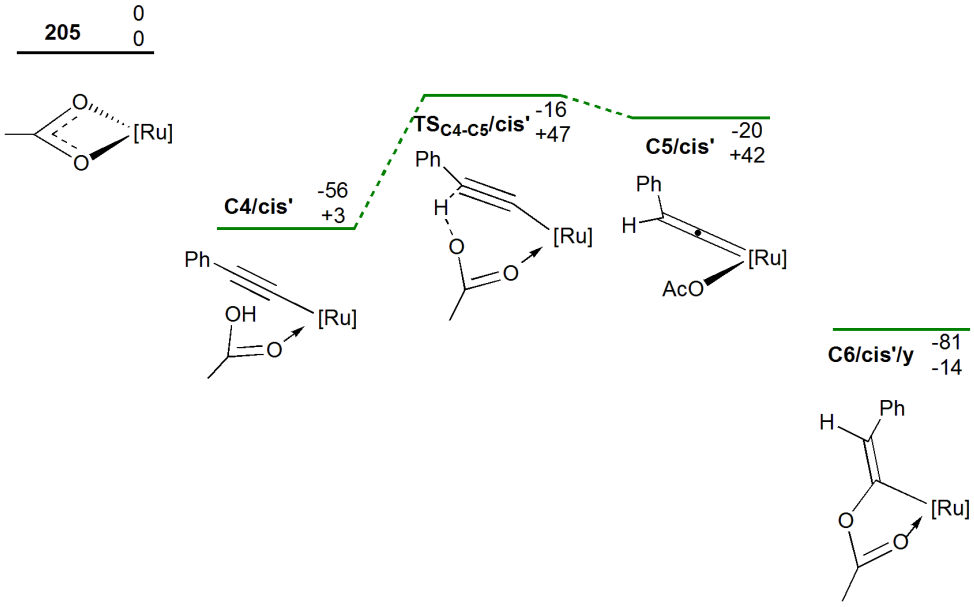

*Figure 2.34 – Selected PES for the **cis'** isomer of system **C**. Energies are ZPE corrected SCF (top) and Gibbs free (bottom) energies in kJ mol^{-1}, relative to **205**. The **cis'** pathway is shown in green. [Ru] = [Ru(OAc)(DPPB)].*

These results hint at a thermodynamic reason as to why the vinylidene **C5** is not observed experimentally, however the global minimum – the metallo-enol ester **C6** – is also not observed. System **A** has an analogous case with the **cis'** phosphine isomer, where the vinylidene **202/cis'** is 20 kJ mol^{-1} higher in energy than the acetylide/acetic acid complex **A5/cis'** (Figure 2.22), suggesting that the *trans*-phosphine isomer is necessary for final formation of the vinylidene product.

2.2.7 Assessment of the Location of cis/trans Phosphine Isomerisation during the LAPS Mechanism

In analysis of systems **A** to **C**, the point of *cis*/*trans* phosphine isomerisation involving mono-dentate phosphine ligands that occurs during the alkyne-vinylidene tautomerization mechanism could not be definitively located. However several observations were made during the study.

During low-temperature NMR experiments seen in section 2.1.1 complex **203/cis"** was identified at 220 K, which then isomerised to **202/trans** upon warming to 255 K. Re-cooling complex **202** did not result in formation of **203**, suggesting that state **203** is an intermediate in the process of formation of **202/trans** (Figure 2.35).

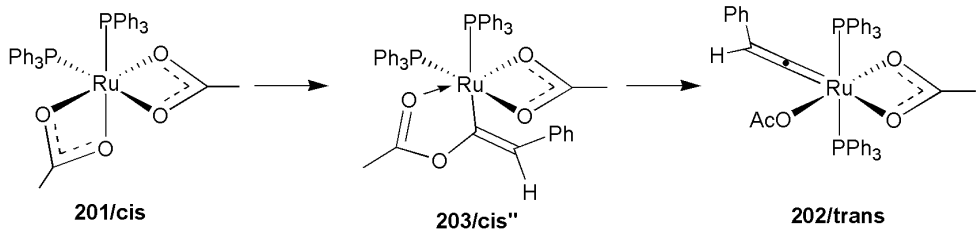

*Figure 2.35 – Simplified scheme showing experimental observation of **203/cis"** leading to **202/trans**.*

However theoretical studies in section 2.2.3 show that **203/cis"** is the highest energy isomer of **203**, being 40 kJ mol^{-1} higher than **203/trans**. This could indicate that **203/cis"** is a kinetic product and that there is (at 220 K) a significant barrier to the isomerisation of **203/cis"** to **203/trans** which is overcome upon warming to 255 K.

Additionally in system **A**, the LAPS mechanism is noticeably lower in energy for the **trans** pathway than both the **cis'** and **cis"** pathways, despite complex **201/cis** being lower in energy than **201/trans**. **A1/trans** possesses a free coordination site and is the highest in energy of the three possible phosphine isomers of this complex, whereas **A2/trans** is the lowest energy isomer, showing a switch in the ordering of the relative energies upon coordination of an η^2-alkyne.

The lack of steric clash between the two triphenylphosphine groups for the **trans** manifold upon coordination of an alkyne ligand could be the driving force behind the *cis*/*trans* phosphine isomerisation. This is further corroborated by system **B**, where the LAPS mechanism for the **trans** pathway is highest in energy of all three isomers, with the smaller phosphine ligands of the *cis*-isomers interacting far less than their triphenylphosphine counterparts in system **A**.

This could suggest that a Berry pseudorotation[218] of the five coordinate complex **A1** or a later state (due to the hemi-labile nature of the acetate groups giving easy access to 5-coordinate complexes) is occurring to form the *trans* isomer. However due to the low-temperature observation of the *cis*-phosphine complex **203**, phosphine rearrangement may not occur prior to the formation of the vinylidene complex.

In conclusion the location of the *cis*/*trans* phosphine isomerisation remains ambiguous at the end of this study. While plausible mechanisms exist for the isomerisation, a single point cannot be verified above all others – with isomerisation potentially occurring at multiple points on the PES.

2.2.8 Summary

This chapter has provided theoretical insight into the mechanism of vinylidene formation that occurs in the reaction of ruthenium *bis*-acetate complexes with terminal alkynes, and shows that a new type of alkyne-vinylidene tautomerization - the acetate-assisted LAPS mechanism - operates here. The LAPS mechanism is a lower energy pathway than classical tautomerization mechanisms for the studied Ru-acetate complexes, which may explain the significantly faster reaction between $Ru(OAc)_2(PPh_3)_2$ and phenylacetylene compared to an analogous reaction with $RuCl_2(PPh_3)_3$.

The LAPS mechanism (depicted below in Figure 2.36) begins with the deprotonation of the terminal alkyne group, forming an acetylide and coordinated acetic acid molecule analogous to the AMLA and CMD mechanisms. This acetic acid ligand then acts as an intramolecular acid to protonate the C_β of the acetylide to form the vinylidene. The acetate ligand effectively acts as a proton-shuttling ligand, which facilitates the movement of protons from one part of an organic substrate to another. It is believed that this type of mechanism may operate in other organometallic transformations, and that it may be possible to exploit this in further stoichiometric or catalytic transition-metal-mediated organic reactions. Finally, the results presented in this chapter can be viewed in a recently published article.[214]

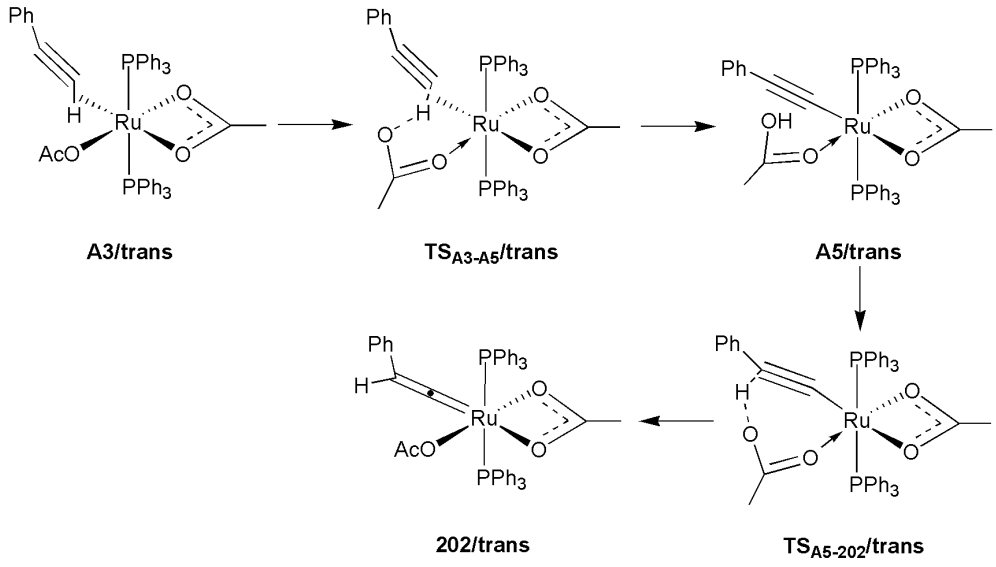

Figure 2.36 – The LAPS mechanism.

3. Further Reactions of Hydroxy-Vinylidenes – Alkene Formation from Propargyl Alcohols

3.1 Introduction

With the LAPS mechanism understood, it was proposed that this acetate-assisted method could engage in further activity beyond the alkyne-vinylidene tautomerization. Focus was placed on the further reactivity of the formed vinylidenes – specifically hydroxy-vinylidenes. In the reaction of **201** and a propargyl alcohol, the hydroxy-vinylidene complex **301** is formed which will be the basis of this chapter (Figure 3.1)

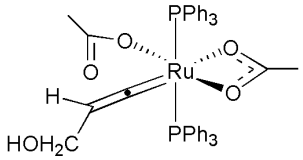

*Figure 3.1 – **301**.*

Hydroxy-vinylidenes are commonly known to form allenylidenes, and it was initially assumed that **301** would react in a similar way. However what was instead shown was the formation of **302** (Figure 3.2) and ethene.

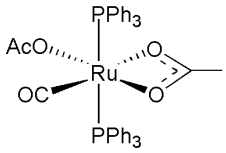

*Figure 3.2 – **302**.*

This chapter shall focus on the theoretical investigation into the unusual formation of **302** and ethene from **301**, specifically in the identification of a plausible reaction mechanism for the system.

3.1.1 Experimental Observations

The initial basis for this chapter relies on experimental work carried out by Dr Christine Welby, which can be found within her published thesis.[215] Propargyl alcohol was added to the *bis*-acetate ruthenium complex **201** which reacts to form hydroxy-vinylidene complex **301**. As before alkyne-vinylidene tautomerization (assumed to be *via* the LAPS mechanism) occurred near instantaneously at 298 K, with no intermediates being observed (Figure 3.3).

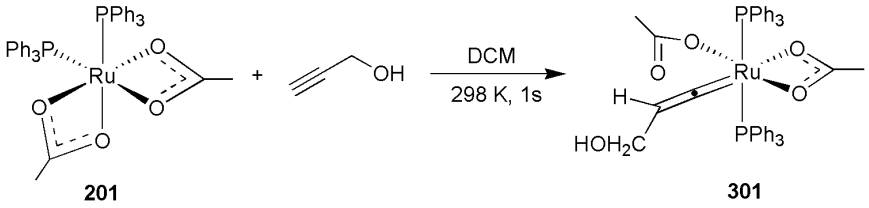

*Figure 3.3 – Formation of **301**.*

As discussed previously in section 1.4.4, dehydration of hydroxy-vinylidenes can occur to form allenylidene complexes with an example reproduced in Figure 3.4. However the loss of water and formation of an allenylidene from **301** was not initially observed experimentally. Attempts were made to encourage dehydration (such as the addition of acid) however this also did not promote allenylidene formation.

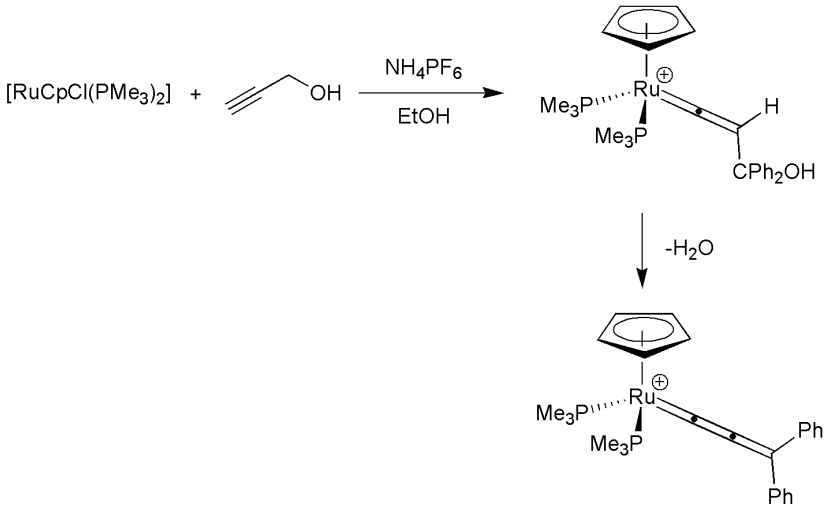

Figure 3.4 – Formation of an allenylidene reported by Selegue.[207]

Instead, NMR measurements performed on the reaction mixture after 48 hours at room temperature indicated the presence of peaks associated with a metal-carbonyl group, as well as peaks characteristic of a free alkene. This metal carbonyl complex was identified as **302** and the alkene as free ethene (Figure 3.5).

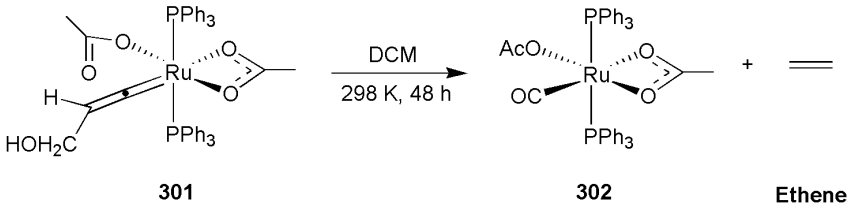

*Figure 3.5 – Formation of **302** and free ethene.*

Parallel studies of the reaction between **201** and (Prop-2-ynyloxy)benzene in dichloromethane solution produced the phenyl-ether substituted vinylidene complex **303** (Figure 3.6).

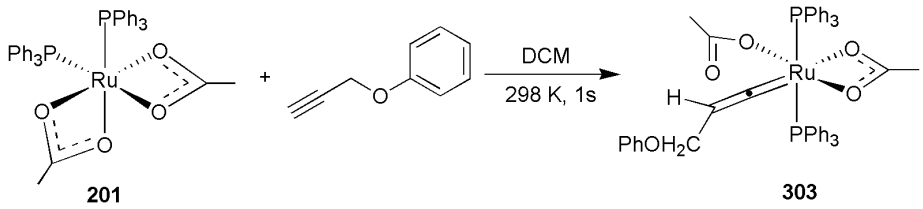

*Figure 3.6 – Formation of **303**.*

Further monitoring of this complex over a period of 16 hours by NMR showed the growth of peaks associated with the formation of complex **304** as well as free phenyl acetate (Figure 3.7). Crystals of **304** were grown successfully and a single crystal X-ray structure was obtained showing carbonyl and vinyl ligands, as well as a single κ^2-acetate. A depiction of the structure is shown in Figure 3.8, with a table of selected bond lengths and angles in Table 3.1.

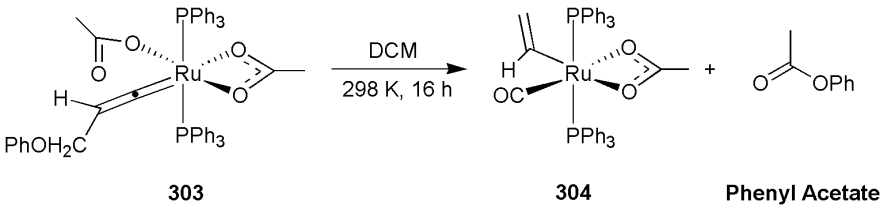

*Figure 3.7 – Further reaction of **303** to **304**.*

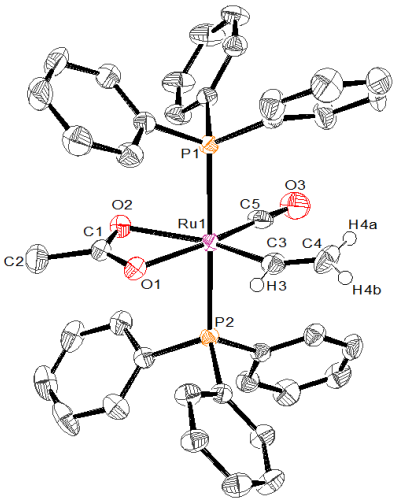

*Figure 3.8 – ORTEP diagram of **304**, thermal ellipsoids (where shown) are at the 50 % probability level. Hydrogen atoms, except for H(3), H(4a) and H(4b), are omitted for clarity.*[215]

*Table 3.1 – Selected bond lengths and angles for **304***[215]

Bond	Bond Length (Å)	Angle	Bond Angle (°)
Ru – P(1)	2.367 (1)	P(1) – Ru – P(2)	179.03(4)
Ru – P(2)	2.381(1)	P(1) – Ru – O(1)	94.56(7)
Ru – O(1)	2.190(3)	P(1) – Ru – O(2)	85.61(7)
Ru – O(2)	2.265(3)	O(1) – Ru – O(2)	58.67(1)
Ru – C(3)	1.987(4)	P(1) – Ru – C(3)	92.64(1)
C(3) – C(4)	1.227(5)	P(2) – Ru – C(3)	88.22(1)
Ru – C(5)	1.841(4)	O(1) – Ru – C(3)	98.46(1)
C(5) – O(3)	1.158(5)	O(2) – Ru – C(3)	156.74(1)
		Ru – C(3) – C(4)	144.5(4)
		C(3) – Ru – C(5)	91.92(2)
		P(1) – Ru – C(5)	86.29(1)
		P(2) – Ru – C(5)	94.14(1)
		O(1) – Ru – C(5)	169.53(1)
		O(2) – Ru – C(5)	111.08(2)
		Ru – C(5) – O(3)	172.5(4)

Due to the presence of a vinyl and carbonyl ligand, it was postulated that **304** may be an intermediate in the formation of ethene. In the reaction of the hydroxy-vinylidene **301** acetic acid is not observed, which may suggest that it protonates the M-C bond of the vinyl ligand to form ethene and **302** at a very rapid rate. This protonation is not possible in the case of the formation of phenylacetate, which does not react further and is observable in the reaction mixture.

In order to verify this, **304** was isolated in a sealed vessel containing a solution of dichloromethane at 298 K, to which acetic acid was then added with the mixture being monitored by NMR spectroscopy. Peaks characteristic for ethene as well as for complex **302** increased in intensity over the course of several hours, confirming that **304** is an intermediate in the formation of ethene (Figure 3.9).

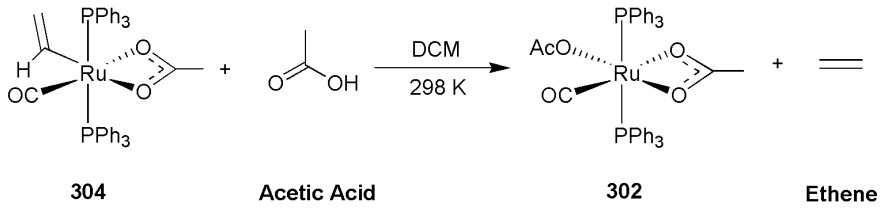

*Figure 3.9 – Addition of acetic acid to **304**.*

The further reaction of hydroxy-vinylidene complex **303** (Figure 3.7) provides a startling revelation. Here, phenyl acetate was produced instead of acetic acid, suggesting that either the oxygen of the carbonyl group of **302** originated from the acetate ligand with the phenyl-ether group transferring to the acetate from the vinylidene, or that the phenyl group itself was migrating to the acetate.

Labelling studies were performed with the use of the ^{18}O labelled **201** to establish the exact origin of the oxygen atom in **302** and **304**. Should the carbonyl group possess a labelled oxygen atom then the oxygen must have originated from the acetate group through an undetermined mechanism. The ^{18}O-labelled structures could be determined by two different methods - either by detecting the total mass of the molecule with mass spectrometry, or by the specific bond stretches associated with a heavier oxygen atom through the use of infra-red spectroscopy.

Complex **201** was labelled with ^{18}O by reacting $[RuCl_2(PPh_3)_3]$ with ^{18}O labelled acetic acid and successful isotopic labelling was confirmed *via* LIFDI-MS with a m/z value of 752.1 (Figure 3.10).

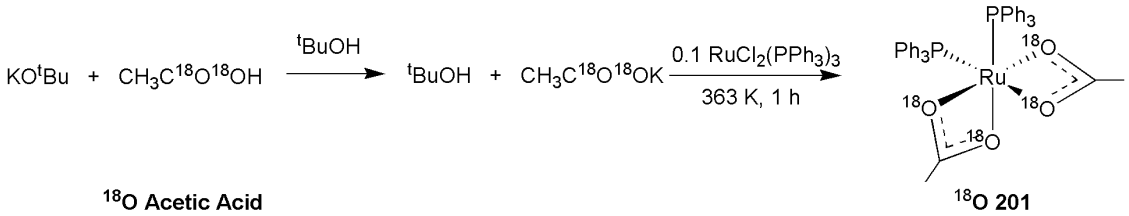

*Figure 3.10 – Formation of ^{18}O labelled **201**.*

^{18}O-labelled **201** was reacted with both propargyl alcohol and (Prop-2-ynyloxy)benzene in two separate reactions. With the reaction of (Prop-2-ynyloxy)benzene, the reaction once again produced complex **304** (Figure 3.11).

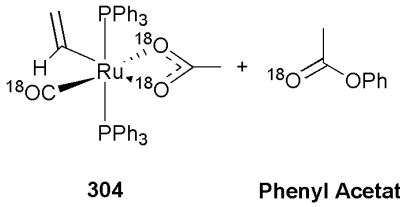

*Figure 3.11 – Labelled **304** ^{18}O locations.*

The location of the ^{18}O labelling was verified with IR spectroscopy. In Figure 3.12 an overlay of the spectrum for labelled (right) and non-labelled (left) **304** shows the C-O stretch for both complexes. In the spectrum the C-O stretch for the labelled complex has shifted by -40.9 cm^{-1} - seemingly consistent with a stretch associated for a heavier oxygen atom.

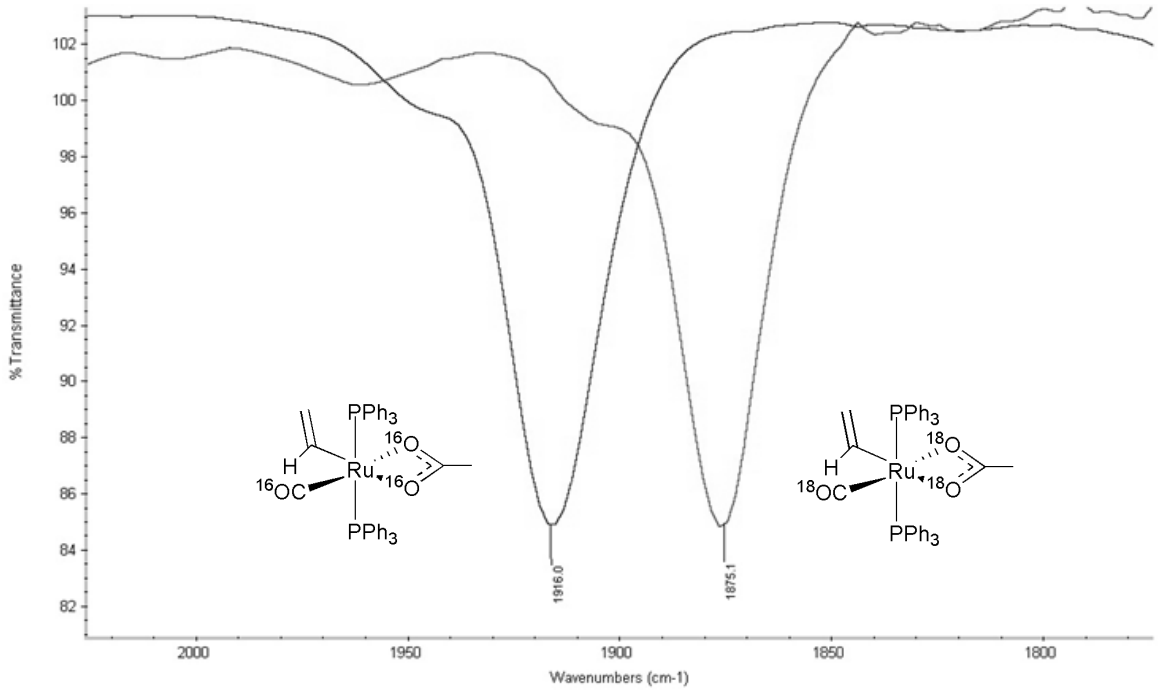

Figure 3.12 - Infrared spectrum of the C-O stretch of non-labelled (1916 cm^{-1}) and ^{18}O labelled (1875.1 cm^{-1}) ***304****.*[215]

Predicted C-O infra-red stretches for the ^{18}O labelled complex were calculated from the values obtained from the non-labelled spectrum with the use of the equations shown below (Equation 3.1-3.4).[222] The ^{16}O experimental and ^{18}O predicted and experimental IR frequencies are displayed below in Table 3.2.

$$\mu_{C^{(i)}O} = \frac{m_1 m_2}{m_1 + m_2} \qquad \textit{Equation 3.1}$$

$$\upsilon_{C^{(i)}O} = \frac{1}{2\pi c}\sqrt{\frac{k}{\mu_{C^{(i)}O}}} \qquad \textit{Equation 3.2}$$

$$\frac{\upsilon_{C^{16}O}}{\upsilon_{C^{18}O}} = \sqrt{\frac{\mu_{C^{18}O}}{\mu_{C^{16}O}}} = \sqrt{\frac{7.20}{6.86}} = 1.0247 \qquad \textit{Equation 3.3}$$

$$\upsilon_{C^{18}O} = \frac{\upsilon_{C^{16}O}}{1.0247} \qquad \textit{Equation 3.4}$$

The predicted values are very close to the experimental IR stretches seen for ^{18}O labelled **304**, with other unrelated stretches such as the C=C stretch remaining relatively unchanged between the ^{16}O and ^{18}O IR spectrum at 1596 and 1594 cm^{-1} respectively.

*Table 3.2 – IR stretches specific to isotope labelling locations of **304**[215]*

IR Stretch	Non Labelled / cm^{-1}	^{18}O Labelled (Predicted) / cm^{-1}	^{18}O Labelled (Experiment) / cm^{-1}
CO	1916	1869	1875
κ^2-OCO_{asym}	1531	1503	1493
CO (ester)	1763	1720	1722

Analysis by LIFDI-MS also indicated a peak at 746.1 m/z, which is calculated as the mass of **304** with three ^{18}O atoms present in the structure. A GC-EI-MS also provided evidence of phenyl acetate containing a single ^{18}O atom.

The reaction of ^{18}O labelled **201** with propargyl alcohol was predicted to give labelled **302** (Figure 3.13). Analysis of the reaction mixture with IR spectroscopy and LIFDI-MS indeed showed the presence of both ^{18}O labelled **302** and **304**, as well as unlabelled **302**. The presence of unlabelled **302** was believed to be a result of exchange between half-labelled acetic acid produced from an already completed reaction, and unreacted **201**.

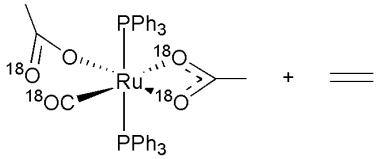

302 **Ethene**

*Figure 3.13 – ^{18}O labelled **302** and ethene. The position of the ^{18}O label within the κ^1-acetate could not fully be determined, and is tentatively presented here.*

These results indicate that the formation of ethene and the carbonyl complex **302** does not occur *via* the allenylidene mechanism postulated by Dixneuf and Bustelo (section 1.4.4, Figure 3.14),[208] where carbonyl and ethene formation proceeded through an allenylidene intermediate.

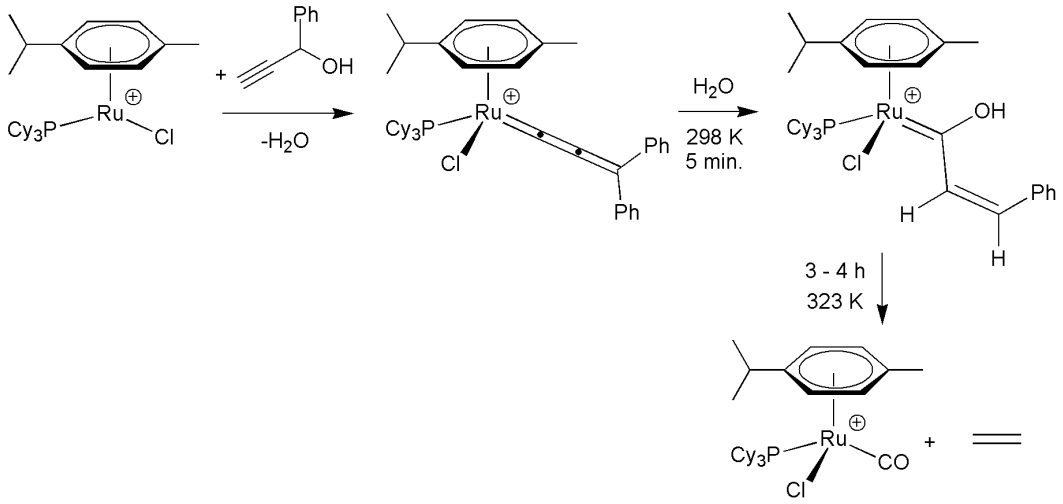

Figure 3.14 – Reaction of HC≡CCHPhOH with complex [(p-cymeme)RuCl(PCy$_3$)][B(Ar$_F$)$_4$].

Instead, results indicate that the acetate ligand is involved in the reaction, with the acetate oxygen atom being transferred to the hydroxy-vinylidene C_α to form the carbonyl ligand. The acetate is then reformed with the lost oxygen atom being replaced by a hydroxy group to form acetic acid. The acetic acid then protonates the vinyl group to form **302** and ethene.

3.2 Results and Discussion

3.2.1 Computational Preamble

It was shown in experimental studies that the formation of **302** and ethene from **301** did not proceed through an allenylidene based mechanism. Here, an acetate oxygen atom transfers from the acetate group to the hydroxy-vinylidene while being replaced by the hydroxy group through an unknown mechanism. Additionally this mechanism may involve the carbonyl vinyl complex **304** as an intermediate in the reaction (Figure 3.15).

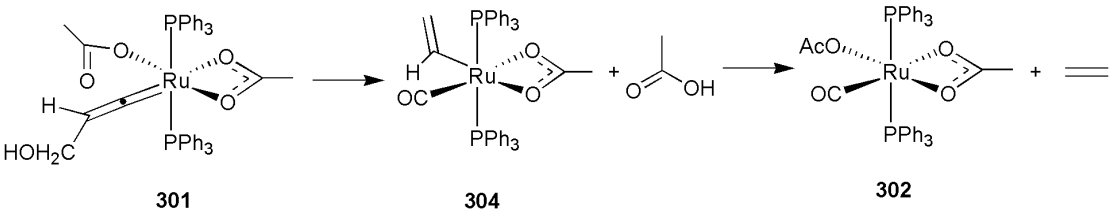

*Figure 3.15 – Reaction of **301** to **302**.*

As the mechanism is unknown, an investigation into the processes forming the organic and organometallic products in the reaction described above was conducted and is reported here. Potential energy surfaces for a variety of mechanistic possibilities were investigated with the use of DFT methods. The general methodology used for these studies is outlined in section 7.1 and DRC analyses were performed on all transition states as per section 7.2. Due to the intramolecular nature of the mechanism and initial lack of charged intermediates and fragments, solvation corrections were initially not applied to the gas-phase energies during this study. However due to the presence of charged fragments and high barriers, some data presented below includes solvation corrections with DCM (using the COSMO method outlined in section 7.3). All energies reported in the text are ZPE corrected SCF energies unless otherwise stated.

3.2.2 Initial Mechanistic Search via an Intramolecular Transition State

In the experimental investigation of **301** to form **302** and ethene, the work undertaken with ^{18}O labelling studies indicated that the acetate C-O bond breaks in order to form **302**. The acetate oxygen atom is also believed to be replaced by the vinylidene hydroxy group. An initial mechanism (Figure 3.16) involves concerted intramolecular hydroxy attack from the vinylidene to the central acetate C while the initial acetate C-O bond breaks.

This mechanism requires the initial formation of the metallo-enol ester **D1**, to allow for hydroxy nucleophilic attack *via* $\mathbf{TS_{D1\text{-}D2}}$, and for the oxygen atom of the acetate ligand to be lost to the vinylidene group in a possible transesterification mechanism. **D2** was also calculated as an intermediate in the mechanism, with a coordinated acetic acid ligand and ketone group.

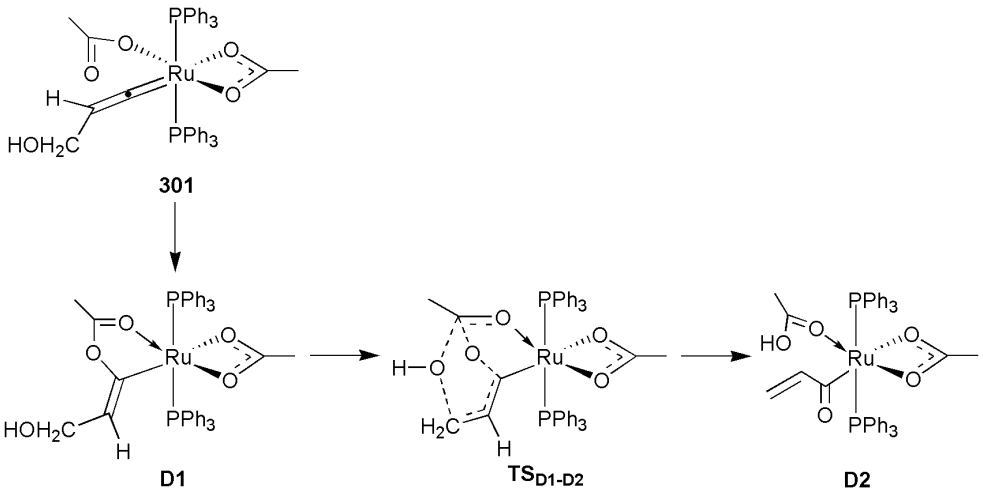

*Figure 3.16 – Mechanistic path from **301** to **304**.*

From **D2**, the loss of acetic acid can form **D3**, which then undergoes migratory de-insertion to form **304**, with protonation of the vinyl M-C bond by acetic acid forming **302** (Figure 3.17). A PES for this mechanism can be seen in Figure 3.18.

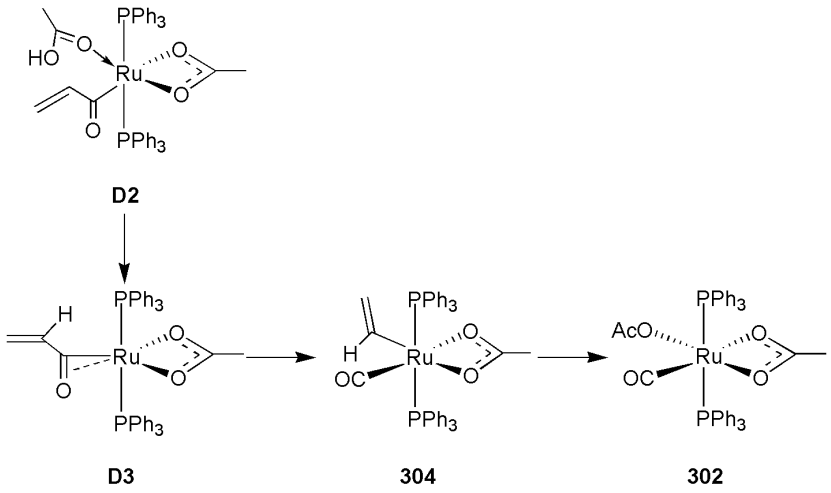

*Figure 3.17 - Formation of **304** from **D2**.*

As can be seen in the PES, the minima of **301** through to **D3** shows a 43 kJ mol^{-1} rise in energy. From **D3**, a large exergonic change is seen with the formation of **304** and **302**, at -102 and -140 kJ mol^{-1} relative to **301**.

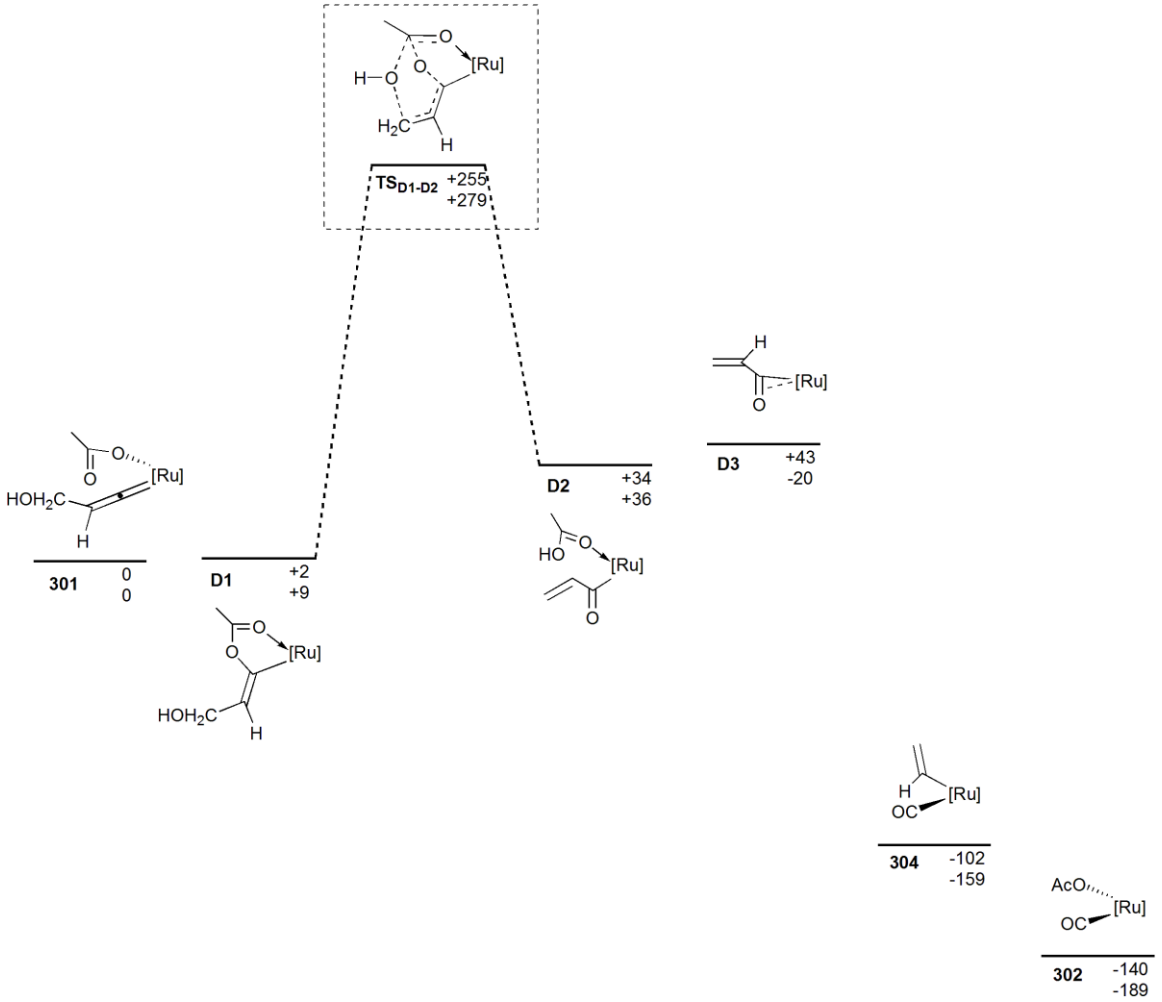

*Figure 3.18 – PES showing the mechanism from **301** to **302**. Energies are ZPE corrected SCF (top) and Gibbs free (bottom) energies in kJ mol^{-1}, relative to **301**. [Ru] = [Ru(OAc)(PPh$_3$)$_2$].*

The geometry of **D3** is also of interest, and is shown in Figure 3.19. Here, a carbon-metal bond exists, with a bond distance of 1.89 Å. However there is also an interaction between the metal and oxygen atoms, with a bond distance of 2.38 Å. This is not without precedent, as ruthenium-cluster complexes which possess an η^2-carbonyl group are known to exist.[223, 224]

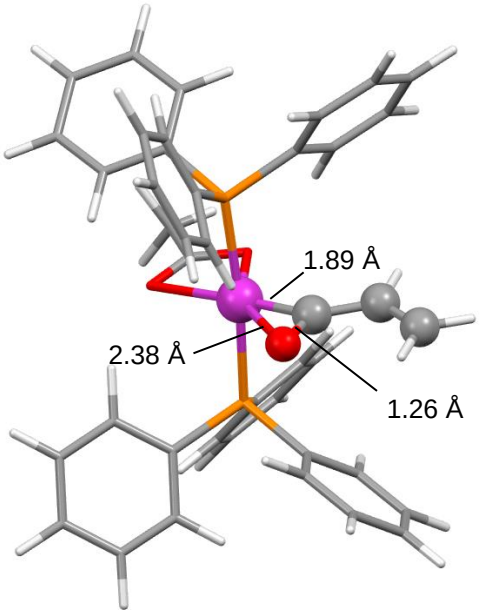

*Figure 3.19 – Optimised geometry of **D3**.*

The low energies of the minima on this PES initially appears to support the mechanism of the acetate-splitting mediated through an intramolecular hydroxide attack; however the transition state $\mathbf{TS_{D1\text{-}D2}}$ presents a significant barrier of +255 kJ mol^{-1} relative to **201**, which is not compatible with the reaction conditions observed experimentally.

The transition state $\mathbf{TS_{D1\text{-}D2}}$ has an imaginary frequency of -447.44 cm^{-1} with stationary points either side of the transition state confirmed by DRC analysis. In the optimised TS structure shown in Figure 3.20, the acetate group possesses a near-tetrahedral geometry, with the bond to O(a) being ca. 0.1 Å longer than the other C-O bond to O(b). Additionally O(c) is significantly far away from both the hydroxy-vinylidene carbon and the acetate group for a transition state, at 1.97 and 1.72 Å respectively. This distance may be the cause of the elevated energy barrier, with the negative charge of the hydroxy group no longer stabilised by the rest of the organometallic complex. Alternatively the high barrier may be caused by the strained geometry found in the transition state.

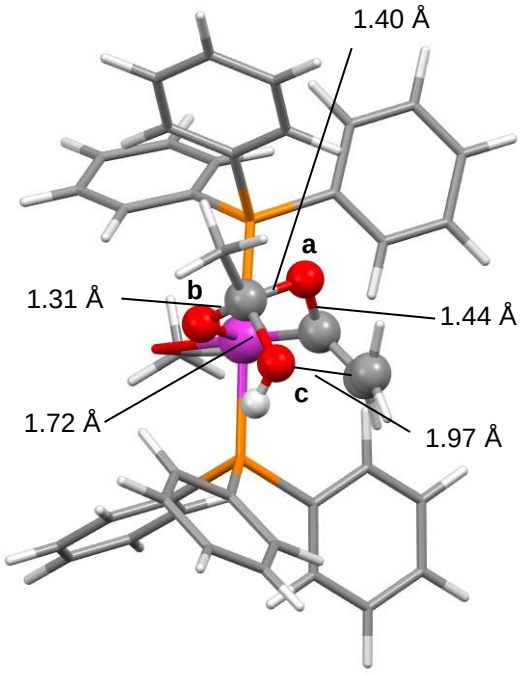

Figure 3.20 – Optimised geometry of ***TS$_{D1-D2}$*** *showing concerted transition state.*

Several functional and basis set combinations were used in conjunction with **D1** and **TS$_{D1-D2}$** including optimisation at the (RI-)PBE0/def2-TZVPP, (RI-)PBE0/def2-QZVPP levels, as well as with B3LYP in order to identify if the high barrier was caused by the functional and basis set combination. However the energy barrier remained high at ca. 250 kJ mol^{-1} relative to **201**. Additionally solvation calculations were performed with DCM at the PBE0/def2-TZVPP level and showed only a ca. 15 kJ mol^{-1} drop in energy.

In order to look for alternative reaction mechanisms that avoid the high energy TS seen with **TS$_{D1-D2}$**, further calculations were performed on similar geometries to **D1** and **TS$_{D1-D2}$**, - **D4** and **TS$_{D4-D3}$** (Figure 3.21) in order to observe the effects of a less constrained geometry on the energy of the TS. This mechanism acts in a similar way to **TS$_{D1-D2}$**, but the acetate group is no longer coordinated to the metal centre. As a result the acetate group should be closer to the attacking vinylidene hydroxy group, potentially lowering the energy of the mechanism.

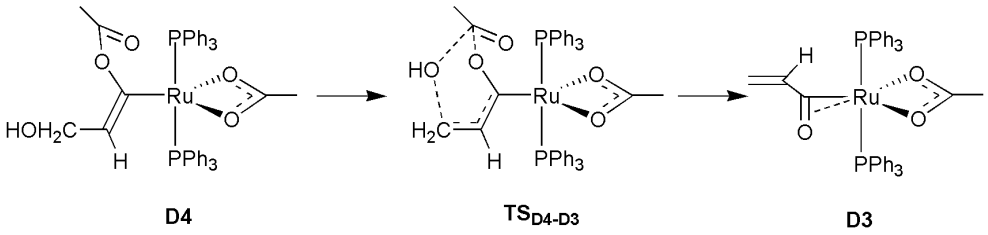

*Figure 3.21 – Mechanistic path from **D4** to **D3**.*

As can be seen in the PES in Figure 3.22, while intermediate **D4** is (at +117 kJ mol^{-1}) potentially too high in energy for the experimental reaction conditions (298 K, 48 h), $\mathbf{TS_{D4\text{-}D3}}$ is confirmed as being inaccessible for the observed reaction conditions at +268 kJ mol^{-1} relative to **201**.

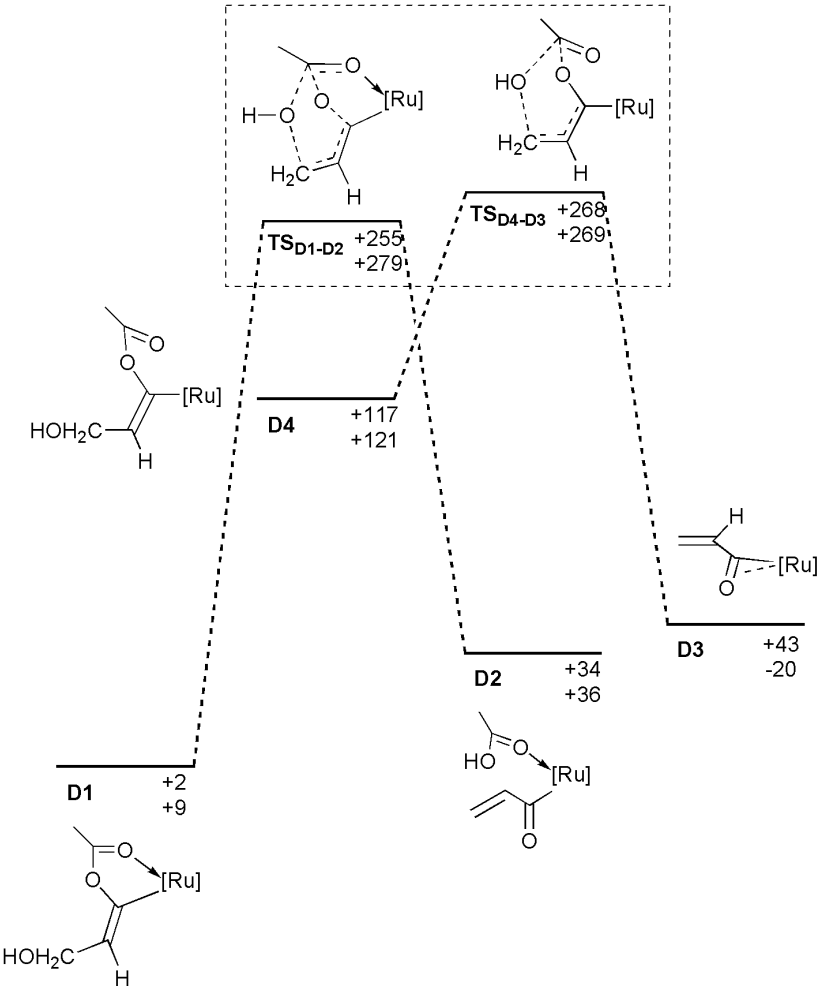

*Figure 3.22 – PES showing the mechanism from **D4** to **D3**, with **D1** and $\mathbf{TS_{D1\text{-}D2}}$ as a comparison. Energies are ZPE corrected SCF (top) and Gibbs free (bottom) energies in kJ mol^{-1}, relative to **301**. [Ru] = [Ru(OAc)(PPh$_3$)$_2$].*

TS_{D4-D3} has an imaginary frequency of -451.25 cm^{-1}, and the geometry (Figure 3.23) has a shorter length from O(c) to the hydroxy-vinylidene and acetate groups, at ca. 1.7 Å each, compared with a 1.97 and 1.72 Å for **TS_{D1-D2}**. The distance between O(a) and the acetate carbon is shown to be 1.96 Å, which is considerably lengthened when compared with 1.40 Å for **TS_{D1-D2}**. This seems to suggest a far more sterically strained transition state than with the geometry of **TS_{D1-D2}**. Additionally a DRC analysis on the transition state showed a progression to complex **D1** instead of **D4**, showing that **D4** is a temporary intermediate on the PES from **D1**.

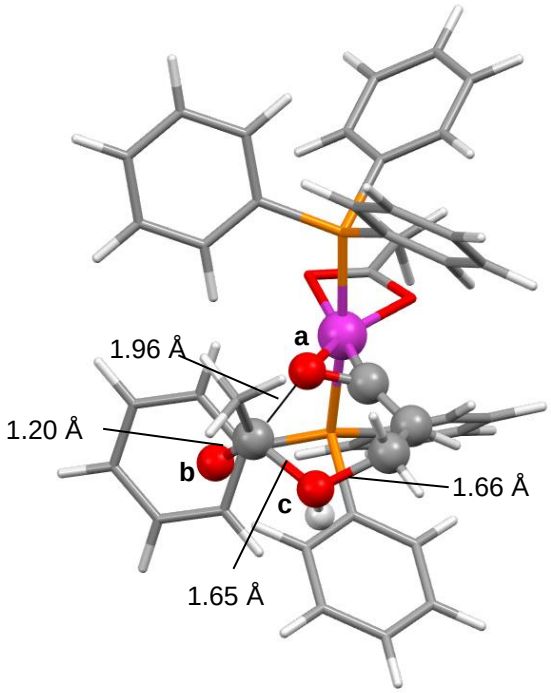

*Figure 3.23 – Optimised geometry of **TS_{D4-D3}**.*

Different triphenylphosphine orientations were also considered as a variable in the search for a transition state with a viable energy, due to the *cis*/*trans* phosphine isomerisation seen in the initial LAPS mechanism in chapter 2. **D1**, **D4**, $\mathbf{TS_{D1\text{-}D2}}$ and $\mathbf{TS_{D4\text{-}D3}}$ were therefore optimised with **cis'** and **cis''** geometries (Figure 3.24).

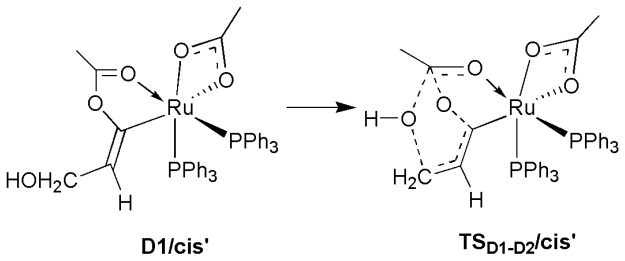

D1/cis' **$TS_{D1\text{-}D2}$/cis'**

Figure 3.24 – ***Cis'*** *isomers of* ***D1*** *and* $\boldsymbol{TS_{D1\text{-}D2}}$.

In the PES shown in Figure 3.25, the energy difference for the concerted mechanism is lowered to +195 kJ mol^{-1} for $\mathbf{TS_{D1\text{-}D2}}$**/cis'** compared with +257 kJ mol^{-1} for $\mathbf{TS_{D1\text{-}D2}}$. This is a significant drop, but still not enough to be feasible at the reaction temperatures and times seen experimentally (298 K, 48 h).

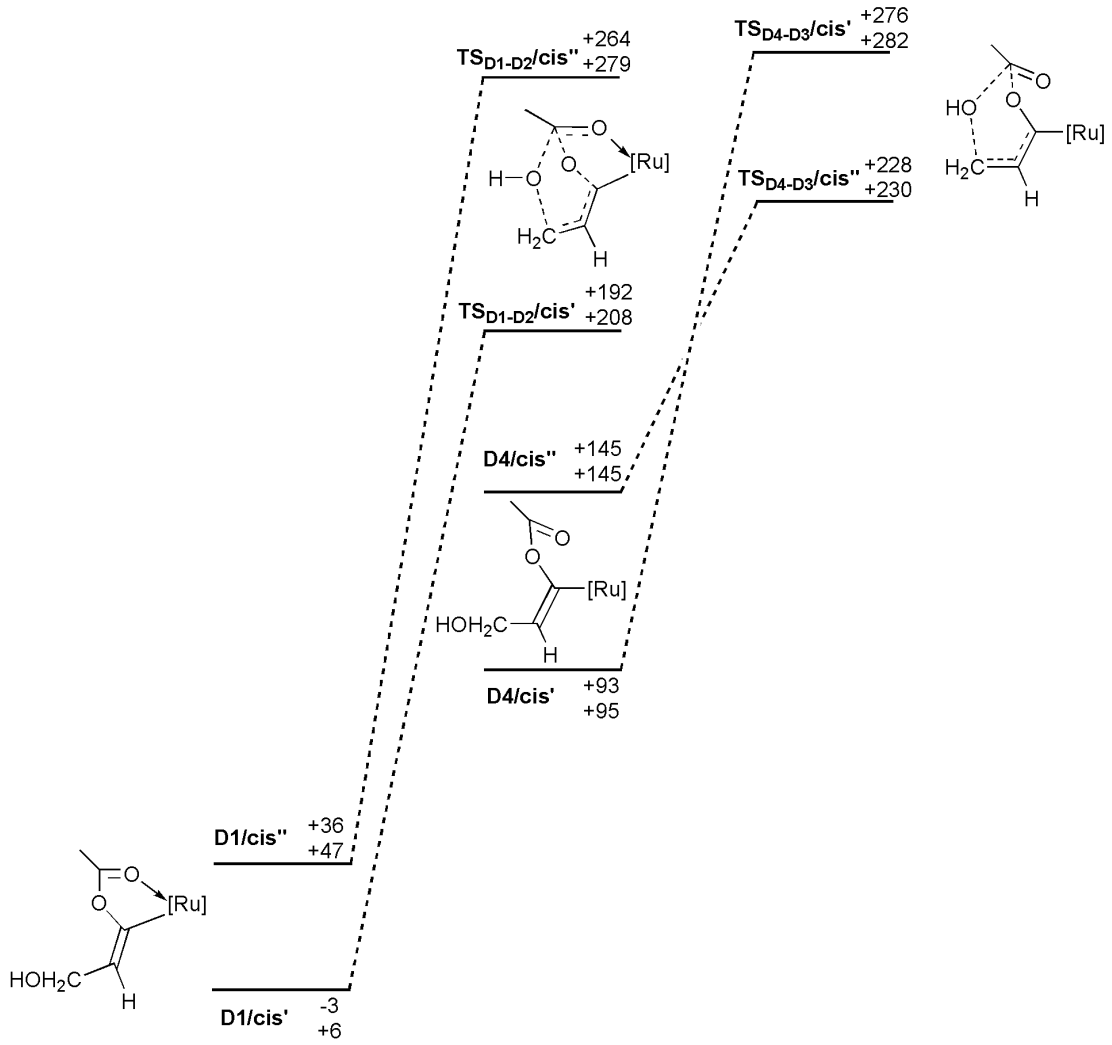

*Figure 3.25 – PES showing **D1/cis'**, **TS$_{D1-D2}$/cis'**, **D4/cis'** and **TS$_{D4-D3}$/cis'**. Energies are ZPE corrected SCF (top) and Gibbs free (bottom) energies in kJ mol^{-1} relative to **301**. [Ru] = [Ru(OAc)(PPh$_3$)$_2$].*

The results suggest that the reaction does not proceed *via* a concerted transesterification mechanism, meaning that the oxygen atom transfer from the acetate group to the former hydroxy-vinylidene must occur through a different mechanism.

3.2.3 Investigations Involving an Allenylidene Intermediate

Due to the high energy of the transesterification mechanism, a new pathway involving allenylidene intermediates was studied, primarily due to a reaction mechanism proposed by Dixneuf and Bustelo in a study of a similar system (section 1.4.4, Figure 3.26).[208]

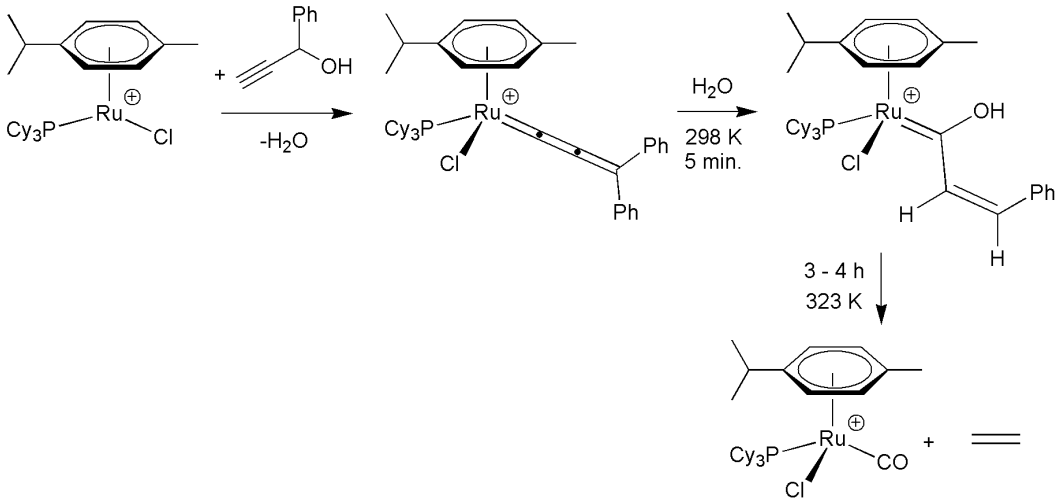

Figure 3.26 – Reaction of HC≡CCHPhOH with complex [(p-cymeme)RuCl(PCy$_3$)][B(Ar$_F$)$_4$].

To form the allenylidene **D5**, dehydration of **301** can occur *via* an intramolecular mechanism in the form of **TS$_{301\text{-}D5}$** (Figure 3.27), where the proton and hydroxy group of the vinylidene are lost as water.

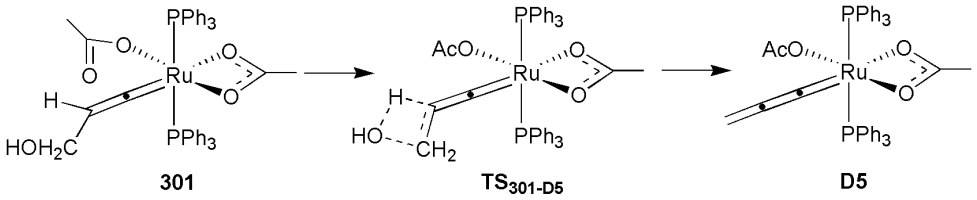

*Figure 3.27 – Formation of allenylidene **D5**.*

Alternately a reverse LAPS-type mechanism can occur with the proton being 'shuttled' from the vinylidene C_β to the hydroxy group by an acetate ligand *via* $\mathbf{TS_{301\text{-}D6}}$ - analogous to the LAPS transition state of $\mathbf{TS_{A5\text{-}202}}$ in chapter 2, with many examples of vinylidene C_β deprotonation being found within the literature.[138, 225, 226] The acetic acid group of **D6** would then act as an intramolecular acid to protonate the hydroxy group, resulting in the loss of water to form the allenylidene **D5** (Figure 3.28).

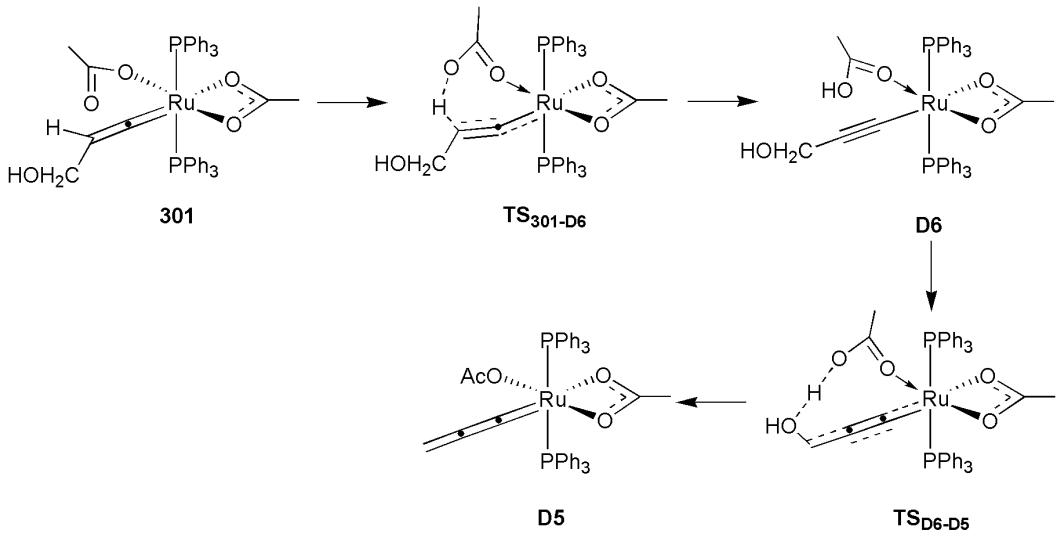

Figure 3.28 – Acetate assisted dehydration of a hydroxy-vinylidene to form an allenylidene.

It was then proposed that once formed, the acetate group of **D5** can engage in a nucleophilic attack on the allenylidene C_α, forming the metallo-enol ester **D7**. The water originally released in formation of the allenylidene can then attack the C_α of the acetate group *via* $\mathbf{TS_{D7\text{-}D2}}$ to form **D2** (Figure 3.29). This mechanism would also split the acetate group, which is consistent with what is observed experimentally.

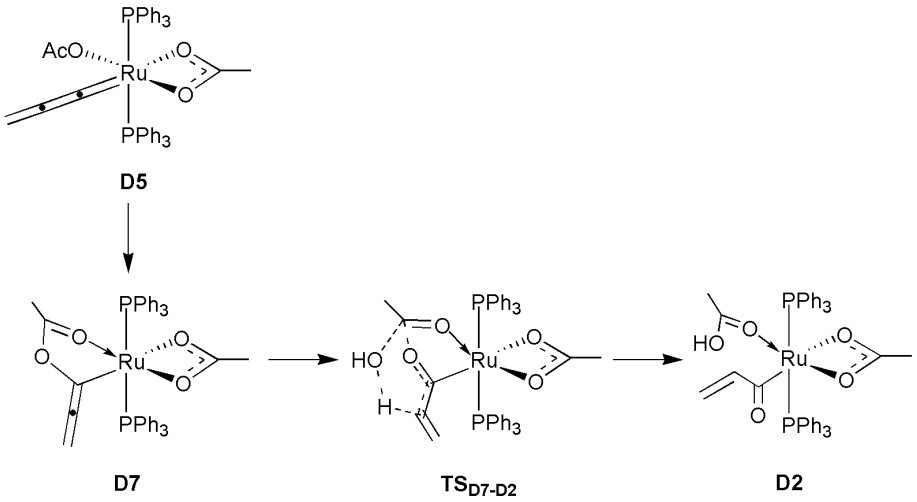

*Figure 3.29 – Formation of **D2** from **D7**.*

It can be seen from the PES shown in in Figure 3.30 that the allenylidene **D5** and the metallo-enol ester **D7** are similar in energy, at ca. 95 kJ mol^{-1} relative to **301**. To form **D5** the intramolecular dehydration transition state $\mathbf{TS_{301\text{-}D5}}$ was found at +243 kJ mol^{-1} relative to **301**, with the acetate-assisted dehydration having a far lower barrier of +138 kJ mol^{-1}. However the pathway to the formation of **D2** through $\mathbf{TS_{D7\text{-}D2}}$ is +258 kJ mol^{-1} (+247 kJ mol^{-1} with solvation relative to **D1**) making this mechanism unlikely.

Additionally, an isomer of $\mathbf{TS_{D7\text{-}D2}}$ with an attacking hydroxy group in place of water was investigated in order to see the effect of a better nucleophile; however the transition state could not be optimised.

In conclusion, an allenylidene mediated reaction mechanism looks to be as unlikely as the concerted transesterification mechanism discussed previously.

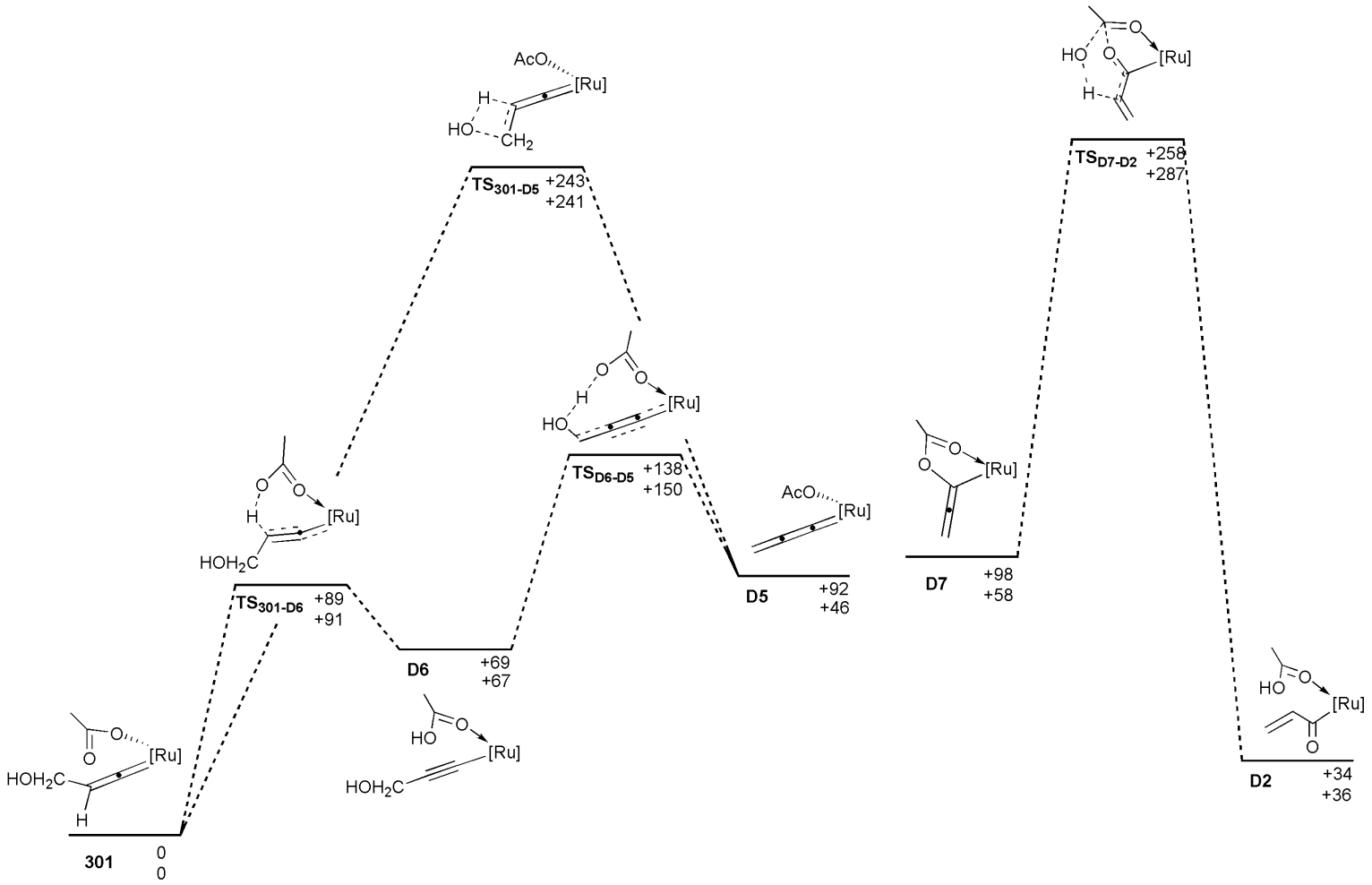

*Figure 3.30 – PES of the allenylidene mechanism. Energies are ZPE corrected SCF (top) and Gibbs free (bottom) energies in kJ mol^{-1}, relative to **301**. [Ru] = [Ru(OAc)(PPh$_3$)$_2$].*

*3.2.4 Investigation into the Formation of **302** and Ethene via Water Addition*

With the concerted transesterification and allenylidene-mediated mechanisms seen in section 3.2.2 and 3.2.3 being found to be unfeasible for the reaction conditions employed, attention was focussed on other reaction pathways. This section details the study of water-mediated mechanisms where the source of water is within the reaction solution, for example a non-dry solvent or by-product of allenylidene formation (see section 3.2.3). Due to the lack of positive results, this section shall only briefly look at the water addition mechanism, with more details being found in appendix section B.1.

Two pathways considered were the addition of a water molecule to take part in a concerted transesterification reaction through $\mathbf{TS_{D1\text{-}D2(H2O)}}$ and $\mathbf{TS_{D4\text{-}D3(H2O)}}$, and through the coordination of water to the metal centre which subsequently attack the acetate group – for example with $\mathbf{TS_{D8\text{-}D9}}$ (Figure 3.31).

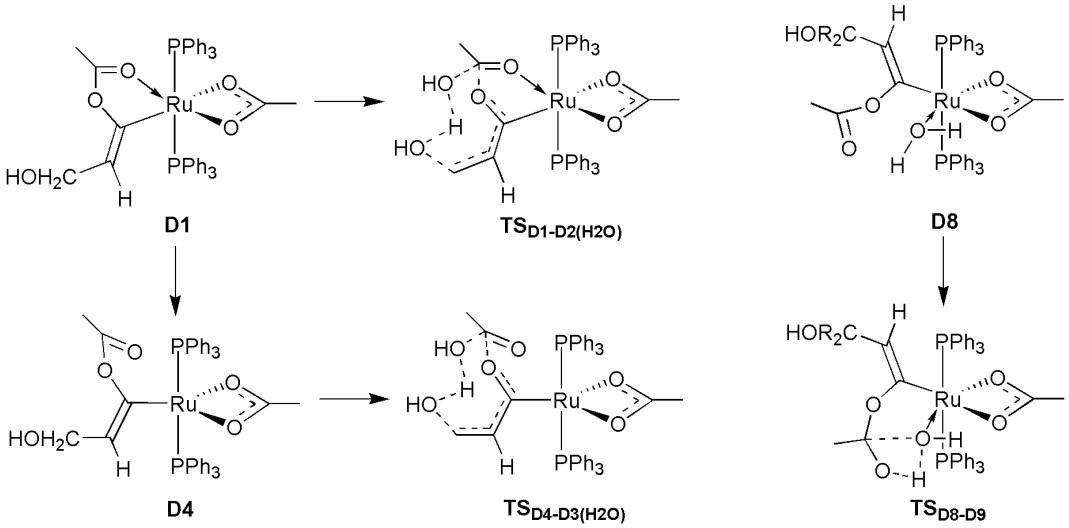

Figure 3.31 – Examples of water addition mechanisms.

The transesterification water-attack transition states $\mathbf{TS_{D1\text{-}D2(H2O)}}$ and $\mathbf{TS_{D4\text{-}D3(H2O)}}$ are too high in energy for the reaction conditions employed, at +151 and +233 kJ mol^{-1} relative to **301**. With respect to the water-coordination mechanism, while **D8** is located at +48 kJ mol^{-1}, the transition state $\mathbf{TS_{D8\text{-}D9}}$ as well as other similar transition states could not be optimised. It is therefore assumed that a water-assisted mechanism is not occurring in the ultimate formation of **302** and ethene.

*3.2.5 Investigation of Formation of **302** and Ethene via a Cationic Intermediate*

The mechanism for formation of **302** and ethene must involve the breakage of the acetate C-O bond, however all previously discussed mechanisms are too high in energy to be feasible for the experimental reaction conditions.

It was proposed that formation of a cationic complex could allow for nucleophilic attack with water (or potentially hydroxide) at the central acetate carbon to occur much more readily than in neutral systems. Additionally in further experimental studies by Elizabeth Smith, complex **303** was reacted with tritylcarbenium tetrafluoroborate forming the cationic complex **305** (Figure 3.32), which was verified with X-ray crystallography.

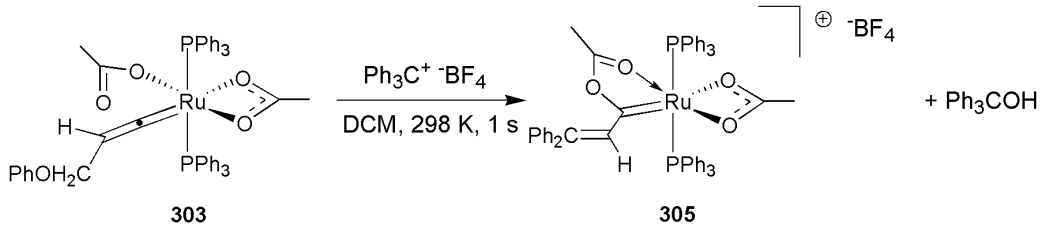

*Figure 3.32 – Reaction of **303** with tritylcarbenium tetrafluoroborate to form **305**.*

Due to the experimental observation of **305** a mechanism through the cationic intermediate **D13** was proposed, which could be formed by either loss of hydroxide from **D1**, or by protonation of **D7**. From **D13** hydroxide attack at the acetate C_α could then occur *via* $\mathbf{TS_{D13\text{-}D14}}$ to form **D14**. Finally breaking the acetate C-O bond would form **D2** *via* $\mathbf{TS_{D14\text{-}D2}}$ (Figure 3.33).

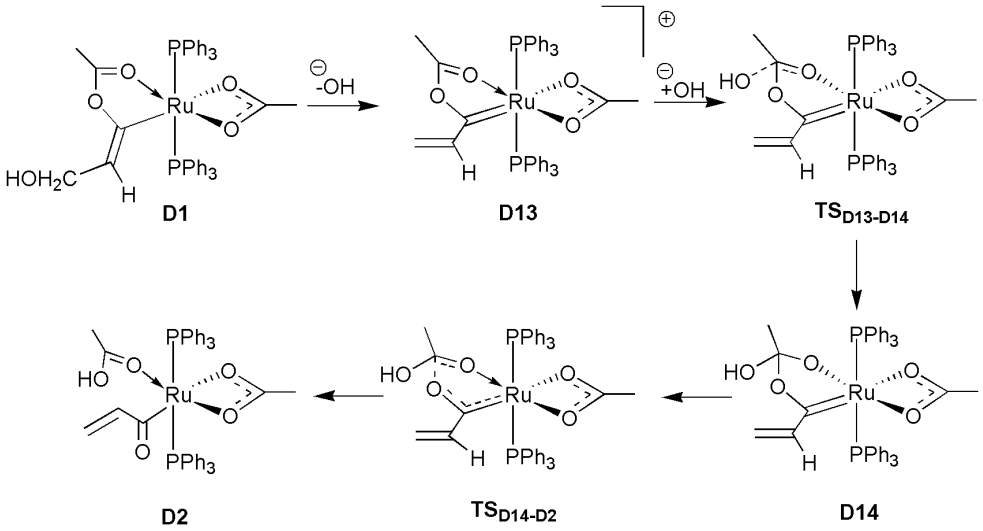

*Figure 3.33 – Mechanism through cation **D13**.*

The transition state $\mathbf{TS_{D13\text{-}D14}}$ could not be optimised, with all initial guess structures instead optimising to **D14**, which can be explained by the two highly charged fragments in close proximity to each other forming a bond during the optimisation process. In the PES shown in Figure 3.34 intermediate **D13** is +644 kJ mol^{-1} relative to **301**, which reduces to +569 kJ mol^{-1} upon DCM solvation correction. However due to the experimental observation of the analogue to **D13** (**305**), it is possible that the energy of **D13** is not being described by current methods adequately. Finally **D14** is +47 kJ mol^{-1} relative to **301**, with the transition state $\mathbf{TS_{D14\text{-}D2}}$ being roughly isoenergetic with **D14** at +52 kJ mol^{-1}.

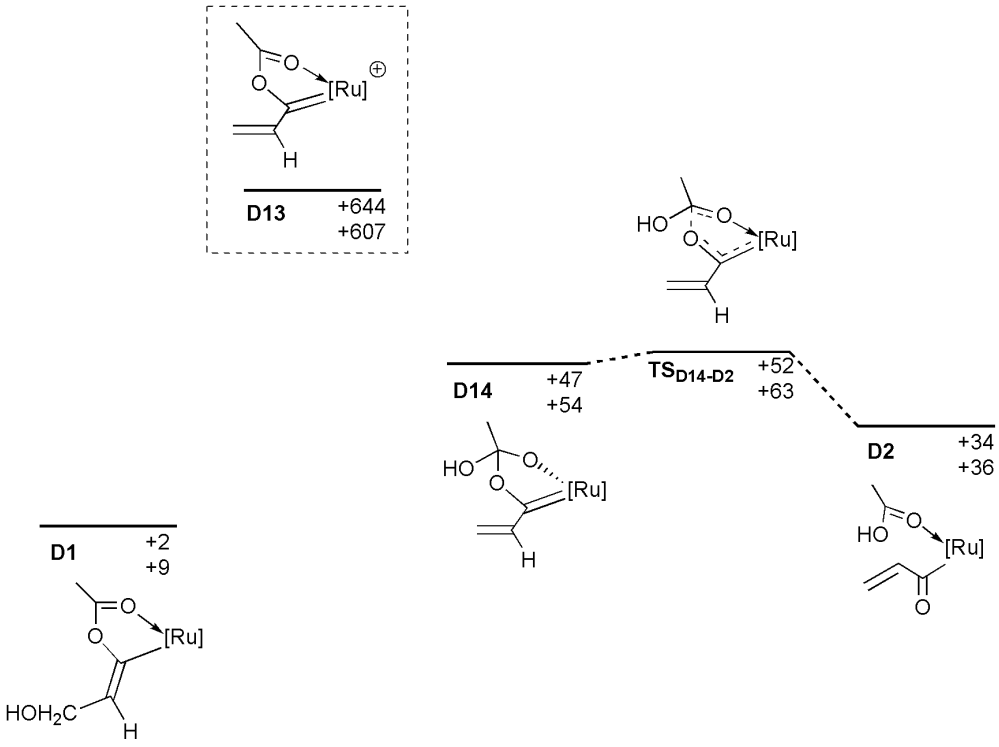

*Figure 3.34 – PES of the 'cationic' mechanism. Energies are ZPE corrected SCF (top) and Gibbs free (bottom) energies in kJ mol^{-1}, relative to **301**. [Ru] = [Ru(OAc)(PPh$_3$)$_2$].*

D14 and the associated transition state to form **D2** were shown to be feasible stationary points under the experimental reaction conditions. However the mechanism for formation of **D14** remains unclear due to **D13** being high in energy and the transition state $\mathbf{TS_{D13\text{-}D14}}$ not being located on the PES. It is possible that **D14** is formed as part of a hydroxide transfer mechanism; however attempts to optimise stationary points that relate to this possibility were not successful.

3.2.6 Summary and Current Conclusions on the Mechanism of Ethene Formation

Experimental results indicated that reaction of the hydroxy-vinylidene complex **301** proceeds to form complex **302** plus free ethene (298 K, 48 h), with formation of **D2** also proposed from the theoretical study. Additionally the experimental observation of **304** and the potential precursor of **D3** are also proposed to be part of this mechanism (Figure 3.35).

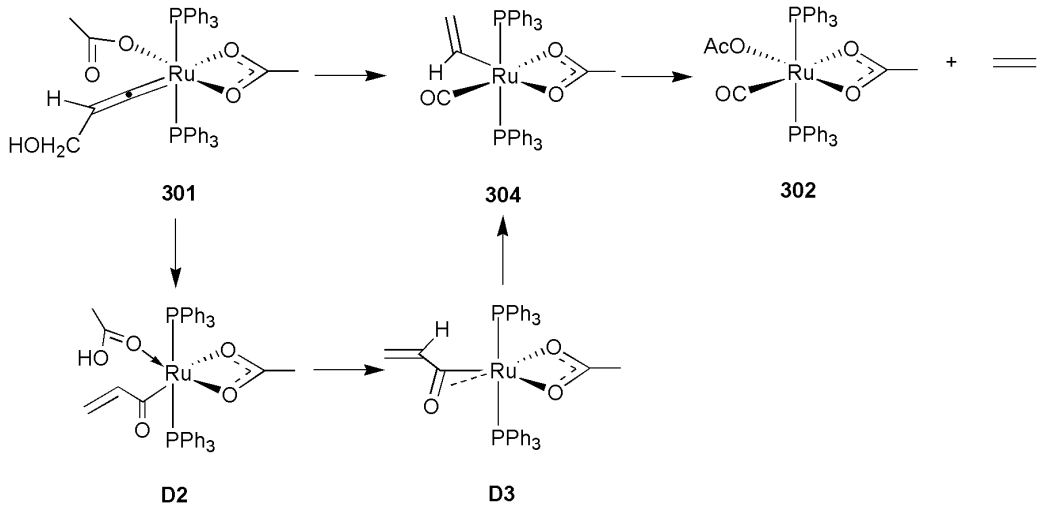

*Figure 3.35 – Reaction of **301** to form **302** and free ethene.*

Several mechanistic pathways were investigated including concerted transesterification, through allenylidene and cationic intermediates, and water attack. All of these possessed high energy transition states which were not consistent with the reaction time (48h to completion) and low temperature (298 K) seen in the experimental study. The mechanism from **D14** through $\mathbf{TS_{D14\text{-}D2}}$ (Figure 3.36) is shown to be feasible, however a mechanism for the formation of **D14** could not be located.

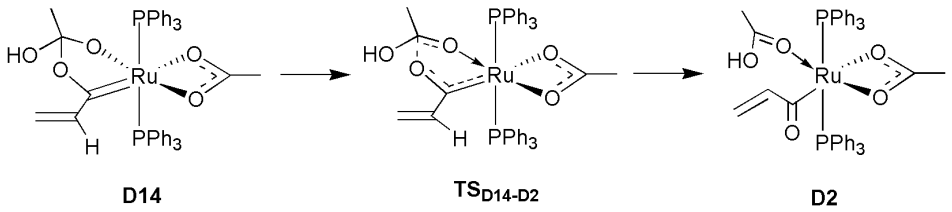

*Figure 3.36 – Mechanism via **D14** and $\mathbf{TS_{D14\text{-}D2}}$.*

Two possible conclusions from these results can be made. The first is that the hydroxide attack mechanism is not being successfully modelled using the methodologies used here, which is possible given the known difficulty in modelling anions such as OH.[227-229]

The second possibility is that hydroxide attack at **D1** is occurring *via* an intermolecular mechanism. The hydroxide involved in the nucleophilic attack of the acetate carbon could originate from a second hydroxy-vinylidene complex **D1** (Figure 3.37). In this mechanism the geometric strain for the concerted transition state of $\mathbf{TS_{D1\text{-}D2}}$ would be eliminated, with the need for attack by a free hydroxide anion or by water no longer being necessary.

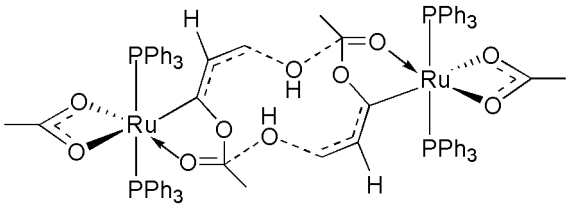

*Figure 3.37 – Possible hydroxy-transfer via a dimer of **D1**.*

Hypothetically this could be verified by another ^{18}O labelling study, with labelled **201** as well as ^{18}O labelled propargylic alcohol, which would form ^{18}O labelled **301**. If a dimer-mediated reaction is occurring, then mixing the labelled **301** with non-labelled **301** should result in the mixed-labelled product seen below in Figure 3.38. If the reaction is intramolecular however, no mixing of the labelled groups would occur.

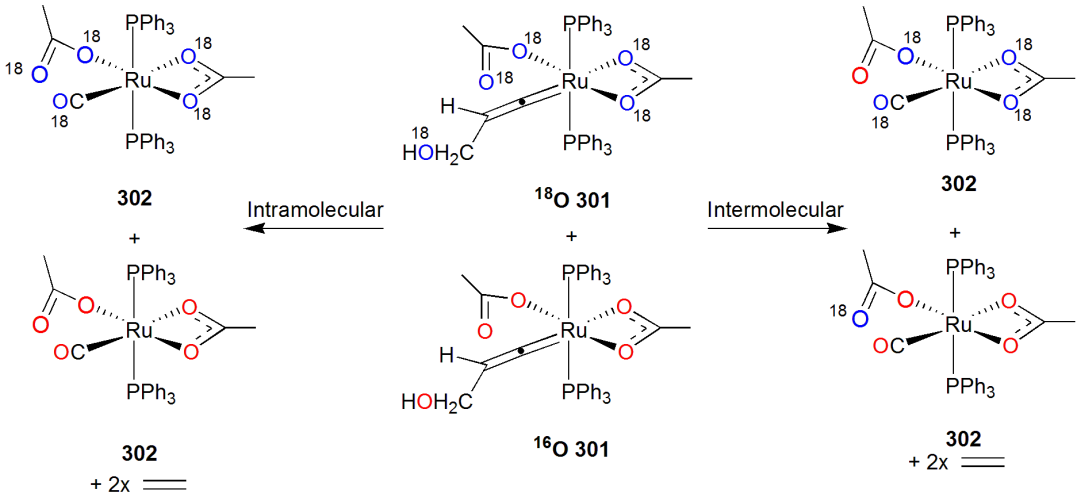

Figure 3.38 – Theoretical labelling study showing inter- and intramolecular products.

In conclusion the mechanism of ethene formation from **301** could not be identified using the methodologies described here, with all investigated transition states being too high in energy to be feasible for the reaction conditions employed experimentally. While the mechanism of formation of **D1** from **301** and the formation of the ultimate product of the reaction (**302**) from **D14** occur with energy changes that are consistent with the experimental conditions and rate of reaction, the pathway connecting these two minima was not identified.

4. Investigation of the Ligand Assisted Proton Shuttle Mechanism in the Presence of a CO Ligand: The CO-LAPS Mechanism

4.1 Introduction

Previous sections involving the LAPS mechanism have shown stoichiometric formation of metal vinylidenes and other complexes through the use of acetate ligands. This chapter shall present a study into a variant of the LAPS mechanism which ultimately shows catalytic activity. Here complex **302** (Figure 4.1 - previously seen as a reaction product in chapter 3) – essentially **201** with a coordinated carbonyl ligand – shows significantly different reactivity to what has been demonstrated previously.

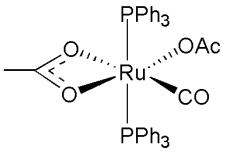

*Figure 4.1 – Complex **302**.*

The reaction of **302** and phenylacetylene produces the ruthenium acetylide **401** as well as the ultimate formation of (*Z*)-*β*-styryl acetate (Figure 4.2), contrary to the expected metal vinylidene.

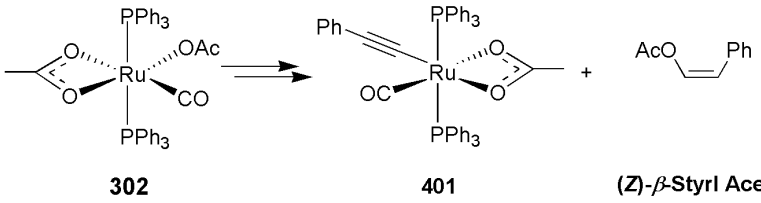

*Figure 4.2 – Simplified scheme showing reaction of **302** with phenylacetylene.*

This mechanism, termed CO-LAPS due to the different reactivity involved with the addition of a carbonyl ligand, was investigated in a joint experimental and theoretical study. This chapter shall present an assessment of the reaction mechanism as well as provide explanation for observed substituent effects.

4.1.1 Initial Experimental Observations

The experimental work seen in this chapter was once again carried out by Dr Christine Welby (unless indicated otherwise), and full details of her work can be found in her published thesis.[215]

Complex **302** was prepared by methods outlined by Wilkinson,[230] as well as by a method developed during the experimental investigation which produced the complex *in situ*.[213] This method involved stirring complex **201** under and atmosphere of CO in DCM, to produce complex **302**. Complex **302** possessed phosphine groups which are mutually *trans*, contrary to the phosphine groups of complex **201** which are mutually *cis*, as well as to an analogous system studied by Robinson *et al.* (Figure 4.3).[231-234]

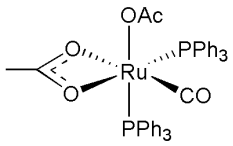

Figure 4.3 – Cis-phosphine complex observed by Robinson.

A single-crystal X-ray structure was obtained and is shown in Figure 4.4, with selected bond lengths and angles shown in Table 4.1.

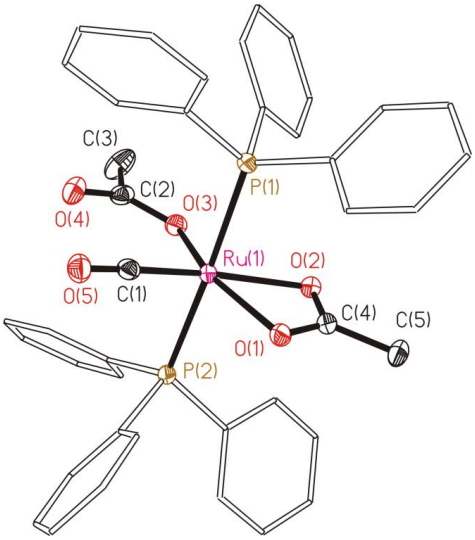

*Figure 4.4 - ORTEP diagram of **302**, thermal ellipsoids, where shown, are at the 50 % probability level. Hydrogen atoms are omitted for clarity.*[215]

*Table 4.1 – Selected bond lengths and angles for **302***[215]

Bond	Bond Length (Å)	Angle	Bond Angle (°)
Ru – P(1)	2.406(4)	P(1) – Ru – P(2)	176.55(2)
Ru – P(2)	2.387(4)	P(1) – Ru – O(1)	95.14(3)
Ru – O(1)	2.147(1)	P(1) – Ru – O(2)	86.12(3)
Ru – O(2)	2.190(1)	P(1) – Ru – O(3)	87.52(3)
Ru – O(3)	2.037(1)	P(1) – Ru – C(5)	91.24(5)
Ru – C(5)	1.832(2)	P(2) – Ru – C(5)	88.21(5)
C(5) – O(5)	1.146(2)	O(1) – Ru – O(2)	60.42(4)
		O(1) – Ru – O(3)	155.62(5)
		O(2) – Ru – O(3)	95.71(5)
		O(1) – Ru – C(5)	104.71(6)
		O(2) – Ru – C(5)	164.49(6)
		O(3) – Ru – C(5)	99.45(6)
		Ru – C(1) – O(5)	175.02(2)

As was the case with the LAPS system, addition of phenylacetylene to complex **302** was expected to produce a vinylidene complex. Instead, the addition of 1.4 equivalents of phenylacetylene to complex **302** in deuterated dichloromethane showed the formation of **401** over the course of several days at room temperature (Figure 4.5). ^{1}H and $^{31}P(^{1}H)$ NMR spectroscopy showed evidence for a single acetate group, as well as a carbonyl and acetylide ligand and two triphenylphosphine groups which were mutually *trans*.

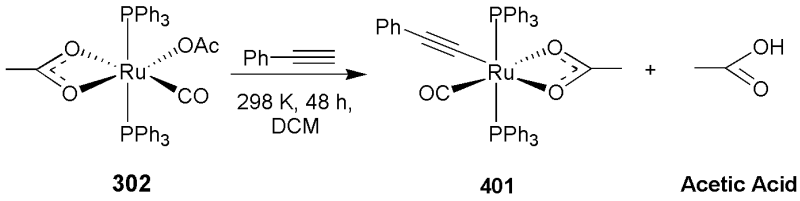

*Figure 4.5 – Formation of **401**.*

A single-crystal X-ray structure of **401** was also obtained and is shown in Figure 4.6, with selected bond lengths and angle shown in Table 4.2.

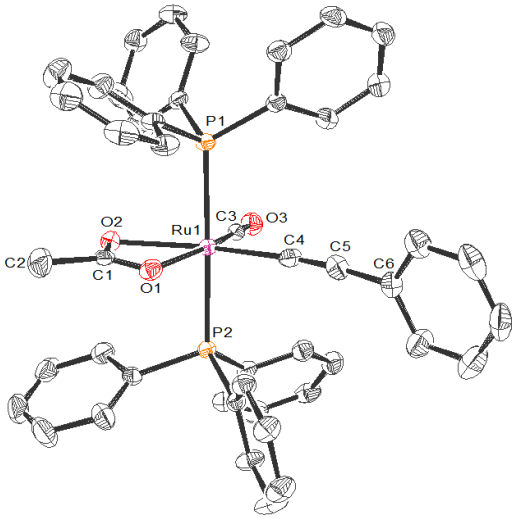

*Figure 4.6 – ORTEP diagram of **401**, thermal ellipsoids, where shown, are at the 50 % probability level. Hydrogen atoms are omitted for clarity.*[215]

*Table 4.2 – Selected bond lengths and angles for **401**[215]*

Bond	Bond Length (Å)	Angle	Bond Angle (°)
Ru – P(1)	2.384(7)	P(1) – Ru – P(2)	178.15(3)
Ru – P(2)	2.368(7)	P(1) – Ru – O(1)	93.14(5)
Ru – O(1)	2.183(2)	P(1) – Ru – O(2)	86.30(5)
Ru – O(2)	2.196(2)	P(1) – Ru – C(3)	89.79(8)
Ru – C(3)	1.824(3)	P(1) – Ru – C(4)	93.16(8)
Ru – C(4)	2.002(3)	P(2) – Ru – C(3)	91.82(8)
C(3) – O(3)	1.138(3)	P(2) – Ru – C(4)	87.69(8)
C(4) – C(5)	1.200(4)	O(1) – Ru – O(2)	59.91(7)
C(5) – C(6)	1.444(4)	O(1) – Ru – C(3)	166.69(9)
		O(1) – Ru – C(4)	100.37(1)
		O(2) – Ru – C(4)	160.16(1)
		C(3) – Ru – C(4)	92.42(1)
		C(3) – Ru – O(2)	107.40(9)
		Ru – C(3) – O(3)	178.3(2)
		Ru – C(4) – C(5)	170.7(3)
		C(4) – C(5) – C(6)	173.0(3)

During formation of **401** the evolution of acetic acid was observed, which then disappeared with the concomitant formation of a new organic product – *β*-styryl acetate – found exclusively as the *Z*-isomer. Additionally a quantity of the starting material **302** remained in the reaction mixture even after 8 days of observation. Comparing the integration of peaks associated with the acetate groups of **401** and (*Z*)-*β*-styryl acetate showed that the two were present in equal quantities, suggesting that an acetate group from **302** was instrumental in the formation of the organic product.

The reaction underwent a period of optimisation, and it was discovered that two equivalents of phenylacetylene were required in order to drive the reaction to completion, as well as reaction conditions of 48 h at 323 K in DCM. The scheme for this reaction in Figure 4.7 suggests that the second equivalent of phenylacetylene acted as both a proton source, and was involved in the regeneration of **401** after the loss of (*Z*)-*β*-styryl acetate.

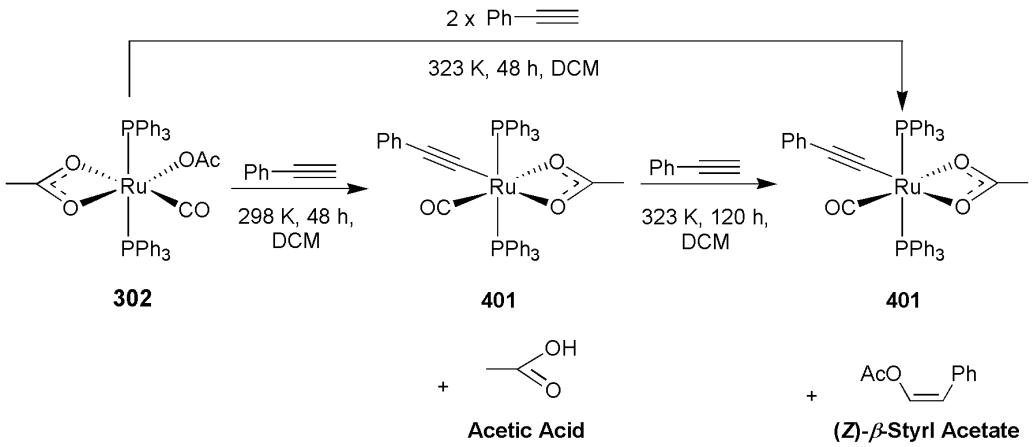

*Figure 4.7 – Reaction of **302** with phenylacetylene to form **401** and (Z)-β-styryl acetate.*

4.1.2 Substituent Effects

Stoichiometric investigations of the reaction of **302** with phenylacetylene showed exclusive formation of (Z)-β-styryl acetate. Further studies performed by Dr Sharifa Hussein, Chris Unsworth and Luke Shilling investigated if the reaction could be conducted under catalytic conditions.

As was seen previously in chapter 1.4.3, the addition of carboxylic acid to an alkyne can show preference for Markovnikov or anti-Markovnikov addition (Figure 4.8), depending on the substrates, base and solvent used - similar to reactions observed by Dixneuf, Yi and others.[194, 197, 201]

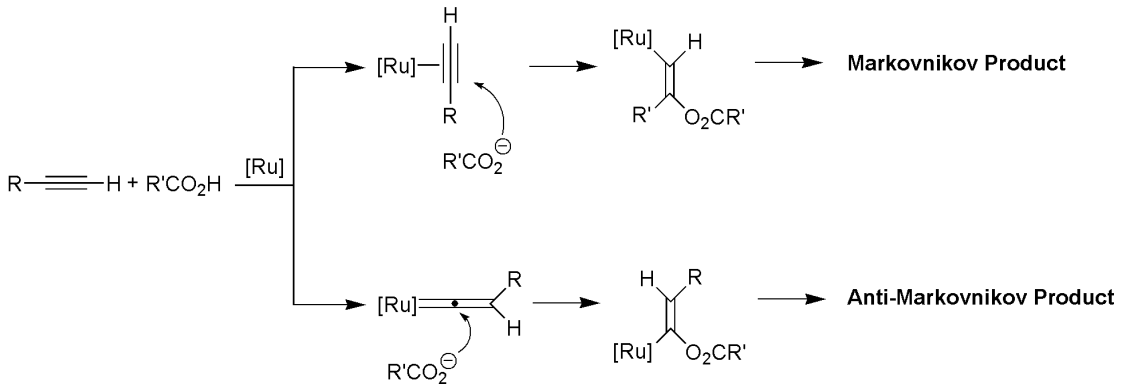

Figure 4.8 – Preference for Markovnikov and anti-Markovnikov addition.[194]

The study used varied carboxylic acid and alkyne substrates to investigate the activity and selectivity of the reaction, with all potential products shown below in Figure 4.9. A table of product yields for each substrate combination is shown in Table 4.3.

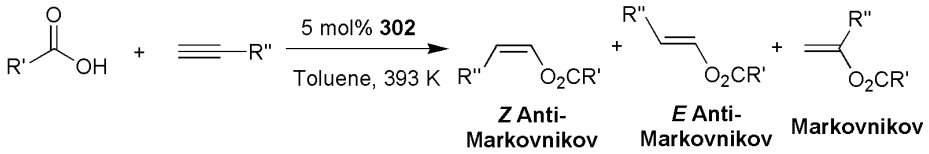

Figure 4.9 - Reaction scheme for catalytic studies.

Table 4.3 – Outcome of catalytic studies for selected substrates

R' (Carboxylic Acid)	R'' (Alkyne)	Selectivity Anti-Markovnikov (%) (*E* +Z Isomers/total enol esters)	Selectivity Markovnikov (%) (Markovnikov Product/total enol esters)	Anti-Markovnikov Z/E Ratio
Me	Ph	100[†]	0[†]	-
Ph(C_6H_5)	Ph	85	15	7
Ph	C_6H_4-*p*-CF_3	100	0	12
Ph	C_6H_4-*p*-F	81	19	7
Ph	C_6H_4-*p*-OMe	4	96	4
Ph	C_6H_4-*p*-NMe_2	2	98	2
C_6H_4-*p*-CF_3	Ph	18	82	5
C_6H_4-*p*-F	Ph	22	78	25
C_6H_4-*p*-OMe	Ph	79	21	15
C_6H_4-*p*-NMe_2	Ph	96	4	30

([†] - further results reported the observation of the Markovnikov product)

From the results there appears to be a change in Markovnikov/anti-Markovnikov selectivity when varying the alkyne and carboxylic acid. With the alkyne it appears that the more electron-withdrawing groups favour anti-Markovnikov addition, with more electron-donating groups favouring Markovnikov addition. In varying the carboxylic acid, the reverse is true with electron-withdrawing groups instead favouring a Markovnikov type addition. This correlated with the study by Yi and Gao, where carboxylic acids with more electron withdrawing groups formed some Markovnikov product, contrary to the trend seen with other carboxylic acids with less electron withdrawing groups present (see section 1.4.3).[201]

These results demonstrate not only the catalytic ability of **302**, but also indicate that the electronic properties of the substrates have a significant bearing on the overall regioselectivity of the reaction, concurring with previously published studies.

4.2 Results and Discussion

4.2.1 Computational Preamble

The conclusions of the experimental study led to a theoretical mechanistic investigation that would focus on three main areas. The first is the unexpected formation of **401**, which is unusual as the *bis*-acetate complex **201** has been shown to react with alkynes to form vinylidene complexes, whereas in this instance an acetylide **401** and free acetic acid is formed (Figure 4.11).

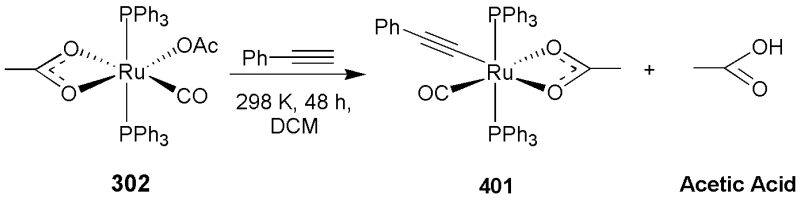

*Figure 4.10 – Formation of **401**.*

The second involves the concomitant formation of the β-styryl acetate product – in particular the selectivity seen for the *Z*-isomer. Thirdly the difference between Markovnikov and anti-Markovnikov selectivity with respect to the stoichiometric investigation seen in section 4.1.1, as well the difference in catalytic selectivity caused by substituent effects, will be presented here.

Potential energy surfaces for the mechanism were investigated with the use of DFT, using methods outlined in section 7.1, with DRC analyses performed on all transition states as per section 7.2. Energies are reported as ZPE corrected SCF energies. Solvation corrections were not employed.

*4.2.2 Investigation of the LAPS Mechanism and Formation of Complex **401***

A starting point for this study involved an investigation for a LAPS-type mechanism that led to the formation of acetylide **401** from **302** (Figure 4.11). It was believed that the first half of the LAPS mechanism was occurring, leading to the formation of **401** and acetic acid, *via* deprotonation of a metal alkyne complex by a coordinated acetate ligand.

As seen in Figure 4.11, the proposed mechanism begins as in previous examples (section 2.2.2), by the creation of a free coordination site in complex **302** forming **E1**. This is followed by coordination of phenylacetylene in an η^2 fashion to give structure **E2**, followed by the rearrangement to give the alkyne σ-complex **E3**.

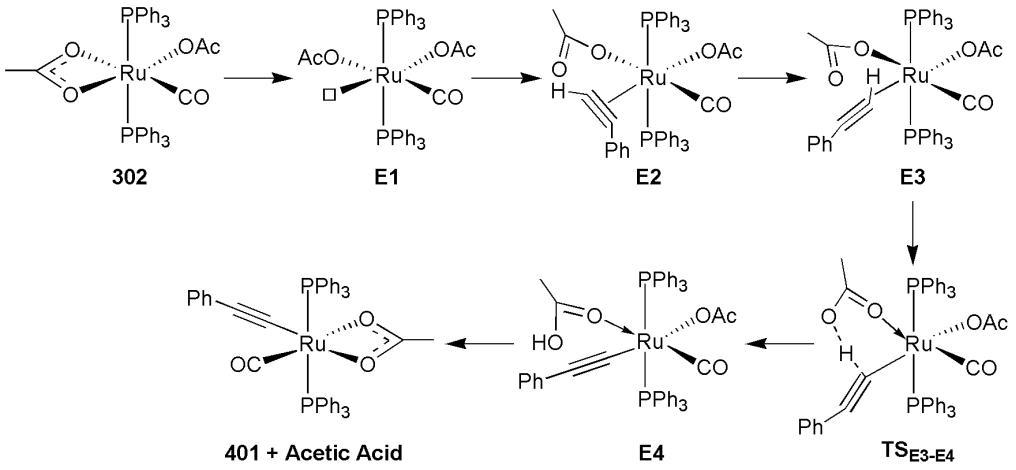

*Figure 4.11 - Key states in the formation of **401** from **302** via the LAPS mechanism.*

Complex **E3** is then deprotonated by an acetate group through transition state $\mathbf{TS_{E3\text{-}E4}}$, forming a complex **E4**, containing coordinated acetylide and acetic acid ligands. Acetic acid is then lost, forming **401** with a change in binding mode of the remaining acetate ligand from κ^1 to κ^2. A PES for this proposed mechanism was constructed and is shown in Figure 4.13.

An isomer of **E1** where the free coordination site was adjacent to the CO group could not be located, instead the isomer shown in Figure 4.12 where the coordination site is *trans* to the CO group (**E1/trans-CO**) was found. This was due to the acetate groups being stabilised by an acetate-CO interaction. The isomer where the free coordination site is *cis* to the carbonyl complex could not be formed due to the acetate groups returning to a κ^2-binding mode during optimisation.

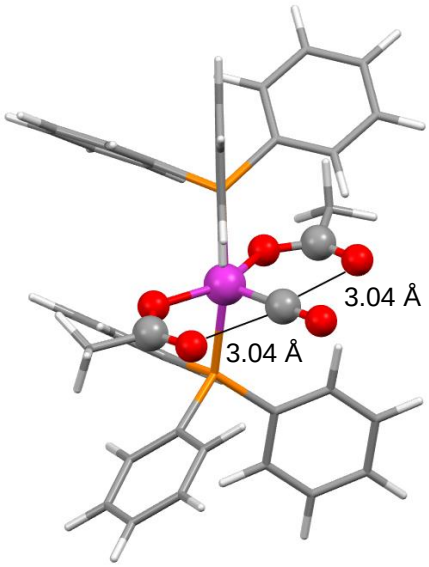

Figure 4.12 – Optimised structure of the isomer of **E1**.

Aside from this, the PES of the LAPS process was very similar to that seen where the carbonyl ligand is not present at the metal centre (chapter 2), with the deprotonation transition state $\mathbf{TS_{E3\text{-}E4}}$ being relatively isoenergetic with **E2** and **E3** at +33 kJ mol^{-1} relative to **302**. Proceeding to **E4** showed a significant drop in energy (-31 kJ mol^{-1} relative to **302**), with the loss of acetic acid and formation of **401** being exothermic compared to all other states. As expected, when entropic effects are taken into account the thermodynamic driving force for the formation of **401** from **302** is larger (ΔG = -40 kJ mol^{-1}, and -70 kJ mol^{-1} from **E4**). However care should be taken here as entropic effects in gas phase calculations are likely to be overestimated compared to the entropy changes in solution.[57, 73]

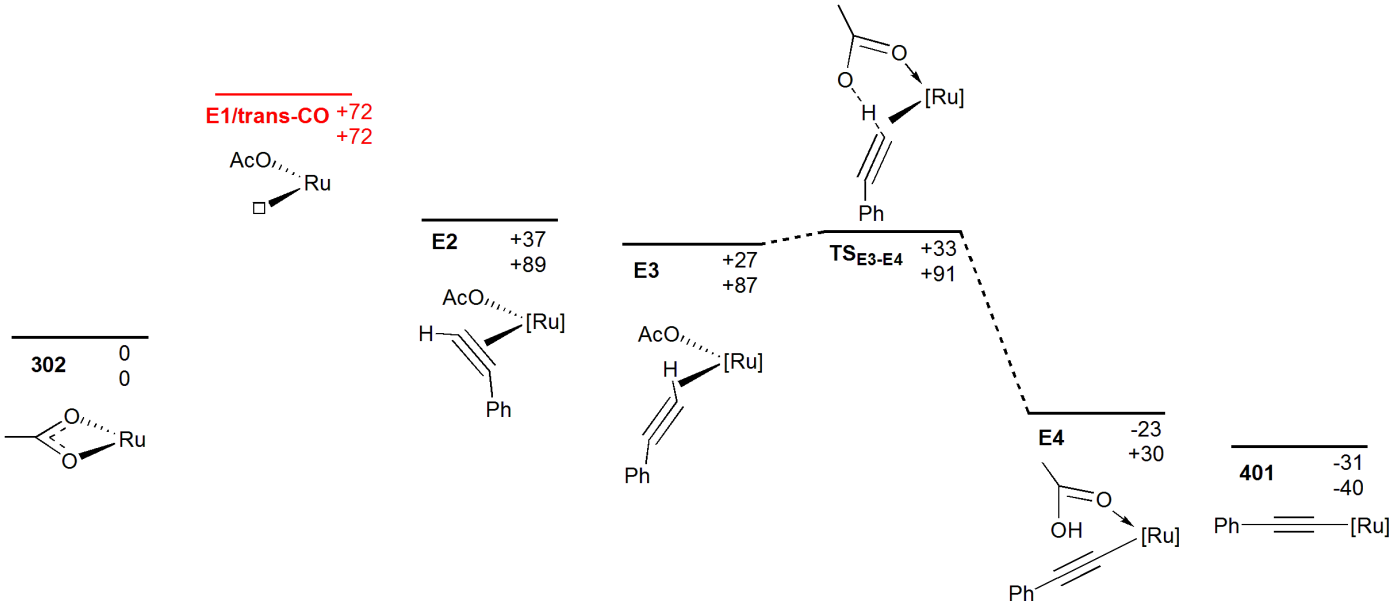

*Figure 4.13 – PES illustrating the formation of **401**. Energies are ZPE corrected SCF (top) and Gibbs free (bottom) energies in kJ mol^{-1}, relative to **302**. [Ru] = [Ru(CO)(OAc)(PPh$_3$)$_2$].*

4.2.3 Formation of Vinylidene Complex and (Z)-β-Styryl Acetate

With the PES for the formation of **401** *via* a LAPS-type mechanism mapped, efforts began to investigate the mechanism of vinylidene formation (**E5**, Figure 4.15) which was the product originally expected in the reaction. Due to the observation in section 2.2.4 of the metallo-enol ester complex **203**, it was proposed that an analogous complex could be formed here, which could be a precursor to the formation of (*Z*)-*β*-styryl acetate in an anti-Markovnikov addition similar to that reported by Dixneuf, Yi and others.[194, 197, 201]

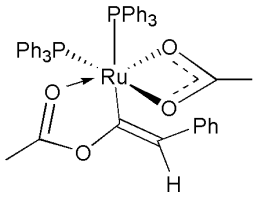

*Figure 4.14 – **203**.*

As can be seen below in Figure 4.15, structure **E4** can proceed to one of two outcomes – either loss of acetic acid to form the acetylide complex **401**, or protonation of the acetylide C_β by the acetic acid group *via* $\mathbf{TS_{E4\text{-}E5}}$ to form the vinylidene complex **E5**, by a LAPS-type mechanism.

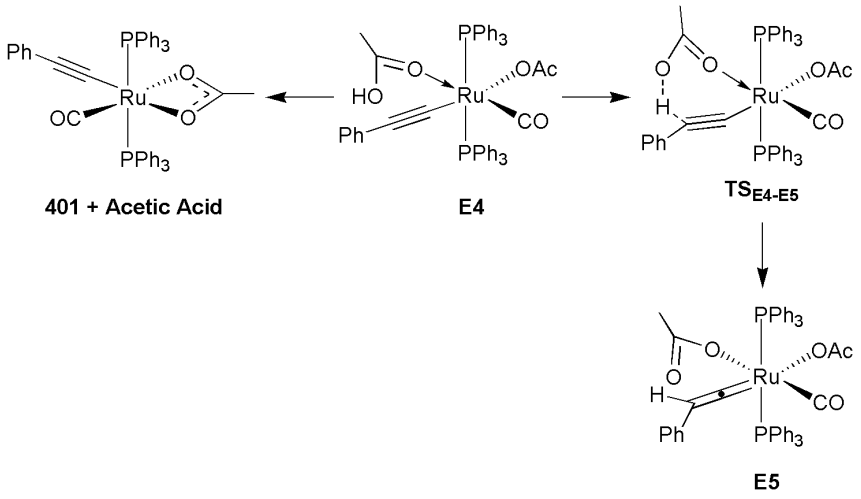

*Figure 4.15 – Alternate reactions of **E4**.*

From formation of **E5** the metallo-enol ester complex **E6** (analogous to complex **203**) can be formed by anti-Markovnikov attack at the vinylidene C_α, which is a precursor to the formation of *β*-styryl acetate. However the formation of **E5** *via* a LAPS-type transition state would form the **x** isomer of **E5**, which is in fact the precursor to the (*E*)-*β*-styryl acetate and not the experimentally observed (*Z*)-*β*-styryl acetate (Figure 4.25).

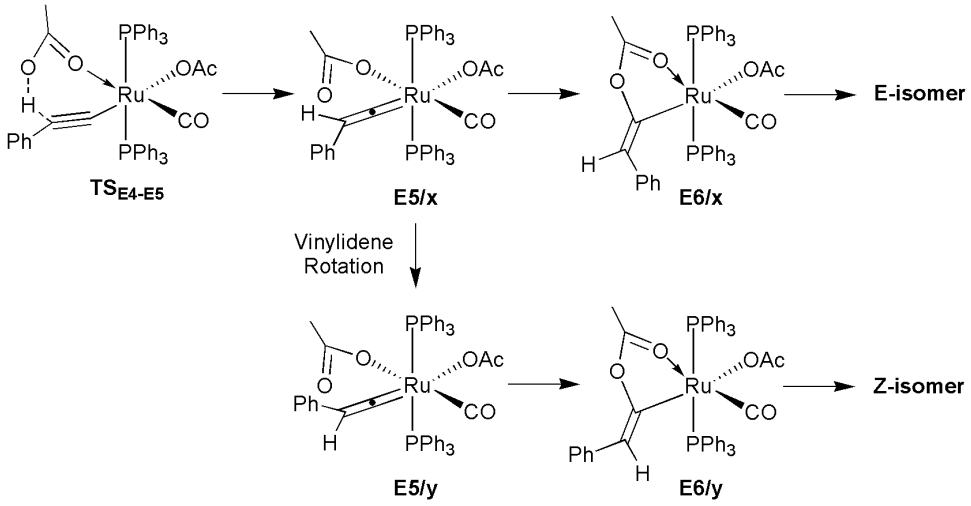

*Figure 4.16 – Stereoselectivity from **TS**$_{E4-E5}$ to the E and Z isomers of β-styryl acetate.*

Formation of the experimentally observed (*Z*)-*β*-styryl acetate product requires structure **E6/y**, which can be formed from **E5/x** through a vinylidene rotation. Vinylidene rotations have been shown to be accessible mechanisms, with a theoretical study by Jia, Lin *et al.* reporting barriers to rotational isomerisation of ca. 10 to 30 kJ mol^{-1}, with lower barriers reported with a coordinated π-acceptor ligand.[235] With this system possessing a carbonyl ligand which can act as a π-acceptor, the barrier to rotation is certainly feasible. However a transition state for this process could not be located.

From **E6/y**, the acetate which forms part of the metallo-enol ester would cease being coordinated to the ruthenium centre, which would coincide with a change in the other acetate ligand's binding mode to κ^2 from κ^1, ultimately forming complex **E7** (Figure 4.17).

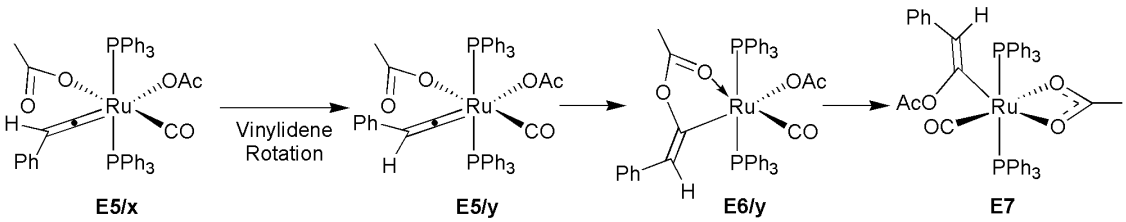

*Figure 4.17 – Ultimate formation of **E7** through **E6/y** from **E5/x**.*

From the PES of this process shown in Figure 4.18, the barrier to formation of the vinylidene **E5** through $\mathbf{TS_{E4\text{-}E5}}$ requires 50 kJ mol^{-1}. **E5** is shown to be +20 kJ mol^{-1} relative to **302**, which is significantly different to the reaction of **201** and phenylacetylene where metal vinylidene formation was the thermodynamic minimum on the PES.

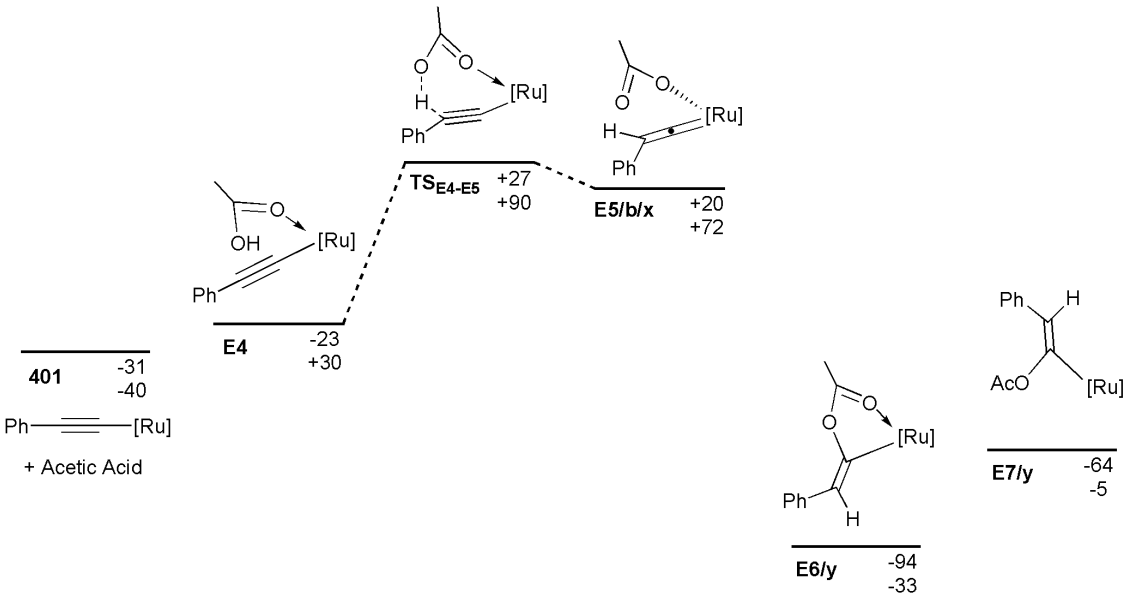

*Figure 4.18 – Formation of **E7** from **401**. Energies are ZPE corrected SCF (top) and Gibbs free (Bottom) energies in kJ mol^{-1}, relative to **302**. [Ru] = [Ru(CO)(OAc)(PPh$_3$)$_2$].*

Nucleophilic attack by the acetate ligand at the vinylidene to form **E6/y** is shown to stabilise the complex significantly at -94 kJ mol^{-1} relative to **302**. Formation of **E7/y** was shown to be -64 kJ mol^{-1} relative to **302** and +30 kJ mol^{-1} relative to **E6/y**. The high energy of the barrier to vinylidene formation, and the low energy of the precursor to (*Z*)-*β*-styryl acetate formation (**E6/y**) initially agrees with the experimental observation that **401** is formed at low temperature, with the majority of (*Z*)-*β*-styryl acetate formation occurring at reaction temperatures of 323 K.

The mechanism from **E7** to the formation of (*Z*)-*β*-styryl acetate was investigated further and proposed to occur *via* protonation of the Ru-C bond of the styryl acetate ligand. The proton required for this step can originate from two different sources – acetic acid or phenylacetylene. With acetic acid the ligand can coordinate to **E7**, forming complex **E8**. Protonation of the styryl acetate group by the coordinated acetic acid could occur, forming *β*-styryl acetate *via* the transition state $\mathbf{TS_{E8\text{-}302}}$. Loss of the organic product from **E8** then reforms complex **302** (Figure 4.19). **302** can then react with phenylacetylene to produce **401** and acetic acid, with **401** being a resting state in the formation of *β*-styryl acetate, explaining the lack of complex **302** observed in the reaction.

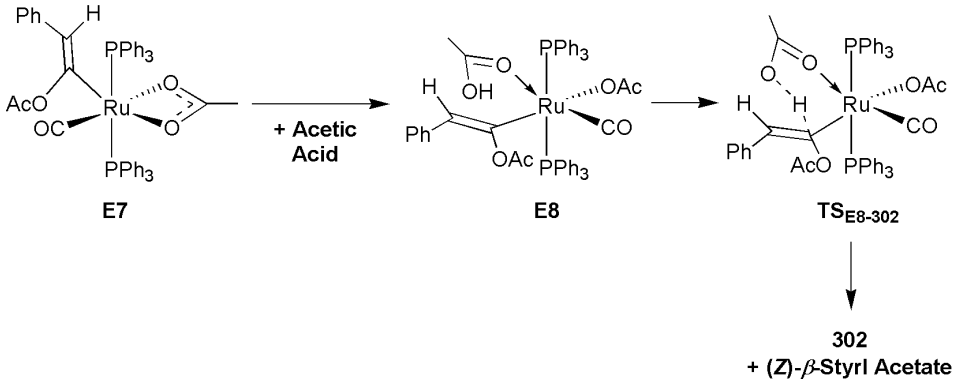

*Figure 4.19 – Formation of the organic product via acetic acid coordination from **E7**.*

With phenylacetylene as a proton-source, coordination of the alkyne initially forms the η^2-bound alkyne complex **E9/trans-co**. This can isomerise to form the σ-complex **E10/trans-co**, which can undergo intramolecular proton transfer from the alkyne to the styryl-acetate group *via* the transition state $\mathbf{TS_{E10\text{-}401}}$, with the loss of (*Z*)-*β*-styryl acetate regenerating complex **401** (Figure 4.20). This mechanism can be considered a *σ*-CAM mechanism, where C-H bond metathesis allows coordination of an acetylide with a parallel formation and loss of *β*-styryl acetate.[236]

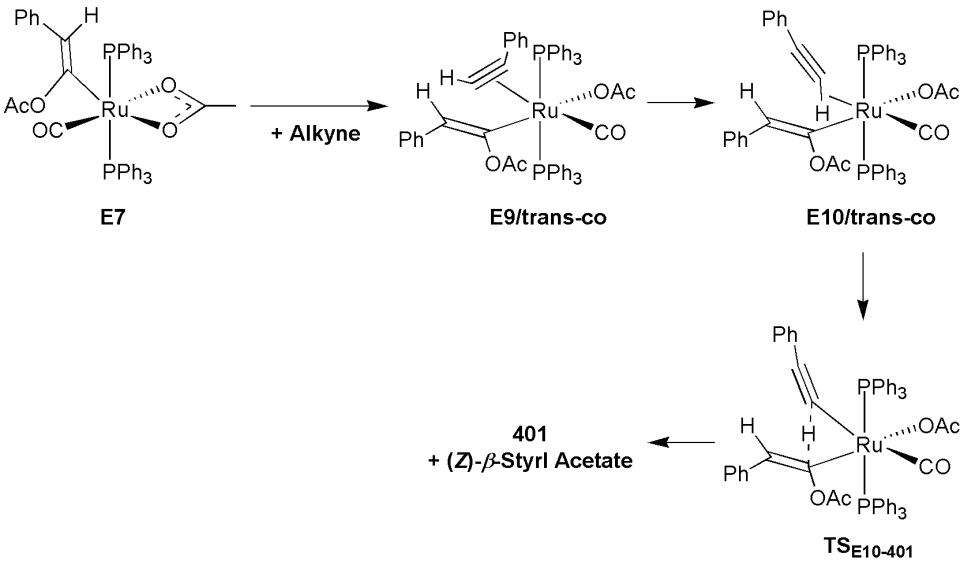

*Figure 4.20 – Formation of the organic product via alkyne coordination from **E7**.*

Additionally there is a second type of alkyne-assisted protonation through a LAPS-type mechanism that could be involved in the formation of (*Z*)-*β*-styryl acetate. If the alkyne were to bind *trans* to the styryl acetate (**E9/trans-sty** and **E10/trans-sty**), then acetate-mediate deprotonation can occur to form complex **E11** *via* the transition state $\mathbf{TS_{E10\text{-}E11}}$. After rotation of the acetic acid ligand from **E11/c** to **E11/d**, the proton can transfer to the *β*-styryl acetate, through $\mathbf{TS_{E11\text{-}401}}$ which again leads to the regeneration of **401** (Figure 4.21).

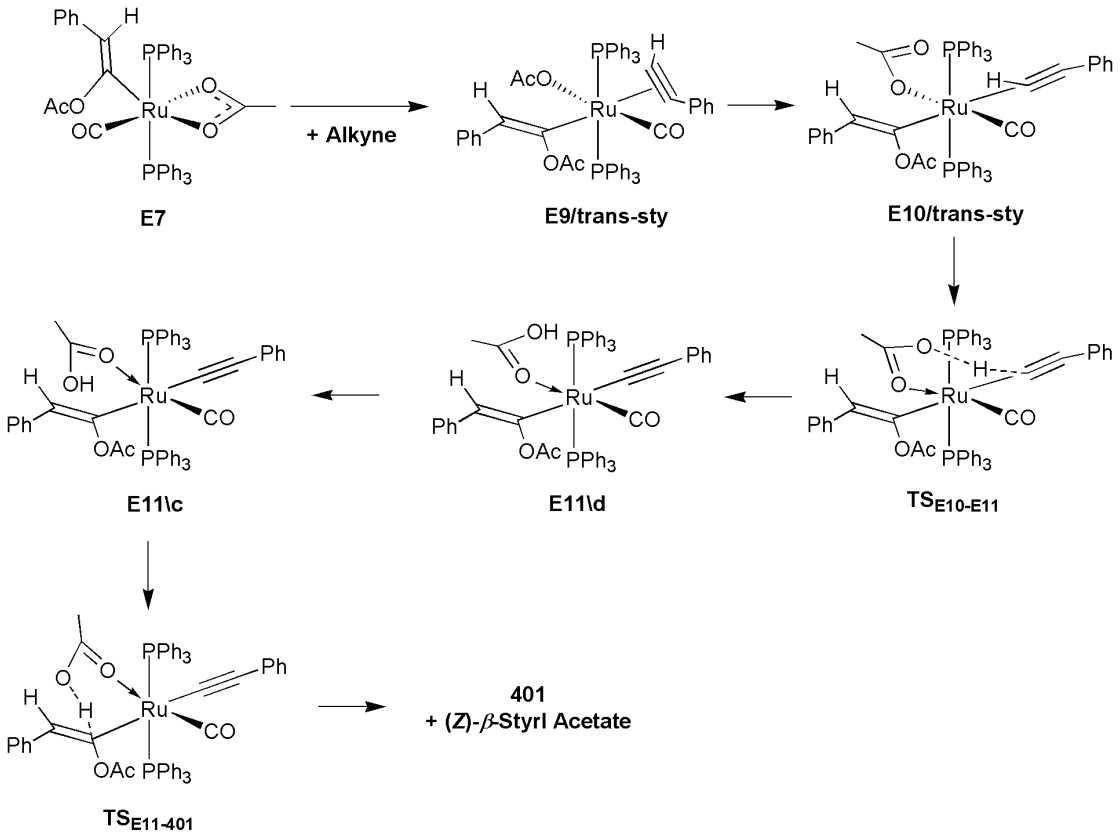

Figure 4.21 – Formation and loss of β-styryl acetate through a second LAPS mechanism.

A PES for the different mechanisms proposed above for protonation of the styryl-acetate M-C bond to form (*Z*)-*β*-styryl acetate is shown in Figure 4.22. Several stationary points could not be located on the PES, specifically the alkyne complex **E9/trans-sty** and the secondary LAPS deprotonation transition state **TS$_{E10-E11}$**. In terms of the mechanism, the acetic acid-mediated protonation of the styryl acetate M-C bond leading to state **302** *via* **TS$_{E8-302}$** is +53 kJ mol^{-1} relative to the initial starting complex **302**, but possess an energetic span of 117 kJ mol^{-1} from complex **E6/y**. With respect to protonation directly from the alkyne, **E9/trans-co** and σ-complex **E10/trans-co** are higher in energy than the transition state for acetic acid protonation at +61 and +35 kJ mol^{-1} relative to **302**, with the transition state **TS$_{E10-401}$** being +73 kJ mol^{-1} relative to **302**.

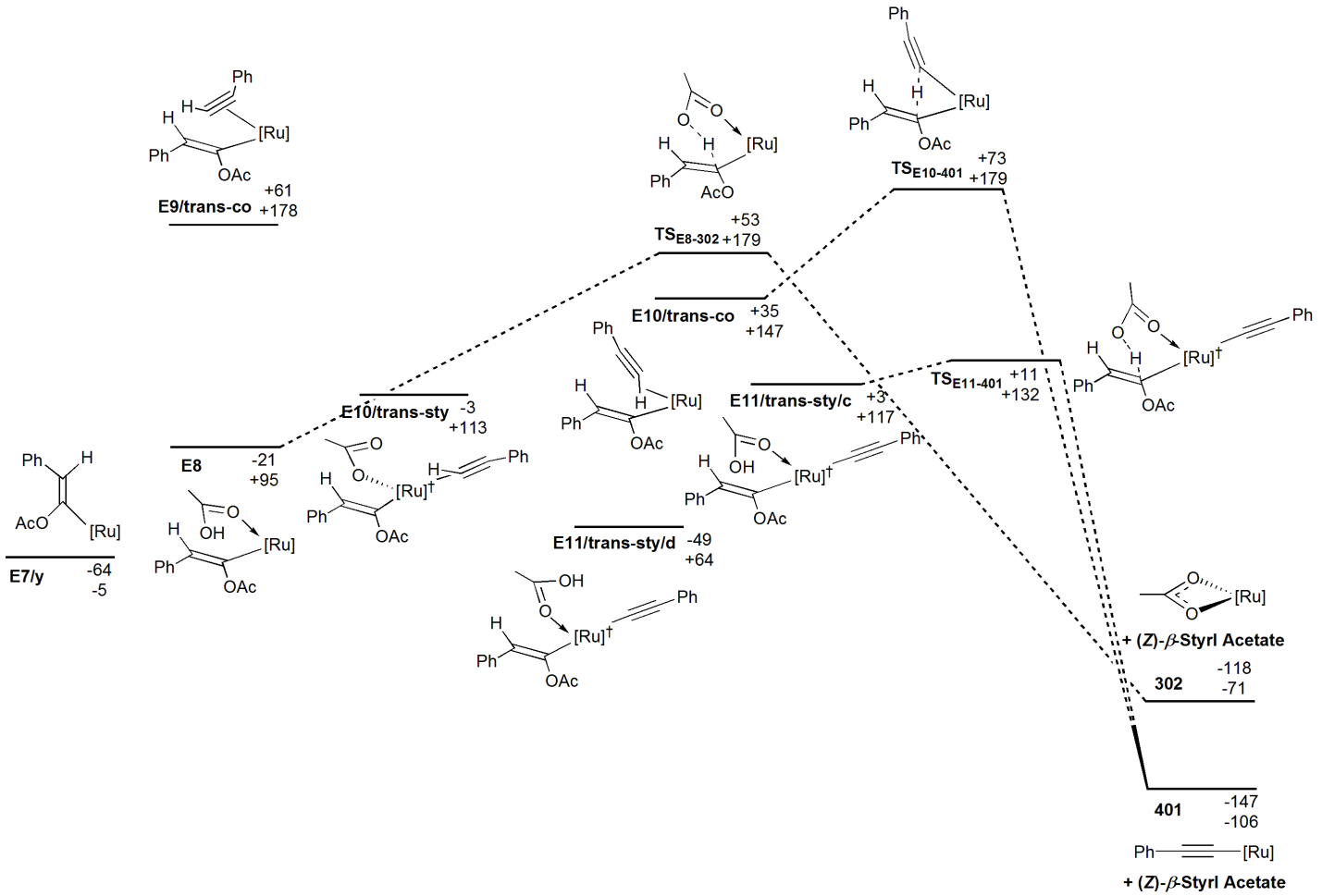

*Figure 4.22 – PES illustrating the formation of (Z)-β-styryl acetate from **E7**. Energies are ZPE corrected SCF (top) and Gibbs free (bottom) energies in kJ mol^{-1}, relative to **302**. [Ru] = [Ru(CO)(OAc)(PPh$_3$)$_2$], [Ru]† = [Ru(CO)(PPh$_3$)$_2$].*

The mechanism involving a second LAPS-type proton transfer after addition of a second equivalent of alkyne has low energy stationary points compared to the competing mechanisms, with **E10/trans-co**, **E11/trans-sty/d** and **E11/trans-sty/c** being found at -3, -49 and +3 kJ mol^{-1} relative to **302**, with the transition state $\mathbf{TS_{E11\text{-}401}}$ at +11 kJ mol^{-1}. The energetic span of this mechanism is 75 kJ mol^{-1}, compared to 117 kJ mol^{-1} for the purely acetic acid-mediated mechanism.

This pathway has the lowest overall energy compared with the other mechanisms, and the addition of a second equivalent of alkyne regenerates complex **401**, which is observed exclusively in the stoichiometric reaction as opposed to complex **302**. While **302** could be regenerated to react further to form **401**, the fact that a second equivalent of alkyne is required to form (*Z*)-*β*-styryl acetate indicates that this is the source of the proton.

In summary, the reaction between **302** and phenylacetylene is likely to proceed (at room temperature) to give complex **401** and free acetic acid *via* the first half of a LAPS mechanism. However upon heating the sample, acetic acid can coordinate to the metal and take part in the second step of a LAPS mechanism to protonate the acetylide ligand to form the vinylidene **E5**. Nucleophilic attack by an acetate ligand at the vinylidene C_α forms the metallo-enol ester **E6/y**, which then isomerises to form **E7** which contains a styryl-acetate ligand and a κ^2-acetate. From this, a second equivalent of alkyne coordinates to the complex *trans* to the styryl acetate group, which is deprotonated by an acetate ligand which then protonates the styryl-acetate Ru-C bond ultimately forming (*Z*)-*β*-styryl acetate and **401** (Figure 4.23).

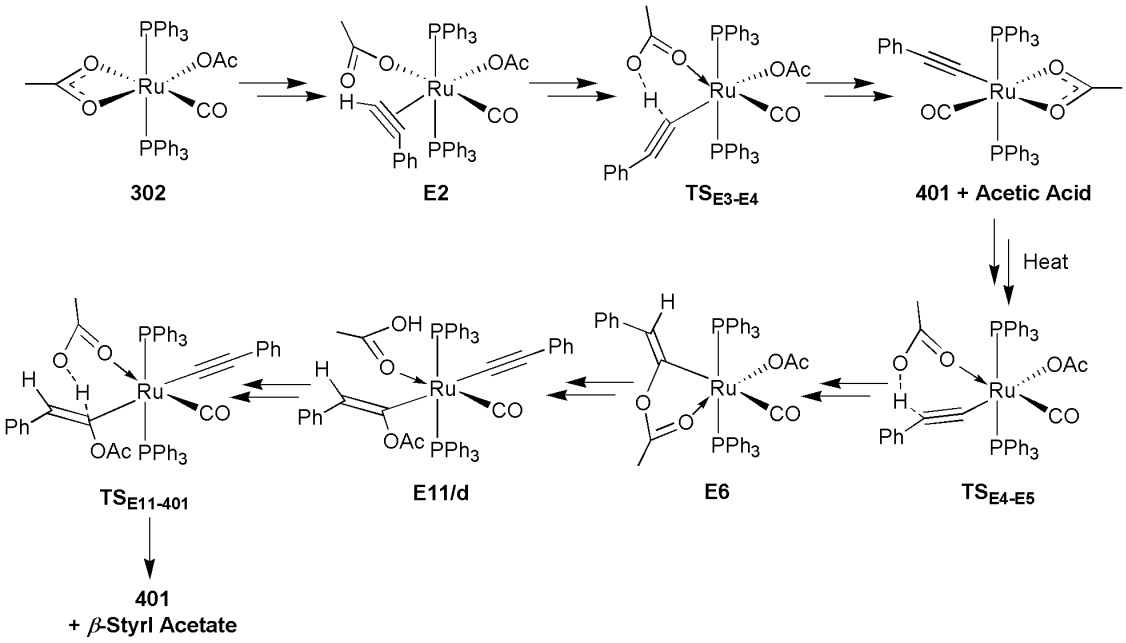

Figure 4.23 – Simplified reaction mechanism.

In relation to the energetic span, while **401** and acetic acid may be low in energy, in the formation of *β*-styryl acetate the TDI is in fact **E6/y**, with the TDTS being **TS$_{E11-401}$**, giving an energetic span of 105 kJ mol^{-1} for the entire reaction. However **E6/y** is not observed experimentally. This may be due to the high barrier of formation for **E6/y,** requiring the reaction to be heated at 323 K. Heating the reaction at this temperature would also allow the mechanism to proceed over the barrier to (*Z*)-*β*-styryl acetate formation, which is the overall thermodynamic minimum on the PES.

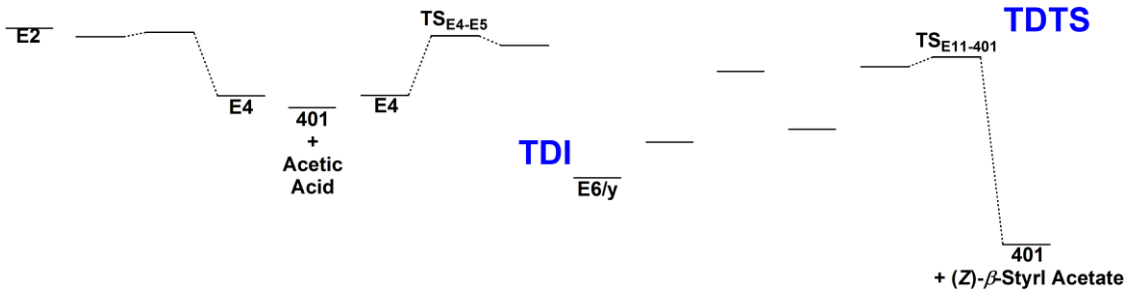

Figure 4.24 – Simplified PES with identification of TDI and TDTS.

*4.2.4 Mechanistic Investigation into Stereo Selectivity in the Formation of β-Styryl Acetate in the Reaction of **302** and Phenylacetylene*

In the stoichiometric reaction of **302** and two equivalents of phenylacetylene, there was a large degree of regio- and stereo-selectivity occurring, with the preference of anti-Markovnikov addition to the alkyne, as well as stereo-selective formation of the *Z* isomer of the *β*-styryl acetate product.

In terms of stereoselectivity, comparing the *E* and *Z* isomers of the *β*-styryl acetate product shows that the *E* isomer is 2 kJ mol^{-1} lower in energy in terms of ZPE corrected SCF and 5 kJ mol^{-1} lower in energy than the *Z* isomer in terms of Gibbs free energy. This suggests a very slight preference for the *E* isomer which does not explain experimental selectivity for the *Z* in both the stoichiometric and catalytic experiments from a thermodynamic perspective.

The prevalence of the *Z*-isomer must therefore be explained within the reaction mechanism itself *via* a kinetic effect. Stereoselectivity becomes a factor after formation of the vinylidene **E5**, with the orientation of the proton transfer transition state $\mathbf{TS_{E4\text{-}E5}}$ initially leading to a vinylidene conformation that would favour formation of the *E* isomer. The reaction mechanism outlined previously in section 4.2.3 assumed a vinylidene rotation in order to produce the pro-*Z* orientation of **E6/y** (Figure 4.25).

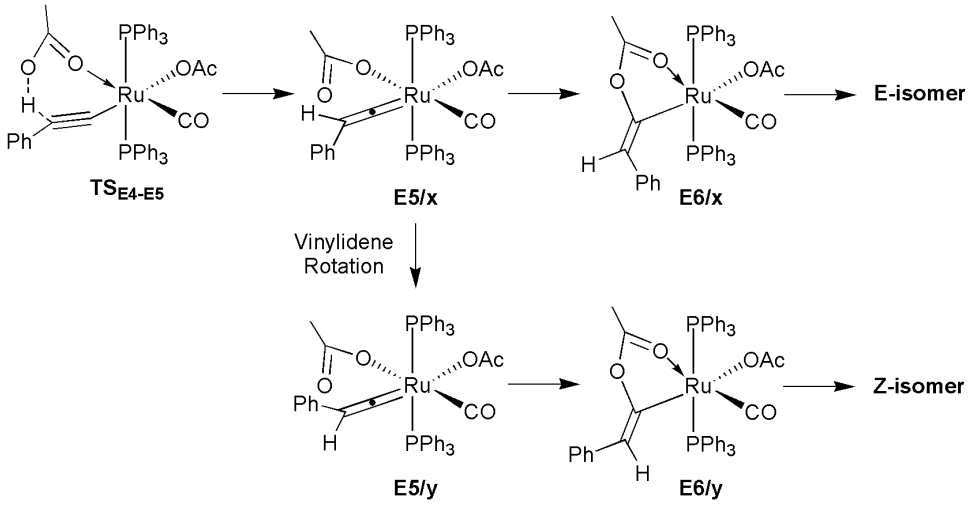

*Figure 4.25 – Stereoselectivity from **$TS_{E4\text{-}E5}$**.*

A direct optimisation of initial guess structures for **E5/x** and **E5/y** resulted in the formation of **E6/x** and **E6/y** during the optimisation (previous discussions used the geometry of **E5/b/x**). In order to optimise structures for the vinylidene **E5**, it was necessary to fix the vinylidene C_α-O distance to that seen in previous optimised acetate vinylidene complexes. These constrained optimisations suggested that the pro-*Z*-isomer **E5/y** of the vinylidene was much lower in energy (by 42 kJ mol^{-1}) than the pro-*E*-isomer **E5/x**.

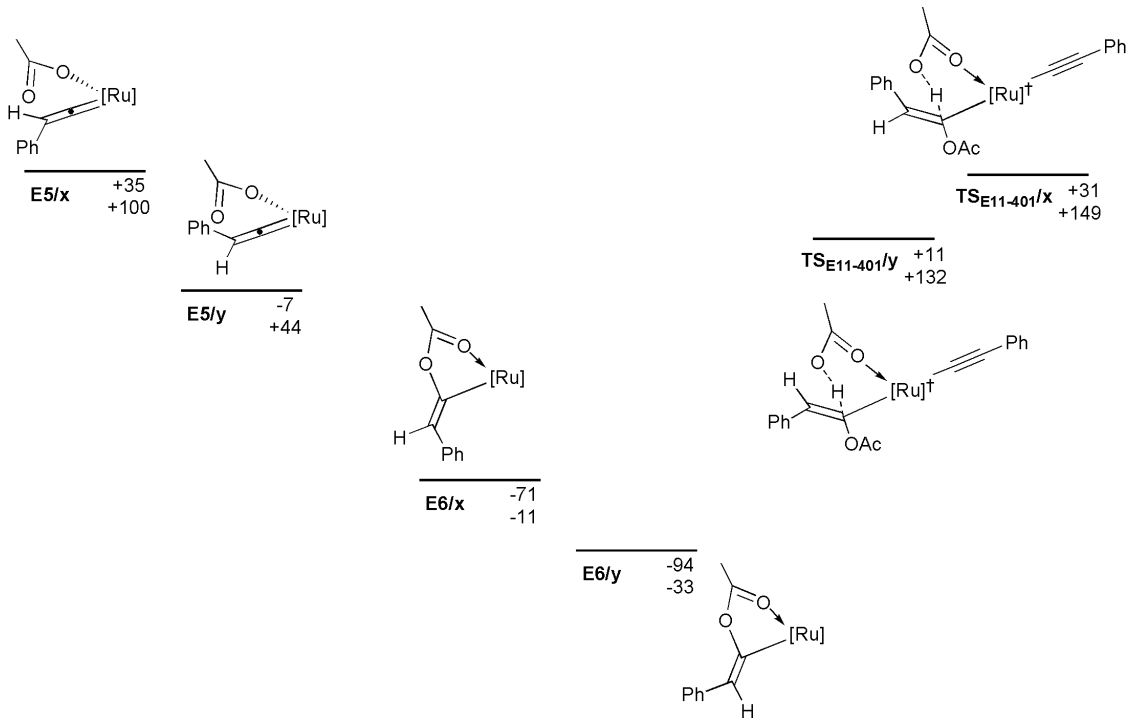

*Figure 4.26 – Relative energies of the stereoisomers of stationary points **E5**, **E6** and the TDTS **TS$_{E11-401}$**. Energies are ZPE corrected SCF (top) and Gibbs free (bottom) energies in kJ mol^{-1}, relative to **302**. [Ru] = [Ru(CO)(OAc)(PPh$_3$)$_2$], [Ru]† = [Ru(CO)(PPh$_3$)$_2$].*

Comparison of **E6/x** and **E6/y** showed a 23 kJ mol^{-1} preference for the *Z* isomer which can be explained largely by steric effects. As can be seen in Figure 4.27, the phenyl group in **E6/x** clashes with the carbonyl group which results in a distortion that leads to a non-planar geometry for the styryl group. **E6/y** possesses no steric clash and is therefore lower in energy. This steric clash is also visible in **E5/x**.

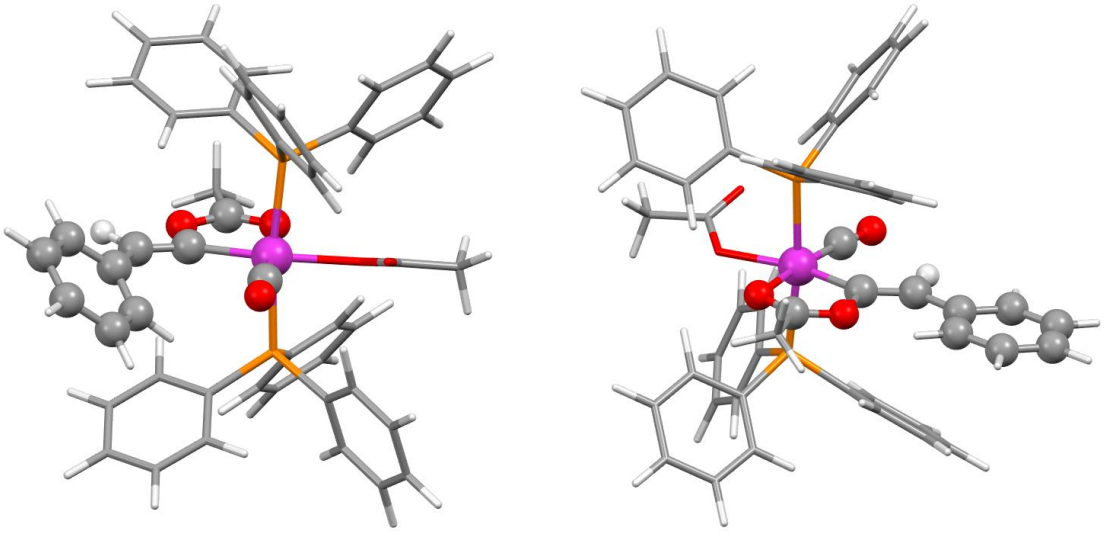

*Figure 4.27 – Optimised geometries of **E6/x** (left) and **E6/y** (right).*

Comparing the pro-*E* and pro-*Z* precursors of the TDTS of $\mathbf{TS_{E11\text{-}401}}$, a similar observation is also found, with the pro-*E* isomer $\mathbf{TS_{E11\text{-}401}}$**/x** being 20 kJ mol^{-1} higher in energy than the pro-*Z* isomer $\mathbf{TS_{E11\text{-}401}}$**/y**. Observing the optimised structures, this difference once again appears to be due to steric effects. As can be seen in Figure 4.28 the bulky phenyl and acetate groups are on either side of the vinyl ligand, limiting the space for the acetic acid. As a result the proton and acetate group are no longer co-planar, something which does not occur with the pro-*Z* isomer.

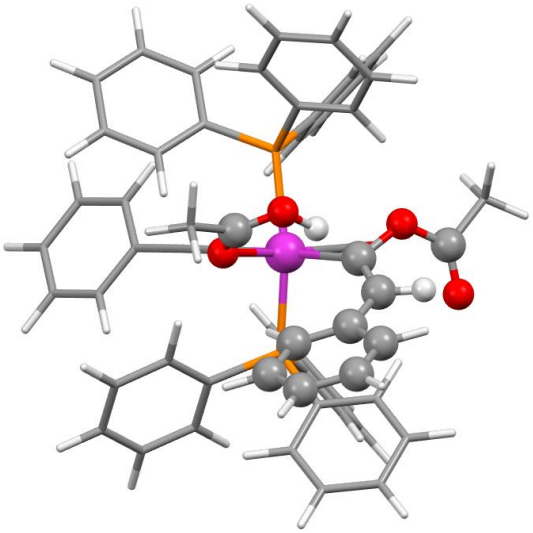

Figure 4.28 - Optimised structure of ***$TS_{E11\text{-}401}$/x****.*

The energetic span for formation of the *E* and *Z* isomer is 102 and 105 kJ mol^{-1} respectively, with the TDI = **E6** and TDTS = $\mathbf{TS_{E11\text{-}401}}$. This result shows a very slight preference for the (*E*)-*β*-styryl acetate of 3 kJ mol^{-1}, which is a small enough difference to be within error. Never the less, the lack of preference for (*Z*)-*β*-styryl acetate disagrees with what is seen experimentally. There are two possible reasons for this discrepancy. The first possibility is that the model does not accurately model the system, or that the preference with respect to the energetic span is too subtle to be described here. The second possibility is that the barrier to formation of **E6/x** from **E5/x** (where the acetate Ru-O bond is broken) is higher in energy than the vinylidene rotation that forms **E5/y**. However as the vinylidene rotation transition state could not be located, this hypothesis cannot be verified.

*4.2.5 Mechanistic Investigation into Regioselectivity in the Stoichiometric Formation of β-Styryl Acetate and 1-Phenylvinyl Acetate in the Reaction of **302** and Phenylacetylene*

While no Markovnikov product was identified in the stoichiometric reaction of **302** and two equivalents of phenylacetylene, catalytic studies revealed a second competing pathway to be present in the reaction leading to the formation of the Markovnikov-addition product 1-phenylvinyl acetate (Figure 4.29). While regioselectivity specific to substituent effects seen in the catalytic study will be discussed in more detail in section 4.2.6, the mechanism of Markovnikov addition will be investigated here.

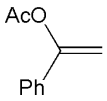

Figure 4.29 - 1-phenylvinyl acetate.

To form the Markovnikov product the acetate group must engage in nucleophilic attack at the non-terminal end of the alkyne group prior to vinylidene formation (similar to reactions observed by Dixneuf, Yi and others.[194, 197, 201]). Therefore, it is likely that Markovnikov addition of the acetate to the alkyne occurs prior to that of the LAPS deprotonation to form **401**.

During the alkyne-vinylidene tautomerization study seen in chapter 2, complex **A6** (Figure 4.34) was identified on the initial LAPS mechanistic PES (section 2.2.4).

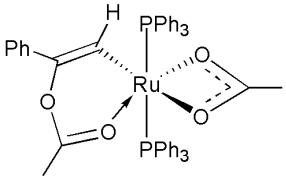

*Figure 4.30 – **A6**.*

Similarly, during the early stages of the investigation into the CO-LAPS mechanism, the geometry of the metallo-enol ester complex **E12** was optimised and is proposed to be an important state in the formation of the Markovnikov addition product (Figure 4.31). The geometry of the structure (Figure 4.31) suggested that formation of **E12** could occur from either complex **E2/y**, or **E3/y**.

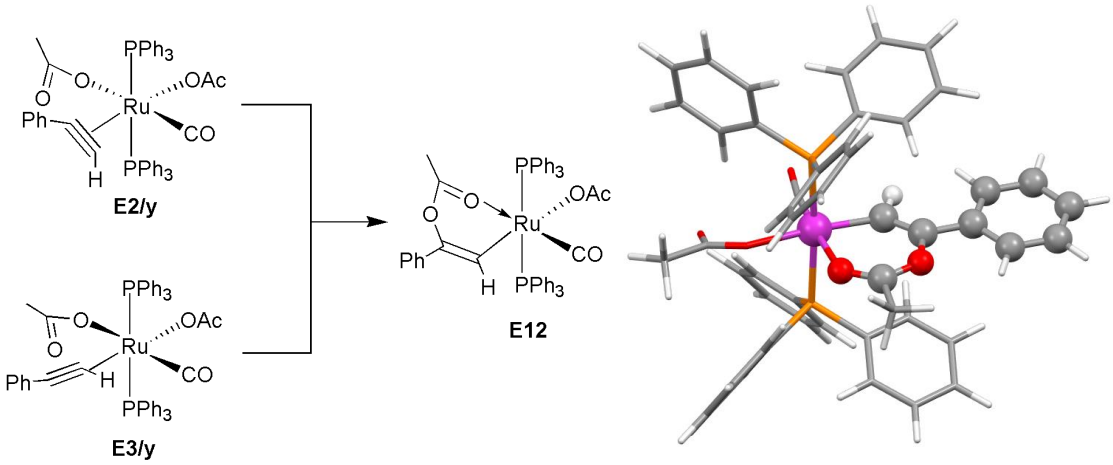

*Figure 4.31 – Formation of **E12** from either **E2/y** or **E3/y** (left) and optimised structure of **E12** (right).*

As can be seen below in the simplified PES in Figure 4.32, the energy of structure **E12** is significantly lower than that of **401** by 33 kJ mol^{-1}. Additionally the transition state for the formation of the vinylidene **E5** *via* $\mathbf{TS_{E4\text{-}E5}}$ is 93 kJ mol^{-1} higher in energy than **E12**. $\mathbf{TS_{E4\text{-}E5}}$ is proposed to be a transition state in the formation of the anti-Markovnikov product, with the comparative stability of the proposed Markovnikov addition intermediate **E12** indicating a preference for the Markovnikov-addition product which is not observed experimentally in the stoichiometric reaction. Therefore it is proposed that the pro-Markovnikov product mechanism must have a higher energy transition state in the formation of **E12**.

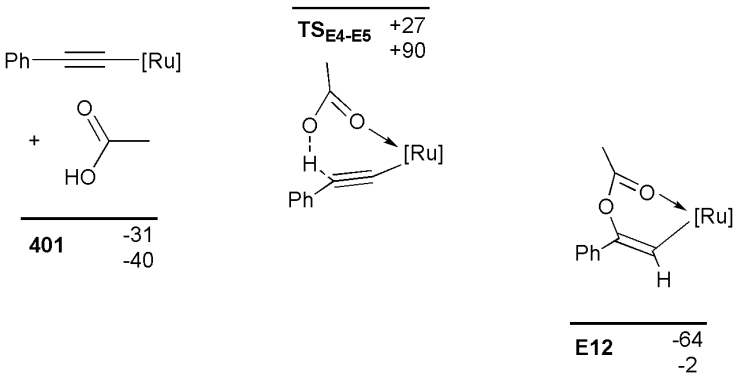

*Figure 4.32 – Comparison of the energy of **E12** to selected stationary points. Energies are ZPE corrected SCF (top) and Gibbs free (bottom) energies in kJ mol^{-1}, relative to **302**. [Ru] = [Ru(CO)(OAc)(PPh$_3$)$_2$].*

A transition state connecting either **E2/y** and **E3/y** to **E12** could not be located using the eigenvector following routine described in section 7.1. As such the reaction coordinate connecting **E2/y** and **E3/y** to **E12** was located using a linear transit approach (by incrementally lengthening the C_1-O_1 distance for complex **E12** and keeping this geometry fixed for the subsequent optimisation - Figure 4.33).

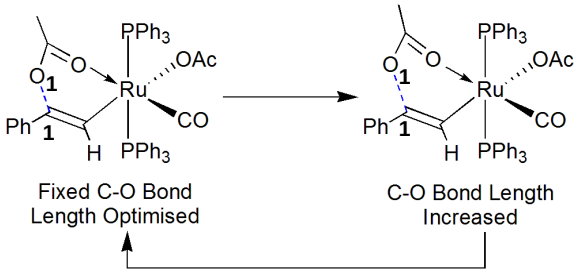

*Figure 4.33 – Linear transit approach method for the location of the transition state forming **E12**. The bond being lengthened is shown in blue.*

The energy profile shown below in Figure 4.34 shows that upon shortening the C-O distance (starting from a structure resembling **E2/y**) there is a 40 kJ mol^{-1} gain in energy, before the C-O bond length decreases and **E12** is formed, with this state (termed **TS$_{E2\text{-}E12}$**) possessing an imaginary frequency. Additionally the non-constrained optimised geometry of **E2/y** is 28 kJ mol^{-1} higher in energy than the previously reported isomer (**E2/x** in Figure 4.13) due to a steric clash between the phenyl and acetate groups. This further increases an already significant barrier to the Markovnikov addition process versus the anti-Markovnikov addition process.

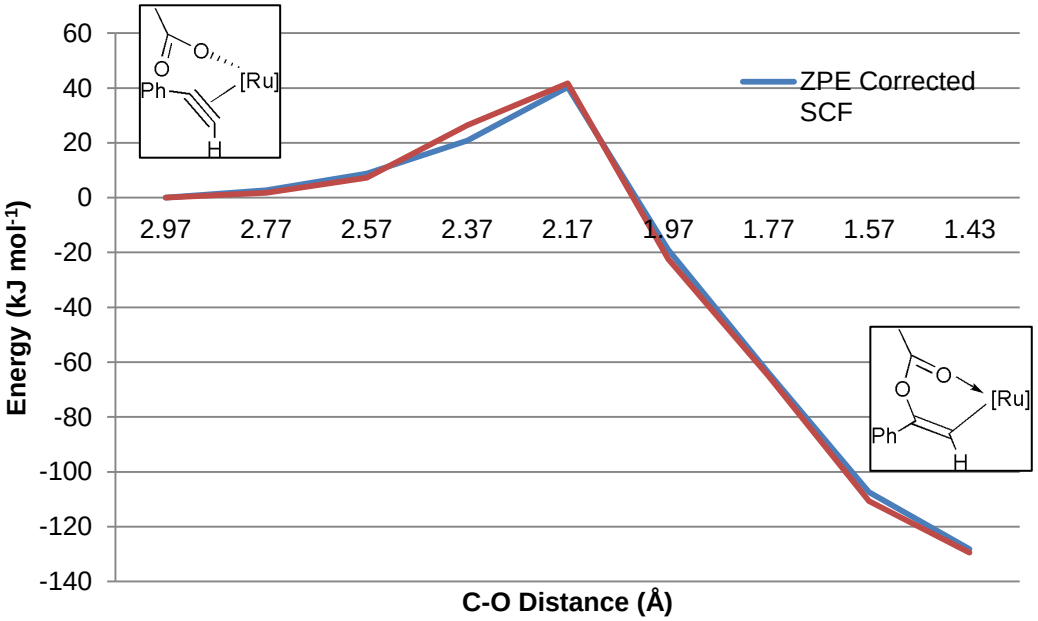

*Figure 4.34 – Energy profile for the lengthening of the C-O Bond in **E12**. Energies are ZPE corrected SCF (blue) and Gibbs free (red) energies in kJ mol^{-1}, relative to **E2/y**. [Ru] = [Ru(CO)(OAc)(PPh$_3$)$_2$].*

As can be seen in the comparative PES of the Markovnikov and anti-Markovnikov mechanisms (Figure 4.35), formation of the pro-Markovnikov intermediate **E12** has to overcome a barrier of 65 kJ mol^{-1} from **E2/x**, with an almost non-existent barrier to formation of **401**, agreeing with the exclusive experimental observation of **401** at room temperature. From **401**, the barrier to formation of **E12** is ca. +125 kJ mol^{-1}, whereas the barrier to formation of **E6/y** is ca. +60 kJ mol^{-1}. If **E12** and **E6/y** are to be considered as intermediates in the formation of the Markovnikov and anti-Markovnikov products respectively, this would agree with the experimental observation of exclusive anti-Markovnikov product formation.

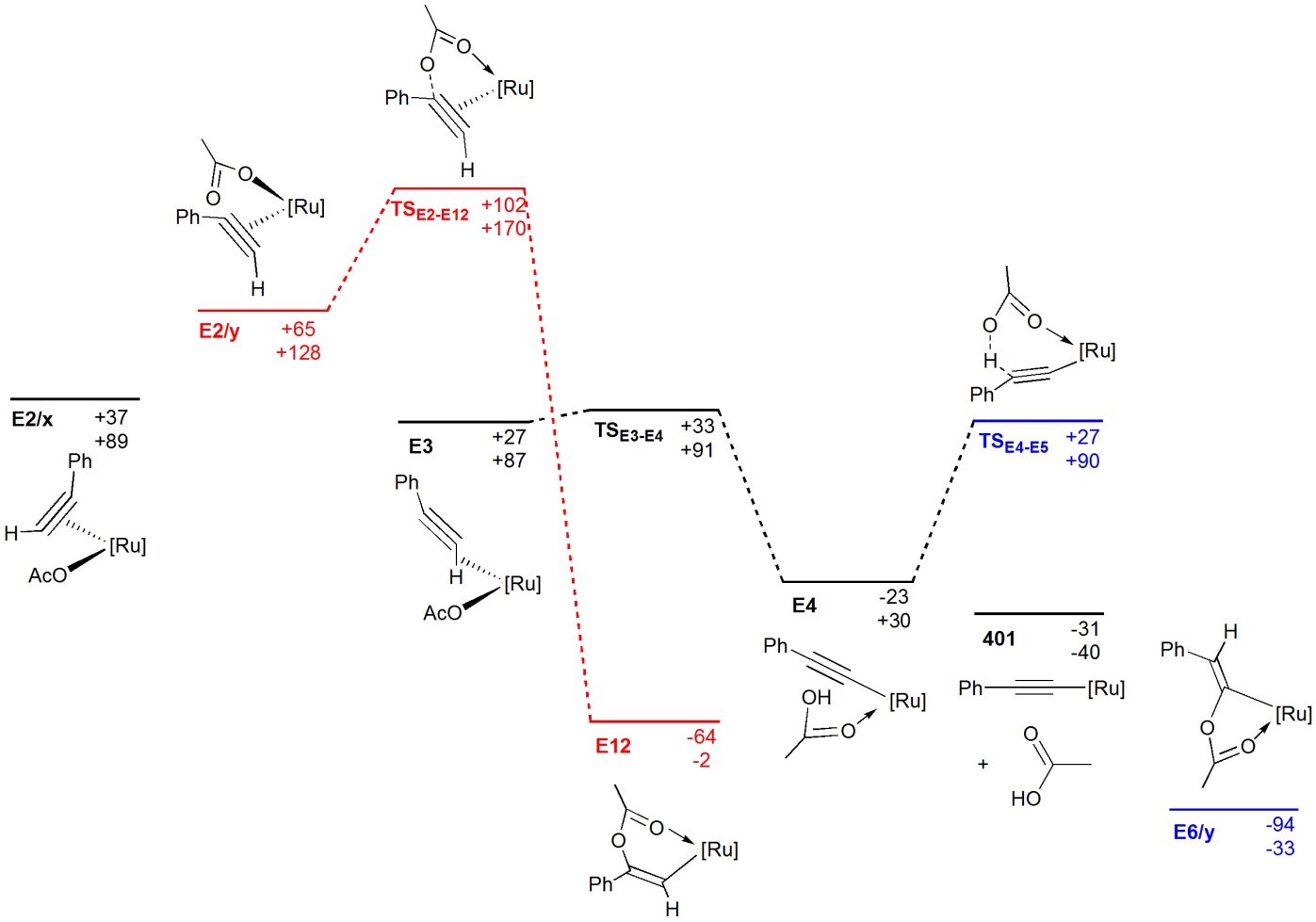

*Figure 4.35 – Simplified PES of Markovnikov (red) vs. anti-Markovnikov (blue) addition. Energies are ZPE corrected SCF (top) and Gibbs free (bottom) energies in kJ mol^{-1}, relative to **302**. [Ru] = [Ru(CO)(OAc)(PPh$_3$)$_2$].*

In order to investigate further, the formation of the Markovnikov product from stationary point **E12** was studied. As in the anti-Markovnikov addition pathway, protonation of the M-C bond must occur in order to liberate the α-styryl ester formed from Markovnikov addition of acetic acid to phenylacetylene to form the 1-phenylvinyl acetate product. In a similar manner to **E7** in the anti-Markovnikov addition pathway, the Ru-O bond in the metallo-enol ester ligand can break, as the other acetate group changes its binding mode from κ^1 to κ^2 (**E13**, Figure 4.36).

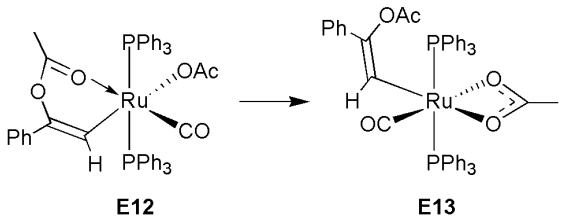

*Figure 4.36 - Formation of **E13** from **E12**.*

As before, there are three possible mechanisms for protonation of the M-C bond with subsequent liberation of the organic product and regeneration of **302** or **401**. The first mechanism involves coordination of acetic acid (**E14**), which subsequently protonates the M-C bond to form 1-phenylvinyl acetate and forms **302**. Alternatively the proton can originate from a second equivalent of alkyne by two different methods – either coordination of the alkyne *cis* to the α-styryl ester ligand with protonation into the M-C bond (**E15/trans-co** and $\mathbf{TS_{E16\text{-}401}}$), or *via* alkyne coordination trans to the α-styryl ester ligand, where the acetate ligand proceeds to deprotonate the terminal end of the alkyne, and protonate the M-C bond of the α-styryl ester ligand in a second LAPS-type mechanism (**E15/trans-sty**, **E17**, and $\mathbf{TS_{E17\text{-}401}}$). These pathways can be seen below in Figure 4.37, with a PES shown in Figure 4.38.

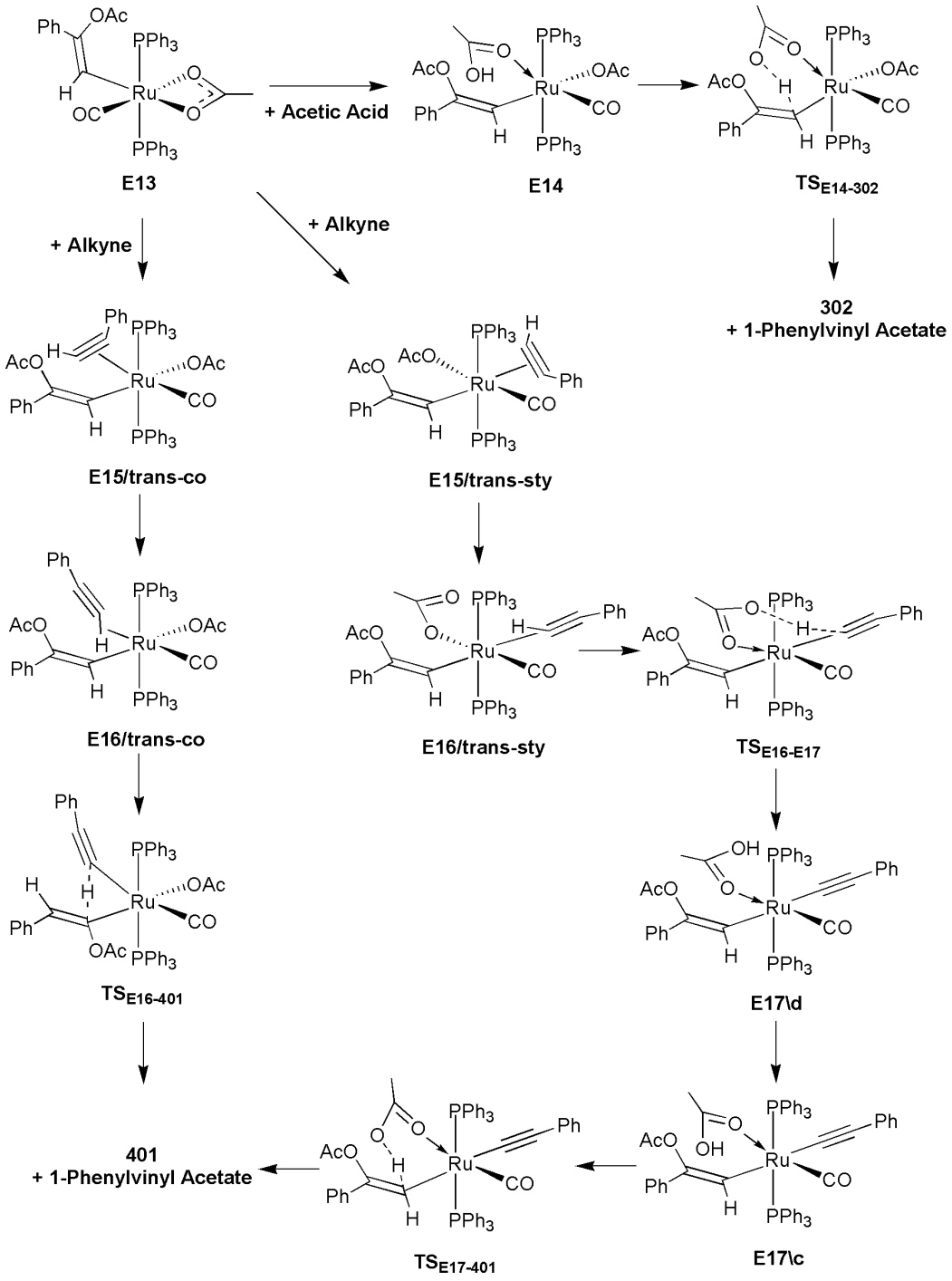

Figure 4.37 – Methods of forming 1-phenylvinyl acetate via three different protonation mechanisms.

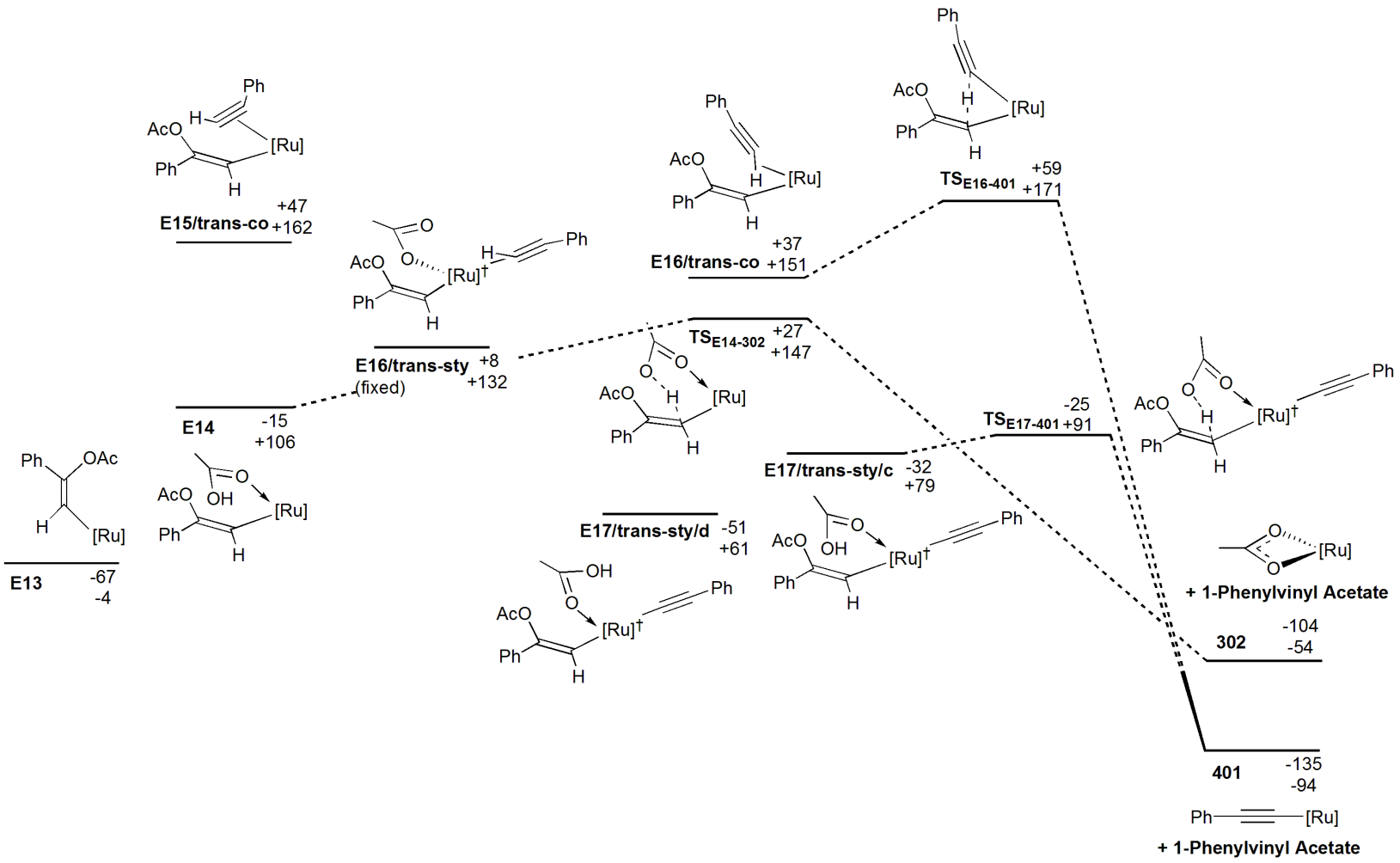

*Figure 4.38 – PES showing methods of forming 1-phenylvinyl acetate via protonation. Energies are ZPE corrected SCF (top) and Gibbs free (bottom) energies in kJ mol^{-1}, relative to **302**. [Ru] = [Ru(CO)(OAc)(PPh$_3$)$_2$], [Ru]† = [Ru(CO)(PPh$_3$)$_2$].*

Several stationary points could not be located on the PES, notably **E15/trans-sty** and **E16/trans-sty**, with all initial guess structures instead optimising to **E17**. An isomer of **E16/trans-sty** was located by fixing the agostic C-H bond distance, however this had two small imaginary frequencies of ca. -20 cm^{-1}. Additionally the alkyne protonation transition state $\mathbf{TS_{E16\text{-}E17}}$ could not be located.

In analysis of the protonation mechanisms from **E13**, the most favourable mechanism is the alkyne coordination (*trans* to the α-styryl ester ligand) and subsequent deprotonation by acetate, and protonation of the α-styryl ester ligand by acetic acid through $\mathbf{TS_{E17\text{-}401}}$. The energy of this transition state is +42 kJ mol^{-1} higher than **E13**, with transition states associated with acetic acid coordination and protonation ($\mathbf{TS_{E14\text{-}302}}$) and direct alkyne coordination and protonation ($\mathbf{TS_{E16\text{-}401}}$) of the α-styryl ester ligand being respectively +40 and +126 kJ mol^{-1} higher than **E13**. This means the second LAPS-type mechanism for protonation and liberation of the 1-phenylvinyl acetate is the lowest energy pathway for protonation.

The energy of the transition states $\mathbf{TS_{E14\text{-}302}}$ and $\mathbf{TS_{E17\text{-}401}}$ are significantly lower than the anti-Markovnikov isomers $\mathbf{TS_{E8\text{-}302}}$ and $\mathbf{TS_{E11\text{-}401}}$ by 25 and 36 kJ mol^{-1} respectively. This is believed to be due to an interaction between the acetic acid ligand and the ester group of the α-styryl ester ligand, which is shown in Figure 4.39. The electron density of the vinyl-acetate group is available to stabilise the proton due to its orientation in this TS - forming a hydrogen bond (2.55 Å). This interaction is unavailable in the analogous transition states seen in the anti-Markovnikov pathway.

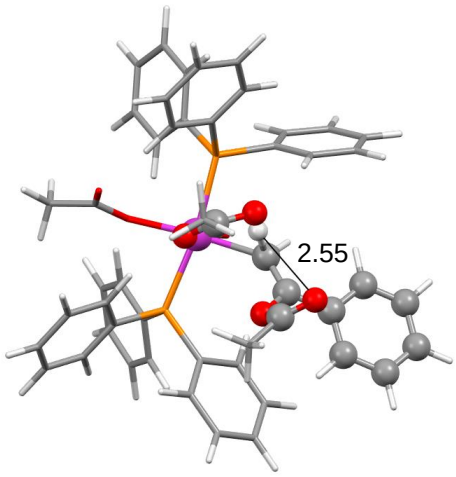

Figure 4.39 – Optimised geometry of $\mathbf{TS_{E14\text{-}302}}$*, showing ester-proton interaction.*

With respect to the energetic span, while the lowest point on the PES is **E13**, at -67 kJ mol^{-1} relative to **302**, the largest energetic span is between **401** (TDI) and **TS$_{E2-E12}$** (TDTS) at 133 kJ mol^{-1}. The energetic span for anti-Markovnikov addition forming the *β*-styryl acetate is 105 kJ mol^{-1} for (TDI = **E6/y**, TDTS = **TS$_{E11-401}$**)

This suggests that regioselectivity is dependent on the energetic span between **401** (TDI) and **TS$_{E2-E12}$** (TDTS). A simplified PES showing the TDI and TDTS for the Markovnikov and anti-Markovnikov mechanisms is shown below in Figure 4.40.

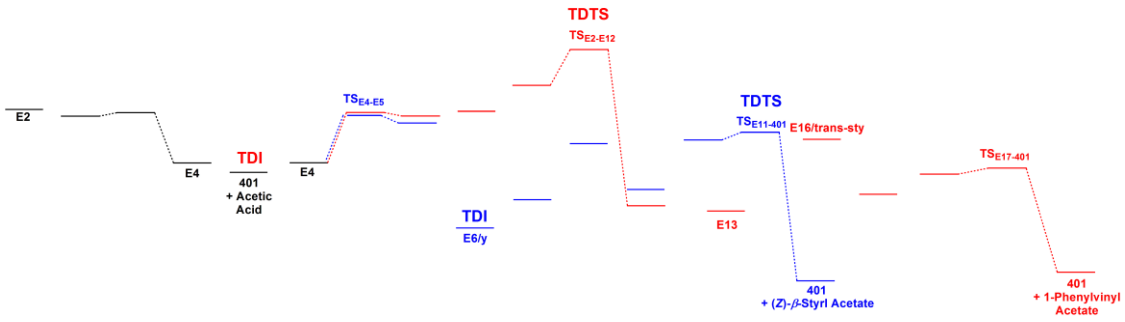

Figure 4.40 – Simplified PES showing energetic spans for the anti-Markovnikov (blue) and Markovnikov (red) pathways.

In summary the mechanism for formation of the Markovnikov product 1-phenylvinyl acetate has been identified. The mechanism proceeds from **401** to **E12** through a Markovnikov-type nucleophilic attack of the acetate at the phenyl-substituted alkyne carbon (**TS$_{E2-E12}$**). Protonation of the α-styryl ester ligand in **E13** occurs *via* addition of a second equivalent of alkyne, which is deprotonated by an acetate ligand. The formed acetic acid then protonates the M-C bond of the α-styryl ester ligand, forming 1-phenylvinyl acetate. The larger energetic span agrees with the preferential formation of the anti-Markovnikov product seen experimentally.

4.2.6 Substituent Effects on the Regio-Selectivity in the Catalytic Addition of Carboxylic Acids to Terminal Alkynes

During the catalytic investigation a number of terminal alkyne and carboxylic acid groups were investigated in relation to their effect on the Markovnikov and anti-Markovnikov regioselectivity. This section shall focus on providing a theoretical explanation for the variation seen in the regio-selectivity of the catalytic reaction using the energetic span model. The different systems studied can be seen below in Table 4.4, which includes the ratio of Markovnikov to anti-Markovnikov addition products, as well as the substituents used in the theoretical study.

Table 4.4 – Studied systems with regioselective ratios and theoretical nomenclature

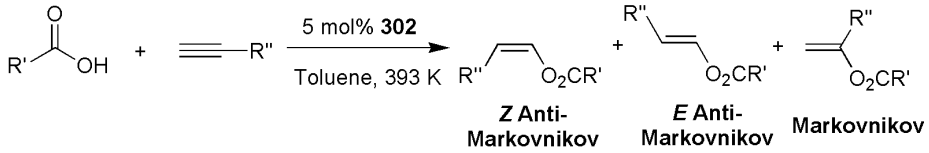

System Name	R' (Carboxylic Acid)	R'' (Alkyne)	Experimental Anti-Markovnikov : Markovnikov Ratio
E	Me	Ph	100 : 0[†]
F	Me	C_6H_4-*p*-CF_3	100 : 0 (where R' = Ph)
G	Me	C_6H_4-*p*-OMe	4 : 96 (where R' = Ph)
H	Me	C_6H_4-*p*-CH_2OH	-
I	Me	C_6H_4-*p*-NMe_2	2 : 98 (where R' = Ph)
J	C_6H_5	Ph	85 : 15
K	C_6H_4-*p*-CF_3	Ph	18 : 82
L	C_6H_4-*p*-OMe	Ph	79 : 21
M	C_6H_4-*p*-NMe_2	Ph	96 : 4

([†] - further results reported the observation of the Markovnikov product)

It was proposed in the previous section, that regio-selectivity is dependent upon the energetic span of the Markovnikov mechanism (TDI = **401**, TDTS = $\mathbf{TS_{E2\text{-}E12}}$). Therefore these two isomers were calculated with the substituent combinations seen in Table 4.3. A scheme of all substituents is shown below in Figure 4.41.

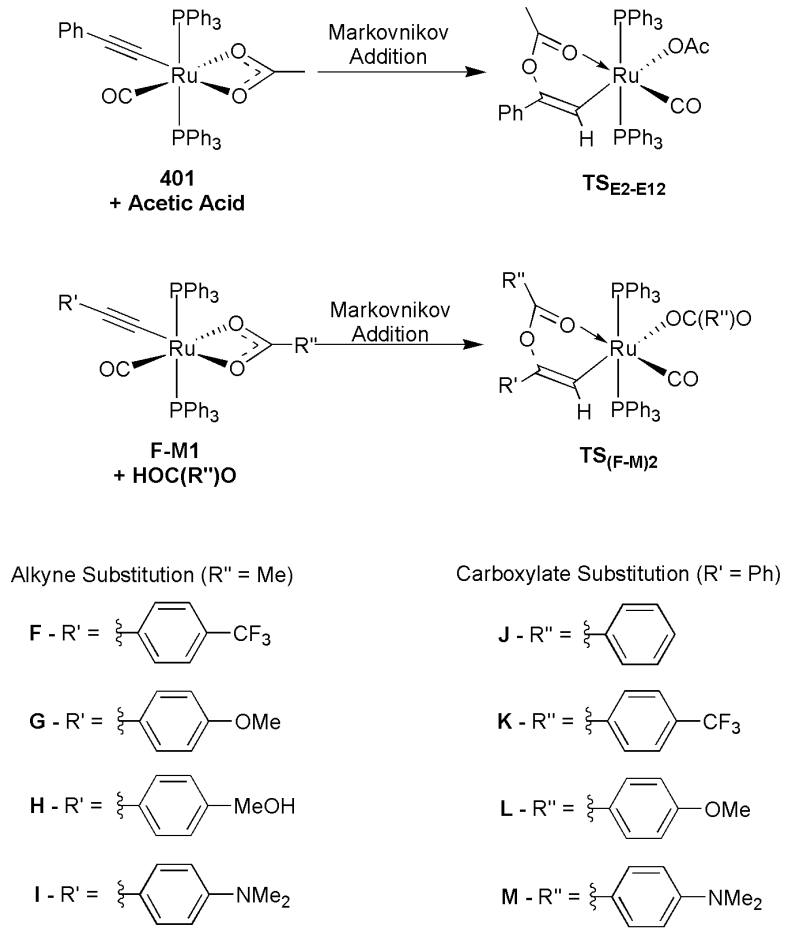

Figure 4.41 – Regioselective TDI and TDTS for the Markovnikov addition energetic span.

In the PES shown in Figure 4.42, the energetic spans for the Markovnikov mechanism have a range of 34 kJ mol^{-1} for the alkyne substituents **E** and **I**, and 26 kJ mol^{-1} for the acetate substituents **J** and **M**, showing a significant difference for both. **G** and **I** were shown to be selective for the Markovnikov product, which is consistent with the smaller barrier for $\mathbf{TS_{G2}}$ and $\mathbf{TS_{I2}}$. Conversely **E** and **F** were shown to have selectivity for the anti-Markovnikov product, which is mirrored in the higher barrier of $\mathbf{TS_{E2\text{-}E12}}$ and $\mathbf{TS_{F2}}$. While no experimental results exist for **H**, the relative height of the TDTS would suggest significant Markovnikov selectivity.

With respect to the carboxylate substituents a pattern was also observed, with the size of the energetic span decreasing in the order **M** – **J** – **L** – **K**, matching the order of anti-Markovnikov product ratio seen experimentally. While $\mathbf{TS_{J3}}$ and $\mathbf{TS_{L3}}$ differ by only 1 kJ mol^{-1}, there appears to be a general correlation with the TDTS and the experimental product ratios. A summary of the energetic spans against regioselectivity is shown in Table 4.5.

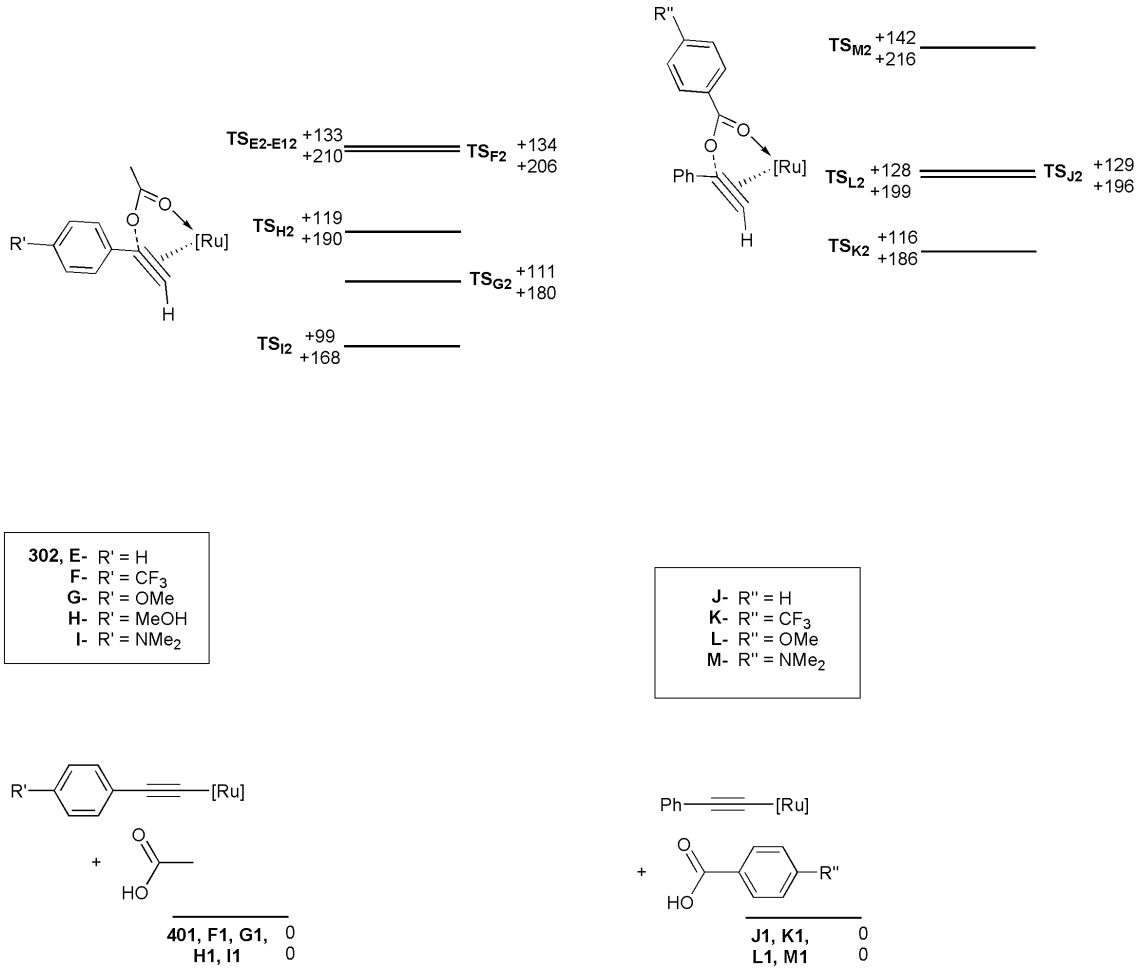

Figure 4.42 – Substituted Markovnikov TDTS and TDI. Energies are ZPE corrected SCF (top) and Gibbs free (bottom) energies in kJ mol^{1}. [Ru] = [Ru(CO)(OAc)(PPh$_3$)$_2$].

Table 4.5 – Studied systems with theoretical nomenclature, regioselective ratios and energetic spans

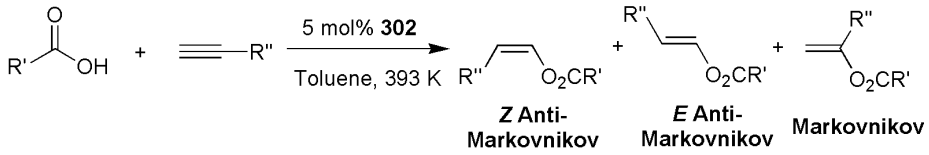

System Name	R' (Carboxylic Acid)	R'' (Alkyne)	Experimental Anti-Markovnikov : Markovnikov Ratio	Energetic Span (kJ mol^{-1})
E	Me	Ph	100 : 0	133
F	Me	C_6H_4-*p*-CF_3	100 : 0 (where R' = Ph)	134
G	Me	C_6H_4-*p*-OMe	4 : 96 (where R' = Ph)	111
H	Me	C_6H_4-*p*-CH_2OH	-	119
I	Me	C_6H_4-*p*-NMe_2	2 : 98 (where R' = Ph)	99
J	C_6H_5	Ph	85 : 15	129
K	C_6H_4-*p*-CF_3	Ph	18 : 82	116
L	C_6H_4-*p*-OMe	Ph	79 : 21	128
M	C_6H_4-*p*-NMe_2	Ph	96 : 4	142

PABOON charges were obtained for all isomers of the Markovnikov transition state (**TS_{E2-E12}**), with a key and table shown in Table 4.6. Correlation between regioselectivity and charges was seen with C_1 and C_5 in varying the carboxylate and alkyne groups respectively. For systems **E**-**I**, higher regioselectivity for the formation of the Markovnikov product roughly correlates with a smaller positive charge on C_5. This suggests that more electron density is available within the aromatic ring to stabilise C_4, consistent with a typical Markovnikov addition where more electron donating substituents stabilise the carbon centre - facilitating addition.

For systems **J**-**M** where the carboxylate group was varied, a higher ratio of Markovnikov addition roughly correlates with a more positive charge on C_1, suggesting that C_1 is stabilising the acetate group by decreasing the electron density present on the ligand.

Table 4.6 – PABOON charges against regioselective ratio

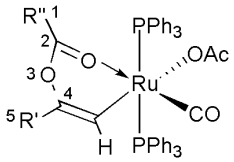

System Name	Experimental Anti-Markovnikov : Markovnikov Ratio	PABOON Charge (C_1)	PABOON Charge (C_5)
E	100 : 0[†]	-0.21	+0.12
F	100 : 0 (where R' = Ph)	-0.23	+0.08
G	4 : 96 (where R' = Ph)	-0.23	+0.05
H	-	-0.23	+0.06
I	2 : 98 (where R' = Ph)	-0.23	+0.05
J	85 : 15	+0.00	+0.05
K	18 : 82	+0.01	+0.05
L	79 : 21	-0.02	+0.06
M	96 : 4	-0.02	+0.06

([†] - further results reported the observation of the Markovnikov product)

In summary the variation in regioselectivity seen upon changing the chemistry of both the carboxylic acid and alkyne groups has been investigated theoretically. It has been shown that the energetic span between **401** and $\mathbf{TS_{E2\text{-}E12}}$ as well as the charges located on the different substituents correlates well with the experimental ratios of Markovnikov to anti-Markovnikov addition.

4.2.7 Summary

In this chapter reaction of **302** with an alkyne has been investigated both theoretically and experimentally. The mechanism was shown to proceed through a variant of the LAPS mechanism (chapter 2), and is termed CO-LAPS due to the presence of a carbonyl ligand on the metal centre. While the LAPS mechanism was found to produce a vinylidene complex at room temperature, reaction of the complex **302** produces the acetylide **401**. This was explained theoretically by a partial LAPS mechanism, where deprotonation of the alkyne by an acetate ligand led to the formation of a metal acetylide which subsequently loses acetic acid to form the stable intermediate **401**.

The application of heat during experimental studies produced (*Z*)-*β*-styryl acetate, with theoretical studies showing that this product is formed *via* the vinylidene intermediate **E5** which subsequently forms the metallo-enol ester **E6**. The relatively high barrier to protonation of the C_β of **401** (+ 58 kJ mol^{-1} from **401**), as well as the significantly lower energy of **E6** compared to the vinylidene isomer **E5**, is proposed to be the reason as to why no vinylidene is observed in this system.

The formation of the acetylide **401** and free acetic acid differs to the reaction of **201** and phenylacetylene which forms a metal vinylidene (chapter 2). This may be due to the *trans* effect of the carbonyl ligand, which causes the elimination of the acetic acid ligand. Additionally two π-acceptor ligands may also be the reason **E5** is higher in energy than **401**.

Protonation of the M-C bond of the styryl acetate ligand in **E13** is proposed to initially proceed *via* the coordination of a second equivalent of alkyne *trans* to the *β*-styryl acetate ligand. An acetate group then deprotonates the alkyne, forming acetic acid when then protonates the styryl-acetate ligand forming free *β*-styryl acetate and **401**. This explains the exclusive observation of **401** experimentally in the stoichiometric reactions.

Stereoselectivity in the formation of (*Z*)-*β*-styryl acetate and (*E*)-*β*-styryl acetate could not be determined theoretically. In terms of regioselectivity in the formation of the Markovnikov and anti-Markovnikov addition products 1-phenylvinyl acetate and *β*-styryl acetate, this is shown to be dictated by the energetic span between **401** and $\mathbf{TS_{E2\text{-}E12}}$, which showed a correlation between the spans and what was seen experimentally.

5. Mechanistic Investigations into the Direct Alkenylation of Pyridine and Pyridine-like Substrates *via* a Half-Sandwich Ruthenium Complex

5.1 Introduction

In this chapter an investigation into pyridine alkenylation *via* a catalytic half-sandwich ruthenium complex shall be reported (Figure 5.1). While diverging from the *bis*-acetate ruthenium complexes seen in chapters 2-4, the metal vinylidene complex employed has a significant role in formation of the substituted pyridine.

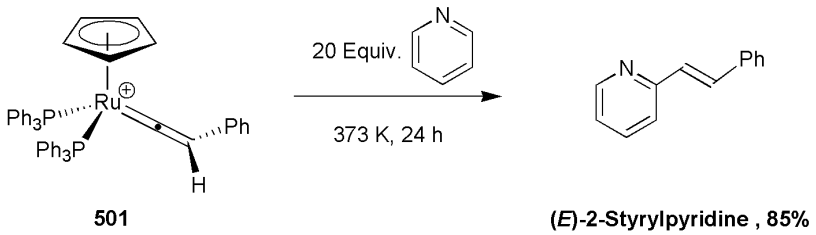

501 **(*E*)-2-Styrylpyridine , 85%**

Figure 5.1 – ***501****.*

Not only does this reaction display excellent regio- and stereoselectivity, but it is shown to progress from unsubstituted pyridine, with potential for 100% atom efficiency. The study and improvement of this system have great implications for natural product and pharmaceutical synthesis, and as such a joint experimental and theoretical investigation was undertaken to investigate the nature of this system.

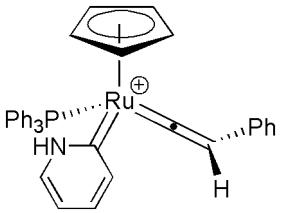

Figure 5.2 – Metal pyridylidene complex.

This chapter shall report on the mechanistic details of the system, observed stereoselectivity, and substituent effects. Additionally the chemistry of pyridylidenes – a relatively unexplored class of metal complexes which take part in the mechanism – will be investigated.

5.1.1 Formation of Substituted Pyridine Molecules

Pyridyl and other substituted N-heterocyclic 6 membered rings are found in a wide array of natural products, pharmaceutical compounds[237] and synthetic building blocks,[238] with the examples below in Figure 5.3 being worth millions of dollars in annual turnover. With pyridine groups being so ubiquitous in useful applications, the direct functionalization of pyridine would be preferential. However examples of using unactivated pyridine as a feedstock in substitution reactions are rare.

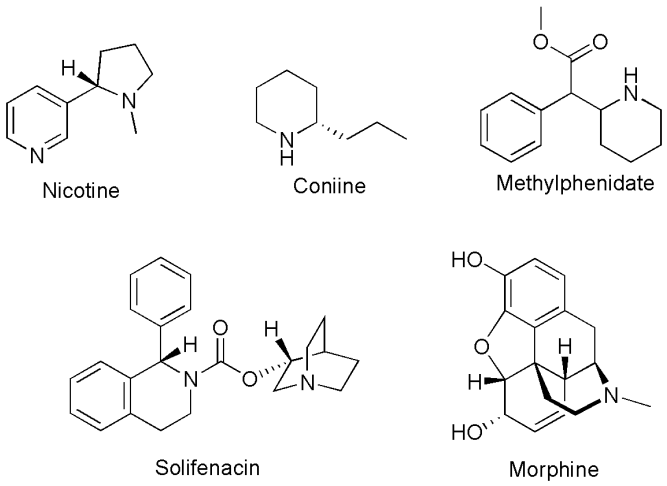

Figure 5.3 - Examples of drugs containing N-heterocyclic groups.

Pyridine itself is a six membered aromatic ring containing a nitrogen group. The aromaticity is supported by a nitrogen π-bond, with the remaining lone pair donating out of the ring, making pyridine basic with a pKa of 5.2 in water. Due to the electronegativity of the nitrogen group there is less electron density present in the aromatic structure than for other aromatic systems such as benzene, meaning electrophilic substitution for pyridine is comparatively slower. Also due to the presence of the nitrogen group, substitution is preferred at the *meta* position. As can be seen in Figure 5.4, the *meta* position is the most stable due to the positive charge of the intermediate being located on the carbon, as opposed to nitrogen with the *ortho* and *para* positions.[239]

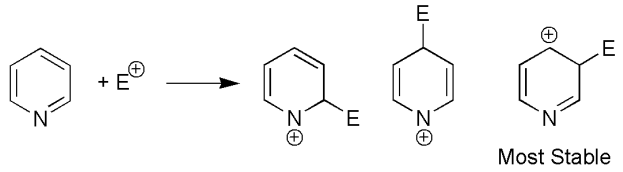

Figure 5.4 – Preference of pyridine substitution at the meta-position.

Due to the lower π electron density, pyridine is likelier to undergo nucleophilic addition than benzene. However substitution reactions involving unsubstituted pyridine require a hydride atom to be a leaving group. As this is unfavourable, pyridine is normally augmented with a more favourable leaving group such as a halogen in order to improve the rate of the reaction.[239]

Examples of electrophilic addition of halogens can occur with molecular chlorine and pyridine at the 2-position,[240] or *via* an aluminium trichloride catalyst at the 3-position[241] for chlorination. For bromination the use of bromine in oleum,[242] or bromine chloride[243] can produce 3 and 2-bromopyridine respectively. Fluoropyridine can be produced through substitution of pre-existing chloropyridines.[244]

Once formed, halogenated pyridines can undergo a large array of reactions, involving reagents such as organolithium compounds, amines and sulfur- and oxygen- based nucleophiles.[239] Typically, the reaction is driven by the electronegativity and leaving group affinity, with fluoropyridine being the most facile halogen leaving group.[245] An example shown below involves the formation of 2-styrylpyridine *via* Suzuki cross-coupling (Figure 5.5).[246]

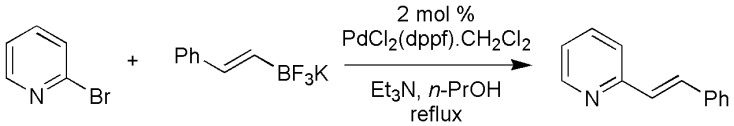

Figure 5.5 – Formation of 2-styrylpyridine from 2-bromopyridine.

Another example of forming substituted pyridines involves the use of pyridine N-oxides, which can then be used in conjunction with Grignard reagents or *via* C-H activation with palladium to induce pyridine alkenylation. Pyridine itself must first be oxidised which can be achieved with a ruthenium trichloride catalyst under an oxygen atmosphere,[247] or originally by oxidation with peracids[248] being two of many examples.[249, 250]

Once formed, the activated pyridine group can react in several ways. The first example involves Grignard reagents, of which the first reported instance in 1965 involved arylation *via* phenylmagnesium bromide[251] with many similar reactions also being reported.[252, 253]

A second example involves using a palladium catalyst to induce C-H activation resulting in addition to the pyridine ring,[254] with Fagnou *et al.* having showed several examples of arylation of pyridine groups with this method,[121, 255, 256] with additional examples of alkenylation having also been found.[257] One relevant example of pyridine alkenylation *via* pyridine N-oxides, is the formation of 2-methylpyridine shown below in Figure 5.6.[258]

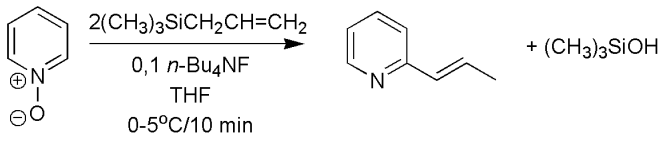

Figure 5.6 – Formation of 2-methylpyridine from pyridine N-oxide.

While the examples above do not encompass the entire field of pyridine functionalization, they do represent the typical expense in terms of reagent preparation, and environmentally unfriendly waste materials. Functionalization of pyridine has been reported using transition metal complexes such as ruthenium,[259, 260] palladium,[261] and rhodium,[262, 263] however the use of unsubstituted pyridine is still very much an unexplored method.

This chapter shall focus on the formation, mechanism and intricacies of an atom-efficient direct alkenylation of pyridine *via* a half-sandwich ruthenium vinylidene complex. Metal vinylidenes are known for atom-efficient catalysis in an array of reactions,[264] with pyridine alkenylation allowing for precursors of important biological and drug molecules to be synthesised easily, and without the aforementioned problems associated with 'traditional' pyridine functionalization.

5.1.2 A Novel Ru-Catalysed Method for the Alkenylation of Pyridine

This chapter is founded upon initial research described in a 2003 paper published by Murakami and Hori.[265] In this publication a half sandwich ruthenium vinylidene complex [CpRu(PPh_3)$_2$(CCHPh)] (**501**) was prepared using a literature method from [CpRu(PPh_3)$_2$Cl],[137] which when reacted with 20 equivalents of pyridine at 373 K for 24 hours produced 2-styrylpyridine with a yield of 85% and selective formation of the *E* isomer (Figure 5.7). The authors also reported an 87% yield of (*E*)-2-styrylpyridine by reacting [CpRu(PPh_3)$_2$Cl] directly with 1-trimethylsilyl-2-phenyl acetylene and pyridine (Figure 5.8).

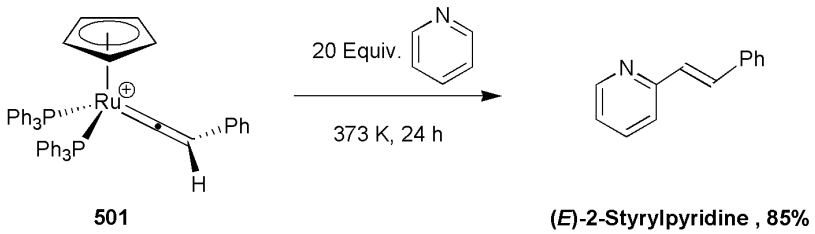

Figure 5.7 - Basic outline of the Murakami and Hori reaction.

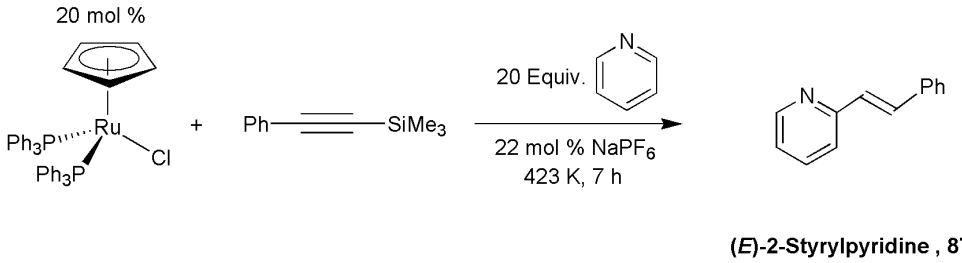

Figure 5.8 – Reaction of [CpRu(PPh_3)$_2$Cl] with 1-trimethylsilyl-2-phenyl acetylene and pyridine.

There were several experimental observations that may shed light on the mechanism of this reaction. The first involved a bi-dentate phosphine analogue of **501**, which failed to react under similar conditions indicating that the loss of a triphenylphosphine ligand may be important for the reaction. Secondly, the acetylide [CpRu(PPh_3)$_2$(CCPh)] (**502**), also failed to react with pyridine. Finally, heating the independently-prepared *Z*-isomer of 2-styrylpyridine at 398 K with the precursor to **501** – [CpRu(PPh_3)$_2$Cl], produced the *E*-isomer, with the authors proposing that overall *E*-selectivity could occur after formation of the *Z*-isomer.

On the basis of this experimental evidence, the authors proposed a possible mechanistic pathway (Figure 5.9). The assumption that a triphenylphosphine ligand is lost over the course of the reaction and that a pyridine molecule must coordinate to the metal centre for the reaction to progress indicated that the first point in the mechanism could be complex **503**. The ortho-position of the pyridine and the C_α of the vinylidene could then undergo a [2 + 2] cycloaddition to form **504**. Subsequent deprotonation could form **505**, with protonation of the Ru-C bond leading to formation of the styrylpyridine product and an assumed regeneration of **503**.

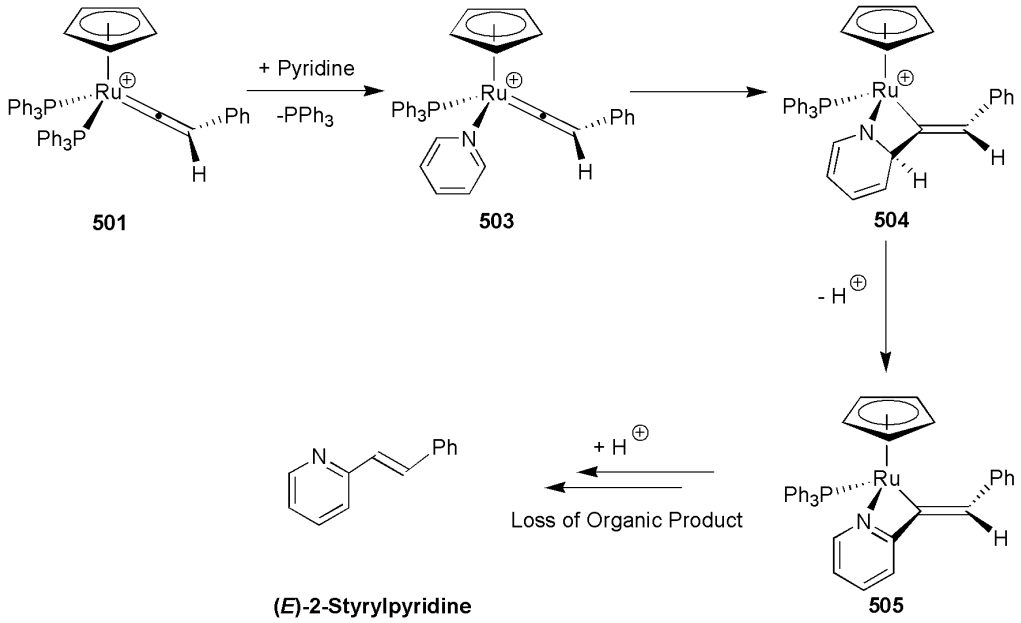

Figure 5.9 – Initially proposed mechanism of pyridine alkenylation.[265]

The authors also looked at a range of vinyl and pyridyl substituents, and with the exception of 2-(2-cyclohexyl-vinyl)-pyridine which had a 2:1 *E:Z* ratio, all reactive alkynes produced yields with 100% *E*-isomer selectivity. In terms of pyridyl regioselectivity, the authors performed reactions with a 1-trimethylsilyl-2-phenyl acetylene, $[CpRu(PPh_3)_2Cl]$ and either 2-methylpyridine or 3-methylpyridine. 3-methylpyridine reacted to leave the methyl group *para* to the vinyl group forming 5-methyl-2-styrylpyridine, whereas 2-methylpyridine failed to react. With 2-styrylpyridine coordinated complexes being known to exist,[266] this may indicate that the mechanism relies on a sterically uncongested ortho position in order to form the substitution product.

In conclusion, this potential catalytic system requires high temperatures and catalyst loading (20 mol %), as well as requiring excess pyridine. However this reaction has demonstrated high atom efficiency and stereoselectivity, and given the relative ease of alkenylation this system has tremendous applications for the formation of pyridine-based compounds. Therefore by taking a mechanism-driven approach to understanding this reaction through a joint experimental and theoretical study, the system can be understood and improved – potentially leading to novel and highly useful catalysts.

5.1.3 Pyridylidenes: Chemistry and Formation

Over the course of this chapter, several complexes in the experimental and theoretical studies can formally be identified as containing a pyridylidene ligand. As a result of this, it is necessary to understand the chemistry and formation of this group.

Pyridylidene is, much like a vinylidene to an alkyne, a high energy carbene tautomer of a pyridine group where the ortho proton has migrated to be bound to the nitrogen group (Figure 5.10). The pyridylidene is ca. 190 – 210 kJ mol^{-1} higher in energy relative to the starting pyridine, with an intramolecular transition state located ca. 355 kJ mol^{-1} above the starting pyridine isomer.[267, 268] Also similar to vinylidenes is the observation that metal pyridylidene complexes are observable and long-lasting, contrary to free pyridylidene.

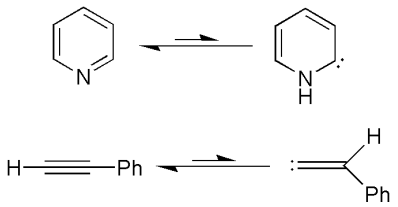

Figure 5.10 – Pyridine to pyridylidene tautomerization with a vinylidene comparison.

A pyridylidene structure was first proposed by Hammick in 1937 to explain the facile decarboxylation of 2-picolinic acid,[269] with one of the first proposed instances of a metal pyridylidene complex being reported in 1983 by Crocianni and co-workers.[270] It was evidenced that protonated pyridyl platinum and palladium complexes showed limited ligand rotation. Evidence for π-back donation from the metal d orbital suggested a formal pyridylidene structure, possibly in resonance with a single metal-carbon bond pyridinium complex (Figure 5.11). Similar complexes were reported with 1-methyl pyridinium complexes.[271]

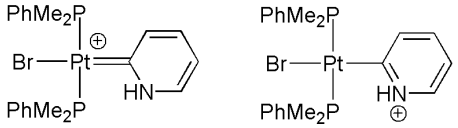

Figure 5.11 – Platinum pyridylidene complex (left) and pyridinium complex (right).

Carmona and co-workers have recently produced a significant body of work into the subject of metal pyridylidene complexes, with a 2006 study on an iridium(III) pyridylidene complexes formed *via* reacting 2-picoline or 2-phenylpyridine with an iridium complex (Figure 5.12).[272] The pyridylidene analogue of unsubstituted pyridine was later reported, with both the bound pyridine and pyridylidene iridium complexes being inconvertible with one another.[273] Bi-pyridine complexes were also observed.[274]

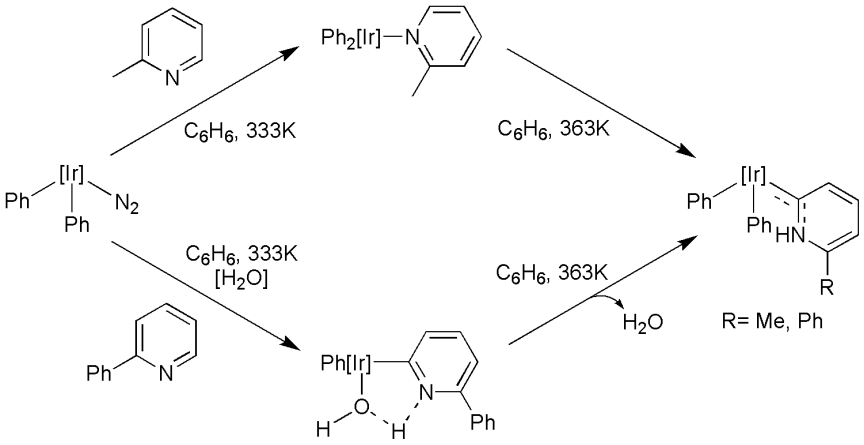

Figure 5.12 – Pyridylidene formation. [Ir] =Tp^{Me2}Ir.

Subsequent theoretical and mechanistic investigations identified pyridylidene formation *via* ligand assisted deprotonation,[221, 275] and deprotonation/protonation mechanisms (Figure 5.13).[276]

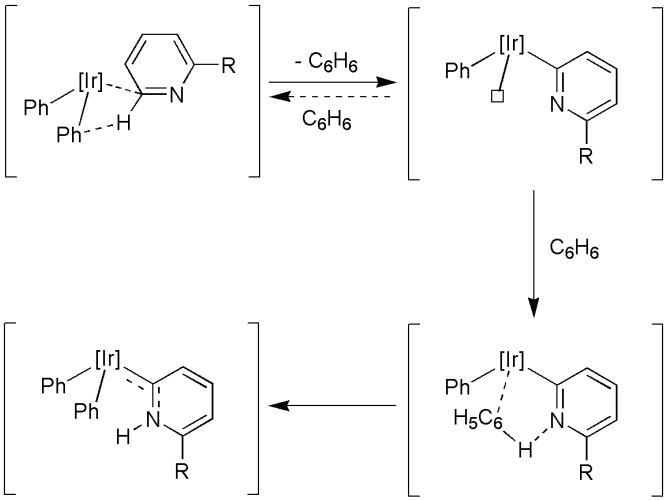

Figure 5.13 – Proposed mechanism of pyridylidene formation. [Ir]=Tp^{Me2}Ir.

During the same time period, Esteruelas and co-workers investigated the use of osmium, iridium and ruthenium complexes with coordinated quinoline- and pyridine- type carbene ligands.[277-279] With regard to the mechanism, a theoretical study indicated carbene formation *via* deprotonation of the C-H bond by a metal-mediated agostic interaction, instead of assistance by coordinated chloride ligands which were instead responsible for stabilizing the protonated nitrogen group.[280]

Similarly, during studies of carbocyclization of benzazoles by Bergman, Ellman *et al*.,[281] it was proposed that the mechanism proceeded through an N-heterocyclic rhodium intermediate (Figure 5.14).[282-284] The intermediate was formed through proton migration from the sp^2 carbon to the unsaturated nitrogen group.

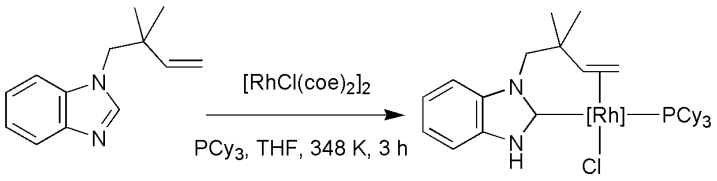

Figure 5.14 – Formation of N-heterocyclic intermediate.

The presence of the intermediate was confirmed with a combined deuterium labelling study and theoretical investigation.[285] In the labelling study, N-methylbenzimidazole was deuterated at the sp^2 position, which showed 88% isotopic incorporation at the nitrogen position upon coordination to the rhodium centre. The theoretical study reported that the formation of the carbene involves activation of the C-H bond, before the proton transfers to the nitrogen atom. The mechanism had a reported $\Delta G^{\ddagger}$ of 118.4 kJ mol^{-1} which agreed with the experimental results.

It is clear from the examples shown that formation of the metal pyridylidene and coordinated N-heterocyclic carbene complex examples normally requires an external proton shuttle in the form of base, ligand or activation with a metal centre, with the uncoordinated tautomerization being shown to be significantly unfavourable for pyridine. In each of the examples, the bonding between the metal and the carbon atom has been demonstrated as a double bond (Figure 5.11), a mesomeric resonance which maintained aromaticity in the heterocycle (Figure 5.13) and a single bond (Figure 5.14). The double bond proposed by Crocianni would be the only mesomer to saturate the coordinating carbon atom, with the other examples showing less than 4 valence bonds. However it is clear that there is disagreement around the formalisation of the metal-carbon bonding.

5.1.4 Initial Experimental Observations

In order to create a firm understanding of the mechanistic process, a joint experimental and theoretical investigation was undertaken. Unless stated otherwise experimental work was performed by Dr Neetisha Mistry (with further details available within her thesis[286]), and all positively charged complexes are presented as their $[PF_6]^-$ salts.

The experimental study began by validating results and methods used in the Murakami & Hori paper. One of the first reactions performed was the reaction of 1-trimethylsilyl-2-phenyl acetylene with pyridine and $[CpRu(PPh_3)_2Cl]$ first shown in Figure 5.8. 2-styrylpyridine was produced, but with a significantly reduced yield, compared to the initial report.

$[CpRu(PPh_3)_2Cl]$ was also heated with phenylacetylene, instead of the 1-trimethylsilyl-2-phenyl acetylene at 323 K. ^1H NMR spectroscopy produced evidence for the acetylide **502**, the singular pyridine coordinated complex $[CpRu(PPh_3)_2(NC_6H_5)][PF_6]$ (**506**) and the *bis*-pyridine complex $[CpRu(PPh_3)(NC_6H_5)_2]$ (**507**) (Figure 5.15). The reaction mixture was left overnight at room temperature with no evidence of further reactivity. However, after heating the mixture again at 323 K for 2 hours the only remaining product was the acetylide **502**.

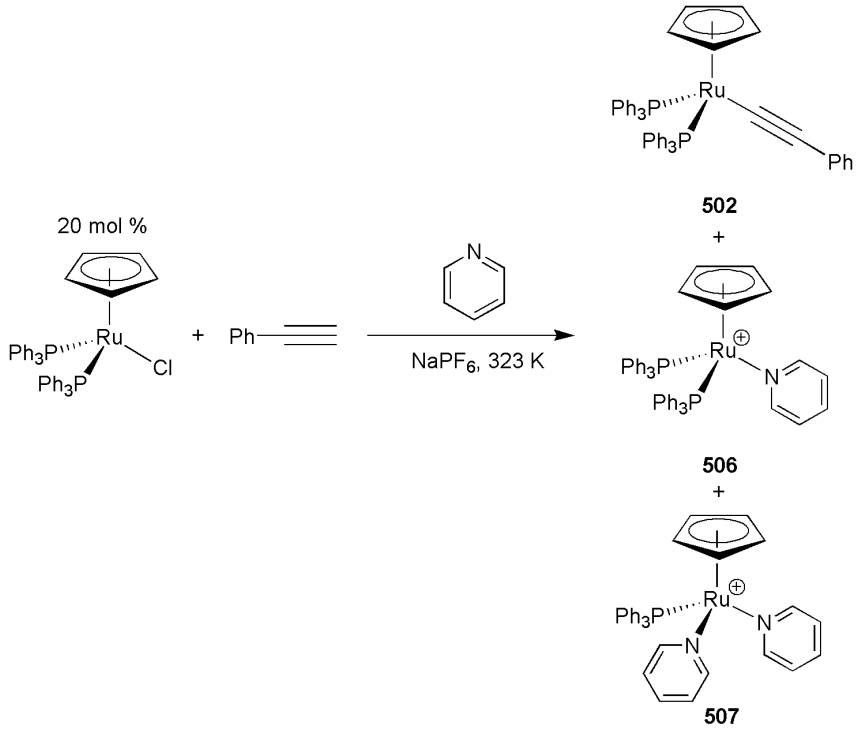

Figure 5.15 – Reaction of $[CpRu(PPh_3)_2Cl]$ with phenylacetylene at 323 K.

The reactivity of the proposed reactive intermediate **501** was then studied, the results of which can be seen in Figure 5.16. D_5-pyridine was added to **501** at room temperature, which immediately led to the deprotonation of the vinylidene and forming a quantity of the acetylide complex **502**, as well as $[CpRu(PPh_3)_2(CO)]$. Heating this mixture at 393 K for 1 hour produced the *bis*-pyridine complex **507** as well as free phenylacetylene and triphenylphosphine.

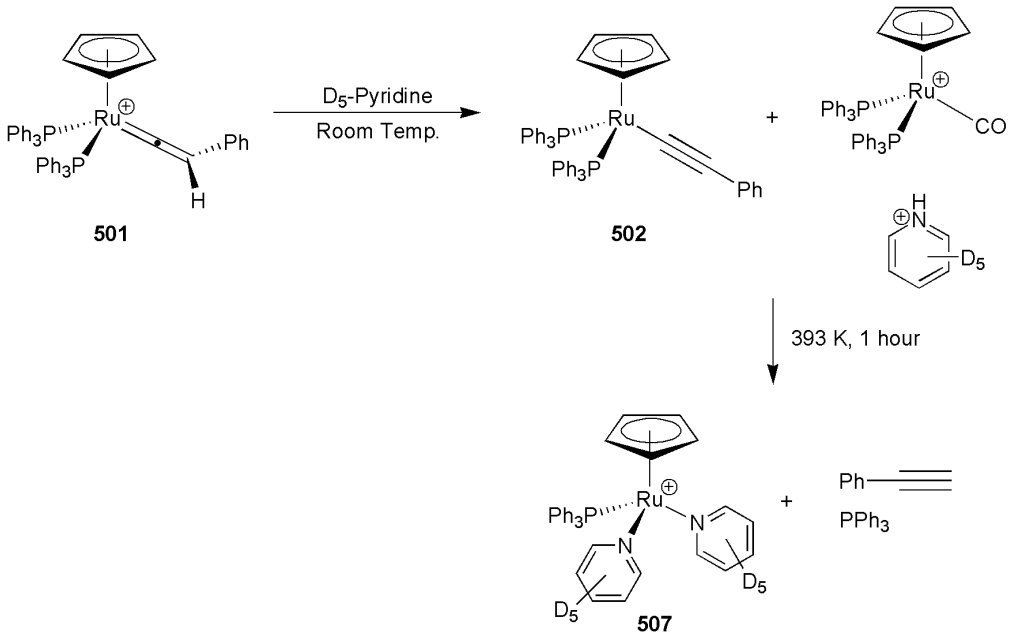

*Figure 5.16 - Initial study of proposed intermediate **501**.*

After these preliminary investigations, catalytic activity was tested on the independently synthesised complexes of the acetylide **502**, the pyridine complex **506** and *bis*-pyridine complex **507**. **502** showed no catalytic activity, matching the original observation by Murakami and Hori.[265] Additionally **506** was also catalytically inactive. However **507** proved to be an active catalyst for the formation of **503** as well as other products at 323 K, and was investigated further.

Initially **507** was reacted with a stoichiometric quantity of phenylacetylene at room temperature in D_2-dichloromethane, with several products being formed (Figure 5.17). One observed product was the pyridine/vinylidene complex **503** – an intermediate on the originally proposed reaction mechanism seen previously in Figure 5.9. Additionally a product of phenylacetylene dimerization – the pi-allyl carbene complex **508** – was also detected, which is similar to complexes observed by Kirchner *et al*..[287-291]

Unusually, **503** reacted further over several hours to form the pyridylidene complex **509**, where the pyridyl and vinyl groups were now connected through a N-C bond – contrary to expected bond formation in the production of 2-styrylpyridine. A single-crystal X-ray structure was obtained (shown in Figure 5.18, with a table of selected bond lengths and angles in Table 5.1) which supported the structural assignment based on NMR and ESI-MS evidence. Over a period of 10 days NMR resonances associated with **503** decreased in intensity, while peaks corresponding with **509** increased, suggesting a direct formation of **509** from **503**. The formal pyridylidene bond determination of **509** is discussed later in section 5.2.13.

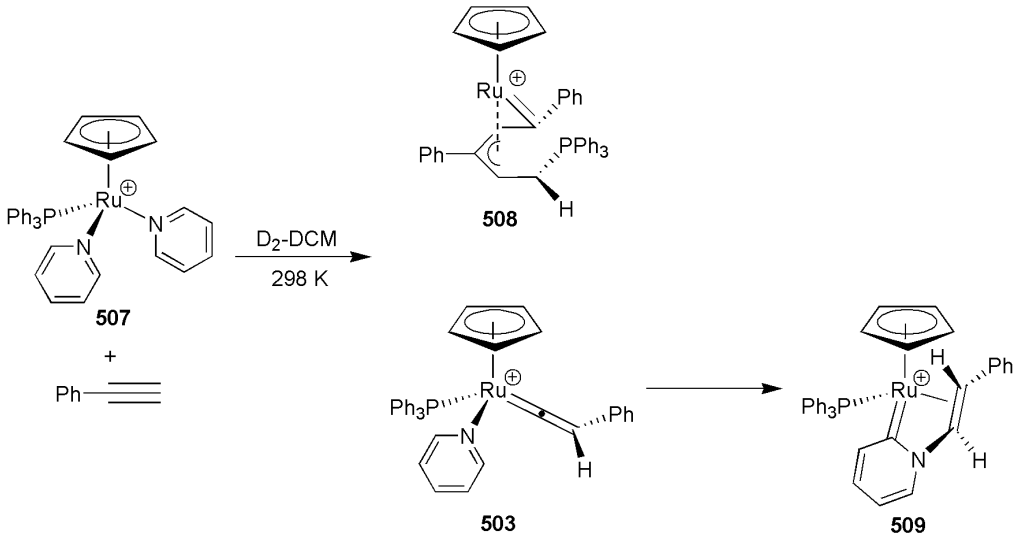

*Figure 5.17 – Reaction of **507** with a stoichiometric amount of phenylacetylene in D_2-dichloromethane.*

The room temperature reaction of **507** with a stoichiometric quantity of phenylacetylene and 2 equivalents of pyridine once again produced **503** and **509** but the π-allyl carbene complex **508** was not observed.

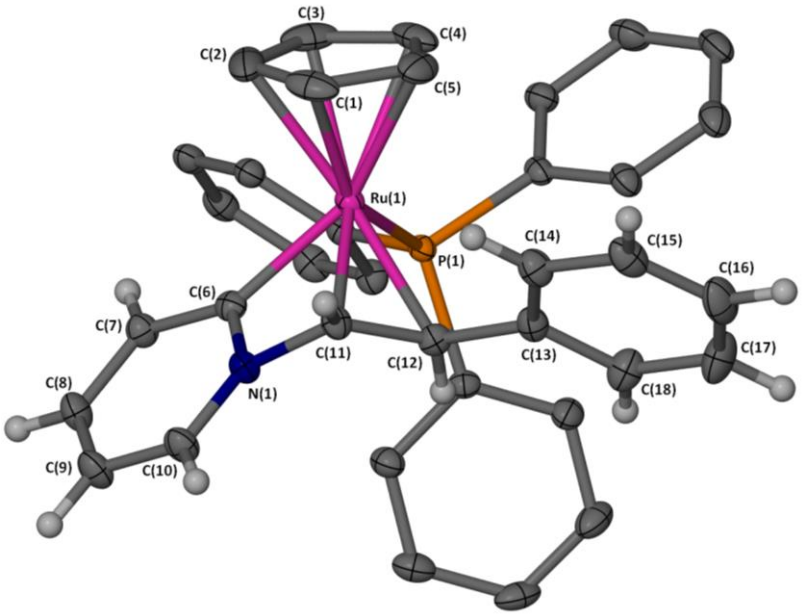

*Figure 5.18 – X-Seed diagram of **509**. Hydrogen atoms and $[PF_6]^-$ omitted for clarity, and thermal ellipsoids (where shown) are at the 50% probability level.*[286]

*Table 5.1 – Selected bond lengths and angles of **509**[286]*

Bond	Bond Length (Å)	Angle	Bond Angle (°)
C(1)-Ru(1)	2.233(2)	C(6)-Ru(1)-C(12)	84.00(7)
C(2)-Ru(1)	2.243(2)	C(6)-Ru(1)-C(11)	63.86(7)
C(3)-Ru(1)	2.224(2)	C(6)-Ru(1)-P(1)	90.66(5)
C(4)-Ru(1)	2.247(2)	C(12)-Ru(1)-P(1)	87.45(5)
C(5)-Ru(1)	2.249(2)	N(1)-C(6)-Ru(1)	99.98(1)
C(6)-Ru(1)	2.039(2)	C(6)-N(1)-C(11)	104.09(2)
C(6)-N(1)	1.359(2)	N(1)-C(11)-Ru(1)	92.03(1)
C(6)-C(7)	1.406(3)	C(12)-C(11)-N(1)	118.05(2)
C(7)-C(8)	1.388(3)	C(11)-C(12)-Ru(1)	67.40(1)
C(8)-C(9)	1.402(3)	C(11)-C(12)-C(13)	120.38(2)
C(9)-C(10)	1.373(3)	N(1)-C(6)-C(7)	115.06(2)
C(10)-N(1)	1.349(2)	C(8)-C(7)-C(6)	119.96(2)
C(11)-N(1)	1.453(2)	C(7)-C(8)-C(9)	121.01(2)
C(11)-Ru(1)	2.152(2)	C(10)-C(9)-C(8)	119.01(2)
C(11)-C(12)	1.405(3)	N(1)-C(10)-C(9)	117.43(2)
C(12)-Ru(1)	2.258(2)		
C(12)-C(13)	1.486(3)		
P(1)-Ru(1)	2.3367(5)		

507 was also reacted with an equivalent amount of phenylacetylene in pyridine solution at 323 K, which resulted in quantitative formation of (*E*)-2-styrylpyridine (Figure 5.19). The $^{31}P(^{1}H)$ NMR spectrum showed that **507** was the major phosphorous containing compound in the reaction mixture.

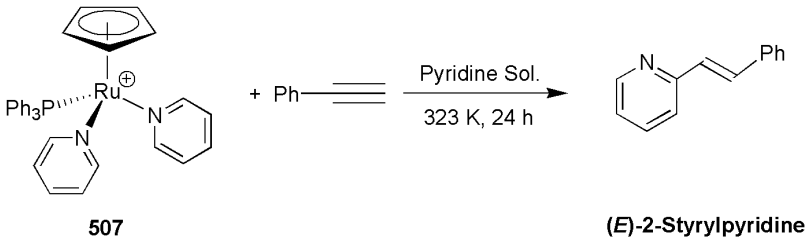

*Figure 5.19 – Reaction of **507** in pyridine at 323 K.*

In order to identify the mechanistic formation of **509**, deuterium labelling experiments were performed. Phenylacetylene was introduced to a deuterium labelled **507**, which was reacted in D_2-dichloromethane, along with 2 equivalents of D_5-pyridine and monitored *via* NMR (Figure 5.20). Once again, evidence for deuterated **503** was seen, as well as deuterated **509** after 24 hours. Peaks associated with deuterated **509** lessened after 5 days due to deuterium scrambling, but results seemed to indicate proton transfer from the pyridyl group to the alkene chain in the formation of **509**.

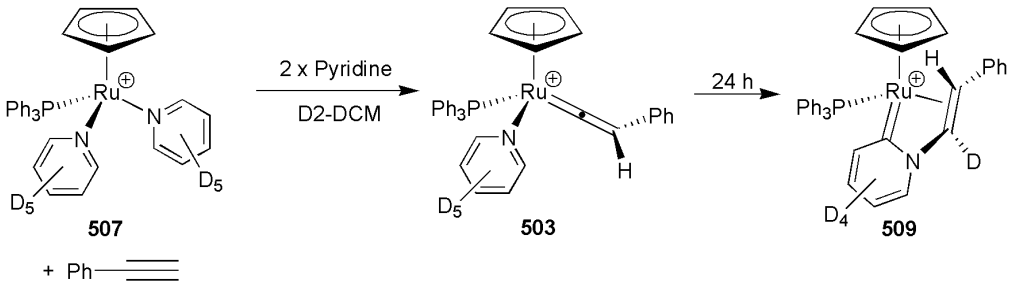

*Figure 5.20 - Reaction of deuterated **507**.*

The reaction of **509** with either pyridine or 1,4-diazabicyclo[2.2.2]octane (DABCO) was shown to deprotonate the vinyl C_β to form the ruthenium pyrrole metallacycle **510** (Figure 5.21).

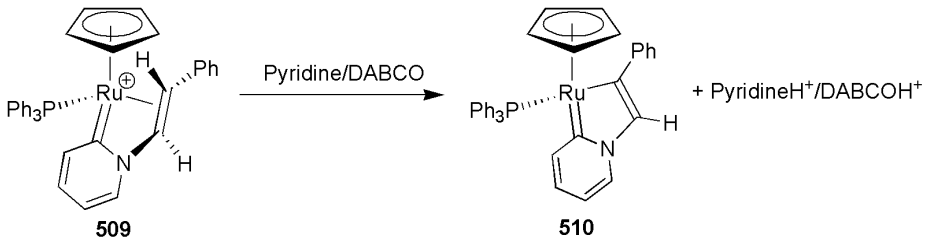

*Figure 5.21 - Deprotonation of **509** to form **510**.*

In order to check for any potential product inhibition of the catalytic reaction, independently synthesised (*E*)-2-styrylpyridine was introduced to a solution of $[CpRu(PPh_3)_2(NCMe)_2]$ which led to the formation of **511** (Figure 5.22). The complex was characterised by NMR spectroscopy and a single-crystal X-ray structure was also obtained (Figure 5.23, with selected bond lengths and angles shown in Table 5.2). It was found that **511** reacted further when dissolved in a pyridine solution (at 298 K) to form both uncoordinated 2-styrylpyridine and the *bis*-pyridine complex **507**.

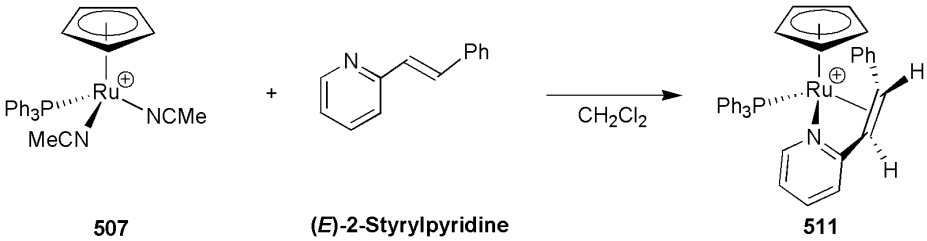

*Figure 5.22 – Introduction of 2-styrylpyridine to $[CpRu(PPh_3)_2(NCMe)_2]$ to form **511**.*

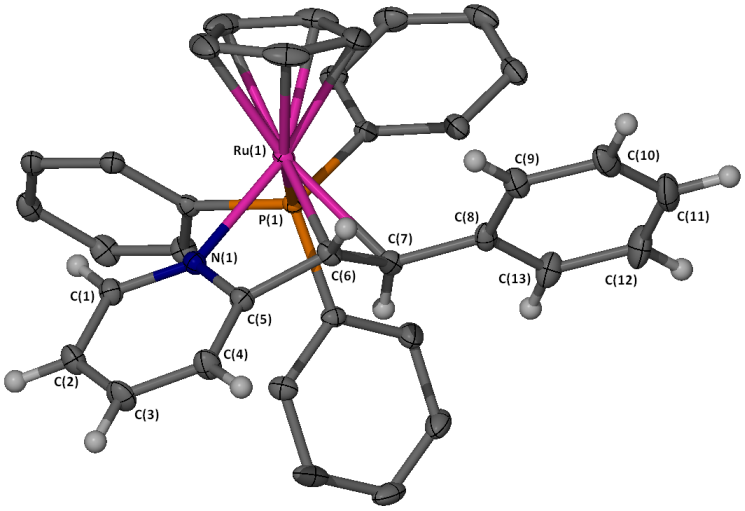

*Figure 5.23 – X-Seed diagram of **511**. Hydrogen, dichloromethane and $[PF_6]^-$ atoms have been omitted for clarity. Thermal ellipsoids (where shown) are at the 50% probability level.*[286]

*Table 5.2 – Selected bond lengths and angles of **511***[286]

Bond	Bond Length (Å)	Angle	Bond Angle (°)
P(1)-Ru(1)	2.350(4)	N(1)-Ru(1)-P(1)	91.71(4)
N(1)-Ru(1)	2.120(1)	C(6)-Ru(1)-P(1)	116.98(4)
C(6)-Ru(1)	2.207 (2)	C(7)-Ru(1)-P(1)	87.55(4)
C(7)-Ru(1)	2.293(2)	N(1)-Ru(1)-C(6)	63.63(5)
C(1)-N(1)	1.341(2)	C(5)-N(1)-Ru(1)	97.84(9)
C(1)-C(2)	1.388(2)	N(1)-C(5)-C(6)	107.64(1)
C(2)-C(3)	1.386(2)	C(5)-C(6)-Ru(1)	90.27(1)
C(3)-C(4)	1.394(2)	C(4)-C(5)-C(6)	129.41(2)
C(4)-C(5)	1.384(2)	C(7)-C(6)-C(5)	120.18(1)
C(5)-N(1)	1.348(2)	C(6)-C(7)-Ru(1)	68.59(9)
C(5)-C(6)	1.478(2)	C(6)-C(7)-C(8)	121.13(1)
C(6)-C(7)	1.399(2)	C(1)-N(1)-C(5)	119.76(1)
C(7)-C(8)	1.484(2)		

5.1.5 Experimental Effects of Substituents - 4-Ethynyl-α,α,α-trifluorobenzene

In order to further understand the reaction mechanism, substituent effects of the alkyne, phosphine (section 5.1.6) and pyridyl (section 5.1.7) groups were investigated. One investigation involved the use of 4-ethynyl-α,α,α-trifluorobenzene instead of phenylacetylene, where a more electron withdrawing alkyne group was hoped to induce different reactivity. The first reaction studied was that of *bis*-pyridyl complex **507** with 4-ethynyl-α,α,α-trifluorobenzene in D_2-dichloromethane with 2 equivalents of pyridine and was monitored by NMR spectroscopy (Figure 5.24).

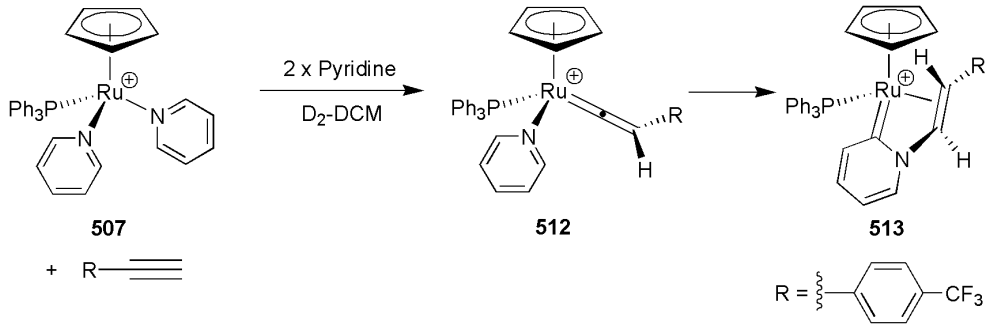

*Figure 5.24 – Reaction of **507** with 4-ethynyl-α,α,α-trifluorobenzene.*

Evidence for the formation of the analogue of vinylidene **503** – **512** – was produced, which reacted further to form the analogue of **509** – **513**. **513** was verified *via* ESI-MS, with a single-crystal X-ray structure also being obtained (Figure 5.25 with selected bond lengths and angles being shown in Table 5.3). This demonstrates once again that **507** is a potential catalyst starting point, and shows the adaptability of this system to other substituents. Interestingly the reaction mixture of **513** was missing many of the side products found in the phenylacetylene case, suggesting an easier formation of the pyridylidene.

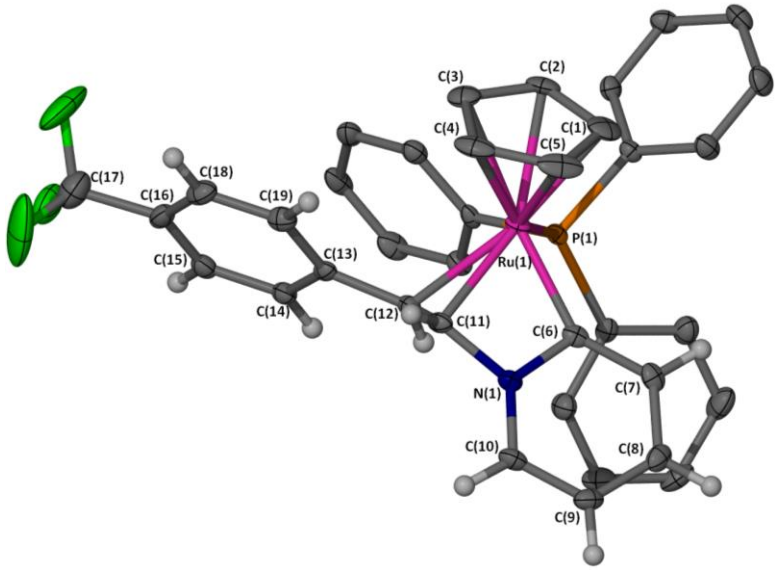

*Figure 5.25 - ORTEP drawing of **513**. Hydrogen atoms, dichloromethane and $[PF_6]^-$ omitted for clarity, and thermal ellipsoids (where shown) are at the 50% probability level.*[286]

*Table 5.3 – Selected bond lengths and angles of **513**[286]*

Bond	Bond Length (Å)	Angle	Bond Angle (°)
C(4)-Ru(1)	2.295(3)	C(6)-Ru(1)-C(11)	64.36(1)
C(3)-Ru(1)	2.243(3)	C(6)-N(1)-C(11)	103.5(2)
C(2)-Ru(1)	2.203(3)	N(1)-C(6)-Ru(1)	99.72(2)
C(1)-Ru(1)	2.212(3)	N(1)-C(11)-Ru(1)	92.25(2)
C(5)-Ru(1)	2.253(3)	C(6)-Ru(1)-C(12)	83.61(1)
C(6)-Ru(1)	2.029(3)	C(6)-Ru(1)-P(1)	88.60(7)
C(6)-N(1)	1.360(3)	C(11)-Ru(1)-P(1)	115.80(8)
C(10)-N(1)	1.353(3)	C(12)-Ru(1)-P(1)	85.76(7)
C(10)-C(9)	1.367(4)	C(12)-C(11)-N(1)	116.9(2)
C(9)-C(8)	1.405(4)	C(11)-C(12)-C(13)	122.9(2)
C(8)-C(7)	1.380(4)	C(10)-N(1)-C(6)	126.6(2)
C(6)-C(7)	1.401(4)	N(1)-C(10)-C(9)	117.6(3)
C(11)-N(1)	1.459(3)	C(10)-C(9)-C(8)	119.1(3)
C(11)-Ru(1)	2.127(3)	C(7)-C(8)-C(9)	121.2(3)
C(12)-C(11)	1.411(4)	C(8)-C(7)-C(6)	119.6(3)
C(12)-Ru(1)	2.245(3)	N(1)-C(6)-C(7)	115.9(2)
C(12)-C(13)	1.474(4)		
P(1)-Ru(1)	2.337(7)		

Much like the phenylacetylene system, excess pyridine introduced to **513** lead to the formation of the CF_3 substituted analogue of **510** (**514**) which can be seen in Figure 5.26.

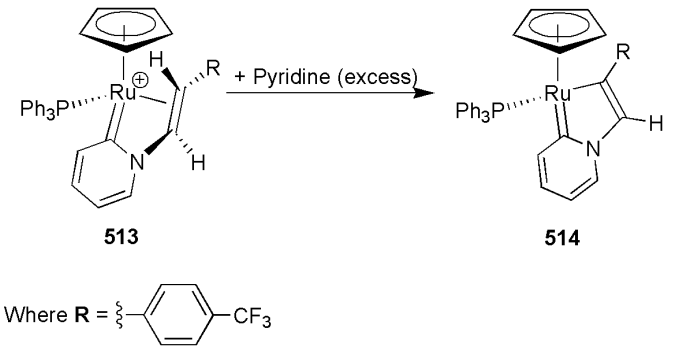

*Figure 5.26 – Reaction of **513** with pyridine to form **514**.*

In order to determine whether **514** and by extension, **510**, represent catalytic intermediates on a productive pathway or are instead deactivation products, **514** was heated to 323, 373 and 423 K in the presence of one equivalent of $[C_5H_5NH]^+$ in a solution of D_5-pyridine. While the reaction at 323 and 373 K produced no discernible change, the reaction at 423 K produced a quantity of (*E*)-2-(4-(trifluoromethyl)styrylpyridine) which was identified by NMR spectroscopy (Figure 5.27)

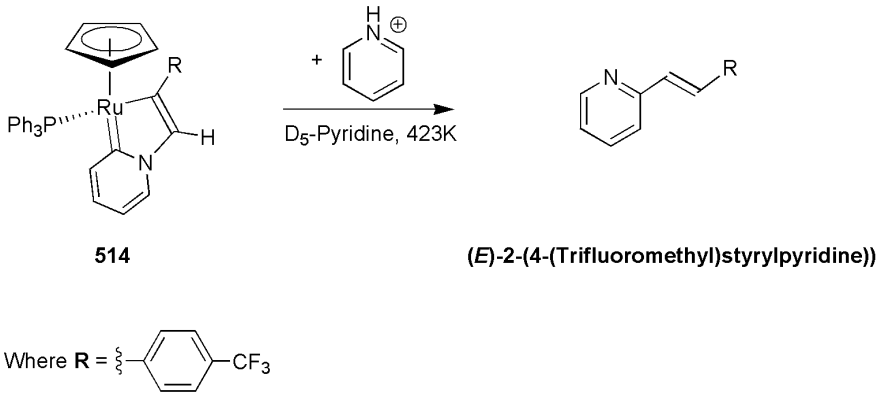

*Figure 5.27 – Reaction on heating **514** with a pyridinium proton.*

While 2-(4-(trifluoromethyl)styrylpyridine)) was produced in this reaction, the high temperatures needed suggest that the intermediates are a deactivation product and not part of the productive cycle which proceeds at 323K with **507** as a catalyst.

Much like the reaction shown in Figure 5.19, addition of 4-ethynyl-α,α,α-trifluorobenzene to **507** in a pyridine solution heated at 323 K for 24 hours produced 2-(4-(trifluoromethyl)styrylpyridine)) (Figure 5.28). This further showed the reactivity of **507**, and the inactivity of **514**.

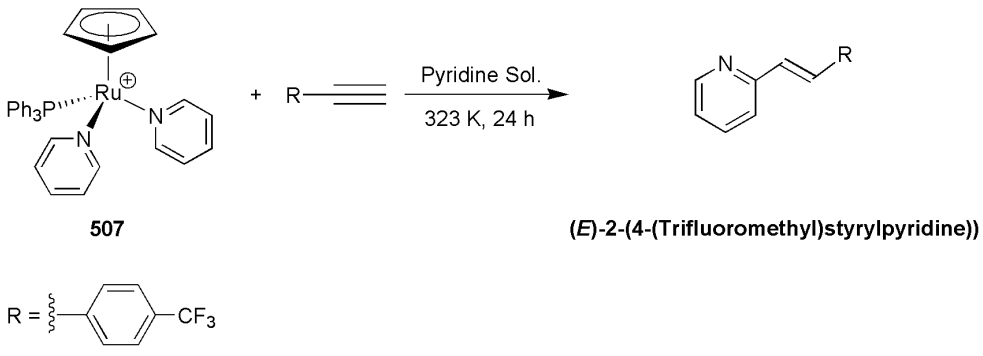

*Figure 5.28 – Reactivity of **507** with 4-ethynyl-α,α,α-trifluorobenzene.*

5.1.6 Experimental Effects of Substituents - Trimethylphosphine

Here, experiments were performed using trimethylphosphine in place of triphenylphosphine ligands. Due to the trimethylphosphine ligands being more electron donating, as well as with a smaller Tolman cone angle of 118° compared to 145° for triphenylphosphine,[292] this could potentially lead to a change in reactivity and was investigated in several experiments.

Phenylacetylene was added to a stoichiometric quantity of the trimethylphosphine analogue of **507** – **515** – in the presence of an excess of D_5-pyridine and was monitored *via* NMR spectroscopy. With no change occurring in the reaction mixture at room temperature, it was heated to 323 K. After 16 hours no peaks associated with phenylacetylene were present; instead complex **516** was identified, along with a free organic product – 2-styrylpyridine. The reaction was also repeated with an excess of pyridine with the same results (Figure 5.29).

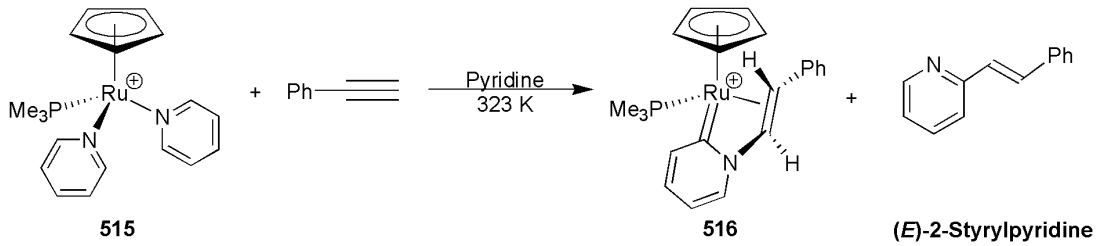

*Figure 5.29 – Reaction of **515** with phenylacetylene in an excess of pyridine.*

516 was verified *via* ESI, MS and X-ray crystallography (Figure 5.30 with selected bond lengths and angles in Table 5.4). Stoichiometric addition of phenylacetylene to **515** in dichloromethane did not produce either **516** or 2-styrylpyridine, instead producing a trimethylphosphine analogue of the pi-allyl carbene complex **508**.

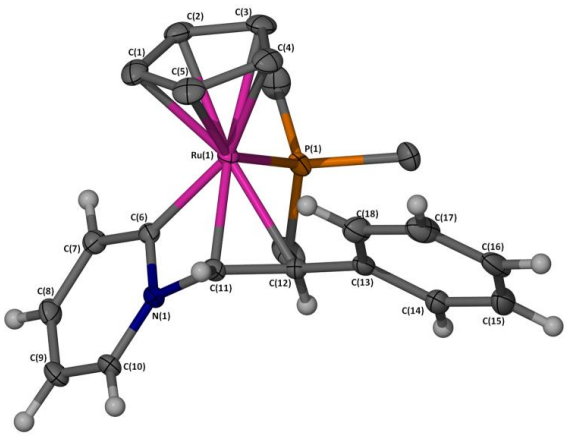

*Figure 5.30 – X-Seed drawing of **516**. Hydrogen atoms and $[PF_6]^-$ omitted for clarity, and thermal ellipsoids (where shown) are at 50% probability level.*[286]

*Table 5.4 – Selected bond lengths and angles of **516***[286]

Bond	Bond Length (Å)	Angle	Bond Angle (°)
C(1)-Ru(1)	2.218(2)	C(6)-Ru(1)-P(1)	86.20(6)
C(2)-Ru(1)	2.199(2)	C(12)-Ru(1)-P(1)	84.51(6)
C(3)-Ru(1)	2.242(2)	C(6)-Ru(1)-C(12)	84.52(8)
C(4)-Ru(1)	2.273(2)	C(6)-Ru(1)-C(11)	64.26(8)
C(5)-Ru(1)	2.243(2)	N(1)-C(6)-Ru(1)	100.20(1)
C(6)-Ru(1)	2.010 (2)	C(12)-C(13)-N(1)	117.14(2)
C(11)-Ru(1)	2.120(2)	C(11)-C(12)-C(13)	121.32(2)
C(12)-Ru(1)	2.224(2)	C(10)-N(1)-C(6)	126.49(2)
C(11)-C(12)	1.414(3)	N(1)-C(10)-C(9)	117.6(2)
C(12)-C(13)	1.484(3)	C(10)-C(9)-C(8)	119.1(2)
C(11)-N(1)	1.449(2)	C(7)-C(8)-C(9)	121.5(2)
C(6)-N(1)	1.355(3)	C(8)-C(9)-C(10)	119.1(2)
C(6)-C(7)	1.397(3)	N(1)-C(6)-C(7)	116.16(2)
C(7)-C(8)	1.377(3)		
C(8)-C(9)	1.397(3)		
C(9)-C(10)	1.360(3)		
C(10)-N(1)	1.348(3)		
P(1)-Ru(1)	2.294(6)		

5.1.7 Pyridine Substituent Effects

In order to identify the steric selectivity for the alkenylation reaction, experiments were performed by Lucy Milner using 3-methylpyridine in place of pyridine, much like the authors of the original paper.[265] In one particular reaction shown in Figure 5.31, 20 equivalents of 3-methylpyridine was reacted with 4-ethynyl-α,α,α-trifluorobenzene, a trimethylphosphine ligand and $[CpRu(C_{10}H_8)]^+$, an air stable complex known to conveniently produce $[CpRu]^+$ fragments.[293] Microwave irradiation of the reaction mixture at 423 K formed the (*E*)-2-(4-(trifluoromethyl)styryl-5-methylpyridine) isomer exclusively.

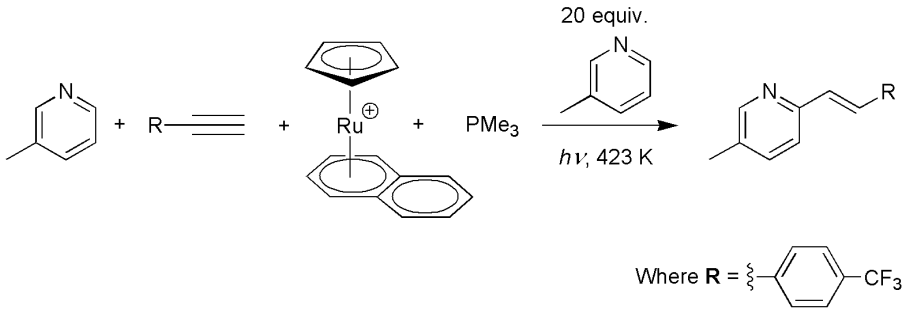

Figure 5.31 – Reaction of 3-methylpyridine with 4-ethynyl-α,α,α-trifluorobenzene.

Conversely, experiments performed by Dr Neetisha Mistry (shown below in Figure 5.32), which differed in the alkyne and phosphine group used as well as using a 3-methylpyridine analogue of **507** with no excess of 3-methylpyridine at room temperature, produced evidence of structures **517/p** and **517/q**.

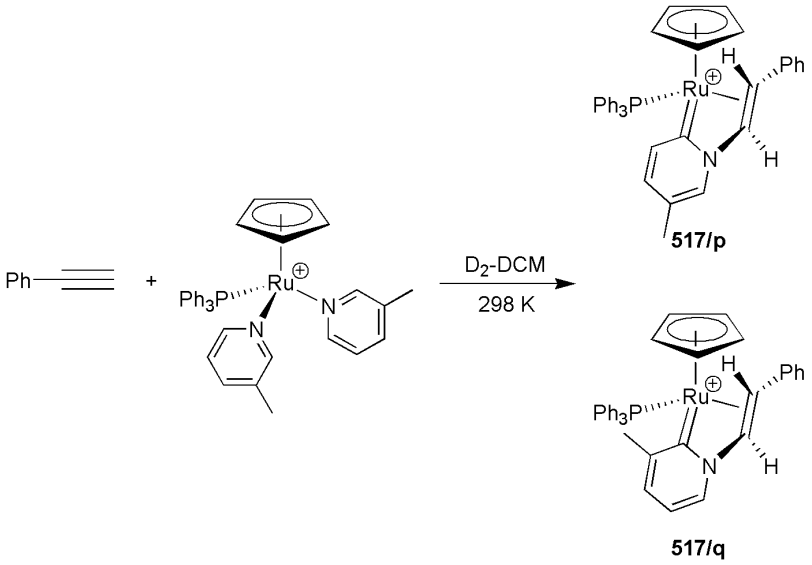

*Figure 5.32 – Formation of **517/p** and **517/q**.*

It appears from experimental results that the methyl group will be *para* to the vinyl group with regard to the formation of (*E*)-2-(4-(trifluoromethyl)styryl-5-methylpyridine) (Figure 5.31). However in formation of the N-C bonded intermediates both regioisomers **517/p** and **517/q** are formed. This suggests that the two sets of products are being formed by differing mechanisms.

5.1.8 Experimental Conclusions

The experimental evidence presented here shows some differences to the original work by Murakami and Hori,[265] and provides some exciting insights into the reaction mechanism. Firstly, it can be assumed that instead of the vinylidene complex **501** which is deprotonated in pyridine to form **502**, the *bis*-pyridine complex **507** is the active catalyst in the reaction. Secondly **503**, much like the original authors suggest, seems to be a part of the overall reaction mechanism. Thirdly the unexpected product **509** may or may not play a role in formation of the overall substituted pyridine product, due to the temperature required to form 2-(4-(trifluoromethyl)styrylpyridine)) from **514** and pyridinium. Finally, the independently produced 2-styrylpyridine complex **511** could be reacted with pyridine in order to form free styrylpyridine and the starting *bis*-pyridine complex **507** readily. This can be summed up in the overall reaction scheme below in Figure 5.33.

Additionally varying the concentration of pyridine experimentally suggests that formation of 2-styrylpyridine requires more pyridine than found on the *bis*-pyridine complex **507**, suggesting it is either needed in a deprotonation step, or to substitute the coordinated 2-styrylpyridine and regenerate the *bis*-pyridine complex. In reactions in pure dichloromethane as a solvent, only **509** was produced which confirms that pyridine is required in product formation.

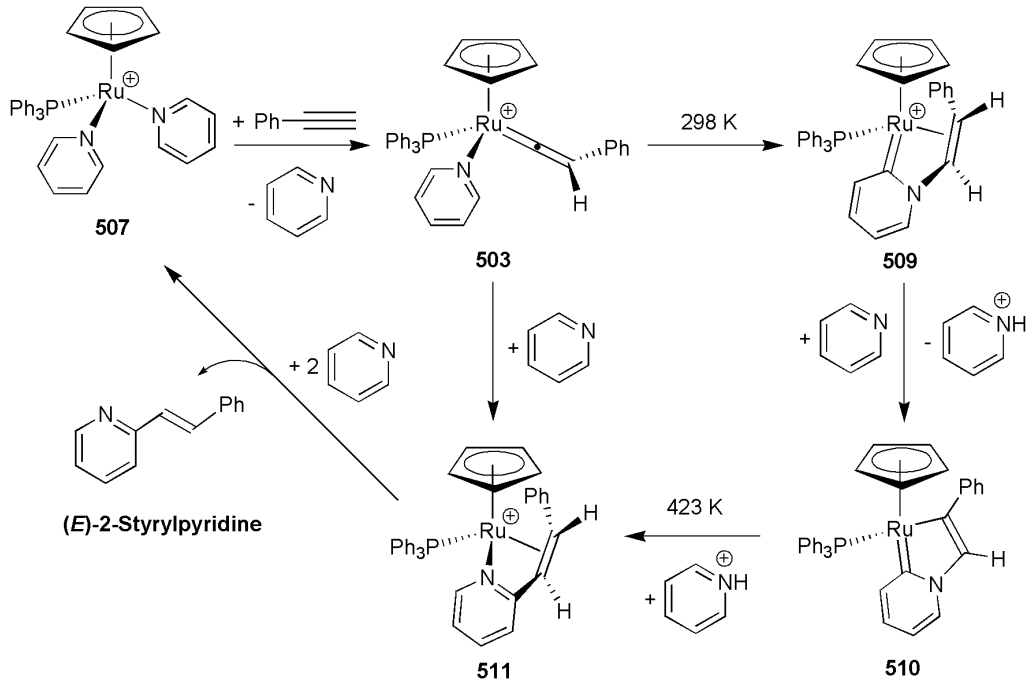

Figure 5.33 – Overall experimental evidence. For clarity only the phenylacetylene pathway is considered.

With relation to substituent effects, formation of 2-(4-(trifluoromethyl)styrylpyridine)) from **507** and 4-ethynyl-α,α,α-trifluorobenzene requires similar conditions as that of phenylacetylene. However formation of **513** is noticeably free of side products, suggesting a lower minimum or reduced kinetic barriers.

Conversely, using trimethylphosphine with the stoichiometric addition of phenylacetylene in dichloromethane produced no evidence for **516**. Instead a trimethylphosphine analogue of the π-allyl carbene complex **508** was produced, suggesting the opposite to the formation of **513** with 4-ethynyl-α,α,α-trifluorobenzene.

5.2 Results and Discussion

5.2.1 Computational Preamble

In order to provide insight into the mechanistic processes forming the organometallic intermediates and organic products, potential energy surfaces of the mechanism were investigated with the use of DFT, using methods outlined in section 7.1, and with a DRC analysis being performed on all transition states as per section 7.2.

Due to the presence of charged fragments, data presented below include solvation corrections with pyridine (using the COSMO method outlines in section 7.3). Solvation corrected numbers for dichloromethane as well as gas-phase energies can be found in the supplementary information. All energies reported in the text are ZPE and COSMO corrected SCF energies.

*5.2.2 Initial Formation of **503***

Given that the pyridine/vinylidene complex **503** is an important intermediate in the original paper by Murakami and Hori,[265] as well as having been identified in experimental investigations, it was necessary to understand the mechanism for the formation of **503**. Potential formation from **507**, the role complexes **502** and **506** play in the early part of the mechanism as well as that of the originally proposed intermediate **501** must be investigated. An overall PES for this section can be seen in Figure 5.37.

The formation of **501** posited by Murakami and Hori was studied first. For simplicity, the starting point for the surface is the side-bound alkyne complex **N1**. This complex can undergo alkyne-vinylidene tautomerization to **501** *via* a direct side-bound 1,2 hydrogen shift transition state $\mathbf{TS_{N1\text{-}501}}$, or after slipping to the alkyne σ-complex **N2**, which can also undergo a 1,2 hydrogen shift *via* $\mathbf{TS_{N2\text{-}501}}$ which can be seen in Figure 5.34.

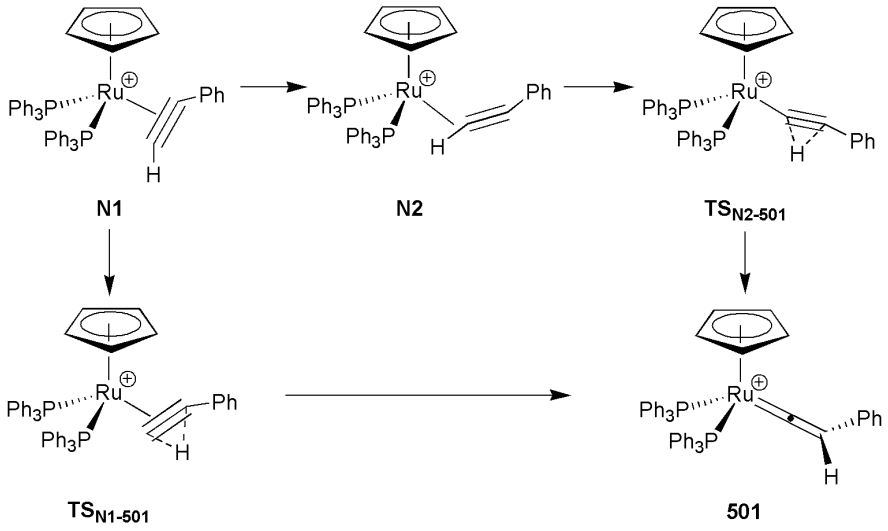

*Figure 5.34 – Formation of **501** from a side-bound alkyne.*

Analysing the surface, it is clear that the side-bound 1,2 hydrogen shift transition state $\mathbf{TS_{N1\text{-}501}}$ is too high in energy to be viable at room temperature or at temperatures used experimentally (323 K), as it has an energy of +200 kJ mol^{-1} relative to **N1**.

The pathway from **501** to the starting complex **507** was also considered, heading through the acetylide **502**, and the experimentally observed complex **506** shown in Figure 5.35.

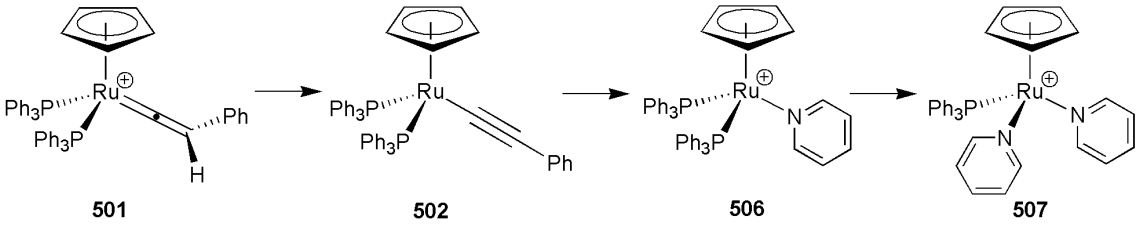

*Figure 5.35 – Potential formation of **507** from **501**.*

As can be seen in the PES, all points were relatively isoenergetic with one another, leading to state **N3** ranging from -52 to -27 kJ mol^{-1}.

Finally the formation of **503** from **507** was investigated through the side bound alkyne complex **N3**, which could either slip to the σ-complex **N4** then through a direct 1,2 hydrogen shift with the transition state $\mathbf{TS_{N4\text{-}503}}$, or directly through a side-bound 1,2 hydrogen shift *via* the transition state $\mathbf{TS_{N3\text{-}503}}$ which is depicted in Figure 5.36.

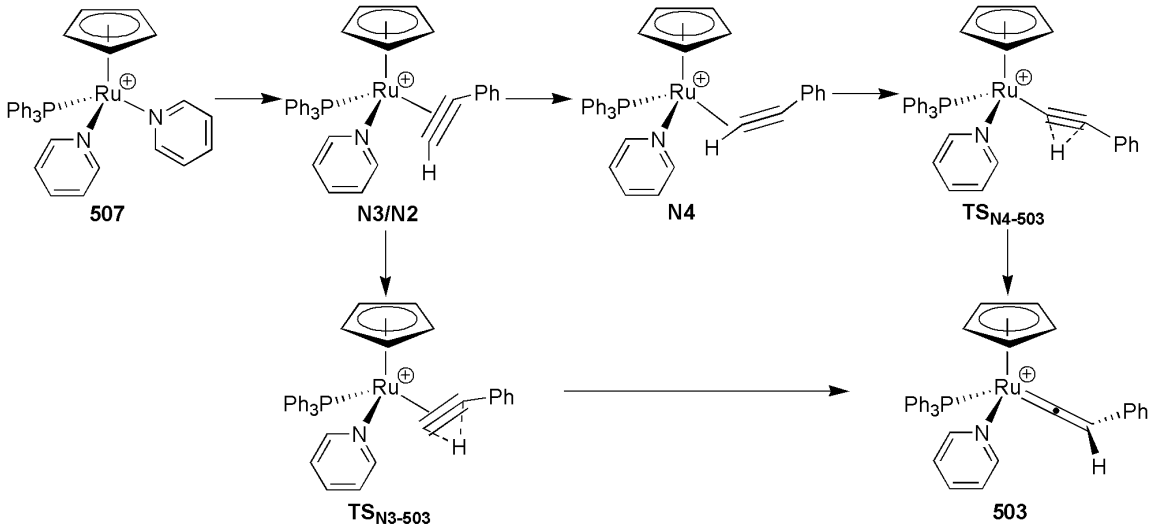

*Figure 5.36 – Formation of **503** from **507**.*

From the PES, **503** can be formed from **507** through the $\mathbf{TS_{N4\text{-}503}}$ transition state with an energy of +41 kJ mol^{-1}, giving an energetic span of 76 kJ mol^{-1} (TDI = **507**, TDTS = $\mathbf{TS_{N4\text{-}503}}$), which is acceptable for the reaction conditions employed. Once again the η^2-bound 1,2-hydrogen shift transition state $\mathbf{TS_{N3\text{-}503}}$ is shown to be too high in energy for the experimental temperatures used being found at +173 kJ mol^{-1}. Finally, **503** is shown to be a thermodynamic minimum compared to **507** at -49 kJ mol^{-1}.

In conclusion, formation of the vinylidene most likely proceeds through a σ-complex transition state, with the η^2 transition states being far higher in energy, which would agree with examples found in the literature.[54, 167] **503** is found to be the thermodynamic minimum, which agrees with experiment. Additionally **507** is shown to be an acceptable starting point for the formation of **503**. A mechanistic route from **501** to **503** however cannot be ruled out, but would still be more than likely to proceed through **507** due to the deprotonation of **502** that is observed experimentally.

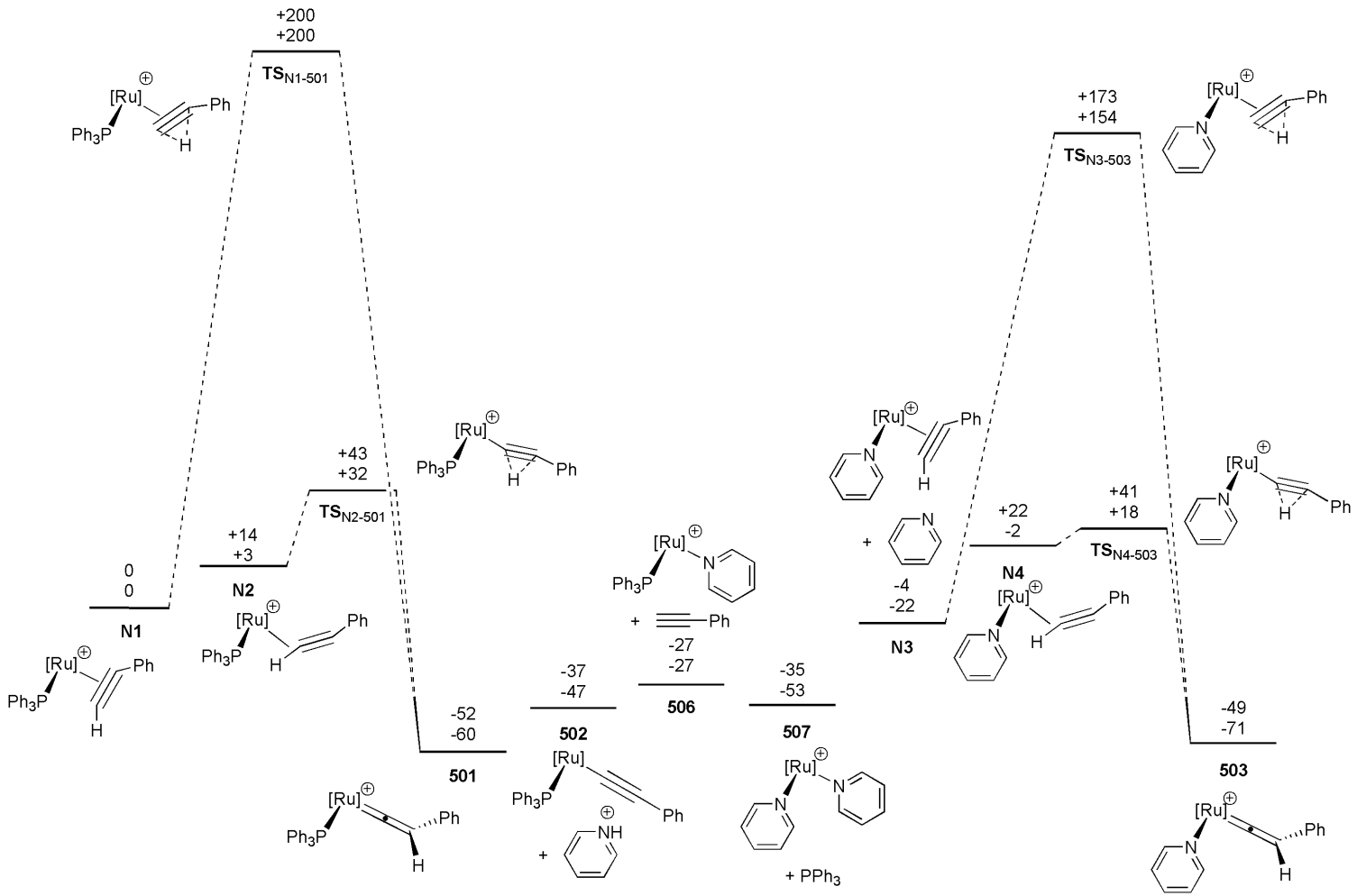

*Figure 5.37 – Potential energy surface for the formation of **503**. Energies are ZPE corrected SCF (top) and Gibbs free (bottom) energies with COSMO solvation in kJ mol^{-1}, relative to **N1**. [Ru] = [CpRu(PPh$_3$)].*

5.2.3 Study of Murakami & Hori's Proposed Mechanism for the Alkenylation of Pyridine

With the formation of **503** understood, the next phase was to investigate the mechanism proposed by Murakami & Hori. From a starting point of **503**, it was proposed that the mechanism must undergo a [2+2] cycloaddition to the intermediate **504** *via* the transition state $\mathbf{TS_{503\text{-}504}}$ (Figure 5.38).

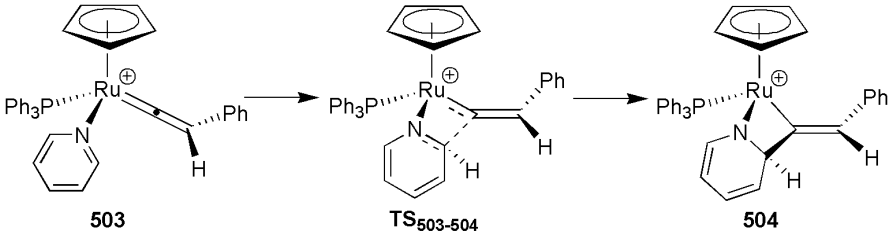

*Figure 5.38 – Formation of **504** from **503**.*

Once **504** is formed, a proton must transfer from the ortho-position of the pyridine ring to the vinyl group (Figure 5.39). This can be performed either by deprotonation by pyridine in solution through intermediate **505**, or by a direct hydrogen shift *via* the transition state $\mathbf{TS_{504\text{-}N5}}$ to form **N5**. With the coordinated 2-styrylpyridine formed, the metal C-H bond can switch from an agostic interaction to a favourable C=C bond metal complex, forming **N6**. The product complex is then eliminated in the presence of pyridine to form free 2-styrylpyridine and **507**. The side-bound version of **N5** - **511**, will be discussed later in section 5.2.6.

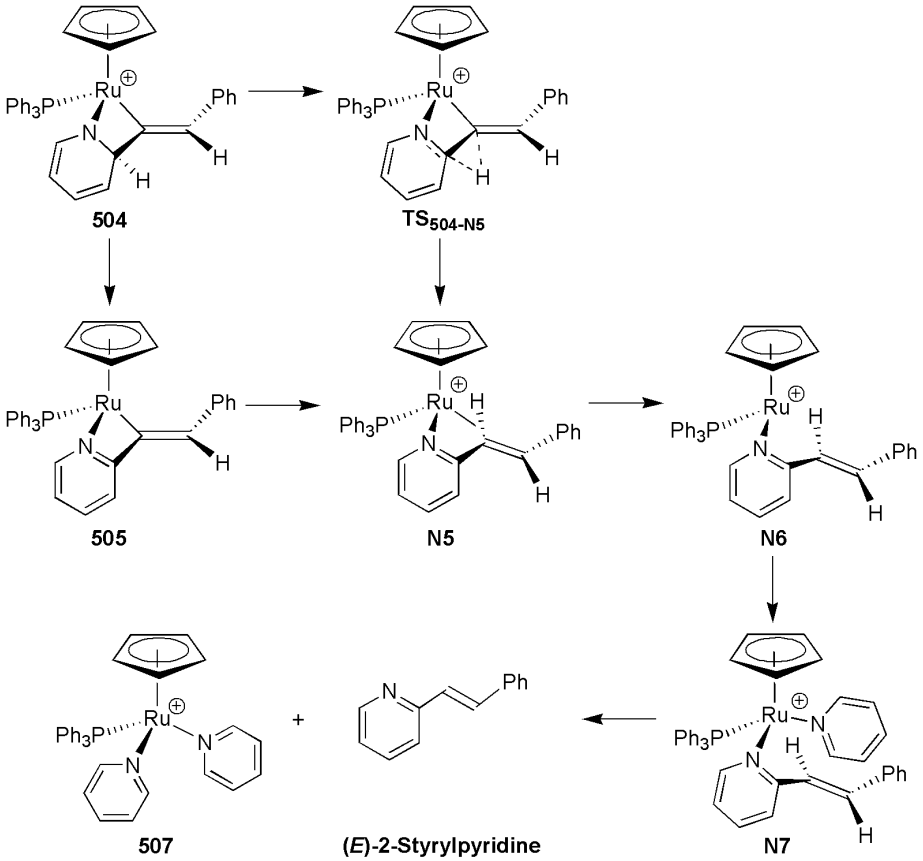

Figure 5.39 – Proton transfer and product formation.

Of note on the PES (Figure 5.40) is the relative energy of not only the transition state **$TS_{503-504}$** but also the intermediate **504** from the proposed [2+2] cycloaddition, at +154 and +136 kJ mol^{-1} respectively relative to complex **507**. The overall mechanism has an energetic span of 168 kJ mol^{-1}, with the TDI being **503** and the TDTS being **$TS_{503-504}$**. While the barriers as well as the energetic span agree with the experimental conditions used in the original study,[265] the proposed [2+2] cycloaddition is inconsistent with new experimental data showing formation of 2-styrylpyridine at 323 K for 24 h – making this mechanism unlikely (section 5.1.4).

Additionally, while the transition state for proton migration across the pyridyl-vinyl C-C bond (**TS_{504-N5}**) is at a high relative energy of +149 kJ mol^{-1}, the intermediate involving deprotonation (**505**) is far lower in energy at -61 kJ mol^{-1}. The low energy of **505** as well as **503** makes the high energy [2+2] cycloaddition mechanism even less likely as a potential reaction pathway.

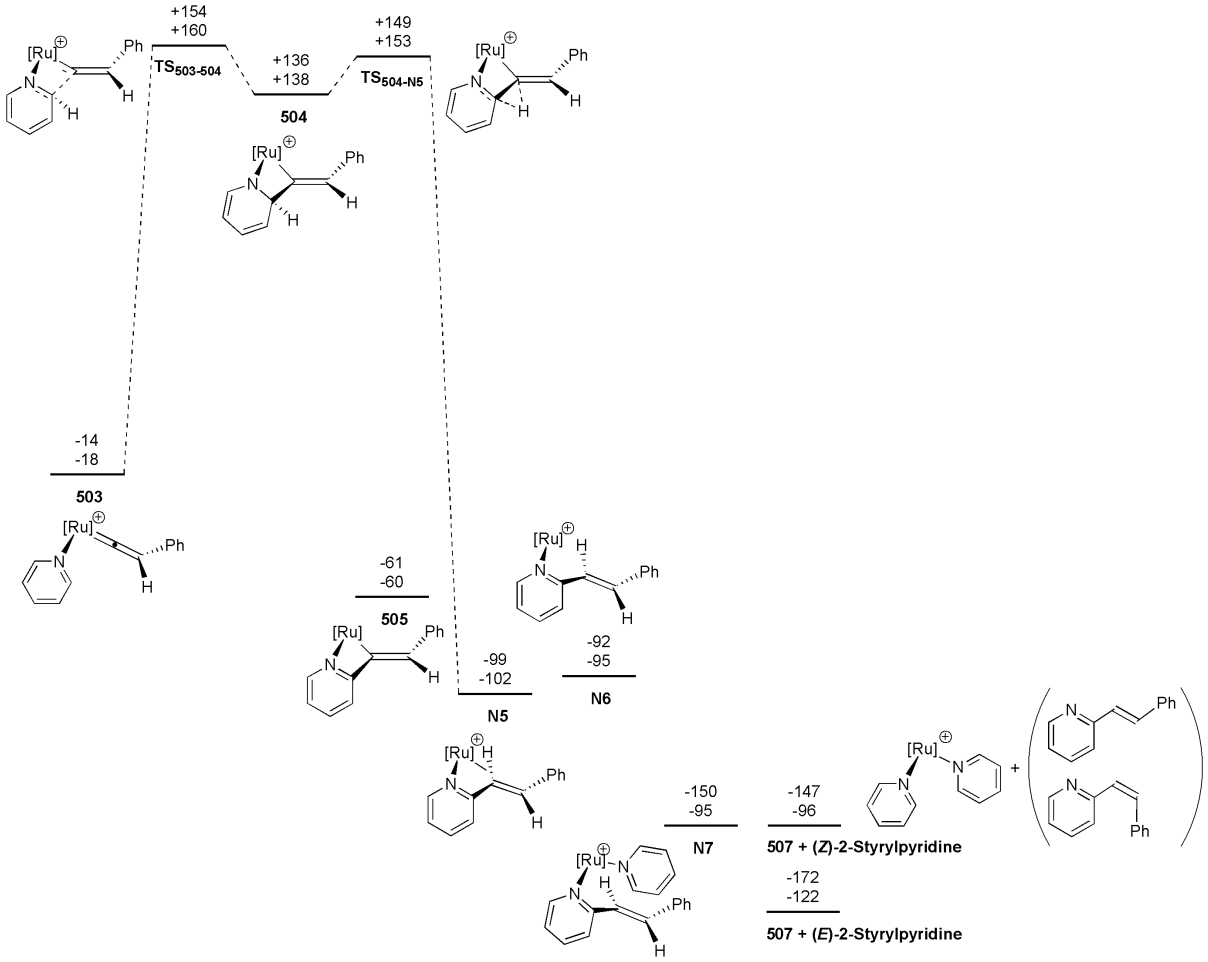

*Figure 5.40 – Originally proposed mechanism for product formation. Energies are ZPE corrected SCF (top) and Gibbs free energies (bottom) with COSMO solvation in kJ mol^{-1}, relative to **507**. [Ru] = [CpRu(PPh$_3$)].*

Finally points associated with the uncoupling of the product – **N5** and **N6** – are both thermodynamically favoured at ca. -95 kJ mol^{-1} compared with **507**, with the addition of an extra pyridine molecule to form **N7** seeing a drop in energy to -150 kJ mol^{-1}. **507** and 2-styrylpryrdine is the overall thermodynamic minimum on the PES, with formation of the (*E*)-2-styrylpryrdine product being favoured over the *Z*-isomer by 25 kJ mol^{-1}.

In conclusion, the originally proposed [2+2] cycloaddition proceeds *via* a high energy pathway that is inconsistent with experimental data showing formation of 2-styrylpyridine at 323 K. The stationary point **505**, as well as points **N5** through to **507** seem to be part of an energetically favourable pathway which may still be part of the mechanism. In addition the initially proposed mechanism does not account for the formation of the potential deactivation products **509** and **510**, therefore further theoretical investigation is necessary.

*5.2.4 Theoretical Validation of the Existence of **509***

Given the unexpected appearance of the intermediate **509** during the experimental study, the crystal structure seen originally in Figure 5.18 (reproduced below in Figure 5.42) was validated by several methods which included a theoretical study of relative energies and calculated bond lengths compared to the obtained crystal structure. Due to the similar electron densities of nitrogen and carbon which determine the structure in X-ray crystallography as well as the counter-intuitive nature of the geometry, the structure could not be verified with certainty - therefore further validation was deemed necessary. Due to the perceived notion that the pyridyl-vinyl carbon-carbon bonded intermediate **511** would be the expected structure - this too was compared in the study. The crystal structure and calculated structures of **509** and **511** can be seen in Figure 5.42.

The energy of structures **509** and **511** were computed first (Figure 5.41), and it can be seen that relative to the *bis*-pyridine complex **507** the proposed intermediate **509** is -84 kJ mol^{-1} lower in energy – a thermodynamically favourable state. However **511** is far lower at -148 kJ mol^{-1}, indicating that **509** is either a low energy intermediate on the way to the final product formation, or that the formation of 2-styrylpyridine is a kinetically controlled product.

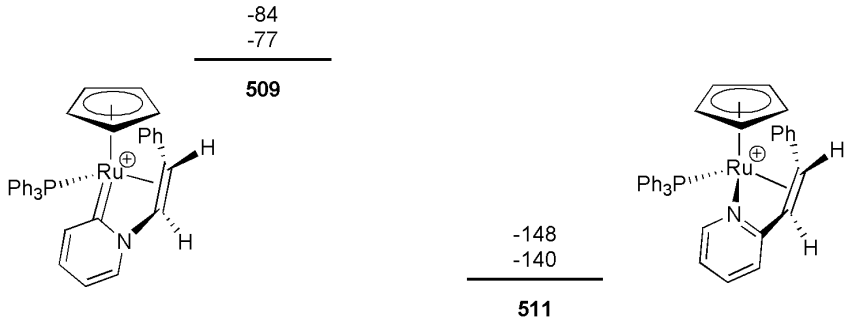

*Figure 5.41 – Energetic comparison of **509** and **511**. Energies are ZPE corrected SCF (top) and Gibbs free (bottom) energies with COSMO solvation in kJ mol^{-1}, relative to **507**.*

For the geometry validation, the bonds being compared are listed in Table 5.5, with a key for the bonds examined found underneath the table. Additionally there is a comparison of several important bond angles. The geometries and raw data can be found on the supplementary information disk.

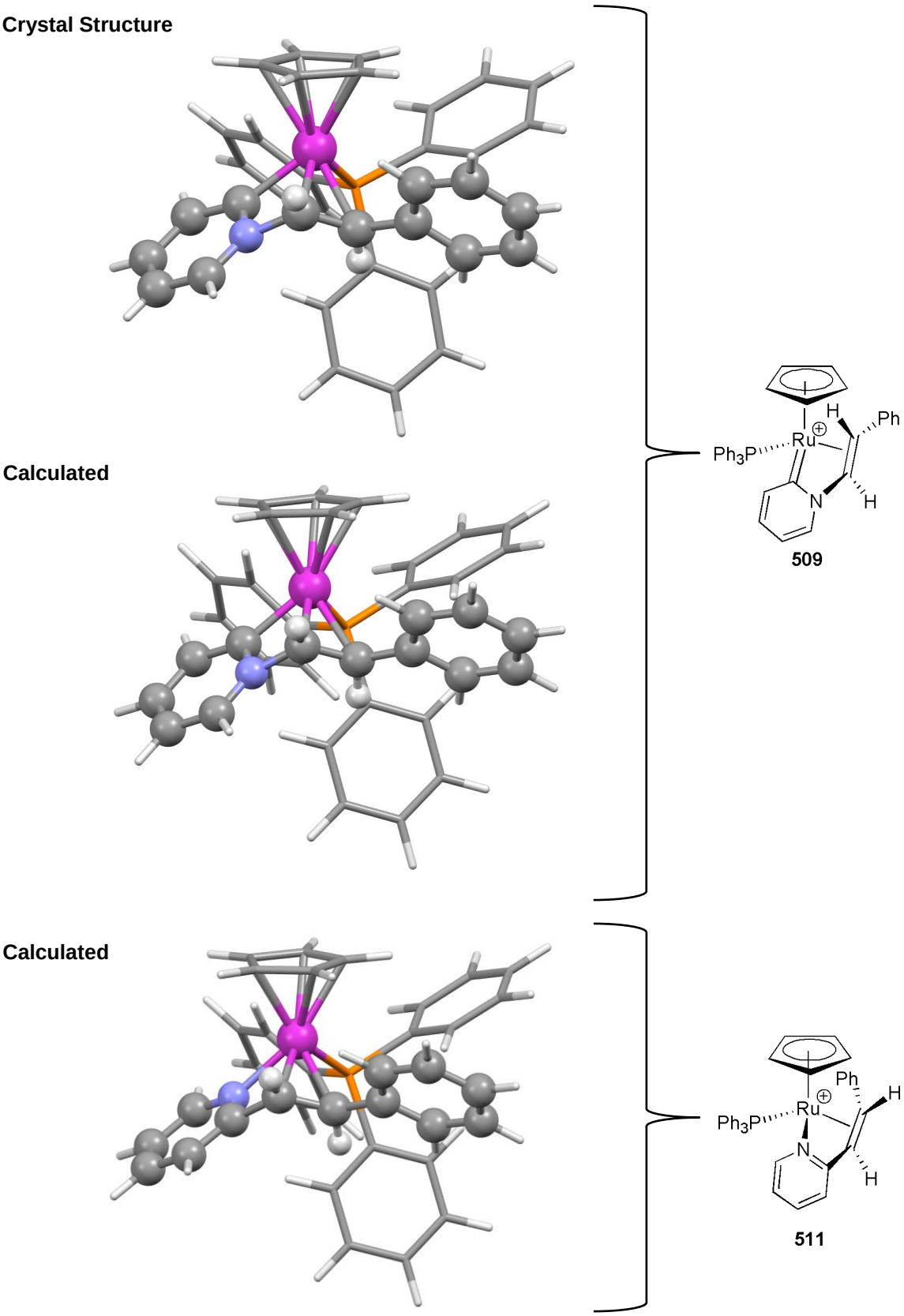

*Figure 5.42 – The crystal and calculated structure of **509** and calculated structure of **511**. A crystal structure of **511** was shown previously in Figure 5.23.*

*Table 5.5 – Comparison of bond lengths, angles, and deviations of **509** and **511** to the crystal structure of **509**. Total bond length deviation refers to sum of all assigned bonds in molecule*

Parameter	509 (Crystal Structure)	509 (Calculated Structure)	511 (Calculated Structure)
Bond length 1, 2 (Å)	2.039(2)	2.03	2.13
Bond length 2, 3 (Å)	1.359(2)	1.38	1.36
Bond length 3, 4 (Å)	1.453(2)	1.46	1.48
Bond length 4, 5 (Å)	1.405(3)	1.43	1.43
Bond length 1, 4 (Å)	2.152(2)	2.14	2.19
Bond length 1, 5 (Å)	2.258(2)	2.28	2.29
Angle of 1, 2 and 3 (°)	99.98(1)	100.2	97.5
Angle of 2, 3 and 4 (°)	104.09(2)	102.7	106.7

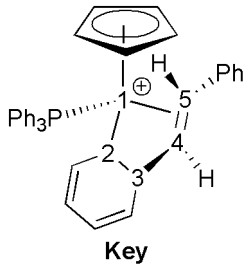

Key

As can be seen from the table, the calculated structure of **509** appears to be closer to the obtained crystal structure than that of **511**. For instance the metal ligand bond of 1-2 for the DFT structure of **511** differs by 0.1 Å compared to the X-ray structure. In terms of bond angles it is again seen that **509** is closer in orientation to the X-ray structure, with the angles being closer than **511** by roughly 2° for both computed angles compared to the X-ray structure. This again would also indicate the likelihood that the X-ray structure of **509** has been correctly interpreted as **509**.

It is worth noting that effects such as crystal packing[58] may be altering bond distances and angles in the X-ray structure compared with those computed in the gas phase, so a perfect fit between experiment and theory is not to be expected. However the method used to optimise the calculated geometry has previously shown agreement with experiment within this thesis, as well as with relevant literature.[52, 294] Therefore the identity of the crystal structure can be verified as that of **509** with a significant degree of confidence. The role that **509** plays in the overall reaction however must also be investigated.

*5.2.5 Investigating the Formation of **509** from **503***

With the experimental proof for **509** as well as the theoretical validation seen in section 5.2.4, the mechanism for the formation of **509** was elucidated. Given the electrophilic nature of the C_α in vinylidene complexes, one potential route to the formation of **507** involves the attack of the pyridyl-nitrogen on the vinylidene C_α of **503** forming complex **N8** (Figure 5.43). As was shown previously in section 1.3.2, the C_α of Fischer-type vinylidenes has a δ+ charge, and given the presence of free pyridine it can be assumed that a nucleophilic attack takes place at this carbon.

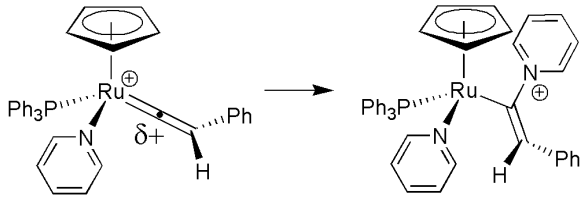

*Figure 5.43 – Pyridine attack at the δ+ vinylidene C_α in **503**.*

Once **N8** is formed, it is proposed that the originally coordinated pyridine molecule is lost, leaving behind complex **N9**. An agostic bond then forms between the *ortho* C-H bond and ruthenium forming **N10** (Figure 5.44).

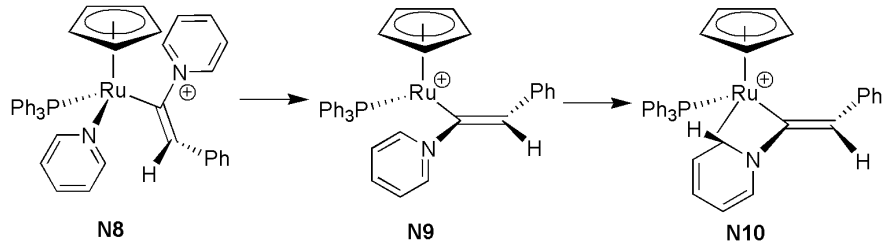

*Figure 5.44 – Formation of **N10** from **N8**.*

The pyridine *ortho* proton can then shift from the pyridine onto the former vinylidene C_α to give **509**. This is not a concerted process and two transition states as well as a shallow intermediate are seen in the PES for the transformation. The intermediate **N11** is a metal hydride complex, which is linked to **N10** and **509** by the transition states **$TS_{N10-N11}$** and **$TS_{N11-509}$** respectively, shown below in Figure 5.45.

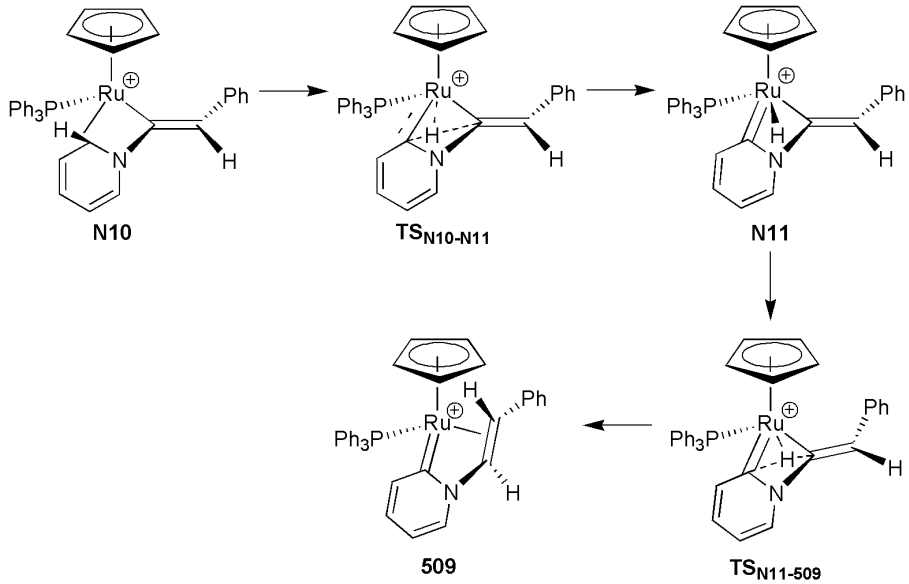

*Figure 5.45 – Formation of **509** from **N10**.*

The structure of **N11** was further analysed to identify the nature of the hydride structure. PABOON analysis revealed a partial charge of +0.085 on the hydrogen, indicating protic rather than hydridic character. Additionally the structure was analysed with NBO with the reference structure shown below in Figure 5.46. The initial reference structure showed no bond from the main complex to the proton, with an LP* (lone pair acceptor) orbital located on the proton. Additionally, second order perturbation analysis showed a donation from the Ru-C_{11} and Ru-C_{20} bond into the proton LP* orbital with a second order perturbation stabilization energy of 478.94 and 353.96 kJ mol^{-1}, showing the proton to be stabilised by the electron density of the metal-pyridyl and metal-vinyl bonds.

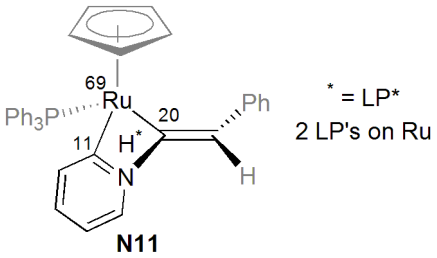

*Figure 5.46 – NBO reference structure of **N11**. For simplicity the positive charge on the complex is not shown.*

As can be seen from the PES in Figure 5.47, the highest energy stationary points for the process are the transition states for the proton transfer from the ortho-carbon of the pyridyl group to the former vinylidene C_α, with the highest barrier of the mechanism being found at the transition state $\mathbf{TS_{N10\text{-}N11}}$ with a value of +58 kJ mol^{-1} relative to **507**. The presence of the intramolecular proton transfer states $\mathbf{TS_{N10\text{-}N11}}$ and $\mathbf{TS_{N11\text{-}509}}$ shows that the formation of **509** does not require proton transfer *via* a pyridine shuttle, concurring with the experimental observation of the formation of **509** in reactions without pyridine in solution (Figure 5.17).

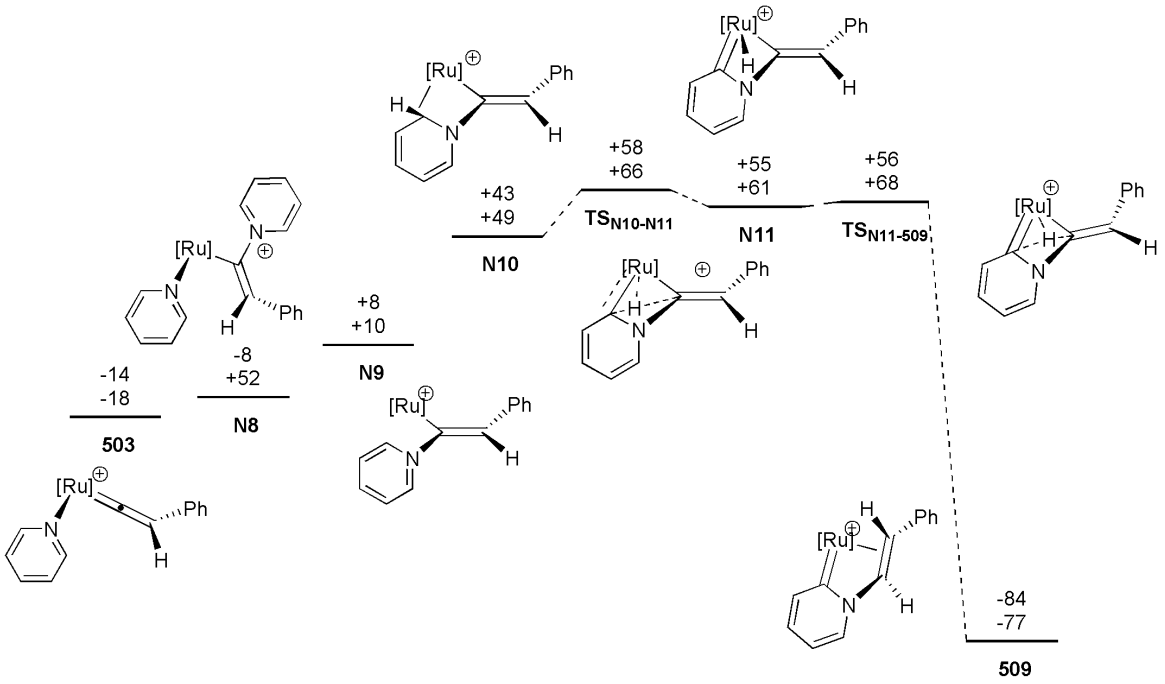

*Figure 5.47 – Proposed mechanism for formation of **509** from **503**. Energies are ZPE corrected SCF (top) and Gibbs free (bottom) energies with COSMO solvation in kJ mol^{-1}, relative to **507**. [Ru] = [CpRu(PPh$_3$)].*

With an energetic span of 72 kJ mol^{-1} (TDI=**503**, TDTS=**TS$_{N10-N11}$**) it is clear that this mechanism is indeed an accessible one with formation of **509** at room temperature conditions, and far lower in energy than the formation of **N5** *via* the high energy barrier of **TS$_{503-504}$** proposed by Murakami & Hori.[265]

5.2.6 Initial Attempts to Identify a Product Formation Pathway

Given the low energy pathway for the formation of **509**, it was assumed that this was a reaction intermediate necessary for the formation of the organic product. As such several mechanisms from **509** were investigated and are reported here.

Experimental evidence showed that addition of pyridine as a base could deprotonate the vinyl C_β of complex **509**, forming the neutral ruthenium pyrrole metallacycle **510**. An alternate deprotonation involving the removal of the proton on the C_α to form **N12** (an analogue of **505**) is also possible (Figure 5.48). This may provide a starting point for the formation of 2-styrylpyridine from **510**.

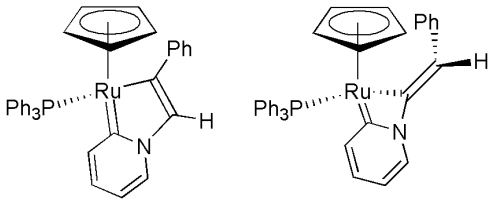

*Figure 5.48 – **510** and **N12**.*

The first investigations involved a transition state where the pyridyl group of **509** would rotate and form a pyridyl-vinyl carbon-carbon bond rather than a carbon-nitrogen bond (Figure 5.49). However the geometry of this transition could not be located.

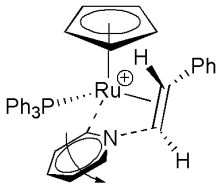

*Figure 5.49 – Rotation of the pyridyl group in **509**.*

The next step involved looking at transition states which broke the pyridyl-vinyl nitrogen-carbon bond for structures **509**, **510** and **N12** forming **N13**, **N14** and **N15** through transition states $\mathbf{TS_{509\text{-}N13}}$, $\mathbf{TS_{510\text{-}N14}}$, and $\mathbf{TS_{N12\text{-}N15}}$ respectively (Figure 5.50). As can be seen in the PES in Figure 5.52, while **N13** is at +29 kJ mol^{-1} relative to **507**, the transition state $\mathbf{TS_{509\text{-}N13}}$ is found at +182 kJ mol^{-1}, giving an energetic span of 266 kJ mol^{-1} (TDI = **509** at -84 kJ mol^{-1}) – too high for the experimental reaction temperatures of 323 K. For the formation of **N14**, the transition state $\mathbf{TS_{510\text{-}N14}}$ is also too high in energy at +187 kJ mol^{-1} (energetic span = 271 kJ mol^{-1}) and so was also discounted.

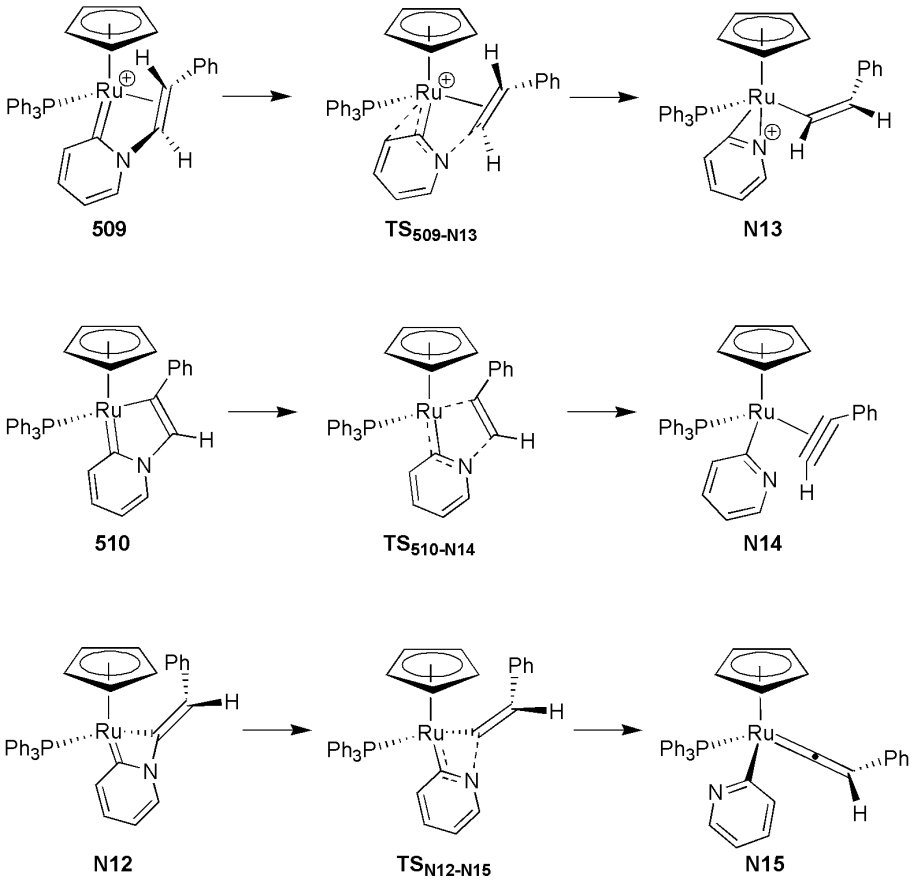

Figure 5.50 – The breaking of nitrogen-carbon bonds for selected complexes.

The final mechanism involved the neutral complex **N12** forming a pyridyl vinylidene **N15**, and both of these minima were seen to be of an acceptable energy for the experimental conditions, at -3 and +62 kJ mol^{-1} respectively. However the transition state **TS$_{N12-N15}$**, unlike the other two investigated mechanisms, was at a relatively acceptable barrier height at +94 kJ mol^{-1} relative to **507**, but was hampered by the low energy of **509** (giving an energetic span of 178 kJ mol^{-1}) as well as the experimental observation that deprotonation only occurred at the vinyl C_β to form **510**.

Given the relatively low barrier height of the transition state **TS$_{N12-N15}$**, this mechanism was probed further. It could be assumed that complex **N15** can undergo pyridyl migration and form **505** *via* the transition state **TS$_{N15-505}$** seen in Figure 5.51. As seen previously in Figure 5.39 on page 247, protonation may then occur to form **N5** which would proceed on to form the final organic product and **507**. Additionally **505** can isomerise to the side bound complex **N16** which could also be protonated forming **511**. These structures can also be viewed on the PES in Figure 5.52

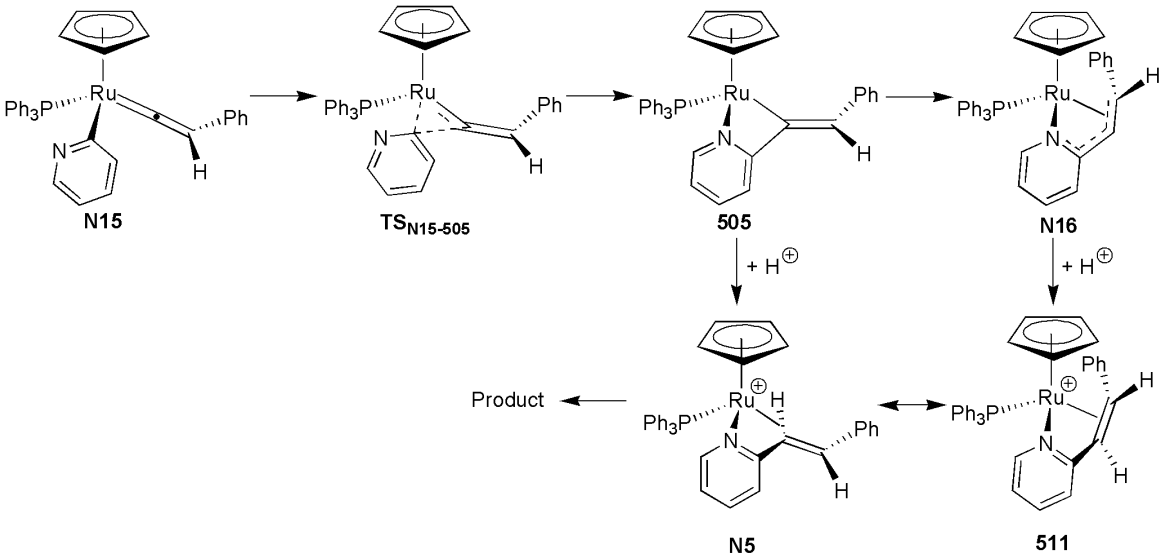

*Figure 5.51 – Pyridyl migration to form 505 and the final product. (Note the pyridyl group of **TS$_{N15-505}$** is more perpendicular than the diagram indicates).*

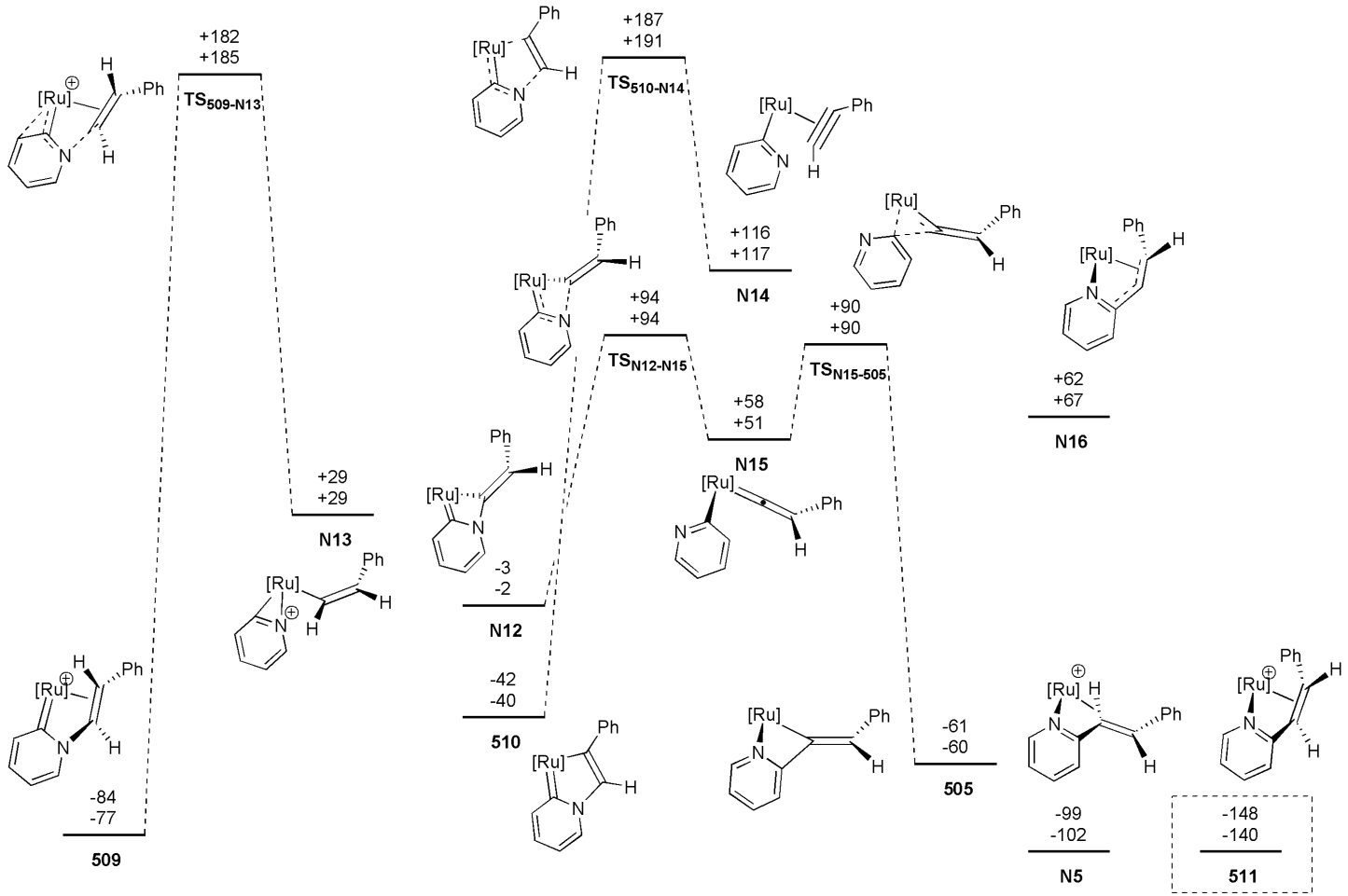

*Figure 5.52 – Attempted mechanisms for the formation of the organic product from **509**. Energies are ZPE corrected SCF (top) and Gibbs free (bottom) energies with COSMO solvation in kJ mol^{-1}, relative to **507**. [Ru] = [CpRu(PPh$_3$)].*

The pyridyl migration mechanism is once again relatively low in energy compared to previously calculated pathways, with a maximum barrier height of +90 kJ mol^{-1} relative to **507**. The protonated products **N5** and **511** are both low in energy at -99 and -148 kJ mol^{-1} respectively, however the logical intermediate connecting **505** and **511** - **N16** is 161 kJ mol^{-1} higher in energy than that of **N5**, suggesting protonation of **505** is a more favourable process than the rearrangement to **N16**. While this could mean that **511** is not a logical step on the PES, it is apparent that it is the second lowest minimum on the surface (with the global minimum being **507** + 2-styrylpyridine), meaning that it may be a stable resting state before being replaced by pyridine coordination to form **507**.

These results indicate that the experimentally-observed intermediates **509** and **510** are deactivation products, with all transition state energies and energetic spans leading to productive pathways being too high for the experimental conditions of 323 K for 24 h. Therefore a different mechanism must be occurring to form the organic product.

5.2.7 Mechanisms Involving Carbene and Pyridylidene Intermediates

As seen in section 5.1.3, pyridylidenes are an emerging area of study. The pyridylidene structure has been used so far in this chapter with the formal bond determinations of **509**, **510** and **N11** (seen below in Figure 5.53 and discussed in more detail in section 5.2.13). Another potential mechanism involving pyridylidenes such as **N17** (also seen in Figure 5.53) was considered as a possible pathway to the formation of 2-styrylpyridine.

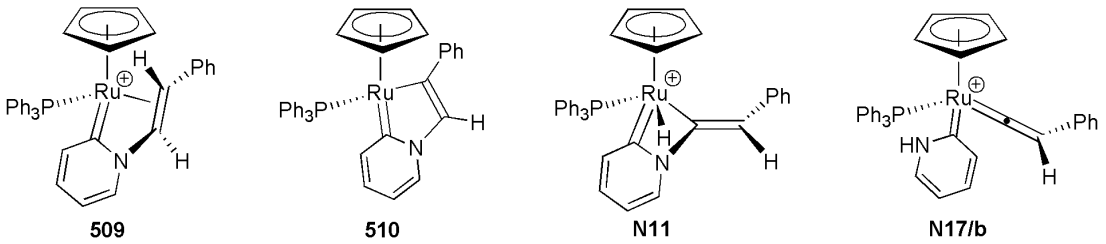

Figure 5.53 – ***509****,* ***510****,* ***N11*** *and* ***N17/b****.*

The study began by investigating the relative stability of pyridylidene analogues compared to their pyridine counterparts. To that end the energy of **503** was compared with **N17**, and **507** and **N3** were compared with **N18** and **N19** respectively (Figure 5.54). All pyridylidene isomers are shown to be higher in energy than their pyridine counterparts by ~ 10-30 kJ mol^{-1}, with **N17** seeing the lowest energy change at +12 kJ mol^{-1}. Given the small difference between **503** and **N17**, a pyridylidene-based mechanism for the formation of 2-styrylpyridine *via* **N17** was then explored.

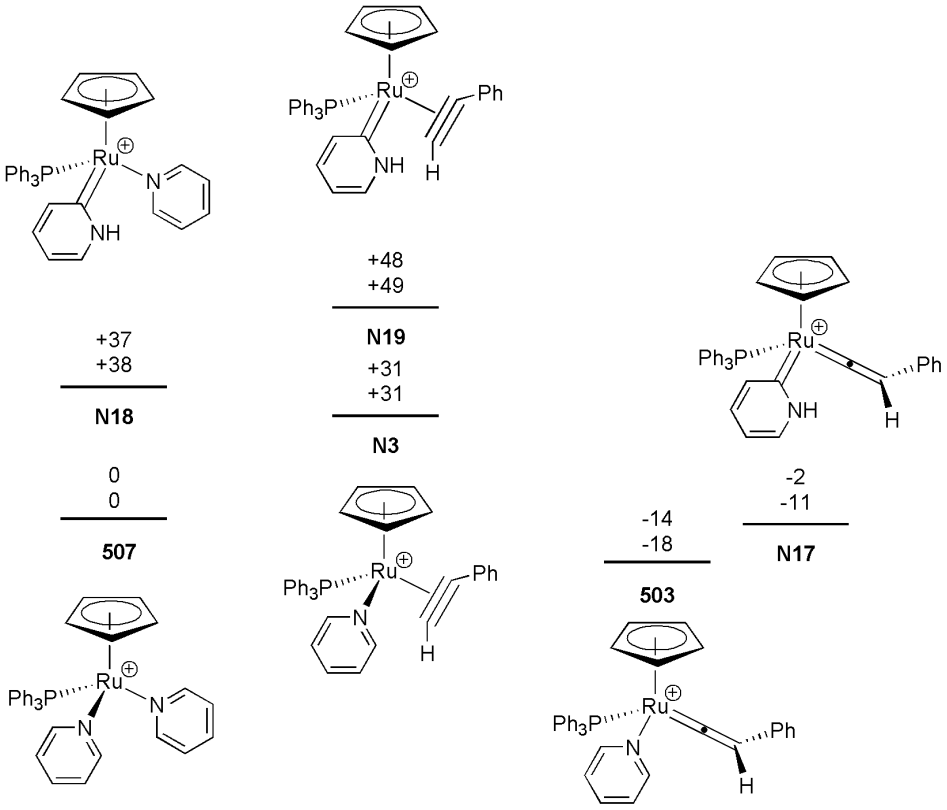

*Figure 5.54 – Comparison of **507**, **N3**, and **503** against **N18**, **N19**, and **N17**. Energies are ZPE corrected SCF (top) and Gibbs free (bottom) energies with COSMO solvation in kJ mol^{-1}, relative to **507**.*

From complex **N17**, it could be assumed pyridine migration occurs through the transition state $\mathbf{TS_{N17\text{-}N20}}$ to form isomer **N20**. As in previous systems, proton transfer would then have to occur either through external deprotonation/protonation through **505**, or by intermolecular proton shuttling, direct transfer *via* $\mathbf{TS_{N20\text{-}N5}}$, or the ruthenium (IV) metal hydride **N21**. A summary of all these mechanisms is shown in Figure 5.55, with a PES in Figure 5.56.

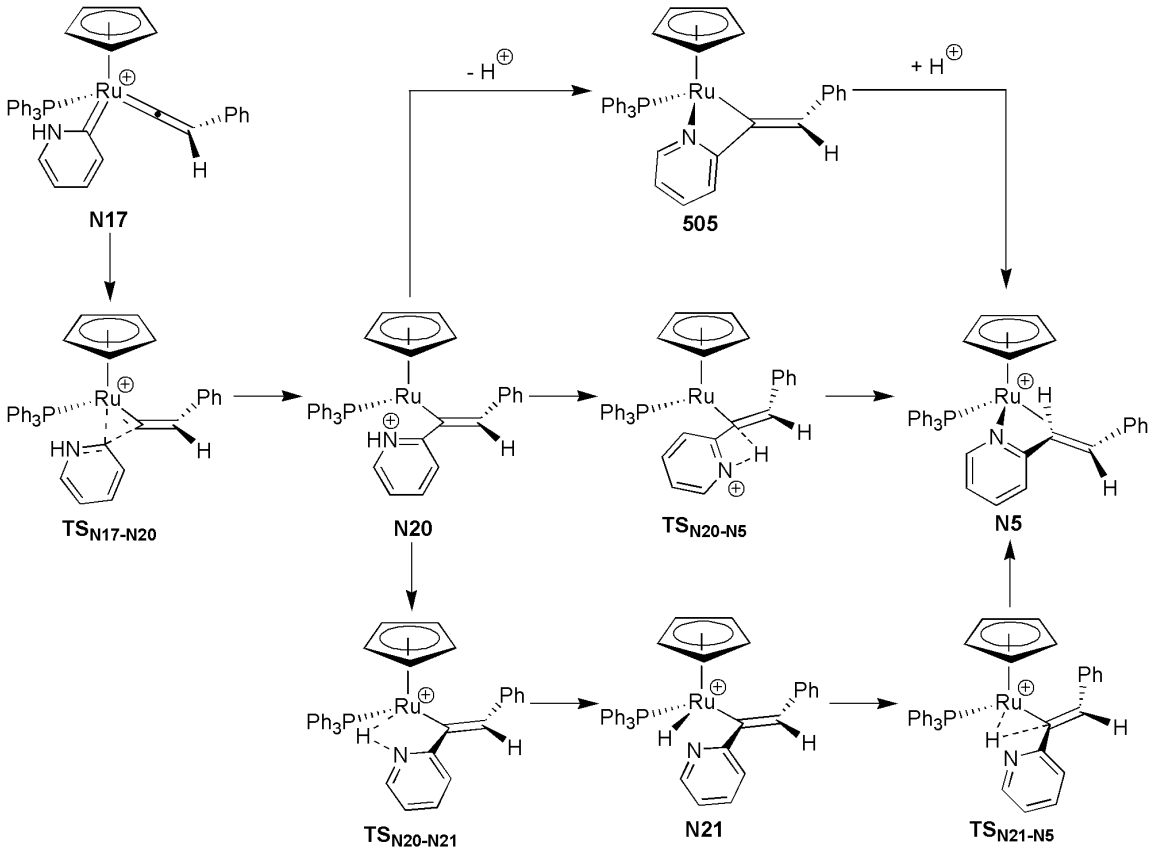

Figure 5.55 – Pyridylidene-based mechanism of product formation.

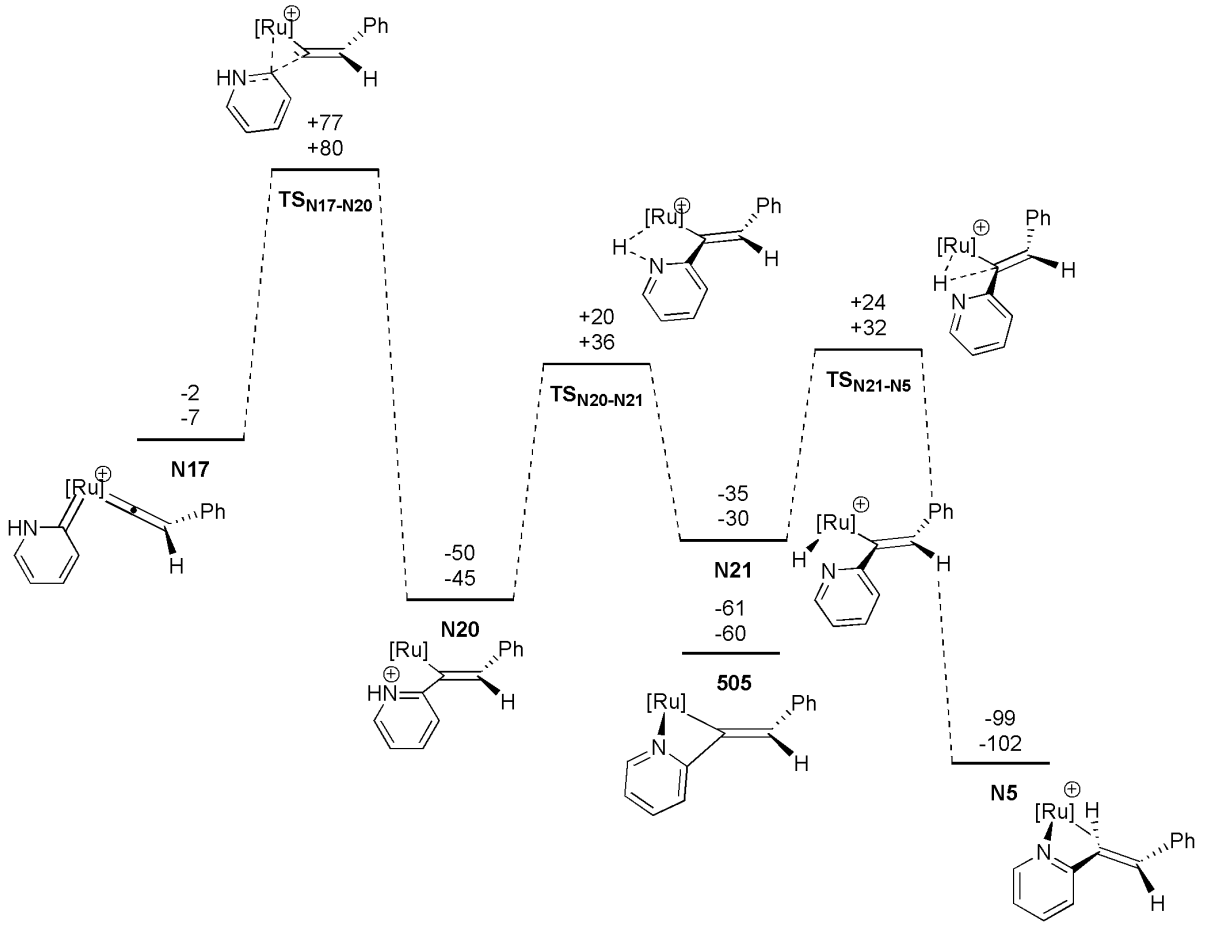

*Figure 5.56 – PES for the formation of **N5** with a pyridylidene-based mechanism. Energies are ZPE corrected SCF (top) and Gibbs free (bottom) energies with COSMO solvation in kJ mol^{-1}, relative to **507**. [Ru] = [CpRu(PPh$_3$)].*

From the PES it appears that this mechanism is one with a feasible barrier for the reaction conditions of 323 K, with the kinetic barrier being $\mathbf{TS_{N17\text{-}N20}}$ at +77 kJ mol^{-1} relative to **507**. This is the lowest energy transition state of all previously discussed mechanisms, giving an energetic span of 91 kJ mol^{-1} (TDI=**503**, TDTS= $\mathbf{TS_{N17\text{-}N20}}$). In terms of pyridyl-vinyl proton transfer, while the lowest pathway appeared to be through the deprotonated complex **505**, the metal hydride-mediated mechanism is still at an acceptable energy for the experimental conditions, adding a level of ambiguity as to the identification of the actual process. The mechanism of direct proton transfer *via* $\mathbf{TS_{N20\text{-}N5}}$ could not be located on the surface, with the geometry optimising to that of **N21** or **N5**.

After examining the method of product formation, attention turned to the generation of the pyridylidene intermediate **N17**. As was seen previously in section 5.1.3, pyridylidenes are usually formed with proton transfer mediated through proton accepting ligands or *via* the metal centre. To this end, a suitable transfer mechanism was investigated from intermediate **503**.

The intermolecular transfer begins with the formation of an agostic pyridine C-H bond in structure **N22**, which then slips to form the pyridylidene through $\mathbf{TS_{N22\text{-}N17}}$, with a brief key and PES shown in Figure 5.57.

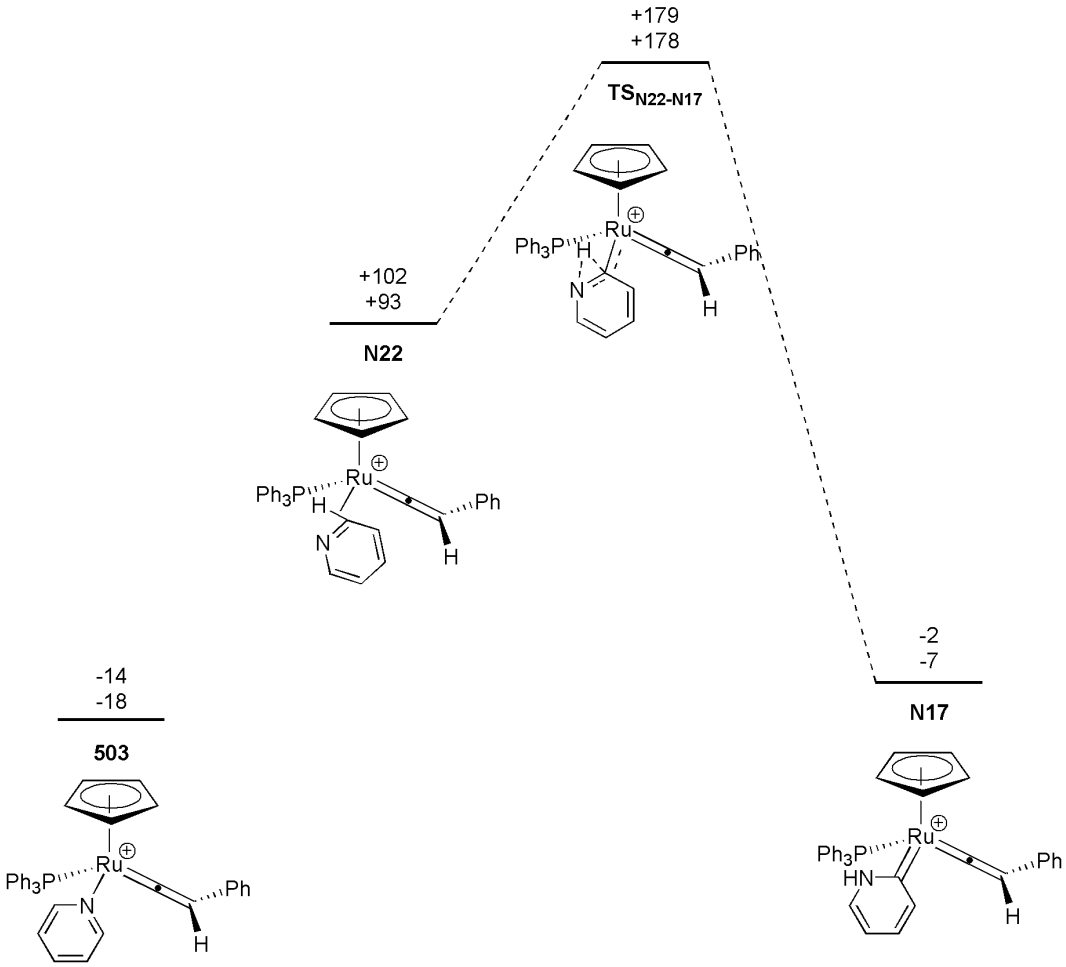

*Figure 5.57 – Formation of the pyridylidene from **503**. Energies are ZPE corrected SCF (top) and Gibbs free (bottom) energies with COSMO solvation in kJ mol^{-1}, relative to **507**.*

The transition state for intramolecular proton migration is shown to be unacceptably high in energy at +179 kJ mol^{-1} for reaction temperatures of 323 K. Therefore it is assumed that formation of **N17** is formed by intermolecular proton shuttling *via* a free pyridine molecule, where deprotonation of the activated ortho C-H group occurs followed by protonation of the nitrogen atom with pyridinium.

5.2.8 Complete Reaction Mechanism to Final Organic Product

Having completed an investigation into several possible methods of forming the final organic product, a complete mechanism can be proposed. Initial work on the mechanism proposed by Murakami and Hori suggested a concerted vinyl insertion on the pyridine ortho-carbon, which is not consistent with the observation in experimental studies of product formation at 323 K, with a barrier height of +154 kJ mol^{-1} relative to **507**.

509 is also shown to be a valid point on the PES both theoretically and experimentally. However attempts to use intermediate **509** and the deprotonated isomer **510** in a product formation pathway proved to be unsuccessful owing to a combination of high barrier heights and the overall stability of **509**. It was therefore proposed that **509** and **510** were deactivation products in the overall reaction, with access to the organic product achievable only with high temperatures from **509**.

The pathways from deprotonated complex **N15** and pyridylidene **N17** involving pyridine migration (seen in Figure 5.52 and Figure 5.56) are both seen to be favourable in energy with the highest energy transition states being found at +77 and +90 kJ mol^{-1} respectively. However a prohibitive barrier with regard to pyridylidene formation (+179 kJ mol^{-1} relative to **507**) as well as the aforementioned problem of forming **N15** directly from **509** means this pathway is problematic. But given the presence of pyridine in the reaction mixture, it may be assumed that deprotonation/protonation can occur. For example the agostic C-H bond in **N10** and **N22** can be deprotonated to form **N15**, with protonation forming the pyridylidene **N17** (Figure 5.58).

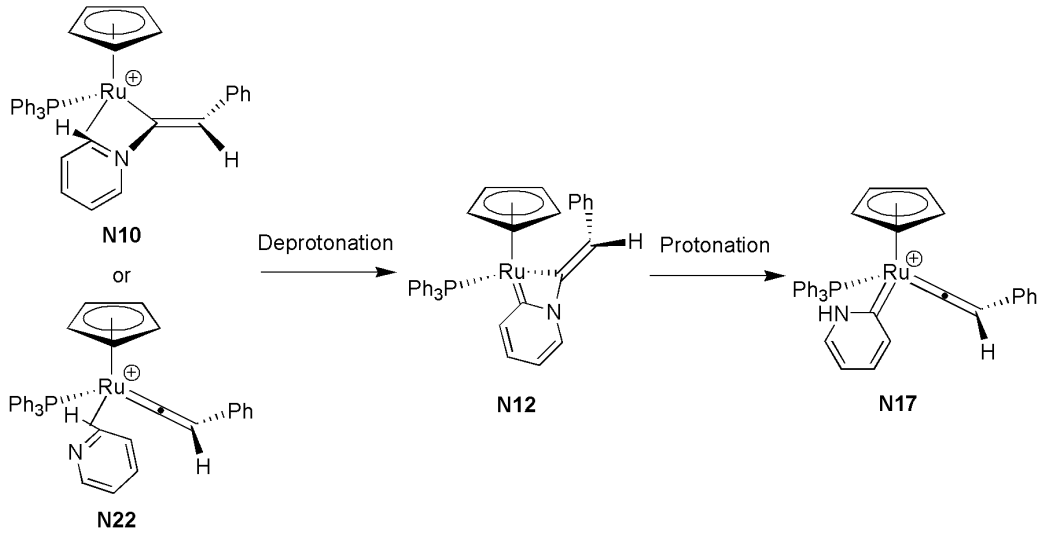

*Figure 5.58 – Formation of **N15** and **N17** through deprotonation/protonation steps.*

The deprotonation mechanism is corroborated by the presence of stationary point **N23**, where the pyridyl C-H bond of **N10** undergoes oxidative addition *via* $\mathbf{TS_{N10\text{-}N23}}$ to the ruthenium centre, followed by deprotonation which forms **N12** (Figure 5.59).

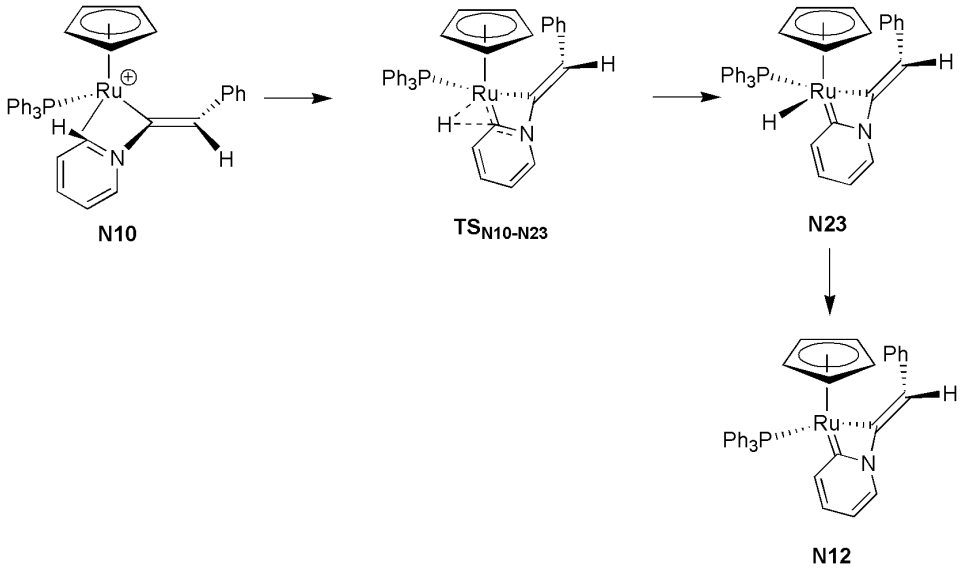

*Figure 5.59 – Formation of **N12** from **N10**.*

$TS_{N10-N23}$ and **N23** was calculated and is shown in the PES below (Figure 5.60). **$TS_{N10-N23}$** and **N23** are shown to be an accessible transition state and stationary point in the formation of **N12**. Additionally the energy of **$TS_{N10-N23}$** is lower than state **N10** with it being possible that **$TS_{N10-N23}$** is actually a direct transition state from **N9**.

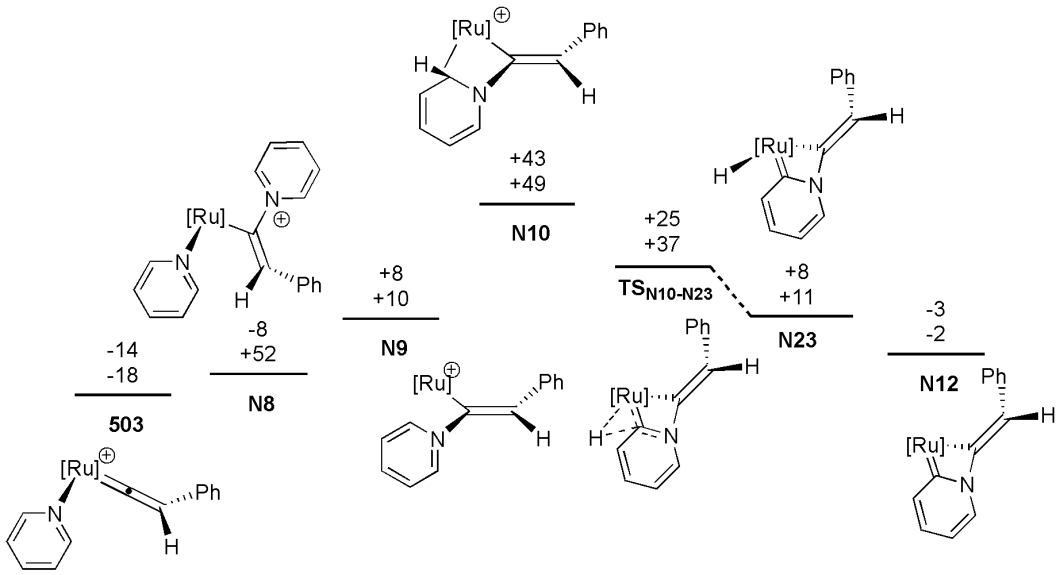

*Figure 5.60 – Formation of **N12** from **503** through **N23**. Energies are ZPE corrected SCF (top) and Gibbs free energies (bottom) with COSMO solvation in kJ mol^{-1}, relative to **507**. [Ru] = [CpRu(PPh$_3$)].*

Supporting the mechanism of deprotonation of either **N10** or **N23** or **N22** (Figure 5.61), a PABOON analysis shows a +0.1267, +0.038 and +0.056 positive charge on the protons of **N10**, **N23** and **N22**.

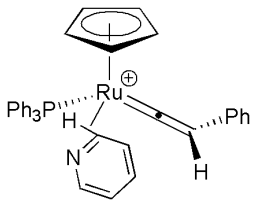

*Figure 5.61 – **N22**.*

This suggests that state **N10**, much like **E4** in chapter 4 has two 'fates'. Proton transfer to the vinyl group *via* **N11** to form **509** can occur under mild conditions, with **509** being the thermodynamic product. However upon application of heat, the reaction proceeds over a kinetic barrier through to intermediate **N15** and finally forming of the organic product and **507** (Figure 5.62).

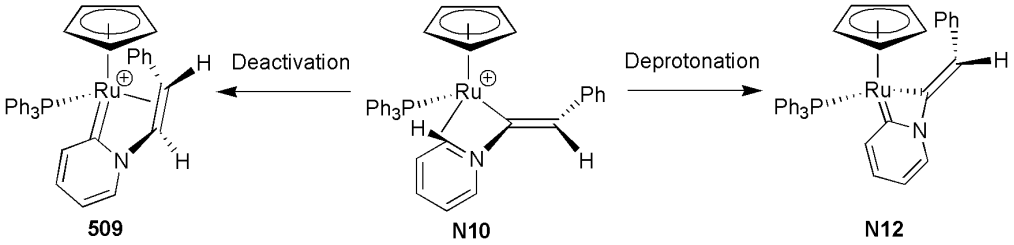

*Figure 5.62 – Two 'fates' of **N10**.*

Through intermediate **N15**, the energetic span is shown to be 108 kJ mol^{-1} (TDI=**503**, TDTS=$\mathbf{TS_{N12\text{-}N15}}$), with **N17** being 91 kJ mol^{-1} (TDI=**503**, TDTS= $\mathbf{TS_{N17\text{-}N20}}$). Both of these barriers are accessible with reaction conditions of 323 K at 24 h.

Finally, the release of the organic product to reform **507** through **N5**, **N6** and **N7** was also shown to be feasible. The side-bound vinyl product **511** was shown to be far lower in energy than these intermediates at -148 kJ mol^{-1}, but given that it is the only coordinated product isomer with a η^2-vinyl interaction, it may not be a directly connected intermediate and may be a resting state. The low energy shows that the reaction has a significant thermodynamic driving force which agrees with experiment.

In summary, it is shown that **509** and **510** are not intermediates in the formation of 2-styrylpyridine but are in fact deactivation products. The formation of 2-styrylpyridine through **N15** is kinetically controlled, with enough heat overcoming the barrier to form the organic product and regenerate the catalyst **507**. A complete and final reaction mechanism can be seen in Figure 5.63.

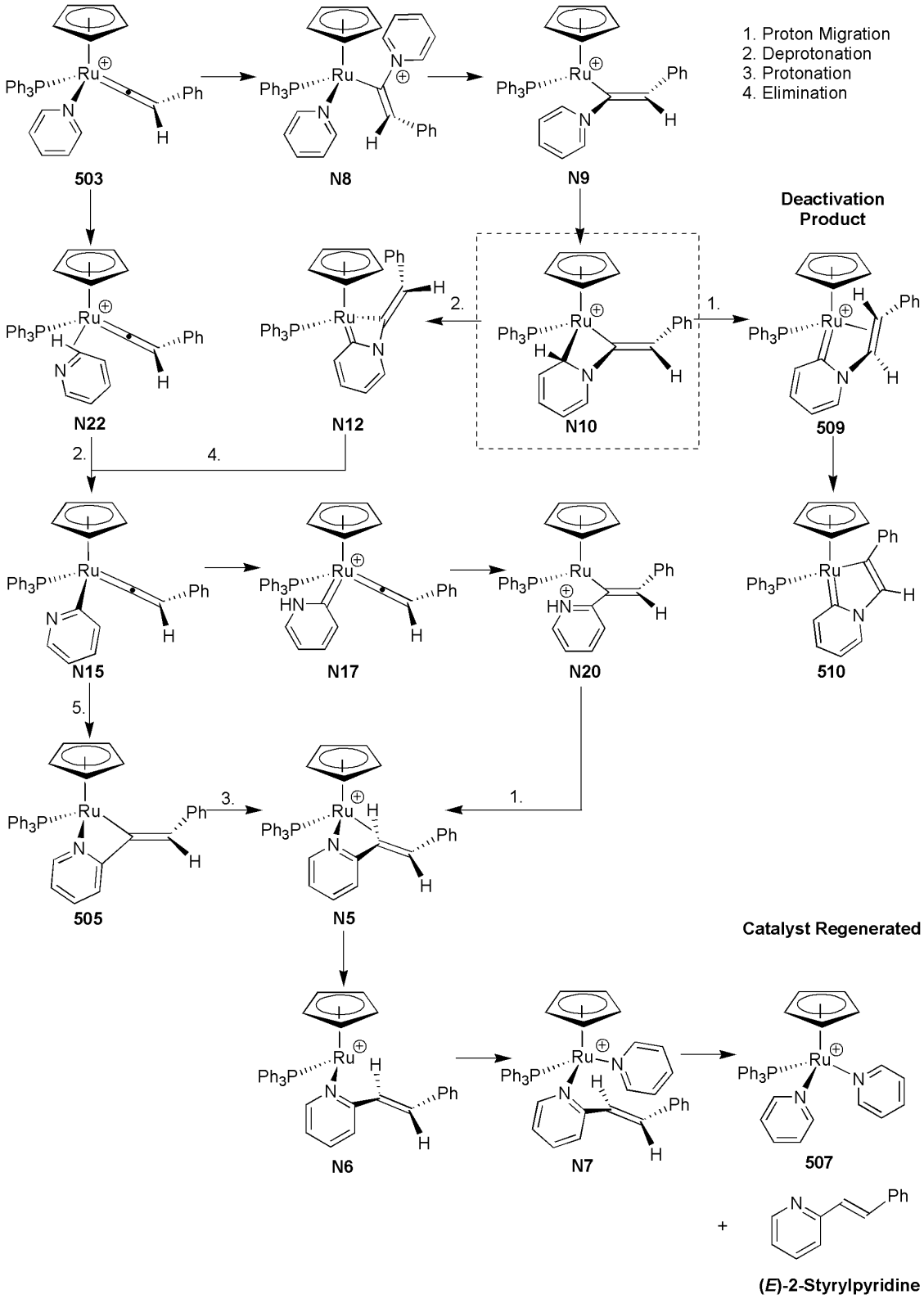

*Figure 5.63 – Complete reaction cycle for formation of organic product. For simplicity formation is shown proceeding from **503**, with several transition states excluded.*

5.2.9 Stereoselectivity of Mechanism

As was seen experimentally, (*E*)-2-styrylpyridine was shown to be the major organic product, implying a degree of stereoselective control, or post-reaction isomerisation which was suggested by Murakami & Hori. To this extent, a complete survey was performed looking at the formation of (*Z*)-2-styrylpyridine, with two surfaces for the 'conventional' and 'pyridylidene' based pathways being shown in Figure 5.66 and Figure 5.67 respectively.

The 'deprotonation-mediated' pathway involves the deprotonation of **N10** or **N22** to form **N15**, after which the pyridyl group migrates to form **505** and the final organic product, shown below in Figure 5.64, with a PES shown in Figure 5.66.

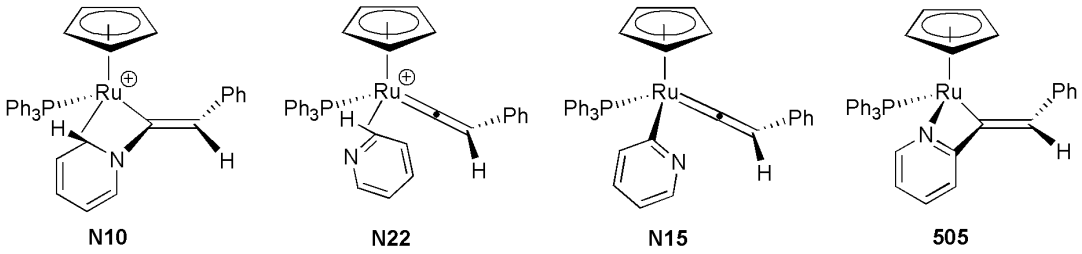

Figure 5.64 – Depiction of the deprotonation-mediated pathway.

The 'pyridylidene' pathway involves the pyridyl carbene complex **N17** undergoing pyridyl migration to form complex **N20**. Proton migration then occurs to ultimately form **N5** and the final organic product. This can be seen below in Figure 5.65, with a PES shown in Figure 5.67.

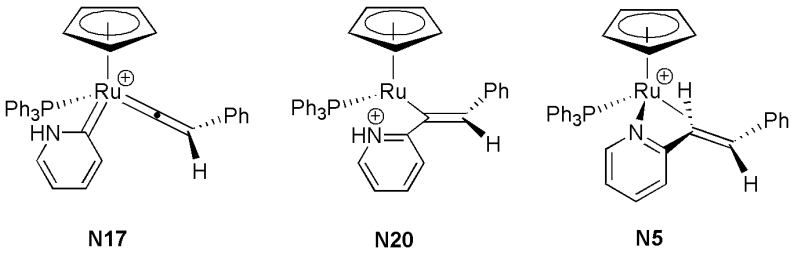

Figure 5.65 – Depiction of the 'pyridylidene' pathway.

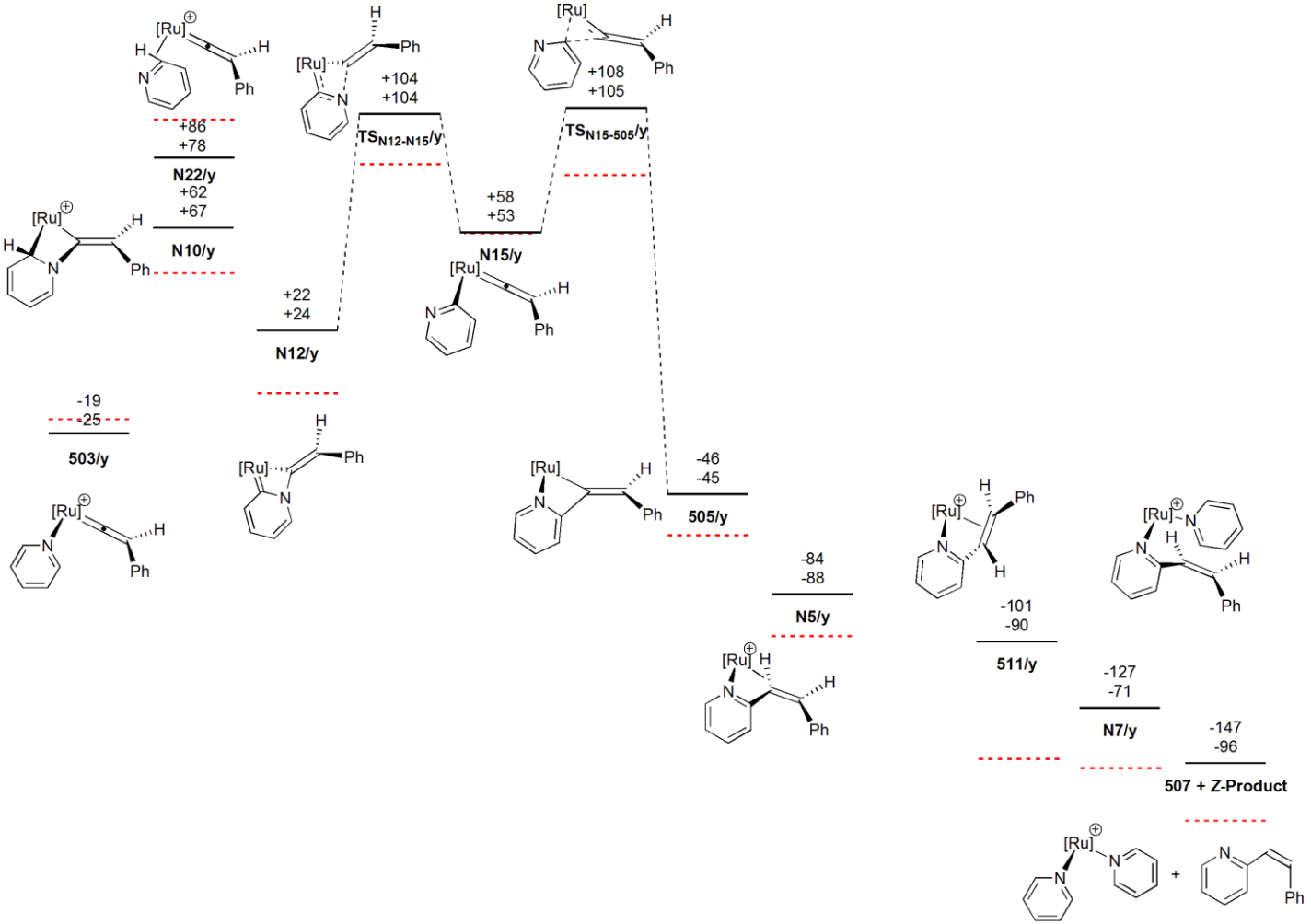

*Figure 5.66 – PES for the formation of (Z)-2-styrylpyridine via 'deprotonation-mediated' pathway. Energies are ZPE corrected SCF (top) and Gibbs free (bottom) energies with COSMO solvation in kJ mol^{-1}, relative to **507**. [Ru] = [CpRu(PPh$_3$)]. Pro-(E)-2-styrylpyridine isomers are shown with red dotted lines.*

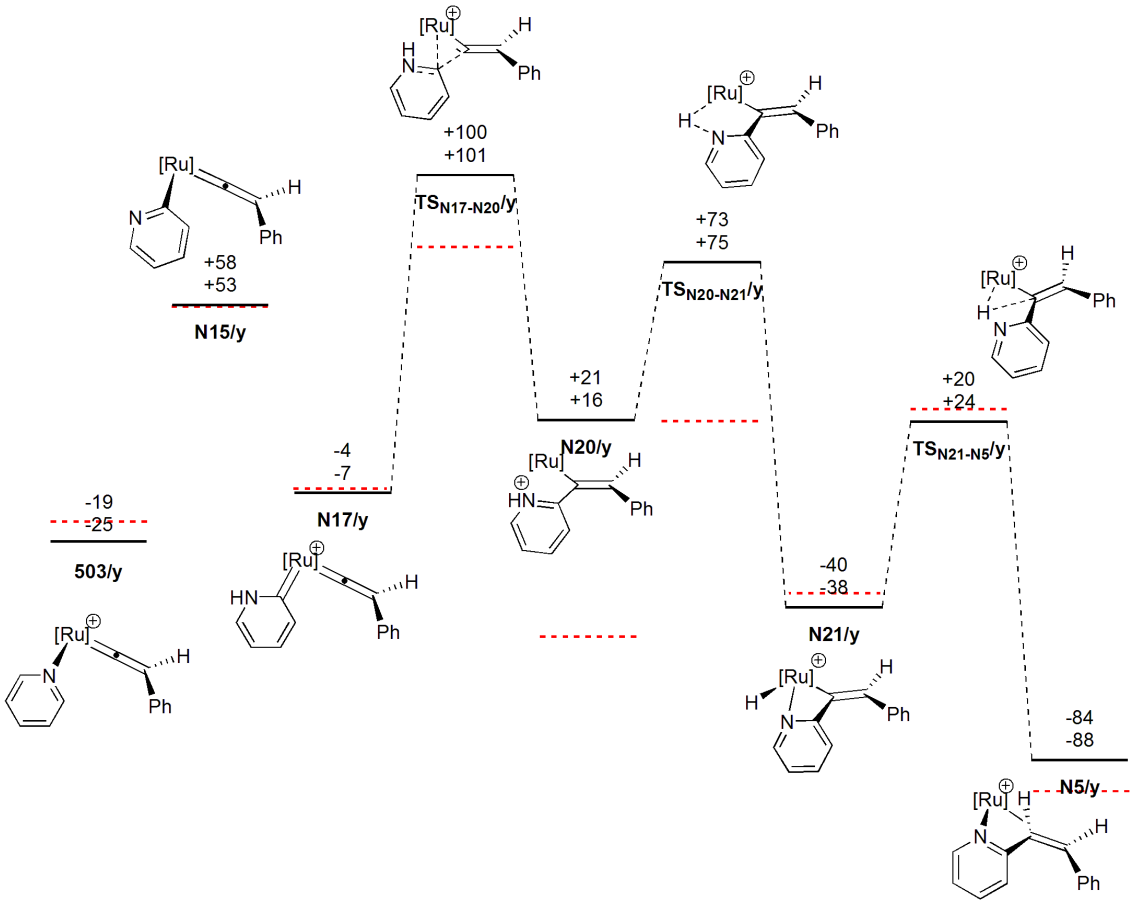

*Figure 5.67 – PES for the formation of **N5** via the 'pyridylidene' pathway. Energies are ZPE corrected SCF (top) and Gibbs free (bottom) energies with COSMO solvation in kJ mol^{-1}, relative to **507**. [Ru] = [CpRu(PPh$_3$)]. Additionally the isomers forming (E)-2-styrylpyridine are shown on the surface with red dotted lines.*

Several key differences are present when compared to the PES for the formation of (*E*)-2-styrylpyridine. Firstly, several stationary points could not be located - most notably the nitrogen-bound product precursor **N6** (shown in Figure 5.52 on page 260 and Figure 5.39 on page 247 respectively) which reverted to complex **N5** when optimised.

Secondly the energetic differences between the two isomers of 2-styrylpyridine seemed to be dependant purely on sterics. For example, in comparison of **507** and the free isomers at the end point of the mechanism in Figure 5.66, (*E*)-2-styrylpyridine was shown to be 25 kJ mol^{-1} lower than the *Z*-isomer. This is simply due to the steric clash of the phenyl and pyridyl groups, shown below in Figure 5.68.

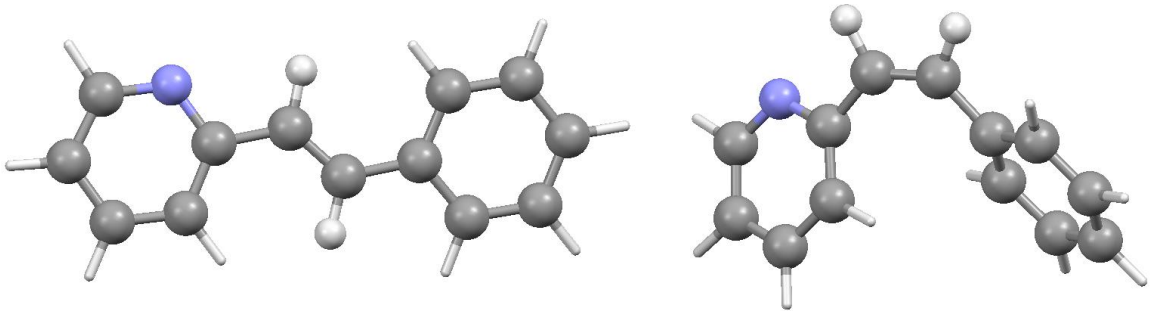

Figure 5.68 – Optimised geometries of (E)-2-styrylpyridine (left) and (Z)-2-styrylpyridine (right).

This phenomenon is responsible for many of the observed gains in energy, for example transition state $\mathbf{TS_{N17\text{-}N20}/y}$ (Figure 5.69) is 23 kJ mol^{-1} higher in energy than the **x** isomer. However for isomers without a vinyl-pyridyl bond, both *E* and *Z* precursors are effectively isoenergetic with one another, one example being **N15/y** (also shown in Figure 5.69).

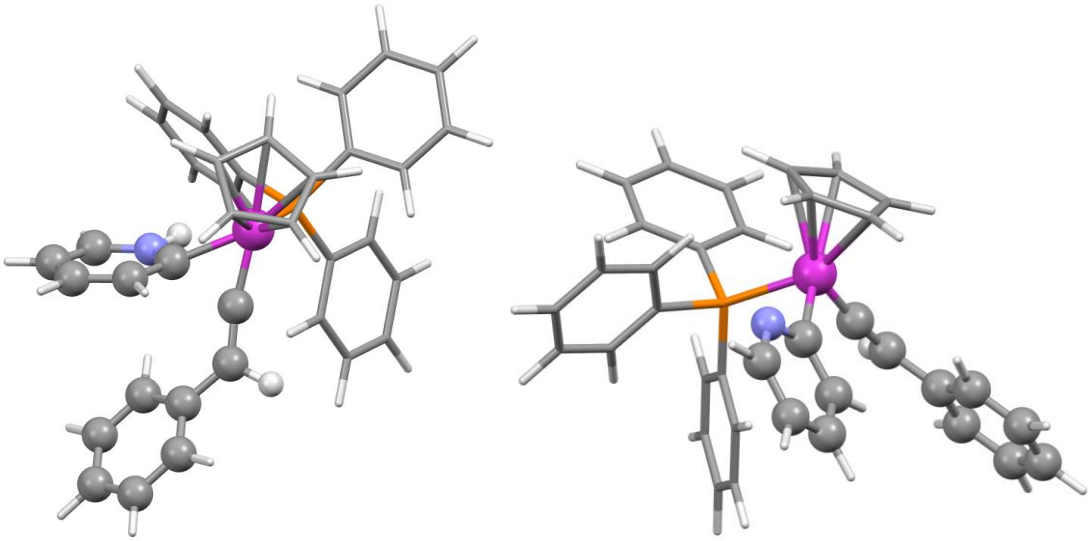

Figure 5.69 – Optimised geometries of ***TS$_{N17-N20}$/y*** *(left) and* ***N15/y*** *(right), showing the effect of sterics on structure.*

Thirdly, the 71 kJ mol^{-1} difference in energy between the two isomers of complex **N20** (Figure 5.67) was explained by a different steric interaction, this time between the phenyl group and the ruthenium centre. The difference between the *E* and *Z* precursor is explained by the lack of an agostic interaction between the ruthenium centre and the phenyl group. As can be seen below in Figure 5.70, **N20/x** possesses a close Ru-C distance with respect to the ortho-phenyl group, which stabilises the otherwise coordinatively unsaturated ruthenium centre. This is something, which due to the phenyl orientation, **N20/y** is unable to do, raising the overall energy of the isomer significantly by 71 kJ mol^{-1}.

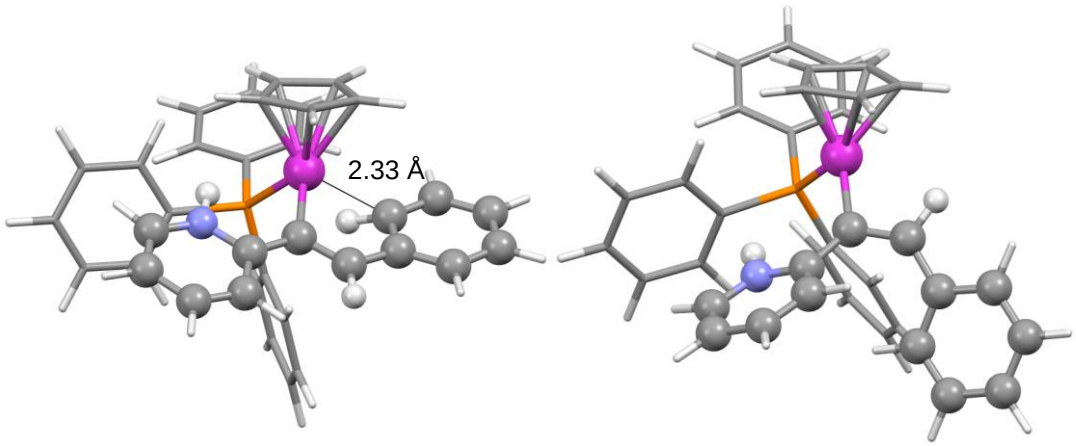

*Figure 5.70 – Optimised geometries of **N20/x** (left) and **N20/y** (right).*

The overall energetic span of the **x** isomers for the 'deprotonation mediated' and 'pyridylidene' pathway was shown previously to be 108 kJ mol^{-1} (TDI=**503**, TDTS=**TS$_{N12\text{-}N15}$**) and 91 kJ mol^{-1} (TDI=**503**, TDTS= **TS$_{N17\text{-}N20}$**) respectively. For the **y** isomer, the span is 127 kJ mol^{-1} (TDI=**503**, TDTS=**TS$_{N15\text{-}505}$**) and 119 kJ mol^{-1} (TDI=**503**, TDTS= **TS$_{N17\text{-}N20}$**) respectively. This clearly shows at least a 19 kJ mol^{-1} rise in energy associated with formation of (*Z*)-2-styrylpyridine.

In the initial research paper by Murakami and Hori,[265] heating the pre-formed *Z*-isomer with [CpRu(PPh$_3$)$_2$Cl] produced the *E*-isomer. While 2-styrylpyridine coordination could provide electron donation into the alkene thus weakening it and allowing rotation, it would seem that selectivity for the *E*-isomer is largely driven by kinetic factors.

5.2.10 Substituent Effects – 4-ethynyl-α,α,α-trifluorobenzene

The role of substituent effects with respect to 4-ethynyl-α,α,α-trifluorobenzene was presented in section 5.1.5, with the substituted alkyne being shown to prevent the formation of side products in the formation of **513** (Figure 5.71), suggesting a lower minimum or kinetic barrier is required to produce the deactivation product. This and other differences were investigated with the construction of a PES for the 4-ethynyl-α,α,α-trifluorobenzene pathway – system **O**. The full key and PES is viewable in appendix section C.1, with the most important points listed here.

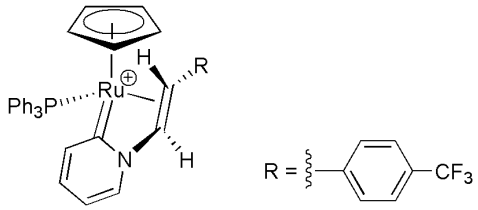

*Figure 5.71 – **513**.*

The formation of **513** is nearly identical to the mechanism seen with phenylacetylene (system **N**) with one major difference. Stationary point **O2**, the analogue of state **N9**, is found to be +69 kJ mol^{-1} in energy relative to **507**, compared with +8 kJ mol^{-1} for **N9**. This difference can be explained by the agostic bond of the phenyl ortho C-H bond which stabilises both isomers (Figure 5.72). While both **N9** and **O2** have the same agostic bond length, **O2** possesses a highly electron withdrawing CF_3 group, removing electron density from the phenyl ring and thus destabilising the unsaturated ruthenium centre.

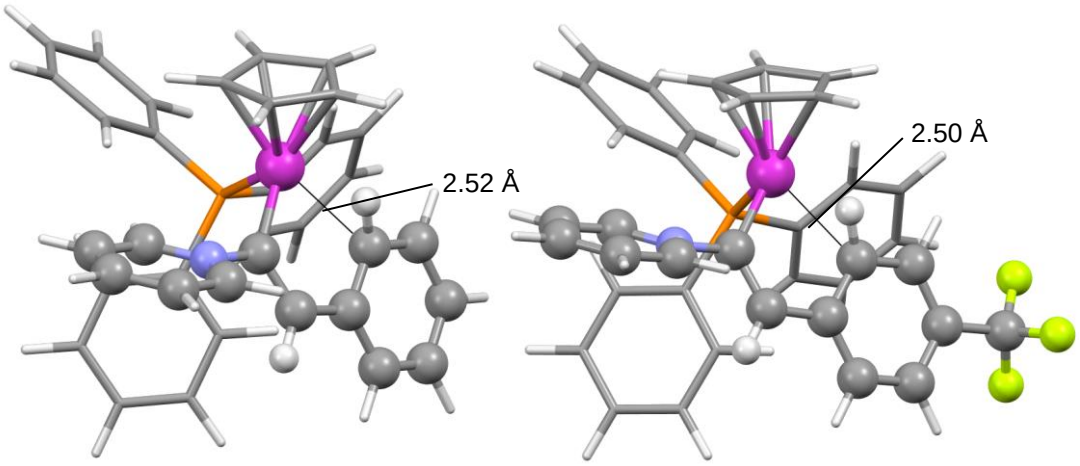

*Figure 5.72 – Structure of **N9** (left) and **O2** (right).*

It is possible that **O2** and **N9** are potential precursors to formation of the pi-allyl carbene dimer side product (**508** in the phenylacetylene pathway - Figure 5.73), meaning the high energy of **O2** may be the reason the dimer is not seen in this system experimentally.

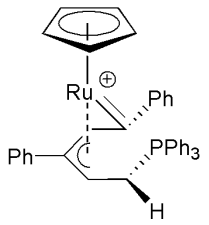

*Figure 5.73 – **508**.*

All other pathways were similar to the phenylacetylene system, with the energy difference of most isomers being no larger than 10 kJ mol^{-1}. In terms of the energetic span for the formation of 2-(4-(trifluoromethyl)styrylpyridine), the 'deprotonation mediated' pathway is shown to be 104 kJ mol^{-1} (TDI =**512**, TDTS = $\mathbf{TS_{O5\text{-}O7}}$) and the 'pyridylidene mediated' pathway is 90 kJ mol^{-1} (TDI = **512**, TDTS = $\mathbf{TS_{O14\text{-}O15}}$). This did not contrast with the phenylacetylene pathway, with an energetic span of 108 and 91 kJ mol^{-1} respectively. This negligible difference in the energetic spans when comparing system **N** and **O** agrees with experiment, where identical temperatures were used for the productive reaction for both alkynes.

5.2.11 Substituent Effects – Trimethylphosphine

In addition to the results of the 4-ethynyl-α,α,α-trifluorobenzene survey, work was also undertaken on the reaction with a trimethylphosphine ligand in place of triphenylphosphine. Experimentally it was shown that the stoichiometric reaction in dichloromethane did not produce the deactivation product **516** (Figure 5.74), instead producing the trimethylphosphine analogue of the pi-allyl carbene complex **508**.

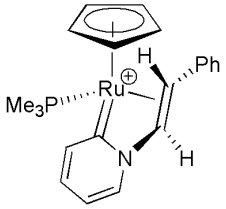

*Figure 5.74 – **516**.*

Additionally the reaction in pyridine at 323 K produced 2-styrylpyridine as well as the deactivation product **516**, which was also not seen in the other ligand/alkyne reactions. A PES was once again constructed for the trimethylphosphine ligand (system **P**), with full details available in appendix section C.3.

The deactivation product is shown to be 9 kJ mol^{-1} lower in energy than with triphenylphosphine, with the energetic span shown to be 73 kJ mol^{-1} (TDI= **P1**, TDTS = $\mathbf{TS_{P4\text{-}P5}}$) - 1 kJ mol^{-1} higher than with triphenylphosphine. Productive mechanisms through the 'deprotonation mediated' and 'pyridylidene mediated' pathways possessed an energetic span of 116 kJ mol^{-1} (TDI= **P1**, TDTS= $\mathbf{TS_{P9\text{-}P10}}$) and 99 kJ mol^{-1} (TDI= **P1**, TDTS= $\mathbf{TS_{P18\text{-}P19}}$) respectively. These are both 8 kJ mol^{-1} higher than the triphenylphosphine mechanistic pathway.

Both the larger energetic span for the productive pathways, and the more stable deactivation product suggest a reason as to why the deactivation product is seen in the reaction with excess pyridine at 323 K. However this does not explain the lack of observed deactivation product when reacted in dichloromethane solution.

5.2.12 Substituent Effects – 3-Methylpyridine

Substituted pyridines were investigated experimentally both in the original paper by Murakami and Hori[265] as well as in experimental investigations by Dr Neetisha Mistry and Lucy Milner detailed in section 5.1.5. The experiments showed that much like with triphenylphosphine, phenylacetylene and pyridine, with the room-temperature reaction in DCM giving the deactivation product **517** (Figure 5.75), with the organic product (*E*)-2-styryl-5-methylpyridine (Figure 5.76) produced upon heating the mixture with an excess of 3-methylpyridine.

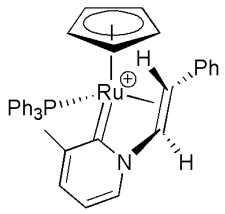

*Figure 5.75 – **517/p**.*

In terms of 3-methylpyridine, it was observed that (*E*)-2-styryl-5-methylpyridine was produced exclusively with little or no formation of the alternate product (*E*)-2-styryl-3-methylpyridine (Figure 5.76). However in the formation of the deactivation product **517**, two distinct orientations of the 3-methylpyridine group were observed.

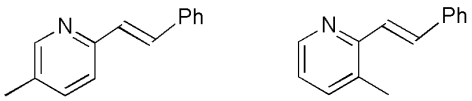

Figure 5.76 – (E)-2-styryl-5-methylpyridine (left) and (E)-2-styryl-3-methylpyridine (right).

To account for this mechanistically, several points key to the formation of both the organic and deactivation product were investigated. A small PES was created, looking at the TDI's and TDTS's involved in production of the deactivation and organic products. 3-methylpyridine's dielectric constant was used in the COSMO solvation calculations.

The PES would allow for the difference between **p** and **q** isomers to be determined, where **p** is the isomer where the methyl group is furthest away from the vinyl group proceeding clockwise around the pyridyl ring, leading to (*E*)-2-styryl-5-methylpyridine in the productive pathway. The **q** isomer is closest to the vinyl group, instead forming (*E*)-2-styryl-3-methylpyridine (Figure 5.77).

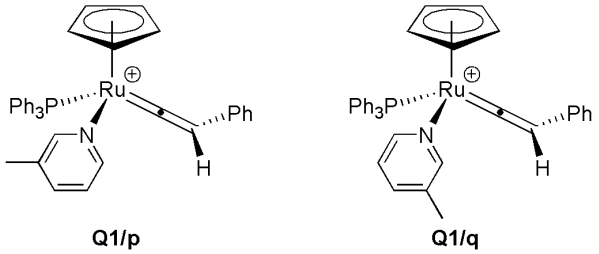

*Figure 5.77 – Difference between **p** and **q** isomers.*

A brief key can be seen below in Figure 5.78, which shows the early intermediates **Q1** and **Q2**, the highest energy transition state $\mathbf{TS_{Q3}}$ and deactivation product **517**, as well as product formation transition states $\mathbf{TS_{Q4}}$, $\mathbf{TS_{Q5}}$ ('deprotonation mediated' mechanism) and $\mathbf{TS_{Q6}}$ ('pyridylidene mediated' mechanism) and the coordinated product intermediates **Q7** and **Q8**. A PES can be seen in Figure 5.79.

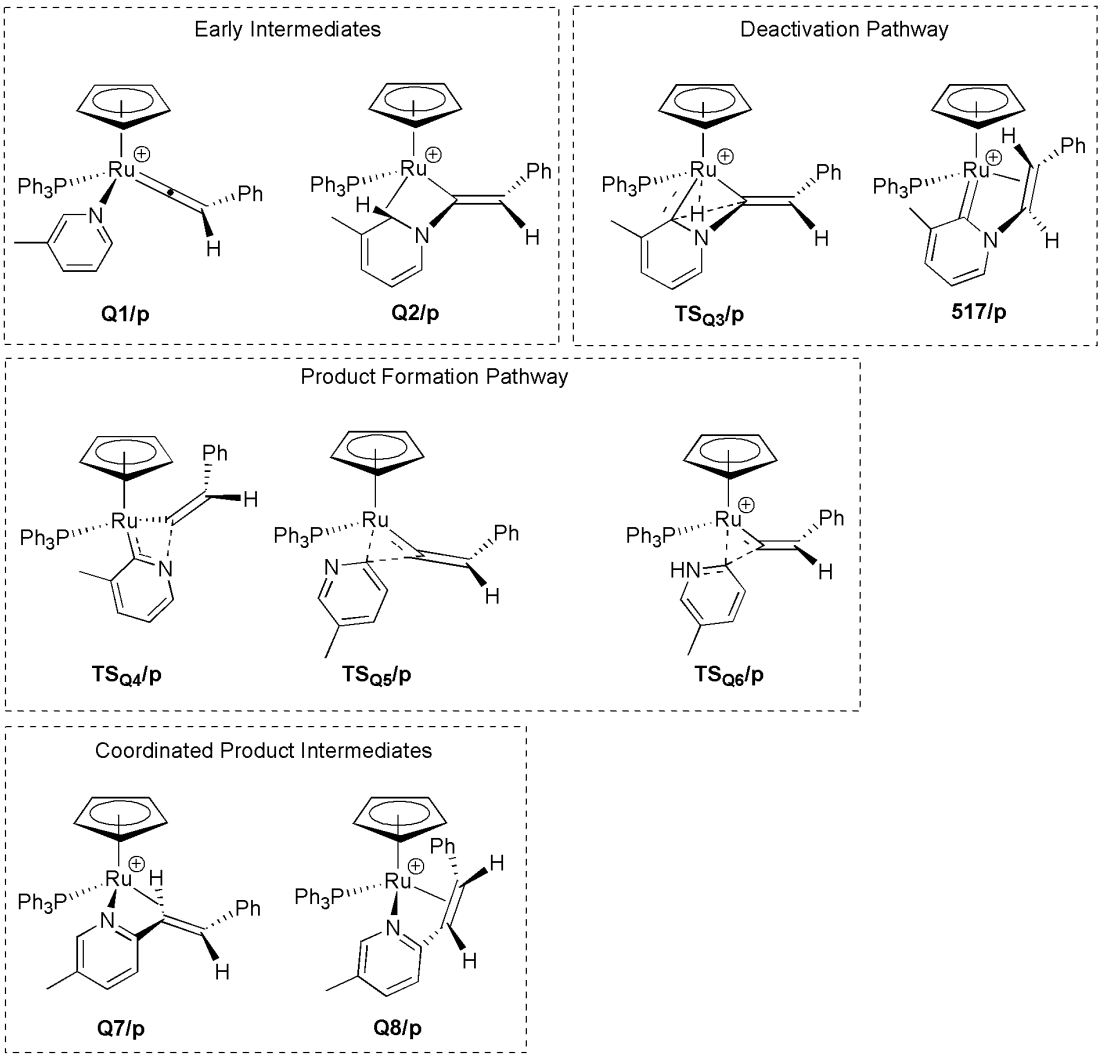

*Figure 5.78 – Key for 3-methylpyridine PES. For simplicity only the **p** isomers are shown.*

As can be seen from the results, the two potential isomers of intermediates **Q1** and **Q2** are isoenergetic with one another, which is due to the methyl group being far enough away from the vinyl group to prevent any steric clash. In the deactivation product formation, while the **p** and **q** isomers are once again roughly isoenergetic, the **q** isomer is slightly lower for **517** by 6 kJ mol^{-1}, but overall little preference for formation of either isomer is shown.

In terms of the overall energetic span, the deactivation product possessed an energetic span of 80 and 82 kJ mol^{-1} for the **p** and **q** isomers respectively. Given the experimental observation of both **p** and **q** isomers of **514**, this agrees with the spans of both isomers being isoenergetic with one another.

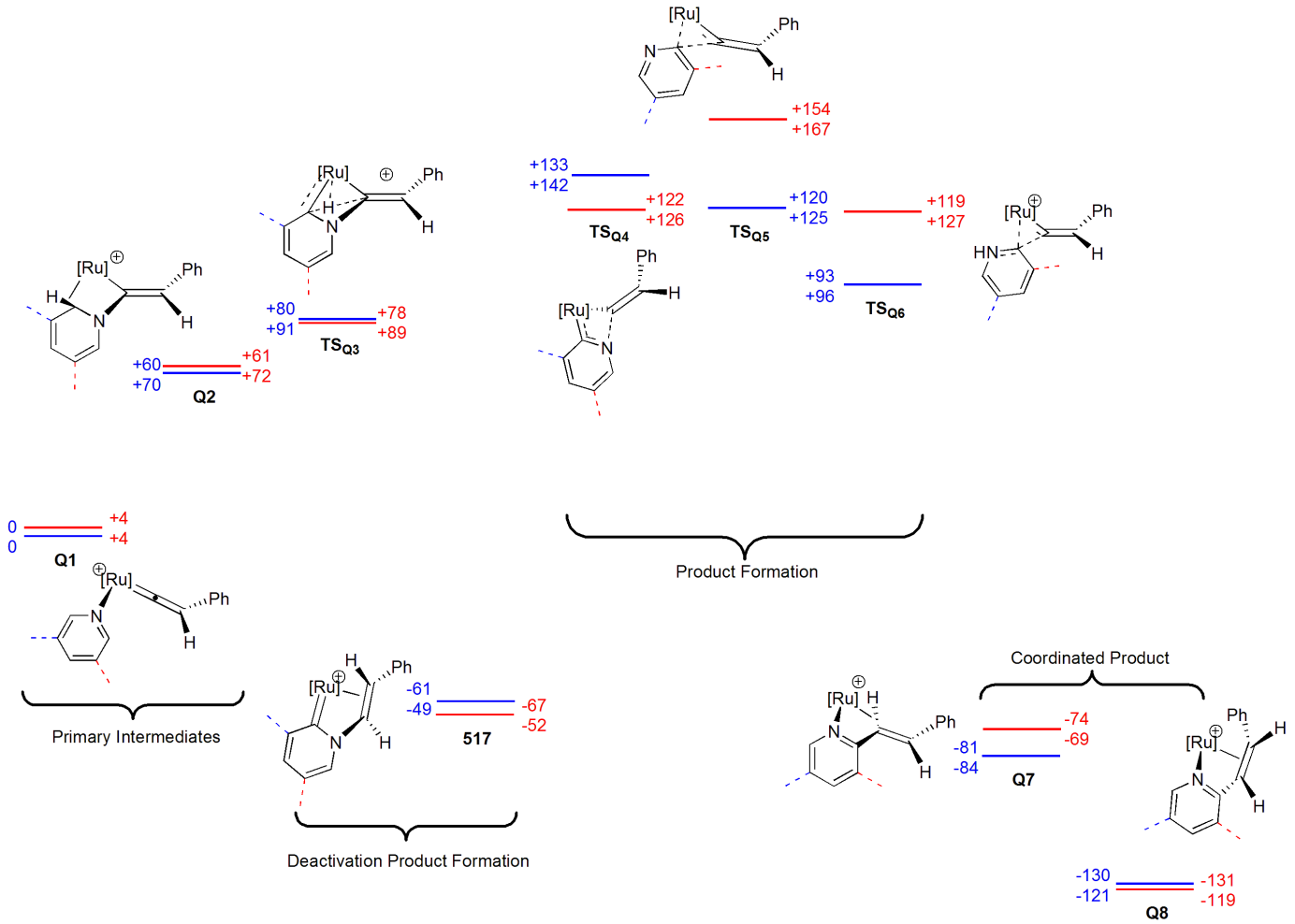

*Figure 5.79 – Small PES with key points for 3-methylpyridine mechanism. **P** isomers are coloured blue, with **q** being red. Energies are ZPE corrected SCF (top) and Gibbs free (bottom) energies with COSMO solvation in kJ mol^{-1}, relative to **Q1**. [Ru] = [CpRu(PPh$_3$)].*

However in the formation of the organic product, a steric clash with the vinyl group favours the **p** isomers by 34 and 26 kJ mol^{-1} for the rate-determining transition states $\mathbf{TS_{Q5}}$ and $\mathbf{TS_{Q6}}$ respectively. The coordinated products **Q7** and **Q8** were once again roughly isoenergetic, with **Q7/p** being lower by 7 kJ mol^{-1}.

In terms of the energetic span, $\mathbf{TS_{Q4}}$ and $\mathbf{TS_{Q6}}$ are the TDTS's for the **p** isomer PES, with $\mathbf{TS_{Q5}}$ and $\mathbf{TS_{Q6}}$ being the TDTS for the **q** isomer. For the **p** isomer, the energetic span was shown to be 133 and 93 kJ mol^{-1} for the deprotonation and pyridylidene mediated mechanisms, with the **q** isomer being 154 and 119 kJ mol^{-1}. This supports the experimental observation shown in section 5.1.5 that formation of the organic product had a preference for the **p** isomer of (*E*)-2-styryl-5-methylpyridine, with the energetic spans for the **q** isomer being ca. 20 kJ mol^{-1} greater in energy.

5.2.13 Verification of Pyridylidene Intermediates

As seen in previous sections, pyridylidene bonds were formally assigned to structures such as **509**, **510**, **N11** and **N17** (Figure 5.80). Given the importance these structures play in the overall mechanism of organic product formation, it was deemed necessary to investigate the nature of these ligands. As was shown in section 5.1.3, pyridylidenes are carbene tautomers of pyridine which are bound to the metal centre through the *ortho* pyridyl carbon. The metal carbon bond has been formally described as a single, partial double or double bond in various studies, and the chemistry of this bond as well as the entire complex is of significant interest. The investigation involved comparing these 'pyridylidene' intermediates against 'pyridyl' structures **N14**, and **N15** (also Figure 5.80) in terms of structural parameters and electronic structure in order to elucidate the nature of the bonding.

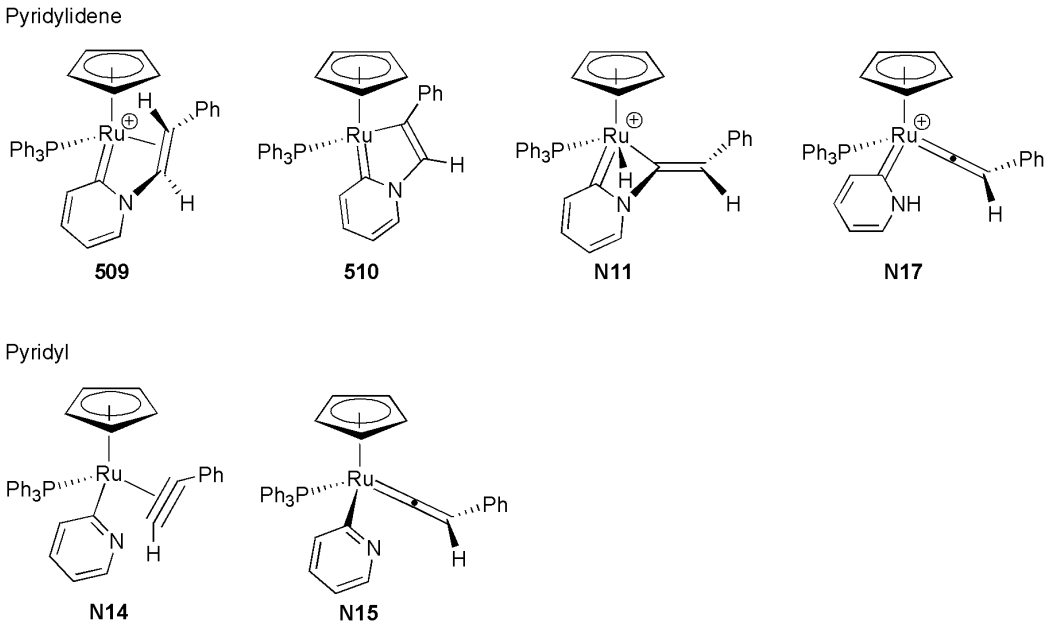

Figure 5.80 – Selected pyridylidene and pyridyl structures.

The bond lengths of the pyridine ring were compared for all six structures, as well as the Ru-C^1 bond length, shown below in Table 5.6. The 'pyridyl' complexes **N14** and **N15** possess the longest Ru-C^1 bond lengths, being in some instances 0.1 Å longer than the pyridylidene structures excluding **N11**. With respect to the N-C^1 bond length, the pyridylidene complexes are shorter in this regard than their pyridyl counterparts, suggesting less double bond character. The crystal structure of **509** was also compared, and shows uneven distribution with respect to the bond lengths, suggesting a breakage of the ring aromaticity. Additionally similar bond lengths for M-C_1 and C_1-N bonds have been reported for iridium and osmium pyridylidene complexes.[221, 275, 276, 295, 296]

Table 5.6 – Bond lengths of pyridylidene and pyridyl complexes

Structure	509 Crystal	509	510	N11	N17	N14	N15
Ru-C^1 Bond Length (Å)	2.039(2)	2.03	2.00	2.06	2.03	2.13	2.08
N-C^1 Bond Length (Å)	1.359(2)	1.38	1.42	1.39	1.38	1.35	1.35
C^1-C^2 Bond Length (Å)	1.406(3)	1.42	1.42	1.40	1.43	1.43	1.43
C^2-C^3 Bond Length (Å)	1.388(3)	1.40	1.40	1.41	1.40	1.40	1.40
C^3-C^4 Bond Length (Å)	1.402(3)	1.42	1.42	1.41	1.42	1.41	1.41
C^4-C^5 Bond Length (Å)	1.373(3)	1.39	1.39	1.39	1.38	1.40	1.40
C^5-N Bond Length (Å)	1.349(2)	1.36	1.37	1.36	1.37	1.34	1.34

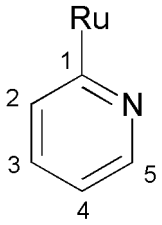

The analysis of the bond lengths for the 'pyridylidene' structures suggests a shorter, stronger metal-carbene bond between ruthenium and the pyridyl carbon for the 'pyridylidene' structures, indicating a metal-carbene double bond.

In order to further examine this, a qualitative examination of the orbital interactions of the 'pyridyl' and 'pyridylidene' structures was undertaken. The HOMO to HOMO-10 orbitals were investigated for complexes **510** and **N15**, with selected results displayed below in Figure 5.81 and Figure 5.82, with the HOMO through HOMO-10 orbitals displayed in the appendix section C.3.

HOMO-2

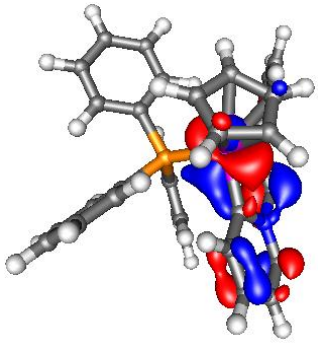

*Figure 5.81 – HOMO-1 and HOMO-2 orbitals of complex **510**.*

HOMO-1 **HOMO-2**

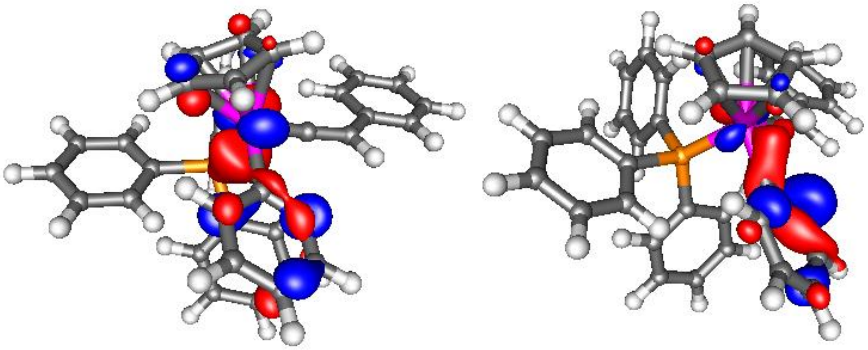

*Figure 5.82 – HOMO-1 and HOMO-2 orbitals of complex **N15**.*

In the examples, it can be shown that the HOMO-2 orbital for **510** possesses what seems to be a metal-carbon π-bond (Figure 5.81), whereas **N15** shows two metal-carbon σ-interactions (Figure 5.82). However the orbital interactions were not conclusive on their own.

In order to finalise the nature of the metal-carbon bond in the ‘pyridylidene’ and ‘pyridyl’ complexes, an NBO analysis was carried out using methods outlined in section 7.4. The reference structures for all complexes shows a single bond between the ruthenium and pyridyl carbon, with a double bond between the carbon and nitrogen atoms (Figure 5.83).

To produce a more complete picture into the stability of all resonance structures, a study similar to an investigation employed in a recent publication using the natural resonance theory module (NRT) was attempted.[297] However due to the unmodified geometry possessing ca. 180 different resonance combinations, a simpler system was used which replaced a majority of the aromatic groups with methyl substituents. This reduced to number of possible combination to ca. 15, however this simplified structure was still too complicated for the NRT subroutine to process.

In order to circumnavigate this, a different primary reference structure was calculated with NBO using the $CHOOSE keyword which possessed a pyridylidene metal-carbon bond (Figure 5.84). In analysis of the total electron density of the primary and alternative reference structures, it can be seen that the ‘pyridylidene’ structures **509**, **510**, **N17** and **N11** show an increase in the non-Lewis density by 0.15, 0.19, 0.25 and 0.14 %, while the ‘pyridyl’ structures **N14** and **N15** show a significantly larger increase of 0.31 and 0.72 %.

Pyridylidene

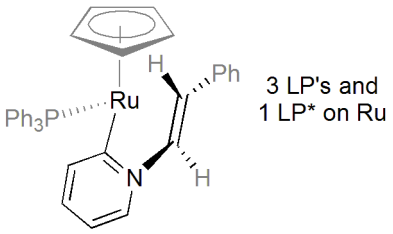

509

Total Lewis = 302.24 (96.87 %)
Total Non-Lewis = 9.67 (3.13 %)

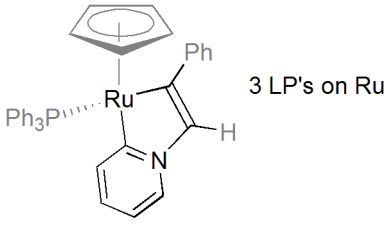

510

Total Lewis = 302.67 (97.00 %)
Total Non-Lewis = 9.33 (3.00 %)

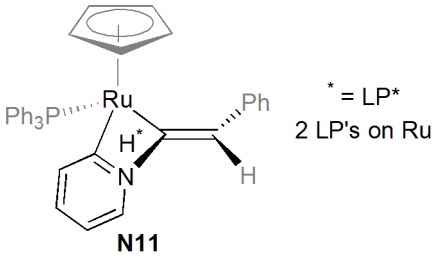

N11

Total Lewis = 301.67 (96.69 %)
Total Non-Lewis = 10.33 (3.31 %)

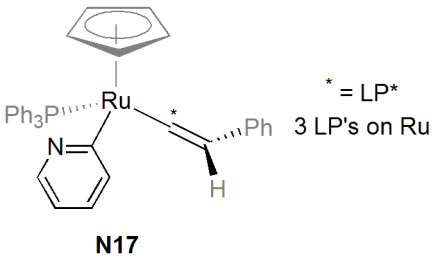

N17

Total Lewis = 302.42 (96.93 %)
Total Non-Lewis = 9.58 (3.07 %)

Pyridyl

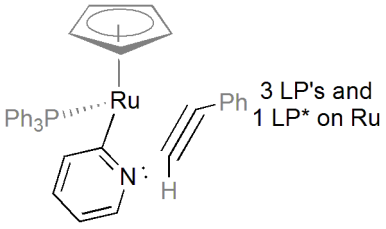

N14

Total Lewis = 302.20 (96.86 %)
Total Non-Lewis = 9.80 (3.14 %)

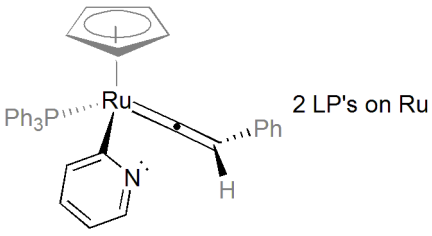

N15

Total Lewis = 302.65 (97.00 %)
Total Non-Lewis = 9.35 (3.00 %)

Figure 5.83 – NBO reference structures. For simplicity, positive charges have been omitted.

Pyridylidene

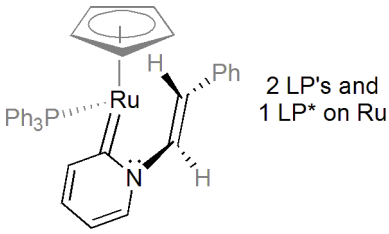

2 LP's and
1 LP* on Ru

509

Total Lewis = 301.75 (96.72 %)
Total Non-Lewis = 10.25 (3.28 %)

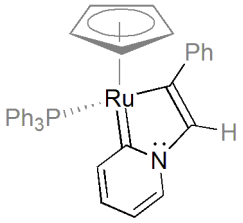

2 LP's on Ru

510

Total Lewis = 302.05 (96.81 %)
Total Non-Lewis = 9.95 (3.19 %)

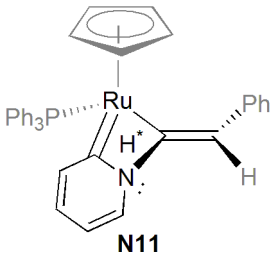

* = LP*
1 LP on Ru

N11

Total Lewis = 301.25 (96.55 %)
Total Non-Lewis = 10.75 (3.45 %)

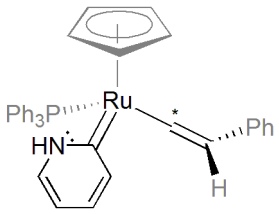

* = LP*
2 LP's on Ru

N17

Total Lewis = 301.63 (96.68 %)
Total Non-Lewis = 10.37 (3.32 %)

Pyridyl

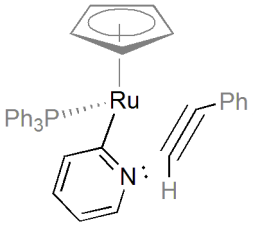

3 LP's and
1 LP* on Ru

N14

Total Lewis = 301.22 (96.55 %)
Total Non-Lewis = 10.78 (3.45 %)

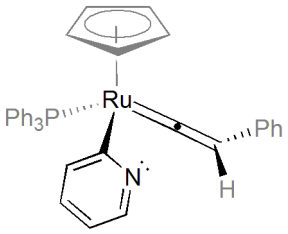

2 LP's on Ru

N15

Total Lewis = 300.39 (96.28 %)
Total Non-Lewis = 11.61 (3.72 %)

Figure 5.84 – Alternative NBO reference structures. For simplicity, positive charges have been omitted.

Additionally, the occupation of the N=C^1 π-bonds and metal-carbon bond in the primary reference structures was analysed, as well as the Wiberg bond indices (WBI) which can be seen in Table 5.7. No correlation between electron density and proposed structure is found for the Ru-C^1 bond, with analysis of the N=C^1 π-bond density showing that the 'pyridyl' structures have the smallest occupation of all complexes. However this difference is not large, and is close to the value obtained for **510**. Analysis of the WBI however shows a significantly smaller bond order in the 'pyridylidene' N=C^1 π-bond, suggesting delocalisation is decreasing the N=C bond strength. Additionally the generally larger WBI for the 'pyridylidene' complexes for bonds C^2=C^3 and C^4=C^5 compared with both the pyridyl complexes and pyridylidene N=C^1 WBI suggests a more localized, less aromatic structure.

Table 5.7 – Electron occupation and Wiberg bond indices of selected bonds

Structure	509	510	N11	N17	N14	N15
Ru-C^1 Occupation (e^-)	1.92	1.88	1.88	1.86	1.88	1.85
N=C^1 Occupation (e^-)	1.78	1.72	1.75	1.80	1.71	1.69
Ru-C^1 WBI	0.67	0.76	0.61	0.67	0.59	0.65
N=C^1 WBI	1.19	1.10	1.16	1.23	1.40	1.40
C^2=C^3 WBI	1.49	1.50	1.45	1.51	1.46	1.47
C^4=C^5 WBI	1.51	1.53	1.50	1.53	1.45	1.44

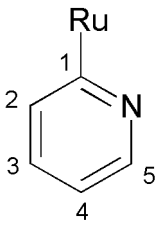

Delocalization into the N=C^{1} π* orbital from the electron density located on the metal was investigated, with a table of occupation and second order perturbation stabilisation energy shown in Table 5.8. Firstly, there is significantly higher occupation in the N=C^{1} π* orbital in all of the 'pyridylidene' complexes when compared with the 'pyridyl' **N14** and **N15**. Additionally **509**, **510** and **N17** show significant donation of metal-based electron density to the π* orbital, with the second order perturbation stabilisation energy being 63, 98 and 71 kJ mol^{-1} respectively, suggesting some π-bond character is being conferred to the R-C bond. This contrasts with **N14** and **N15**, with a smaller N=C^{1} π* occupation and second order perturbation stabilisation energy.

Table 5.8 – Occupation of N-C^{1} π orbital with second order perturbation stabilisation energy*

Structure	509	510	N11	N17	N14	N15
N=C^{1} π* Occupation (e^{-})	0.478	0.545	0.516	0.461	0.366	0.362
Total Second Order Perturbation Stabilisation Energy (kJ mol^{-1})	63	98	19	71	34	31

One anomaly found in the 'pyridylidene' results was **N11**, which features a small contribution from the metal electron density. This is potentially due to electron density being used to stabilise the LP* of the proton (see section 5.2.5 for further analysis). However this does concur with the longer M-C bond length for **N11** seen in the optimised geometries (Table 5.6).

In summary, the bond length, qualitative orbital interactions and the electron structure of 'pyridylidene' complexes has been investigated. It is apparent that the classification of these structures as pyridylidenes is a valid one due to a combination of the M-C bond length and a break in the aromaticity of the pyridyl group shown in the bond length and in an analysis of the electronic structure of the complexes.

5.3 Summary

In conclusion, the mechanism for the original Murakami and Hori type reaction has been elucidated and verified through a joint theoretical and experimental investigation. The starting precursor was shown to be the *bis*-pyridine complex **507**, as opposed to the *bis*-triphenylphosphine complex **501**, although **507** could be produced *via* ligand loss from **501**. The pyridine/vinylidene complex **503** was shown to be an important and accessible intermediate in the reaction agreeing with the original Murakami and Hori proposal (Figure 5.85). However, the initially proposed productive mechanism *via* cycloaddition ($\mathbf{TS_{503\text{-}504}}$) possesses a prohibitive barrier.

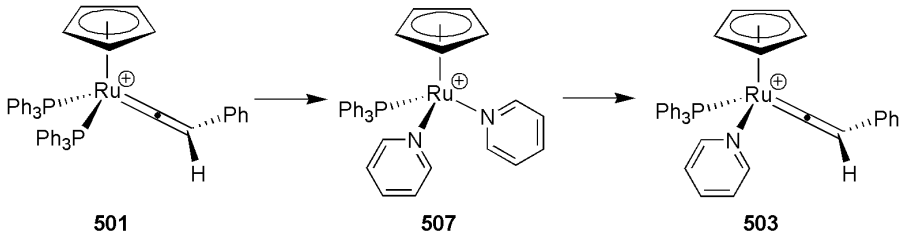

Figure 5.85 – Initial reaction steps.

During experimental investigation, **509** was shown to be a product on the overall potential energy surface and verified experimentally and theoretically. This is shown to be achievable from **503** *via* pyridine attack on the δ+ C_α forming **N8** with pyridine loss forming **N10**, and proton transfer forming **509**. While low in energy, prohibitively high energetic spans from **509** to a productive mechanism meant that it was not a pathway on the productive surface, most likely being a deactivation product (Figure 5.86).

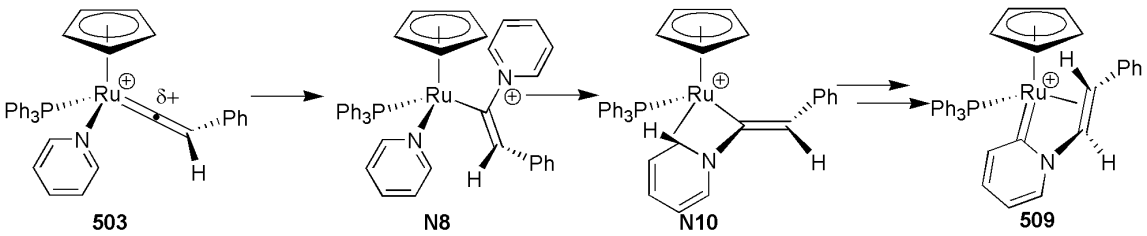

*Figure 5.86 – Formation of **509**.*

Stationary point **N10** can proceed to another mechanism, where deprotonation by pyridine (which could also occur with **N22** or **N23**) forms **N12**. The pyridyl-vinyl N-C bond of **N12** can then break to form **N15**.

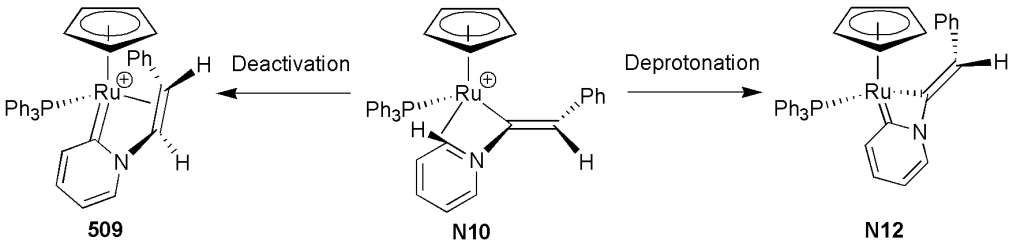

*Figure 5.87 – Two 'fates' of **N10**.*

From **N15** 2-styrylpyridine can be formed through $\mathbf{TS_{N15\text{-}505}}$. Alternatively protonation of **N15** to form the pyridylidene **N17** can also produce 2-styrylpyridine through $\mathbf{TS_{N17\text{-}N20}}$, with both pathways forming the coordinated product complex **N5** (Figure 5.88). Pyridine can then replace the organic product, forming **507** and free 2-styrylpyridine. Both energetic spans for these mechanisms are acceptable for the reaction conditions employed experimentally.

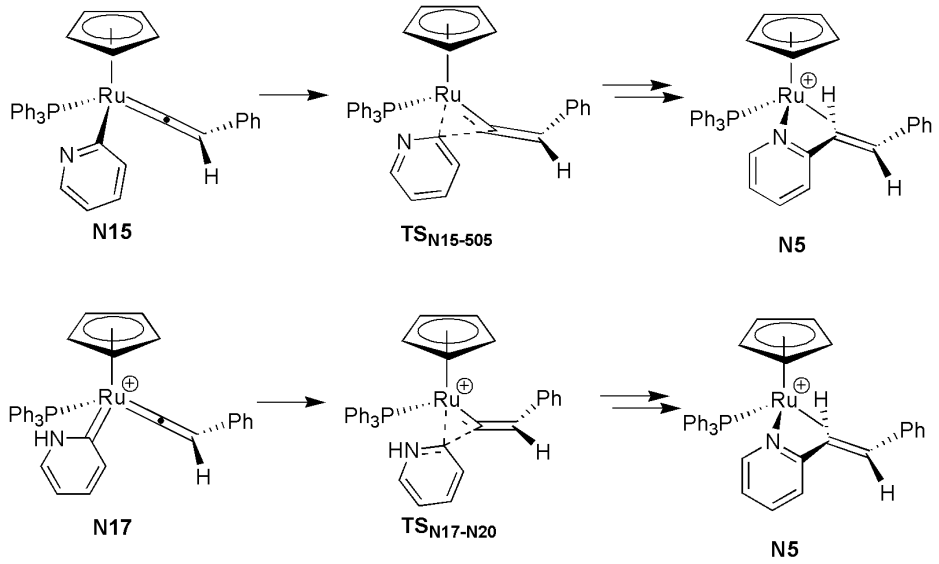

Figure 5.88 – Summary of productive pathways.

In terms of stereoselectivity, exclusive formation of (*E*)-2-styrylpyridine as opposed to (*Z*)-2-styrylpyridine is due primarily to a steric clash between phenyl and pyridyl groups, but also the loss of phenyl agostic stabilisation in certain pro-*Z* stationary points. Due to the lack of any perceivable phenyl/pyridyl clash in the TDI of **503**, this has the effect of increasing the energetic span, and therefore favouring production of the *E* isomer. This steric clash of groups is also seen with the use of 3-methylpyridine as a substrate, with the methyl group preferring to face away from the reaction centre.

The use of solvent was also seen to be of importance within the reaction, with experiments showing the formation of 2-styrylpyridine requiring at least 2 equivalents of pyridine. The many roles of pyridine seen in the mechanism is of importance, with the pyridine attack on the δ+ vinylidene C_α seen with **N8**, various deprotonation and protonation steps, as well as the coordination of pyridine to form the *bis*-pyridine complex **507 -** releasing the 2-styrylpyridine product. Formation of the deactivation product **509** without pyridine was further corroborated by the intramolecular proton transfer step $\mathbf{TS_{N10\text{-}N11}}$ and $\mathbf{TS_{N11\text{-}509}}$, negating the requirement for pyridine-assisted proton shuttling.

Several intermediates formally assigned as pyridylidene structures were verified theoretically, with the optimised geometries as well as the electronic structure showing agreement with the classification of the structure.

Additionally, mechanistic insight into the substituent effects of 4-ethynyl-α,α,α-trifluorobenzene, trimethylphosphine and 3-methylpyridine was observed. In the case of 4-ethynyl-α,α,α-trifluorobenzene, the productive pathway has a similar energetic span to that of phenylacetylene – matching what was seen experimentally. With regard to the lack of side products for the formation of the deactivation product **513**, the energetic span is shown to be once again similar to that of the phenylacetylene pathway. However it was postulated that stationary point **O2** may be a precursor to a pi-allyl carbene dimer (such as **508**), which owing to the higher energy of **O2** compared with the equivalent stationary point **N9** in the phenylacetylene system could be responsible for the lack of dimer observation in the 4-ethynyl-α,α,α-trifluorobenzene system.

With regard to trimethylphosphine, a larger energetic span is seen for the productive pathway, with a more exergonic deactivation pathway, potentially explaining the reason for the presence of the deactivation product during the reaction with excess pyridine. However the lack of the deactivation product **516** when reacted without pyridine in solution could not be conclusively determined.

In closing, joint experimental and theoretical studies have elucidated a significant amount of detail involved with the pyridine alkenylation reaction. Productive and deactivation pathways, substituent effects, and the bonding of intermediates have been discovered, contributing to the knowledge of a potentially important tool for pyridine alkenylation. A final reaction cycle can be seen below in Figure 5.89, with parts of this chapter also reported in a recent publication.[296]

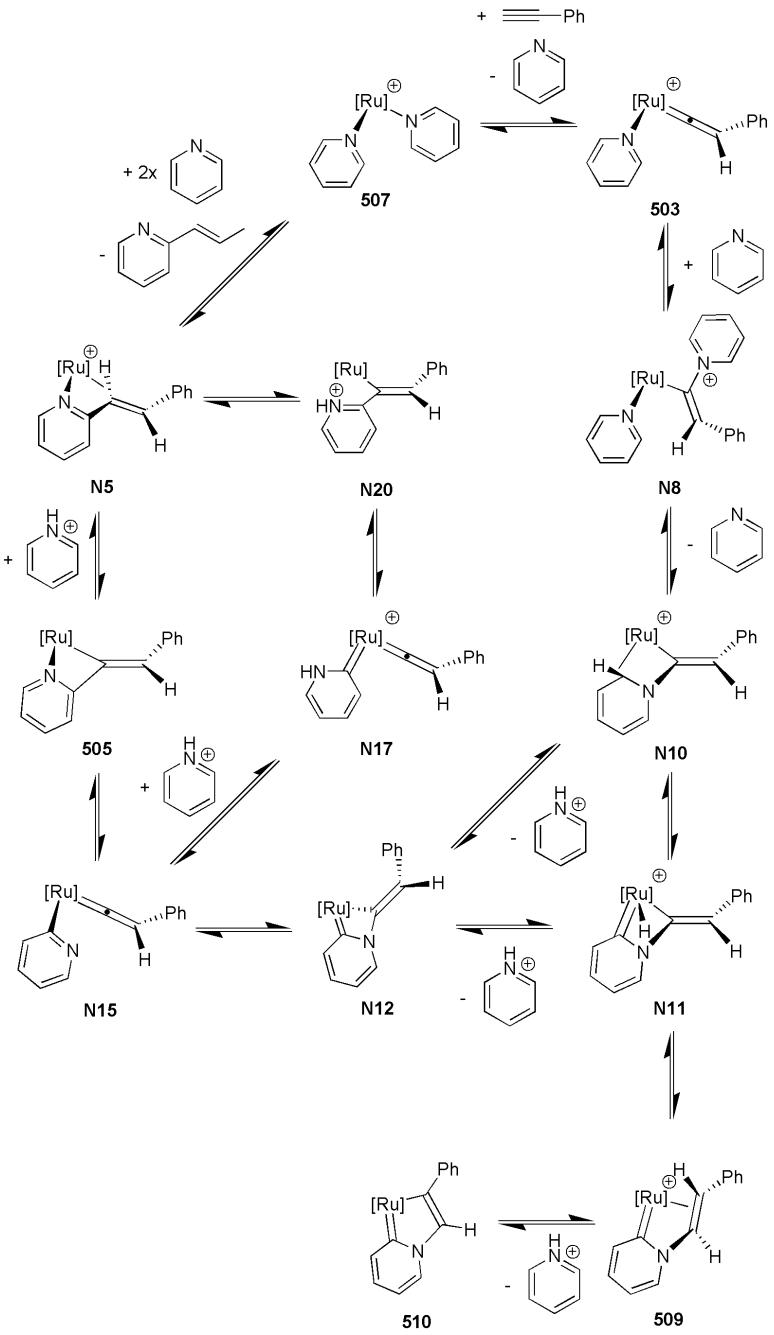

Figure 5.89 – Mechanistic cycle of the pyridine alkenylation reaction.[296]

6. Epilogue

This thesis has investigated the two main areas set out in the introduction, involving the *bis*-acetate ruthenium vinylidene complexes such as **202**, and the half-sandwich ruthenium vinylidene complexes such as **503** (Figure 6.1).

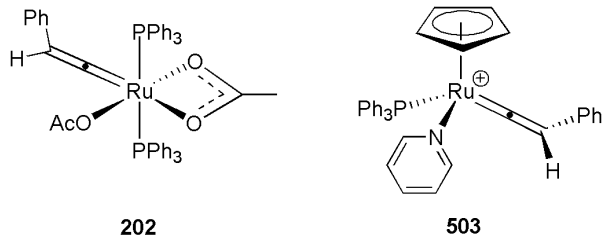

202 **503**

*Figure 6.1 – The two general areas of interest involving complexes such **202** and **503**.*

With the former group of systems, an alkyne-vinylidene tautomerization involving a *bis*-acetate complex **201** and phenylacetylene to form complex **202** was studied first. A ligand assisted proton shuttle mechanism (LAPS) was proposed, and verified as the lowest energy pathway to formation of the vinylidene **202** (Figure 6.2).

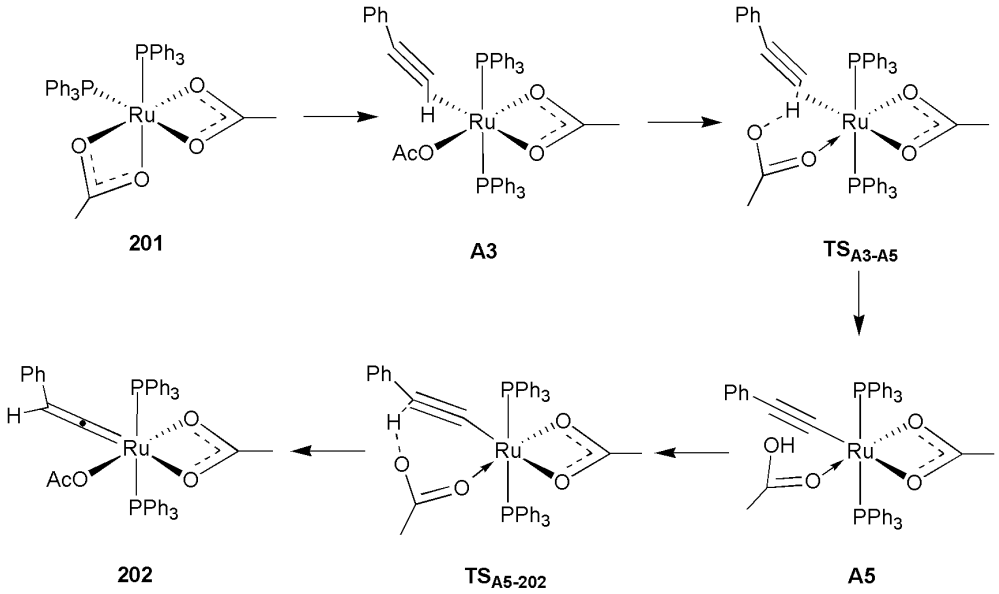

Figure 6.2 – The LAPS mechanism.

Near-instantaneous vinylidene formation was also seen in the second system with the case of the reaction of propargyl alcohol and **201**, forming a hydroxy-vinylidene **301**. Dehydration of **301** to an allenylidene did not occur, instead reacting further to **302** and ethene (Figure 6.3).

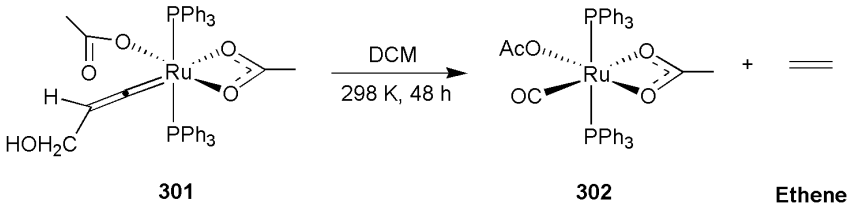

301 **302** **Ethene**

*Figure 6.3 – Formation of **302** and ethene.*

Further experimental studies revealed that formation of **302** occurs through nucleophilic attack of the vinylidene C_α with the acetate group, and not *via* an allenylidene complex originally proposed in similar studies. While theoretical results were shown to agree with the experimental system up to formation of the carbonyl and splitting of the acetate group, the study revealed that concerted, allenylidene intermediate mediated, and nucleophilic water attack mechanisms are too high in energy to be feasible. It was suggested that the mechanism proceeded through a cationic mechanism owing to the evidence of such complexes in further experimental studies, or through a tentative dimer-complex mechanism.

A change in the chemistry of the ruthenium complex also saw a change in reactivity with respect to the fourth chapter, with identification of the CO-LAPS mechanism. Here, the *bis*-acetate carbonyl complex **302** reacts with phenylacetylene to form complex **401** during experimental studies, with the application of heat forming (*Z*)-*β*-styryl acetate.

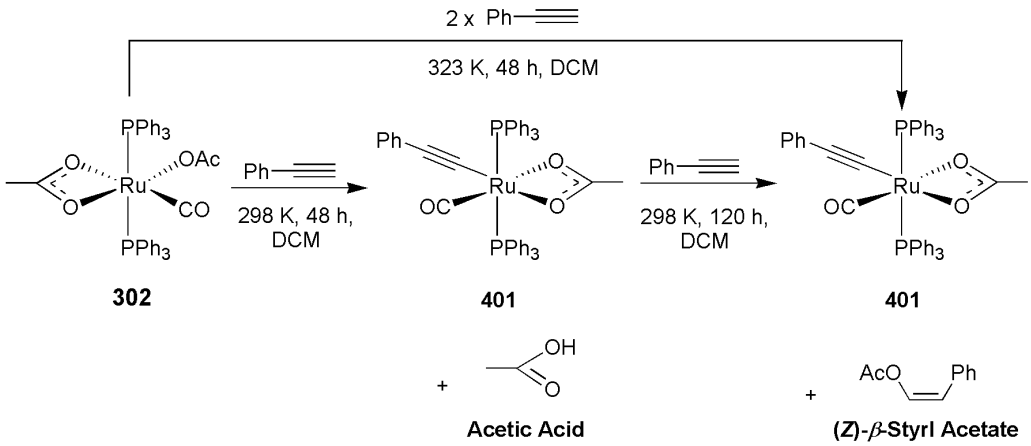

*Figure 6.4 – Reaction of **302** with phenylacetylene to form **401** and (Z)-β-styryl acetate.*

The first half of a LAPS-type mechanism was proposed in the formation of **401** from **302**, with acetic acid being lost. Vinylidene formation proceeds through a high energy transition state, which upon formation, reacts further in a mechanism involving protonation *via* a second LAPS mechanism and a second equivalent of alkyne to form the *β*-styryl acetate. While this mechanism was anti-Markovnikov in nature, a competing Markovnikov mechanism was identified, with the energetic span of the substituent effects showing good agreement with experimental selectivities.

With respect to the half-sandwich ruthenium vinylidene system, the mechanism proposed for pyridylidene alkenylation to form 2-styrylpyridine from **501** in previously reported studies was shown to be incorrect in a joint experimental and theoretical investigation (Figure 6.5).

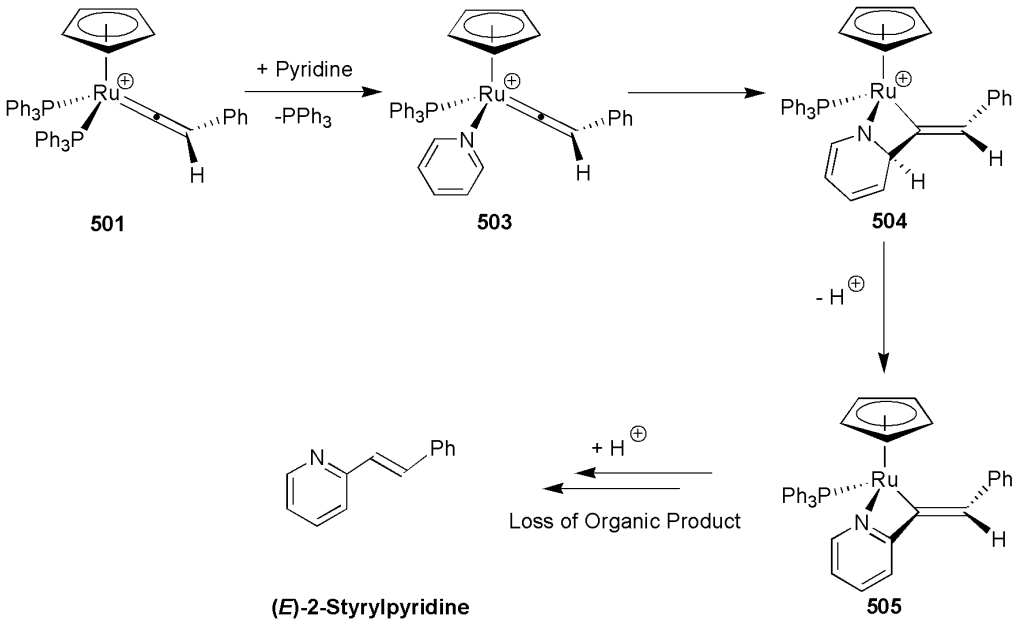

Figure 6.5 – Initially proposed mechanism of pyridine alkenylation.

Experimental evidence was produced for the unusual pyridylidene complex **509** (Figure 6.6), which was verified experimentally and theoretically.

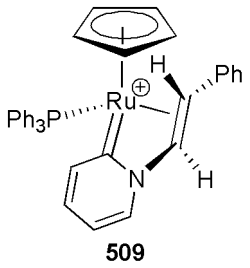

Figure 6.6 – Unusual pyridylidene complex.

The investigation revealed that complex **N10** had two 'fates' – either proton transfer to form **509** (the deactivation product) or proceed *via* deprotonation and subsequent rearrangement to form the pro-2-styrylpyridine complex **N5**. Finally, several pyridylidene structures were verified with the use of theoretical methods such as the NBO program, identifying significant evidence for a ruthenium-carbon double bond.

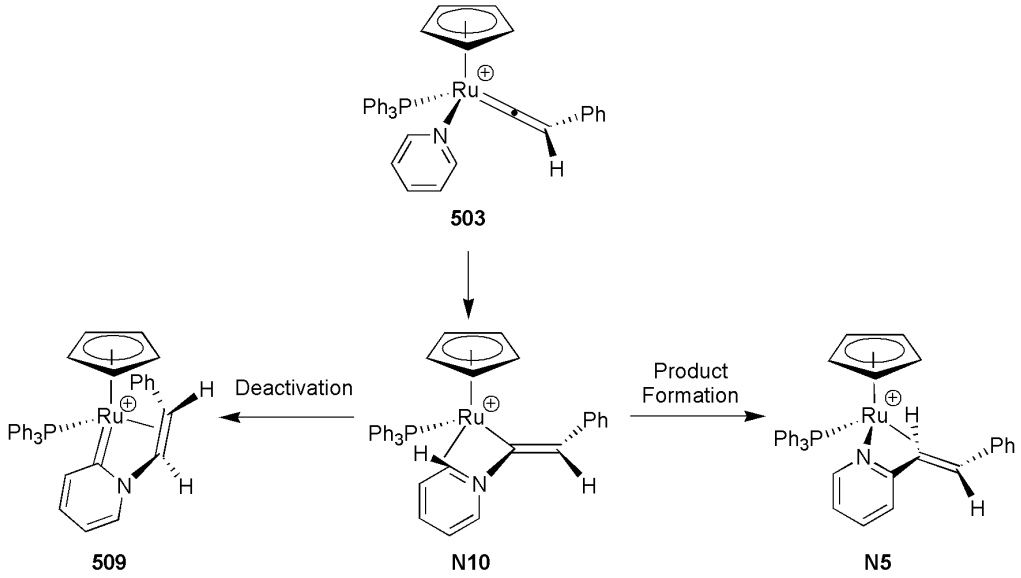

*Figure 6.7 – Two 'fates' of **N10**.*

In summary, two different classes of ruthenium-vinylidene complexes have been investigated theoretically, providing insight into the reactions involving these complexes. Additionally joint experimental and theoretical studies have provided a significantly more in depth picture than if performed separately, enhancing the overall quality of the studies, and providing access to a far more comprehensive set of results.

7. Experimental Procedures

7.1 Optimisation of Structures and Assessment of Energies with TURBOMOLE

Potential energy landscapes were assembled with the use of the TURBOMOLE v5.10[40, 298-305] program. For all minima, a geometry optimisation was performed on an initial structure guess using the (RI-)BP86/SV(P)[30, 31, 306-308] functional and basis set combination, with a 28-electron effective core potential used for ruthenium.[309] This was followed by a vibrational frequency calculation using the AOFORCE module at the same level of theory to characterise the nature of the stationary point (zero imaginary frequencies for a minima) and to provide thermal and entropy corrections. Once an optimised geometry had been successfully obtained, a single point energy calculation was performed at the (RI-)PBE0/def2-TZVPP[32-34, 310-312] level.

For transition states the TURBOMOLE program's transition state searching algorithms (which use an eigenvector following routine) were employed. This involved making an initial structure guess, with the atoms that were thought to move along the reaction coordinate constrained in an orientation that would be expected within the transition state. A constrained optimisation and subsequent vibrational frequency analysis was then performed to identify the transition vector to follow during a transition state optimisation. All constraints were then removed and a transition state optimisation and subsequent vibrational frequency analysis was performed.

Zero point energy corrections were obtained from the vibrational frequency analysis, with Gibbs energy calculated as SCF energy + chemical potential. The chemical potential was calculated using TURBOMOLE's freeh script on the vibrational frequency analysis.

7.2 Use of TURBOMOLE's Dynamic Reaction Coordinate (DRC) routine

In order to establish that transition states located using the method outlined in section 7.1 connected to the stationary points that had been identified on either side of the saddle point, the DRC module of TURBOMOLE v6.4 was executed on obtained transition states.[39]

In a similar method to the intrinsic reaction coordinate (IRC) of the Gaussian program,[313] DRC performs automatic dynamic reaction coordinate calculations forward and backward along the imaginary vibrational mode of a transition state structure until a minimum is located on either side of the saddle point.

7.3 Use of COSMO Solvation Models

The conductor-like screening model (COSMO[44]) module of TURBOMOLE v5.10 was used to obtain corrected SCF energies in order to account for solvent effects present in studies seen in chapter 5. Several dielectric constants representing different solvents were used, which are listed below in Table 7.1.

Table 7.1 - List of Solvents Used and their Dielectric Constants

Solvent	Dielectric Constant
Dichloromethane	8.93[314]
Pyridine	13.26[314]
2-Methylpyridine	9.95[315]
3-Methylpyridine	11.64[315]

7.4 Understanding Electronic Structure Using NBO and NRT Analysis

At the time of writing, TURBOMOLE does not possess a means of interacting with the natural bond orbital (NBO) 5.9 program[59]. Therefore, where the use of NBO was required, calculations had to first be performed with the Gaussian 09[316] program.

Optimised geometries from calculations using TURBOMOLE were obtained, which were performed in the same method to section 7.1. A single point calculation was performed using the Gaussian program at the PBE1PBE(Gaussian version of PBE0)/def2-TZVPP[32-34, 310-312] level. During this calculation, the *pop=NBORead* and *$NBO archive file=gennbo $END* keywords were added in order to generate a file for analysis by the NBO program (*gennbo.47*). This file was used by the GenNBO module to generate a standard NBO output. In addition to this, the use of the *$CHOOSE* keyword in the *gennbo.47* file allowed for the specification of alternative reference structures to be analysed by the program.

The typical output of an NBO file contains analysis of the electron density of the natural bonding orbitals, the donation and conferred stability to the structure with the use of second order perturbation analysis, and the bond order present with Wiberg bond indices (WBI).

Appendix

A. Chapter 2 Additional Information

A.1 PES of the LAPS Mechanism with Ruthenium Complexes of 1,2-bis(diphenylphosphino)butane

Only two isomers of the 1,2-*bis*(diphenylphosphino)butane (DPPB) system were possible due to the enforced *cis*-phosphine geometry. These are labelled **cis'** and **cis''** in a similar way to systems described previously (Figure 0.1). A scheme showing key stationary points is shown in Figure 0.2, and the PES is shown in Figure 0.3.

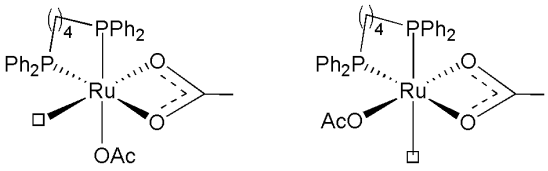

C1/cis' **C1/cis''**

*Figure 0.1 – Different isomers of DPPB ligand complex **C1**.*

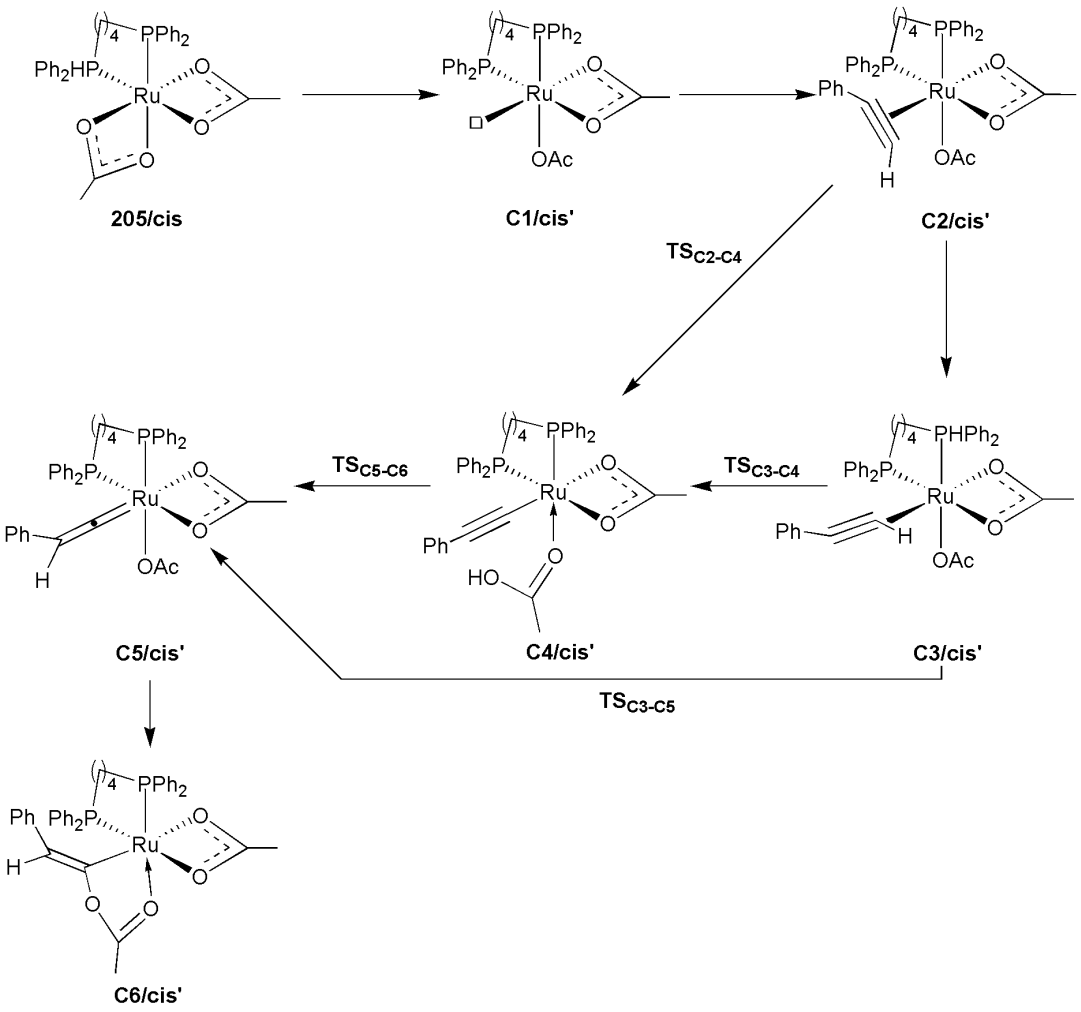

*Figure 0.2 - Scheme showing the key points of system **C**.*

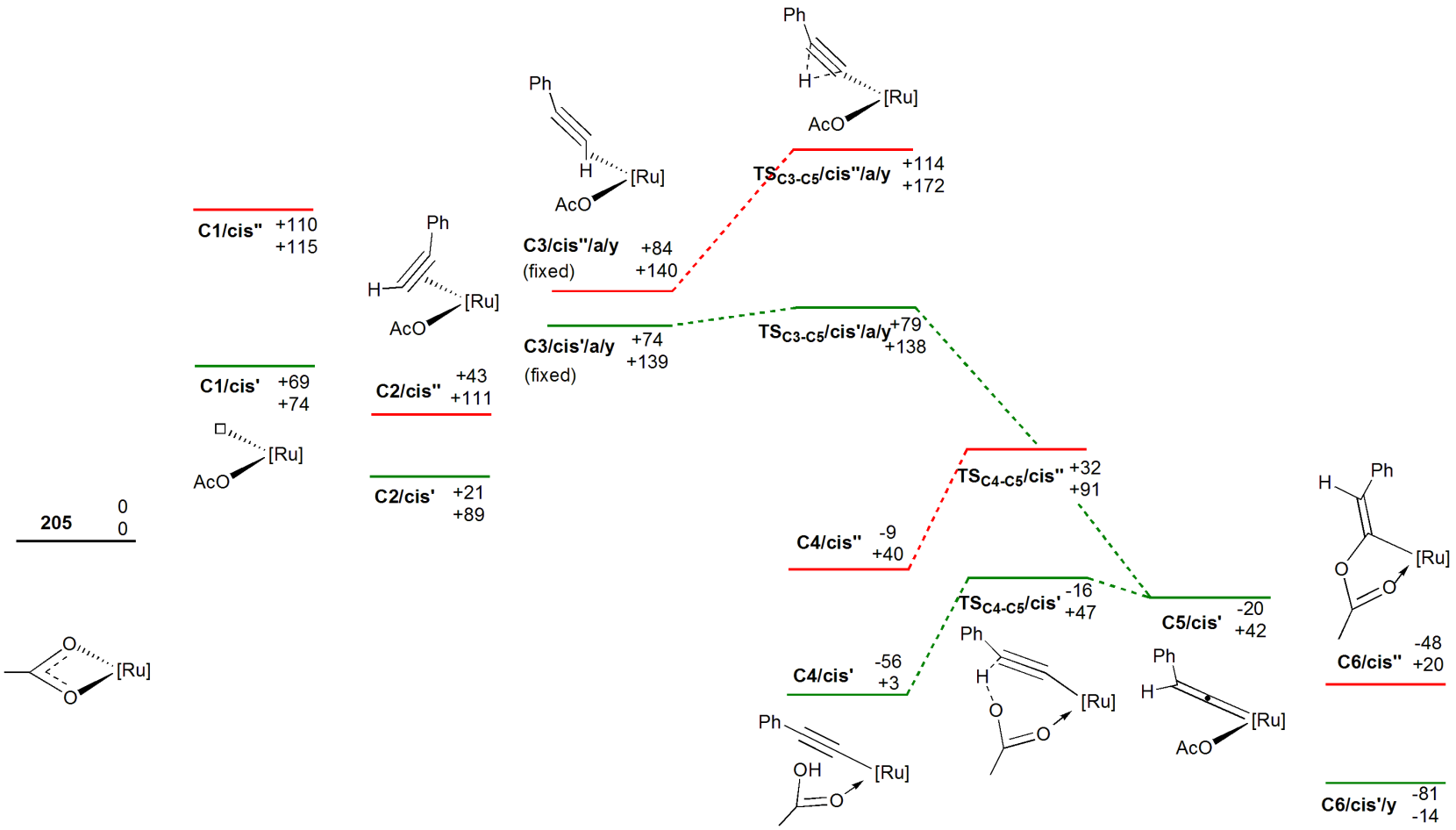

*Figure 0.3 – PES of system **C**. Energies are ZPE corrected SCF (top) and Gibbs free (bottom) energies in kJ mol^{-1}, relative to **205**. The **cis'** and **cis"** pathways are shown in green and red respectively. [Ru] = [Ru(OAc)(DPPB)].*

B. Chapter 3 Additional Information

B.1 Water-attack Mechanism

This section shall explore the water-attack mechanism investigated in chapter 3 in greater detail, involving direct water transesterification and water-coordination mechanisms. While the allenylidene-mediated mechanisms seen in section 3.2.3 also produced water, the reactions were isodesmic - with the attacking water molecule having been produced in a previous step along with the complex undergoing attack (Figure 0.4).

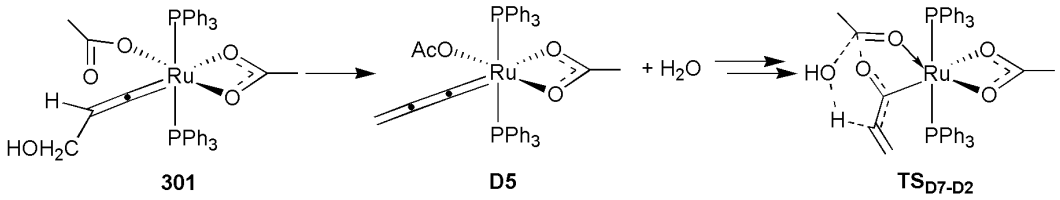

Figure 0.4 – Allenylidene-mediated water attack mechanism.

In the pathways presented here, water is assumed to either be produced separately or exist in the reaction system initially (e.g. from incompletely dry solvents or reagents). The first mechanism considered involved $\mathbf{TS_{D1\text{-}D2(H2O)}}$ and $\mathbf{TS_{D4\text{-}D3(H2O)}}$ (Figure 0.5). These transition states are almost identical to $\mathbf{TS_{D1\text{-}D2}}$ and $\mathbf{TS_{D4\text{-}D3}}$, with the difference being an additional water molecule being found between the acetate and hydroxy group which engages in nucleophilic attack of the central acetate carbon while protonating the hydroxy group. This would reduce the steric strain seen in $\mathbf{TS_{D1\text{-}D2}}$ and $\mathbf{TS_{D4\text{-}D3}}$, and given that water is consumed but also produced simultaneously in this mechanism, only a catalytic quantity of water would be required in the reaction mixture to facilitate this mechanism.

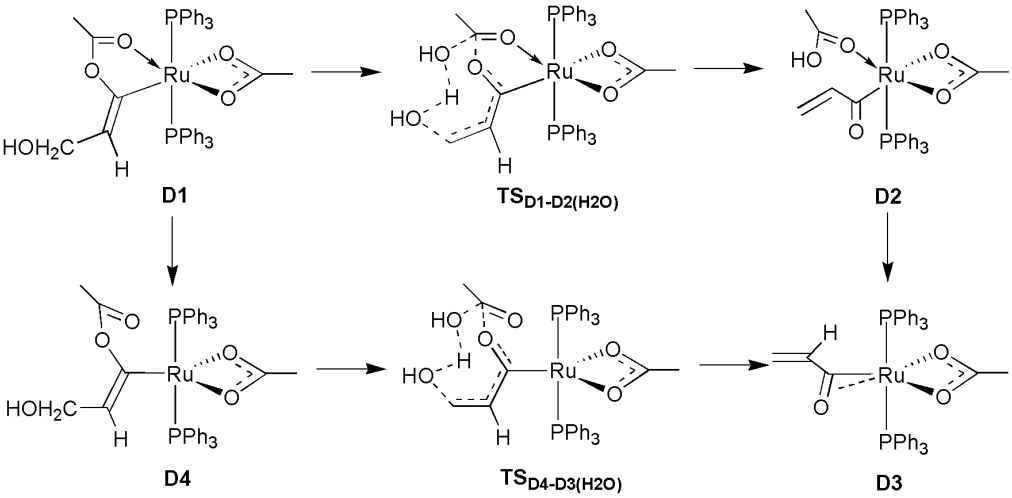

Figure 0.5 – Mechanism through ***TS$_{D1-D2(H2O)}$*** *and* ***TS$_{D4-D3(H2O)}$****.*

A second mechanism involved the coordination of water to the ruthenium centre through **D8** - essentially **D4** with an additional coordinated water molecule. Water attack through **TS$_{D8-D9}$**, where the OH group of water attacks the acetate carbon while simultaneously being deprotonated by the acetate oxygen, can occur to form **D9**. Additionally water coordination can proceed from **D10** through **D11** and **D12** *via* a similar mechanism (Figure 0.6).

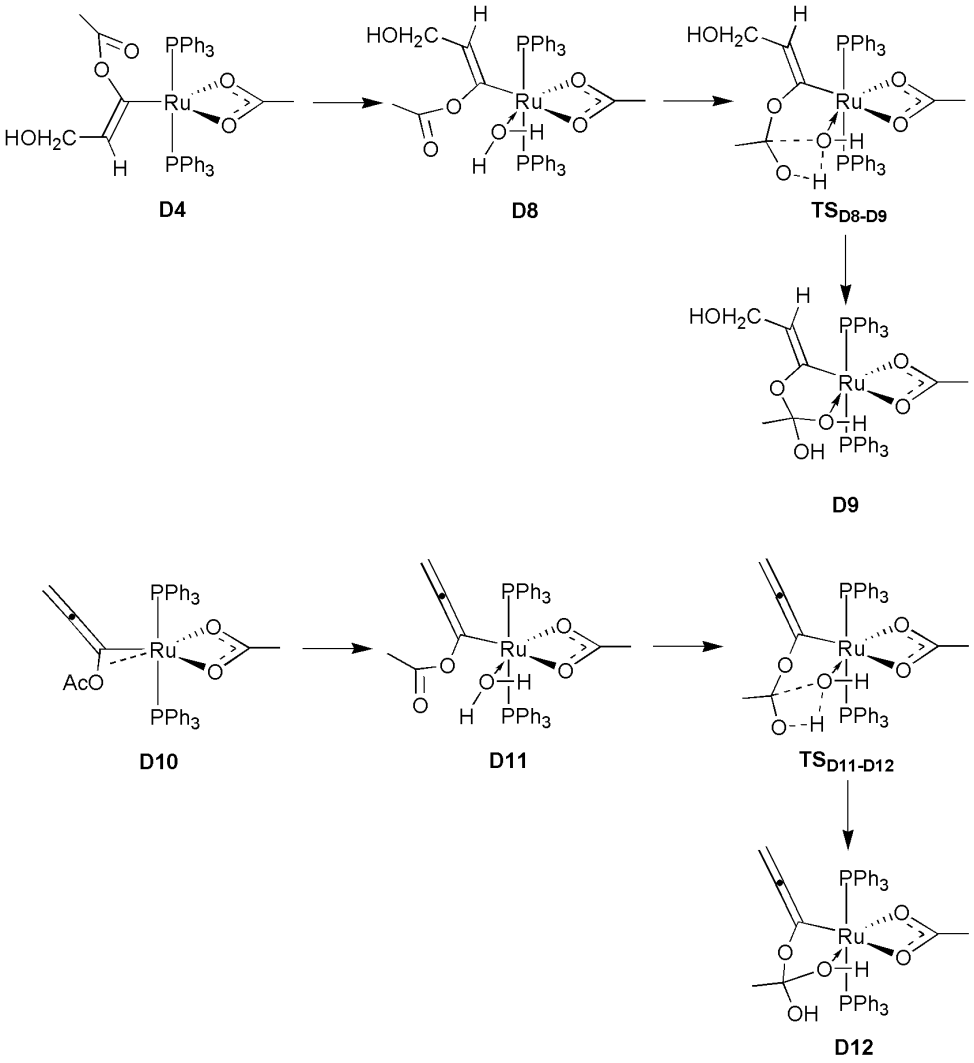

*Figure 0.6 – Water-mediated mechanism from **D4** and **D10**.*

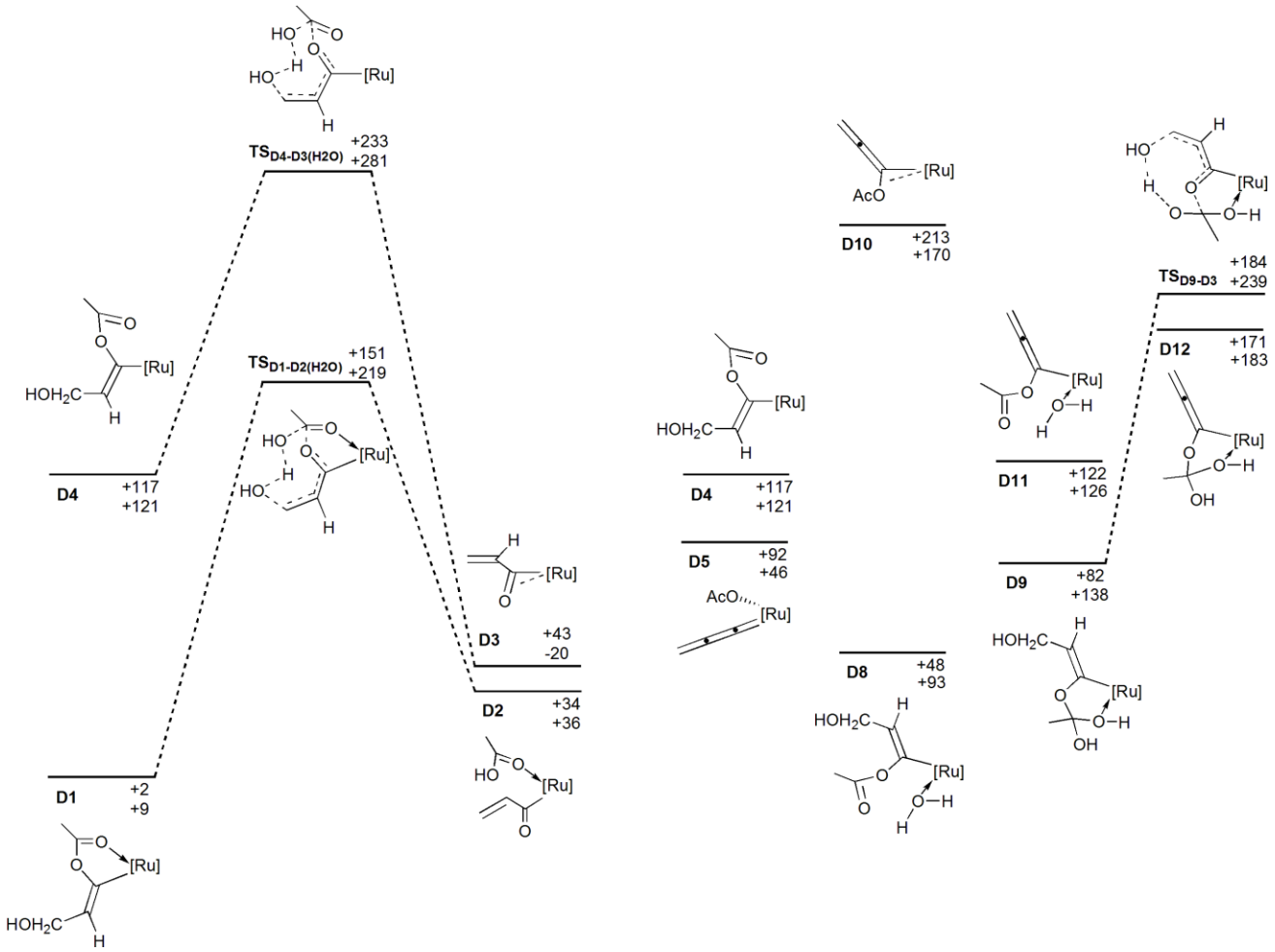

*Figure 0.7 – PES of water attack mechanisms. Energies are ZPE corrected SCF (top) and Gibbs free (bottom) energies in kJ mol^{-1}, relative to **301**. [Ru] = [Ru(OAc)(PPh$_3$)$_2$].*

Two stationary points could not be located on the PES seen in Figure 0.7, namely the water attack transition states of $\mathbf{TS_{D8\text{-}D9}}$ and $\mathbf{TS_{D11\text{-}D12}}$. In analysis of the PES the water attack mechanisms of $\mathbf{TS_{D1\text{-}D2(H2O)}}$ and $\mathbf{TS_{D4\text{-}D3(H2O)}}$ are too high in energy to be feasible for the experimental reaction conditions being found at +151 and +233 kJ mol^{-1} respectively. This is also the case for the pathway from complex **D10**. **D8** and **D9** are potentially feasible at +48 and +82 kJ mol^{-1} relative to **301** respectively, however the lack of information about transition state $\mathbf{TS_{D8\text{-}D9}}$, as well as the high energy of **D4** means that we do not have sufficient information to assess the likelihood of this pathway compared to the other proposed mechanisms.

In order to probe the reactivity from **D9**, transition state $\mathbf{TS_{D9\text{-}D3}}$ (Figure 0.8) was optimised and added to the PES in Figure 0.7. The transition state involved proton transfer from the acetate group to the hydroxy-vinylidene while simultaneously breaking the former acetate C-O bond. The energy of this transition state is +184 kJ mol^{-1} relative to **301**, which also suggests that this mechanism is unlikely given the observed reaction conditions of 48 h at 298 K.

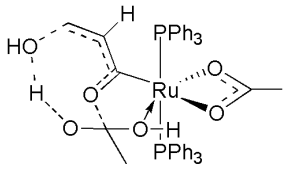

Figure 0.8 - ***$TS_{D9\text{-}D3}$.***

C. Chapter 5 Additional Information

C.1 Substituent Effects – 4-ethynyl-α,α,α-trifluorobenzene

A PES was constructed featuring 4-ethynyl-α,α,α-trifluorobenzene in place of phenylacetylene. The two areas to be reported upon would be the formation of the deactivation product **513** and formation of the organic product 2-(4-(trifluoromethyl)styrylpyridine) and **507** with the deprotonated (through $\mathbf{TS_{O7\text{-}O8}}$) and pyridylidene-mediated (through $\mathbf{TS_{O14\text{-}O15}}$) mechanisms. A scheme for these three pathways can be seen in Figure 0.9 and Figure 0.10, with an overall PES being shown in Figure 0.11, Figure 0.12 and Figure 0.13 respectively.

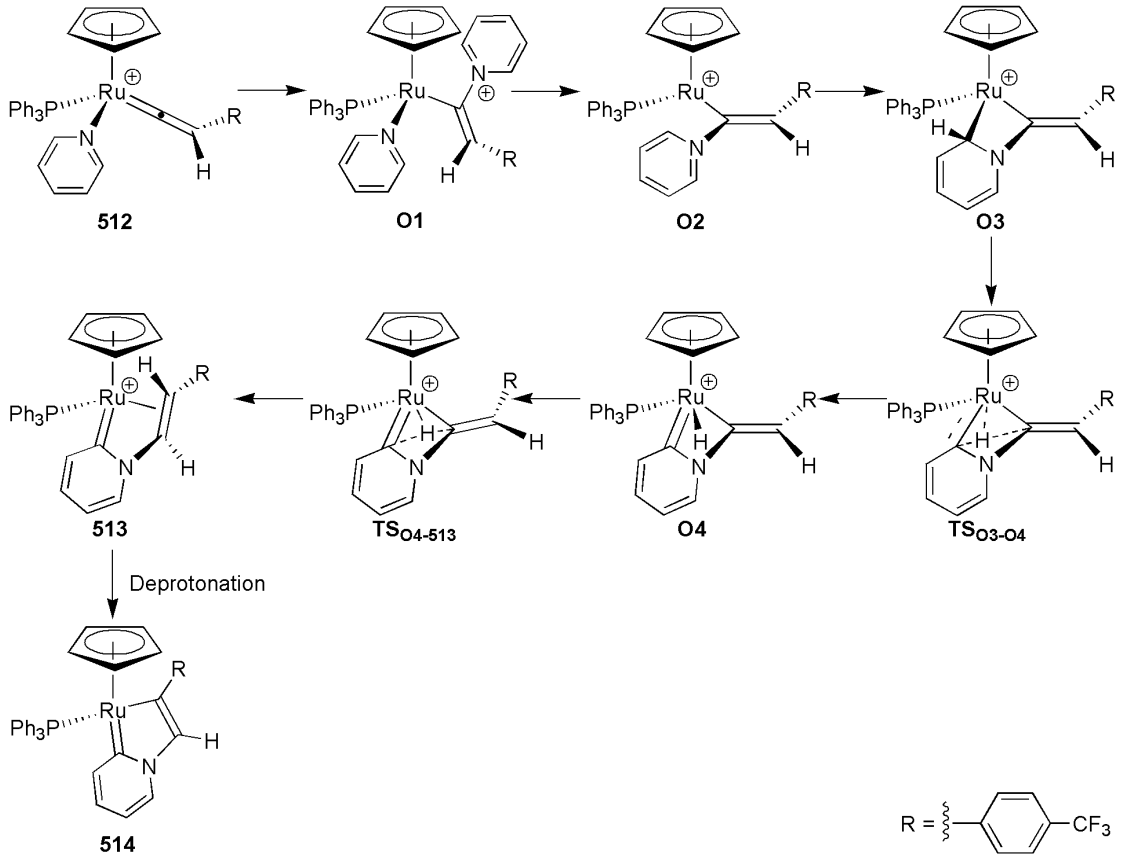

Figure 0.9 – 4-ethynyl-α,α,α-trifluorobenzene deactivation product key.

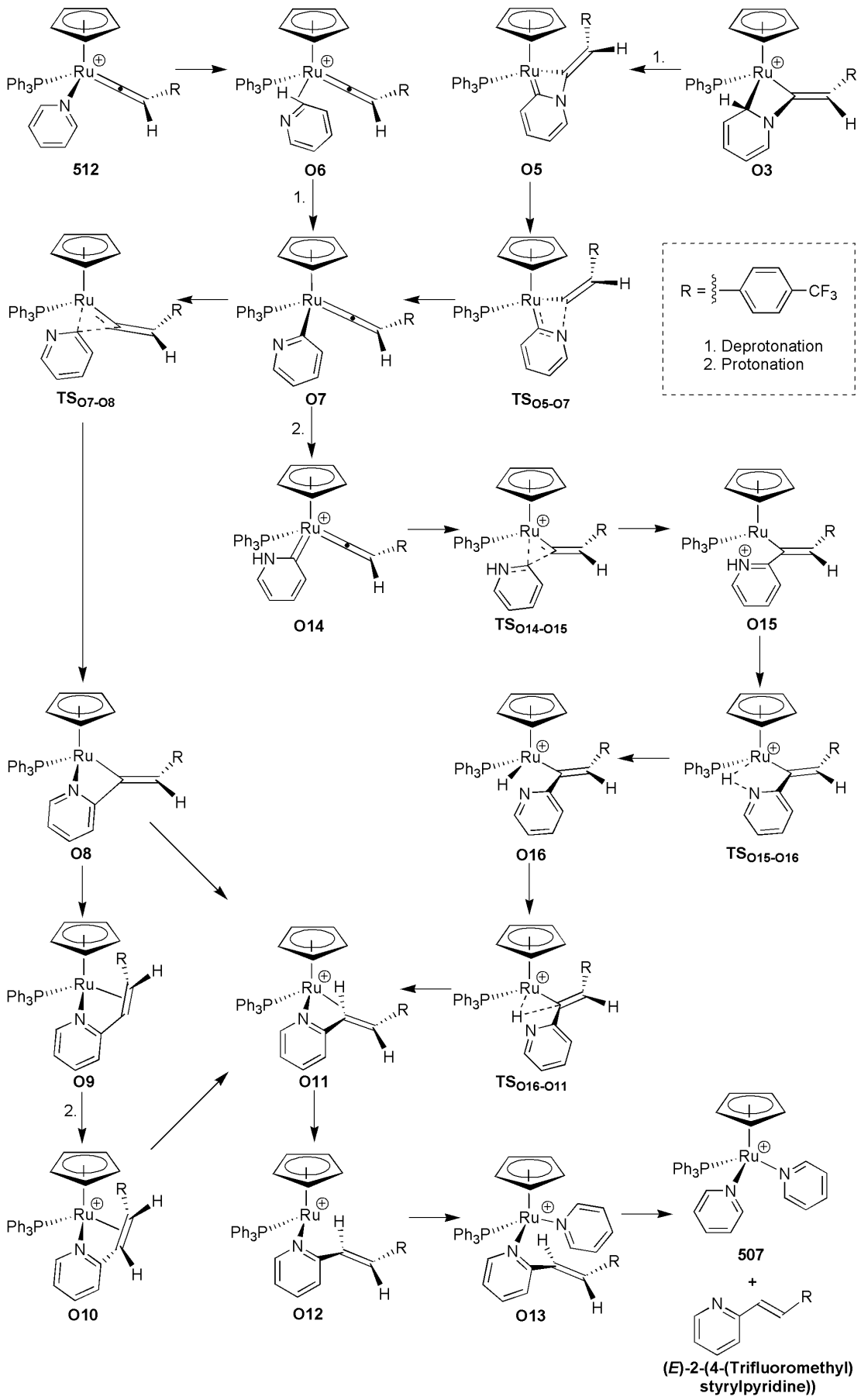

Figure 0.10 – 4-ethynyl-α,α,α-trifluorobenzene product formation pathway key.

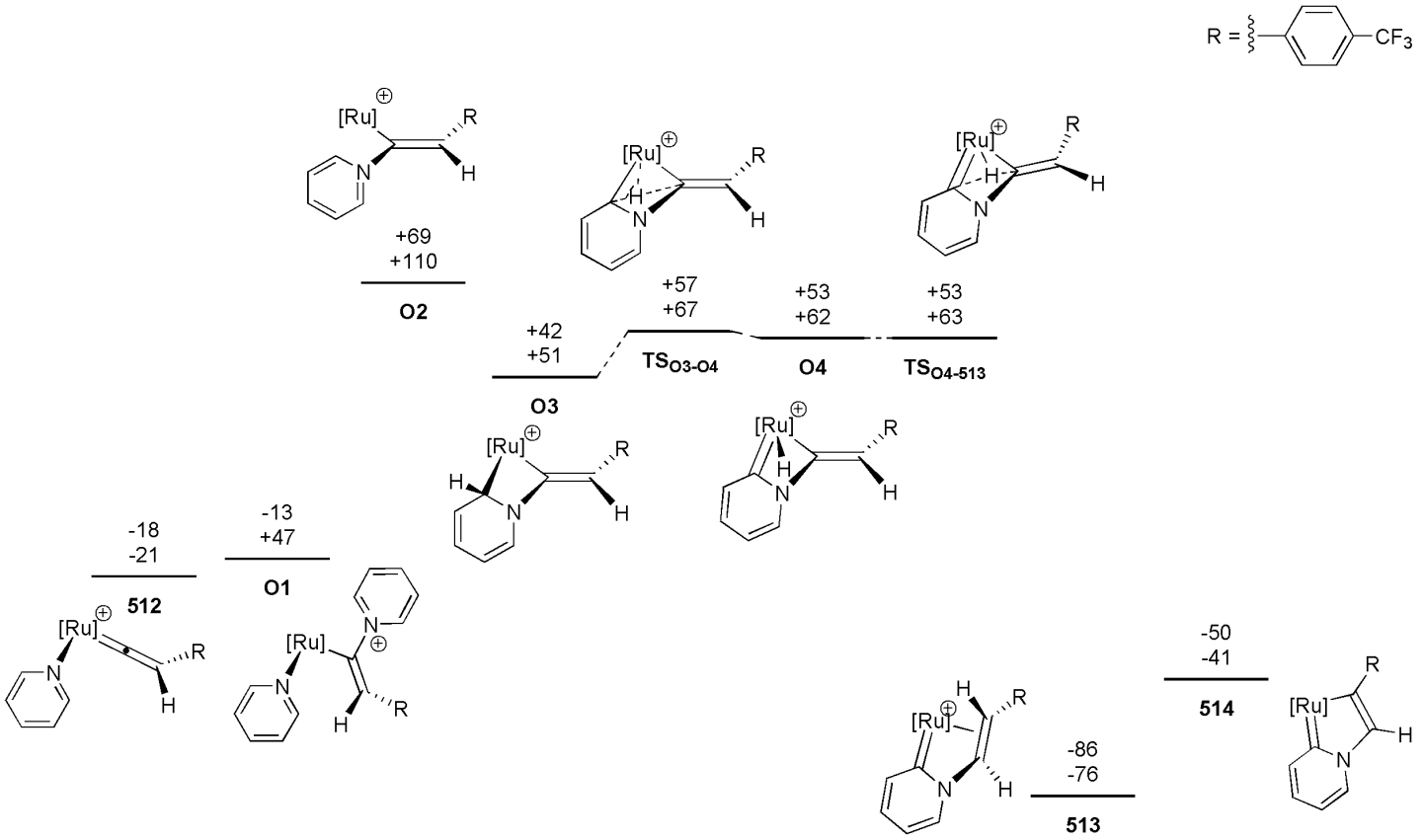

*Figure 0.11 – PES for the formation of deactivation product with 4-ethynyl-α,α,α-trifluorobenzene. Energies are ZPE corrected SCF (top) and Gibbs free (bottom) energies with COSMO solvation in kJ mol^{-1}, relative to **507**. [Ru] = [CpRu(PPh$_3$)].*

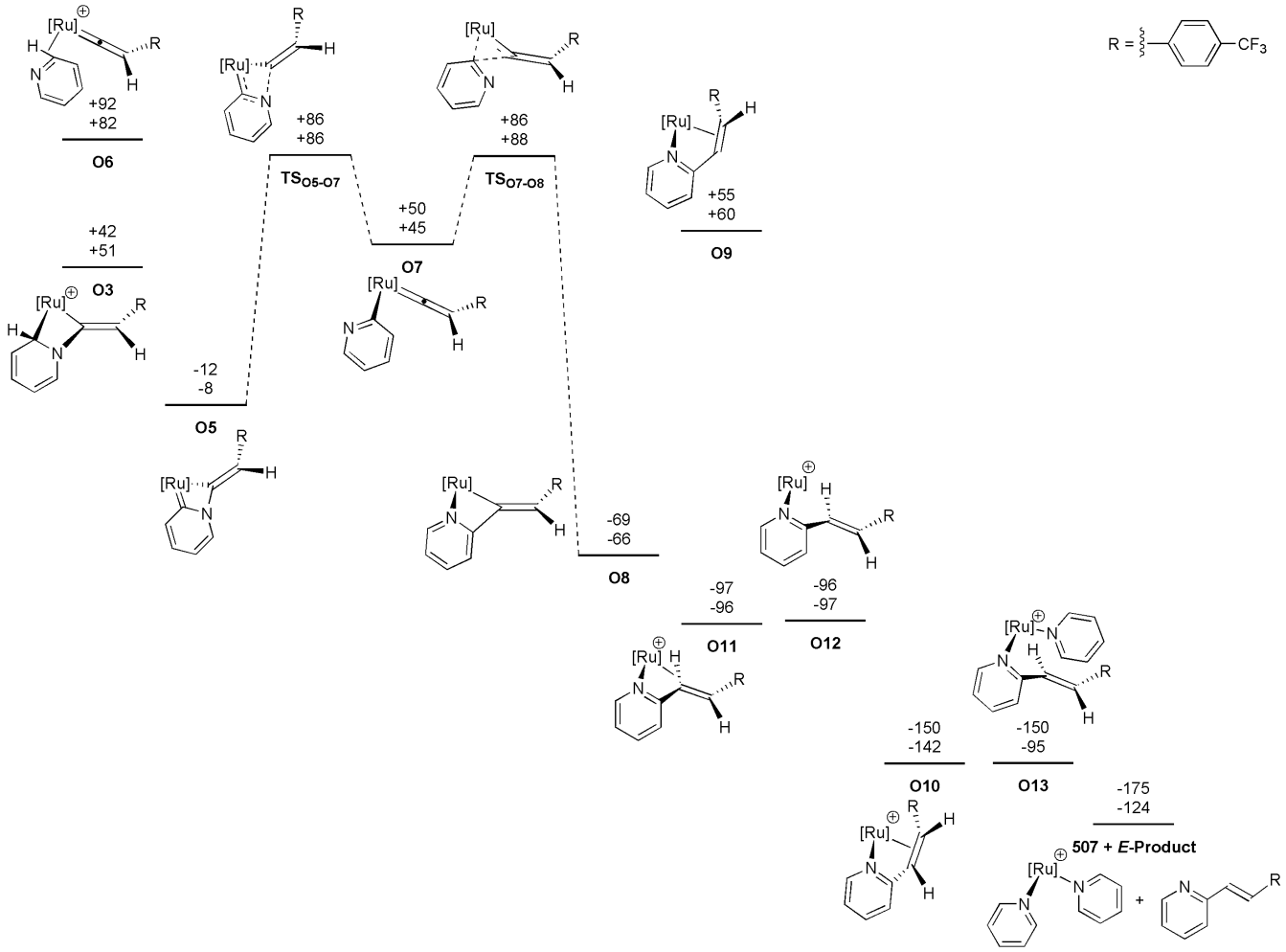

*Figure 0.12 - PES for the formation of organic product with 4-ethynyl-α,α,α-trifluorobenzene. Energies are ZPE corrected SCF (top) and Gibbs free (bottom) rnergies with COSMO solvation in kJ mol^{-1}, relative to **507**. [Ru] = [CpRu(PPh$_3$)].*

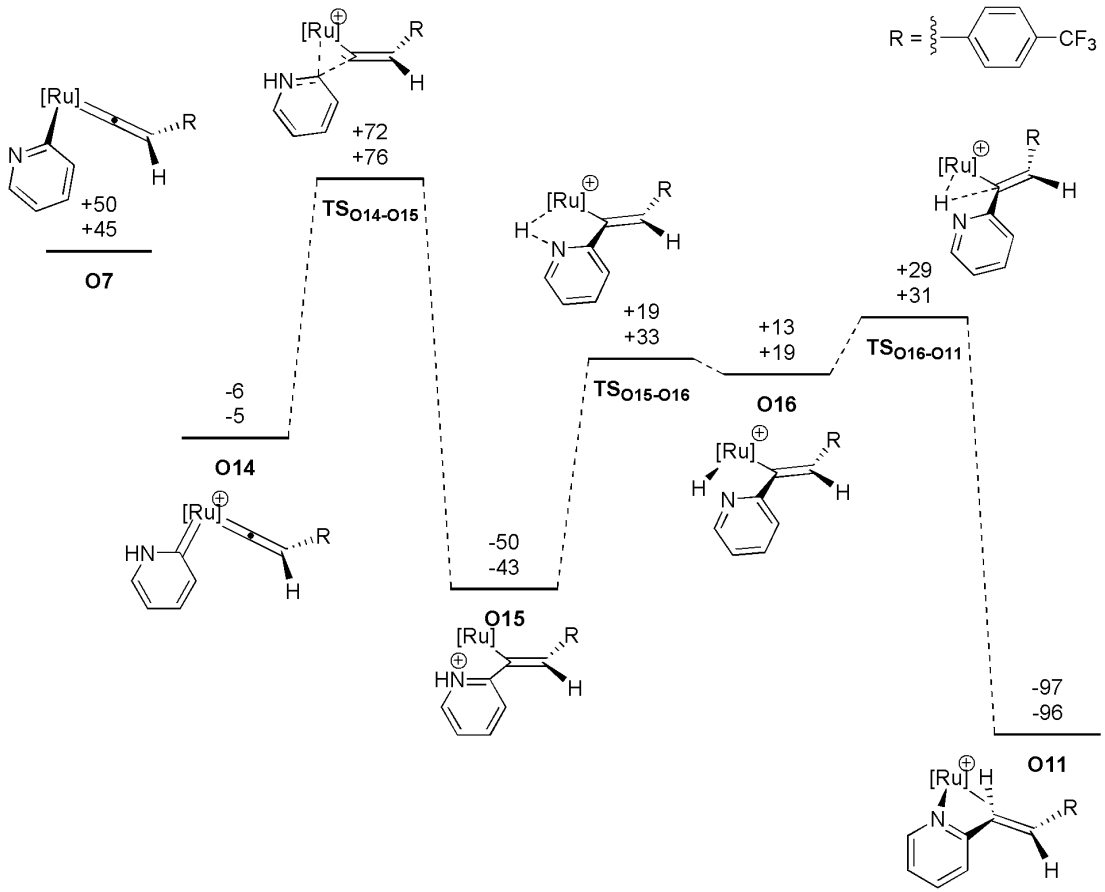

*Figure 0.13 – PES for the formation of organic product precursor **O11** with 4-ethynyl-α,α,α-trifluorobenzene via the pyridylidene pathway. Energies are ZPE corrected SCF (top) and Gibbs free (bottom) energies with COSMO solvation in kJ mol^{-1}, relative to **507**. [Ru] = [CpRu(PPh$_3$)].*

C.2 Substituent Effects – Trimethylphosphine

A scheme for all stationary points involved in the deactivation and productive pathways is shown in Figure 0.14 and Figure 0.15 respectively. The deactivation PES can be seen in Figure 0.16, with the organic product being formed *via* deprotonation and the pyridylidene mediated pathways in Figure 0.17 and Figure 0.18 respectively.

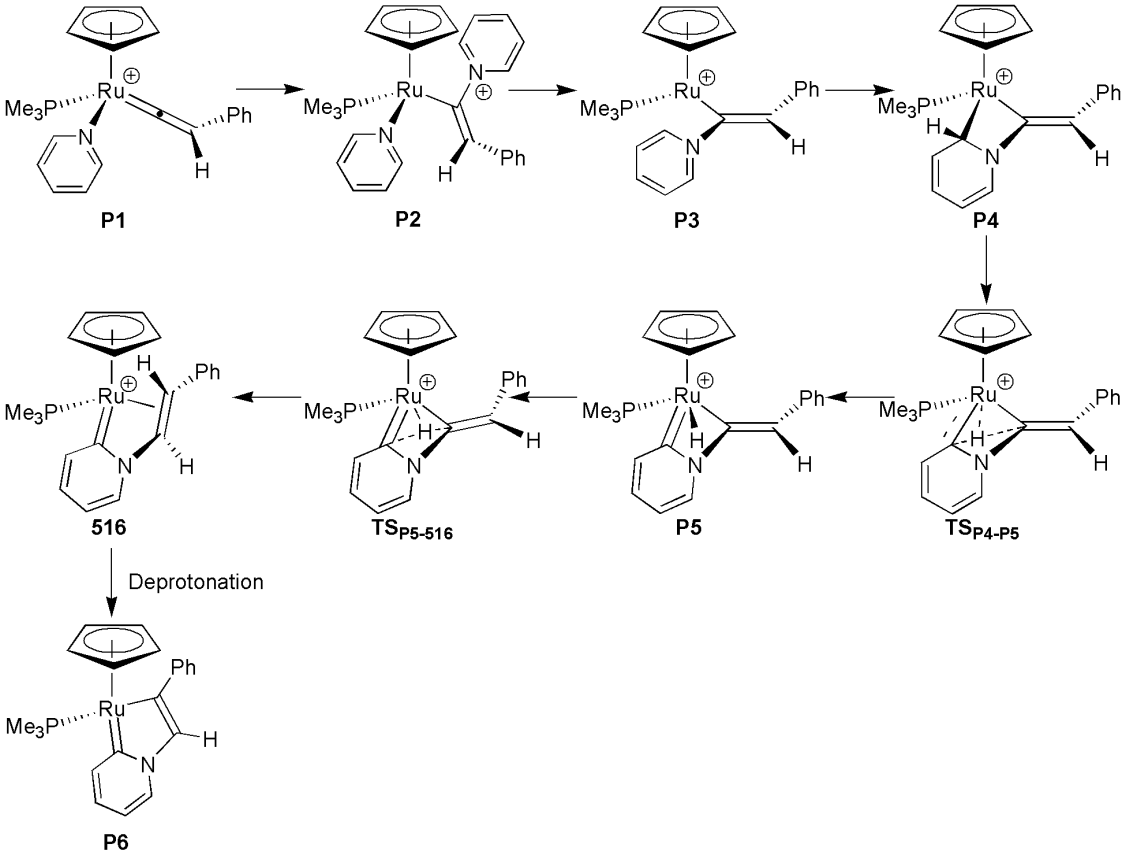

Figure 0.14 – PMe_3 deactivation product scheme.

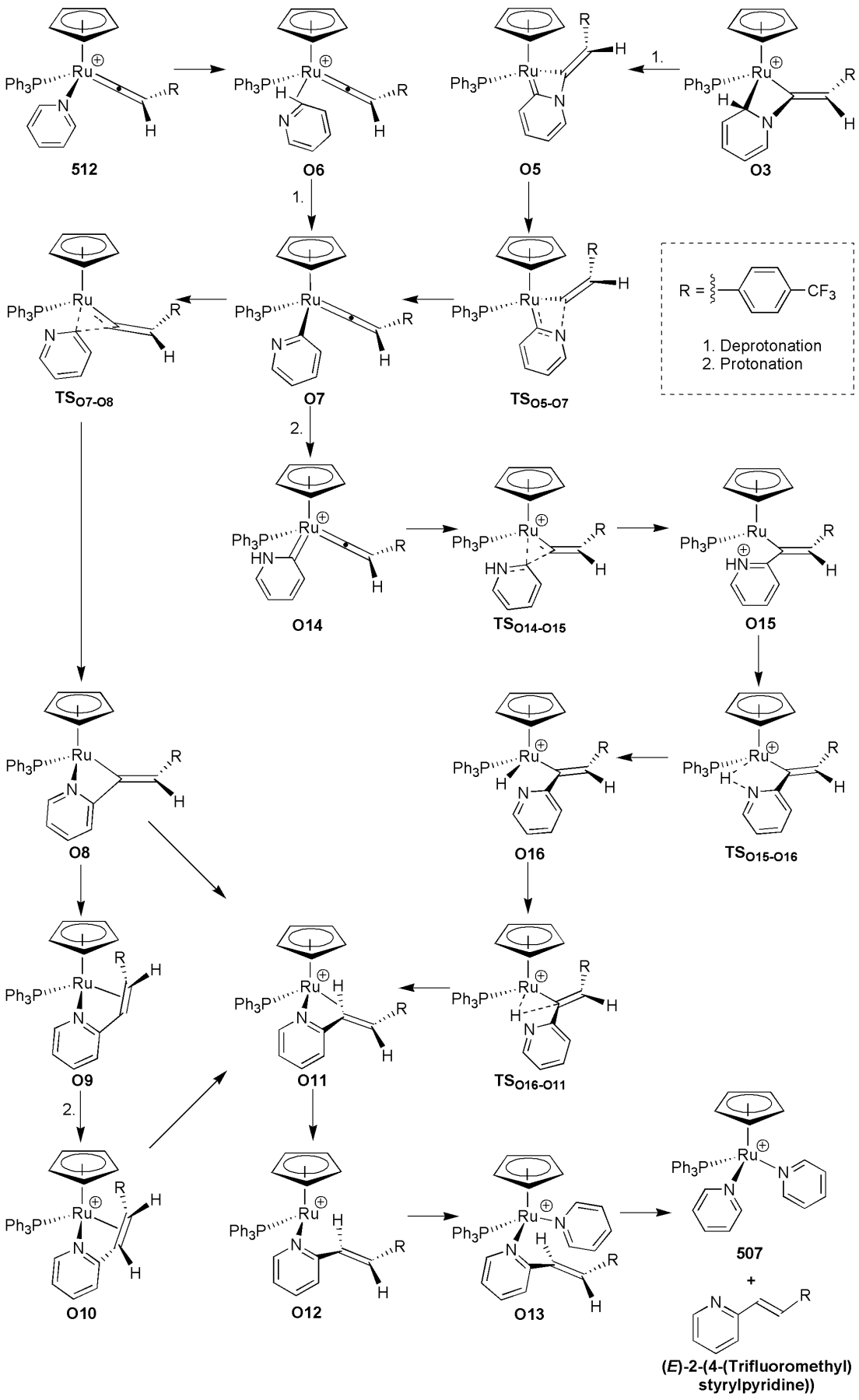

Figure 0.15 – PMe_3 product formation pathway scheme.

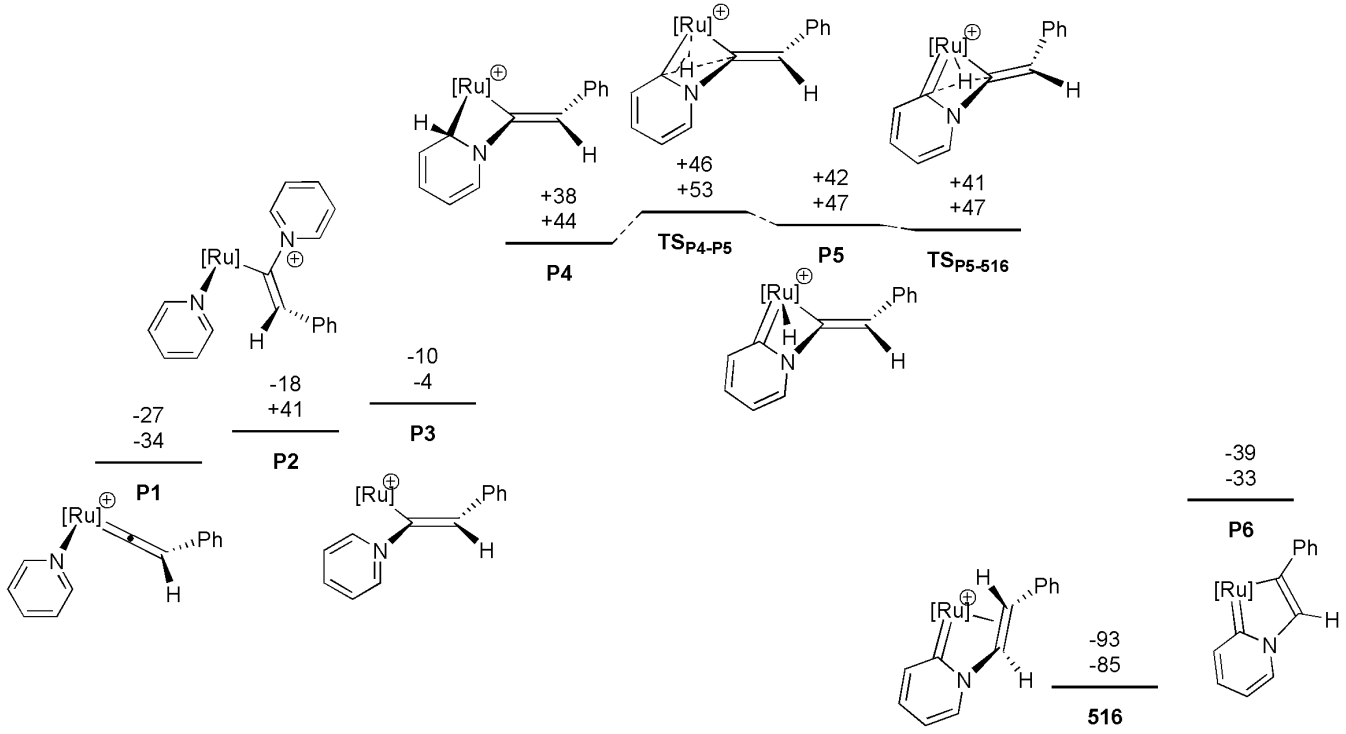

*Figure 0.16 – PES for the formation of the deactivation product with PMe_3. Energies are ZPE corrected SCF (top) and Gibbs free (bottom) energies with COSMO solvation in kJ mol^{-1}, relative to **515**. [Ru] = [CpRu(PMe_3)].*

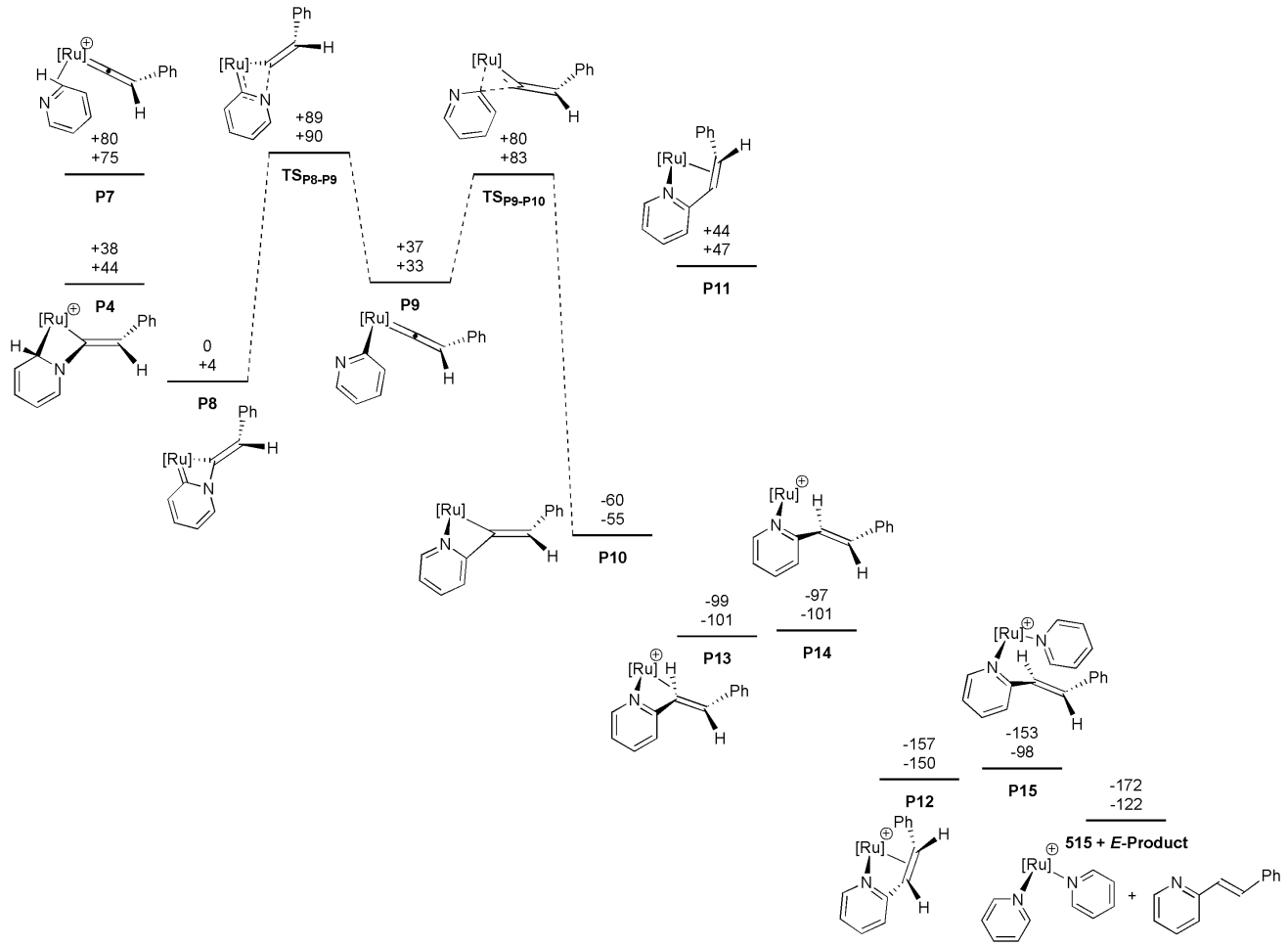

*Figure 0.17 – PES for the formation of the organic product for PMe_3. Energies are ZPE corrected SCF (top) and Gibbs free (bottom) energies with COSMO solvation in kJ mol^{-1}, relative to **515**. [Ru] = [CpRu(PMe_3)].*

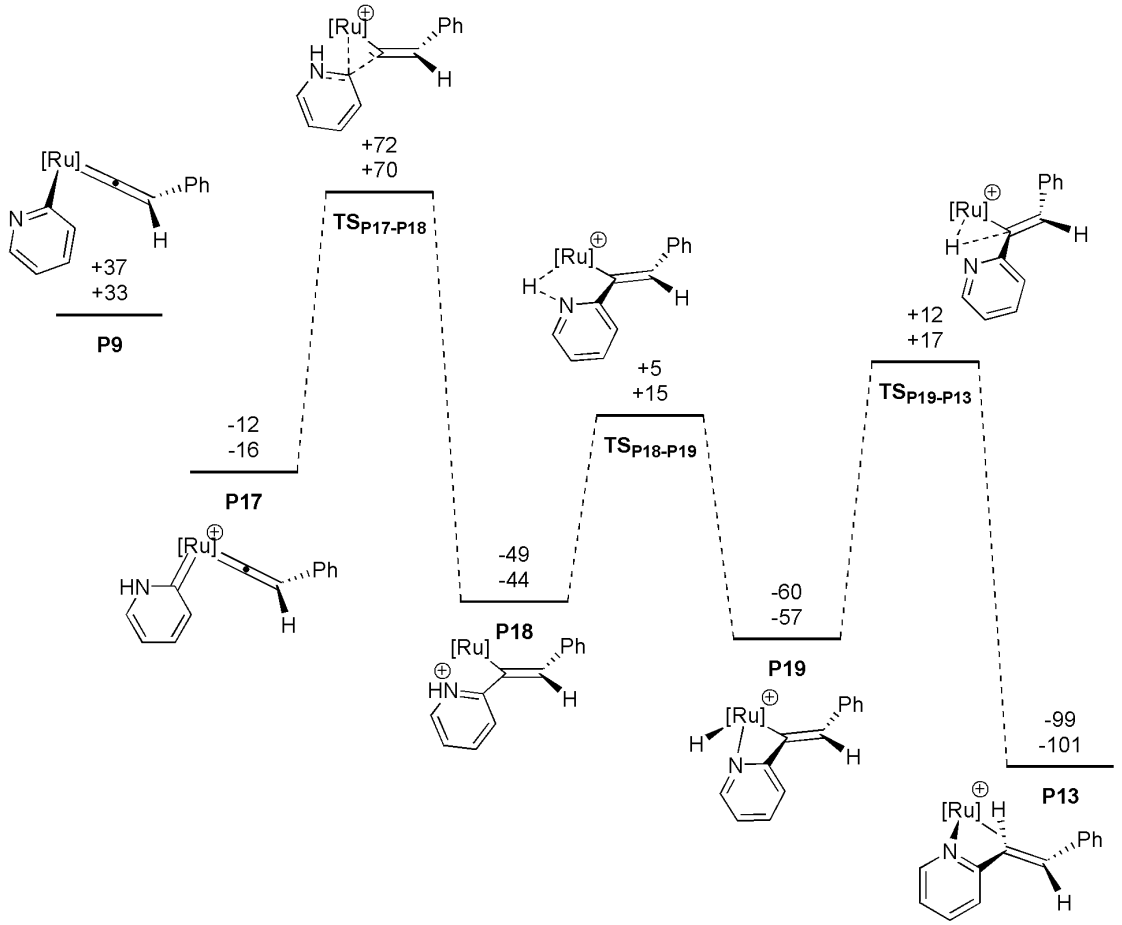

*Figure 0.18 – PES for the formation of the intermediate **P13** via the pyridylidene pathway for PMe_3. Energies are ZPE corrected SCF (top) and Gibbs free (bottom) energies with COSMO solvation in kJ mol^{-1}, relative to **515**. [Ru] = [$CpRu(PMe_3)$].*

C.3 Section 5.2.13 Orbital Diagrams

C.1.1 – ***510***

HOMO 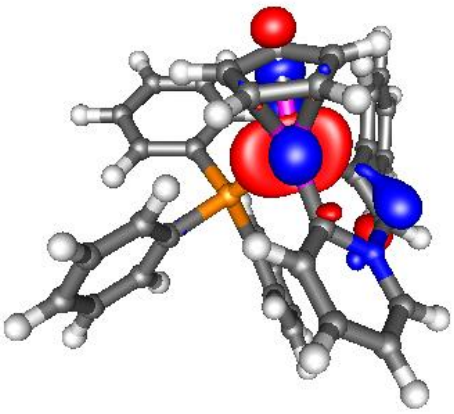	HOMO-1 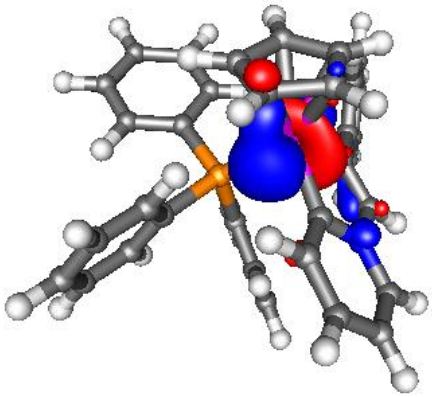
HOMO-2 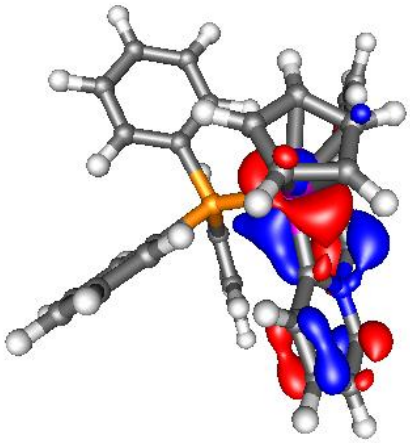	HOMO-3 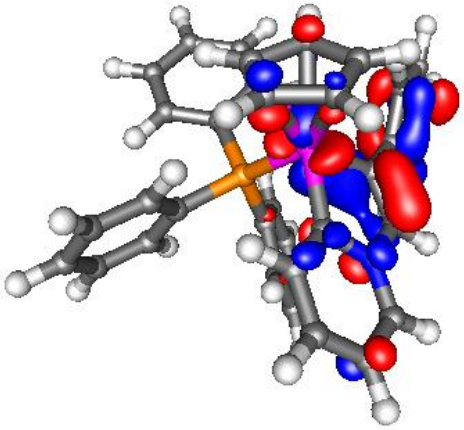
HOMO-4 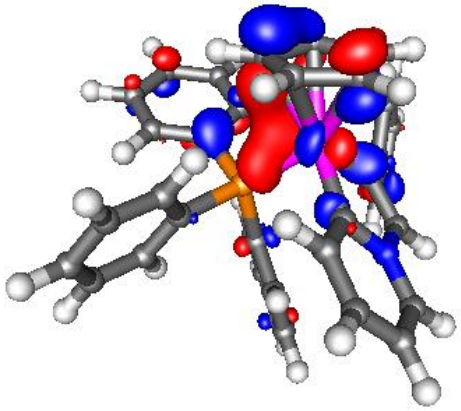	HOMO-5 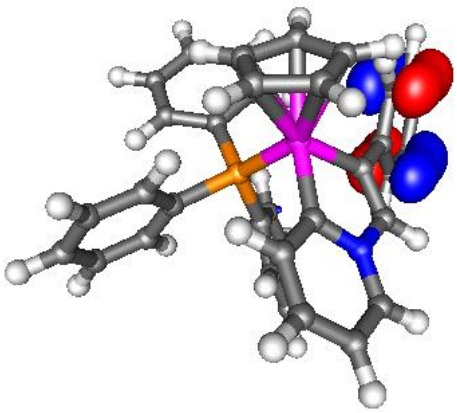

HOMO-6 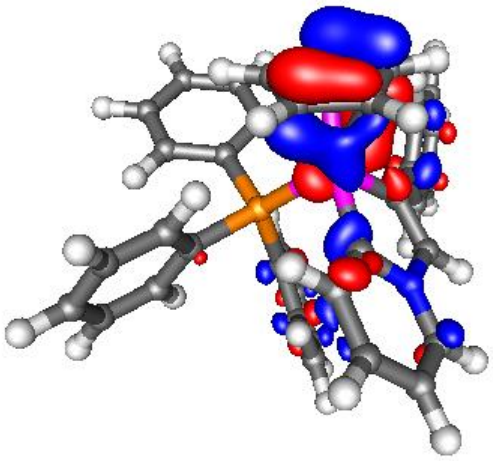	HOMO-7 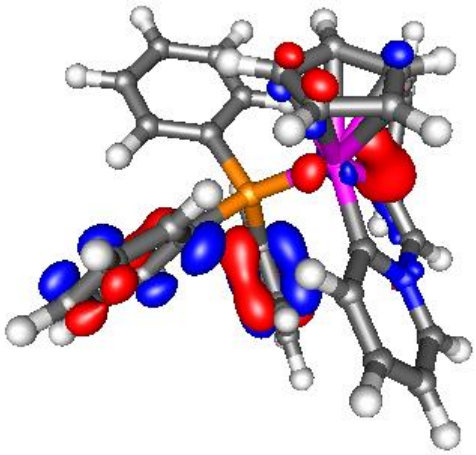
HOMO-8 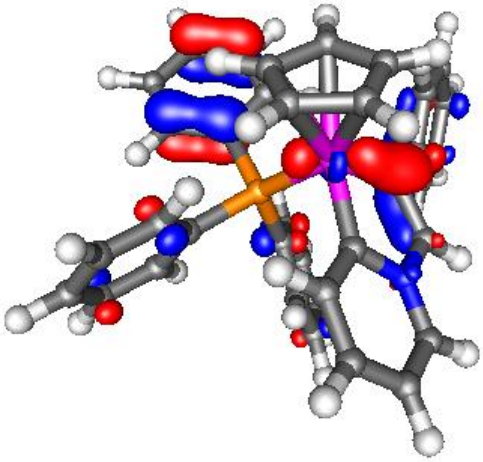	HOMO-9 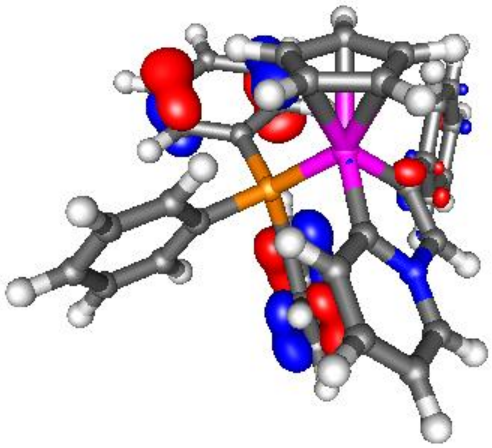
HOMO-10 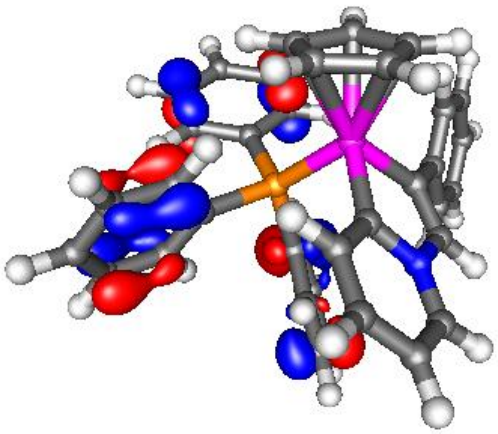	

C.1.2 – ***N15***

HOMO 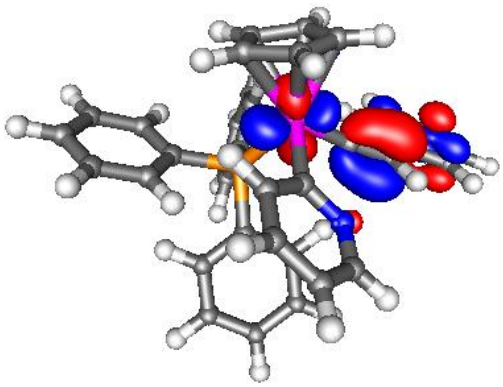	HOMO-1 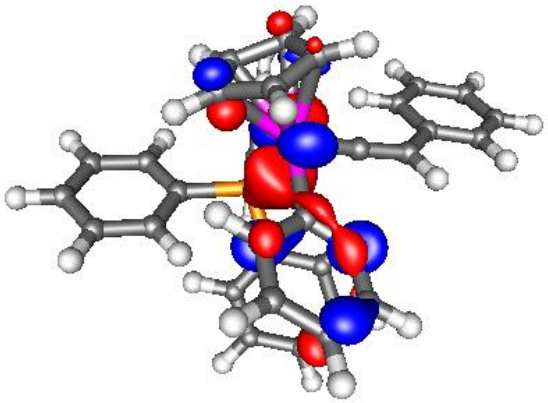
HOMO-2 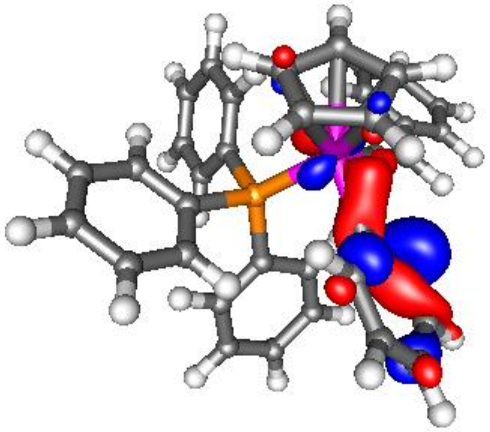	HOMO-3 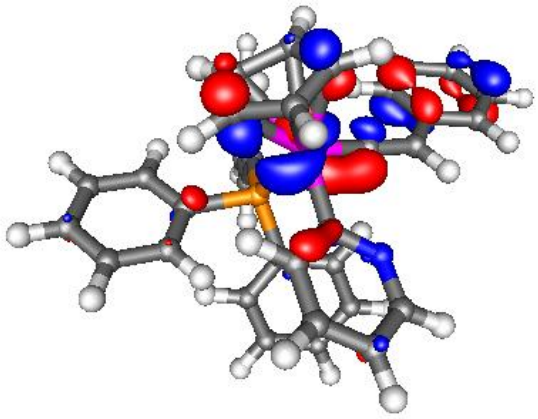
HOMO-4 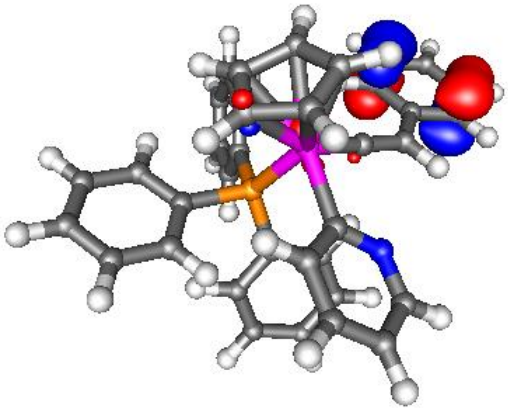	HOMO-5 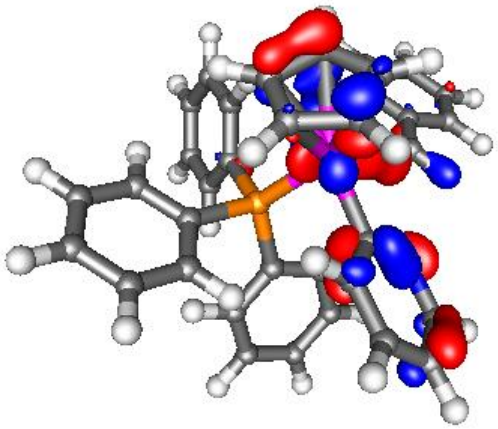

HOMO-6 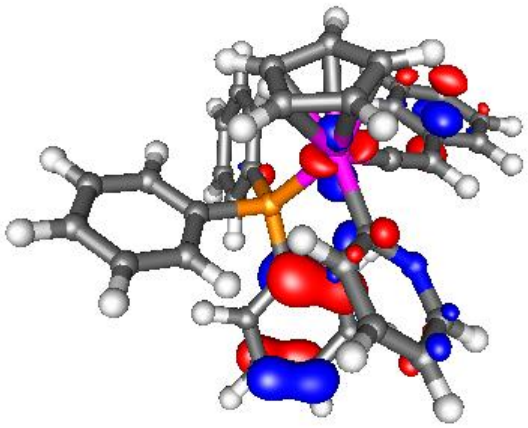	HOMO-7 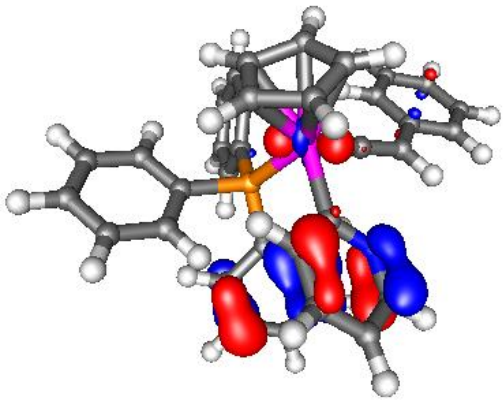
HOMO-8 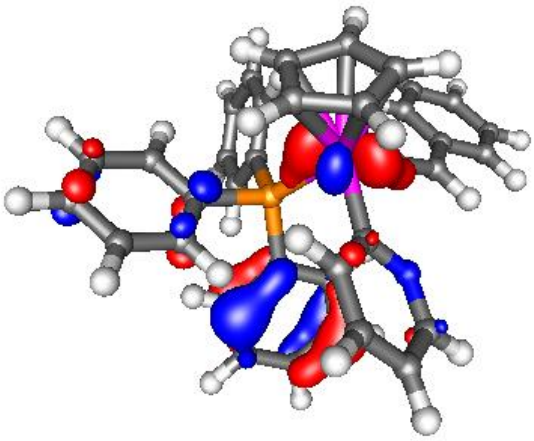	HOMO-9 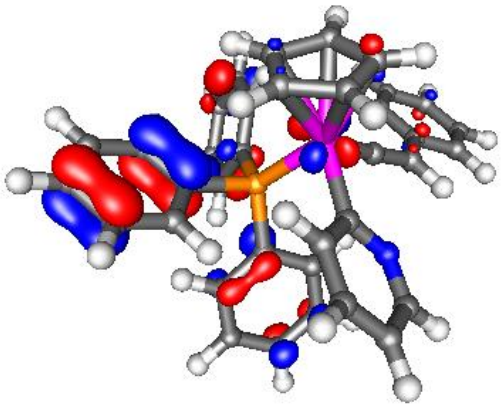
HOMO-10 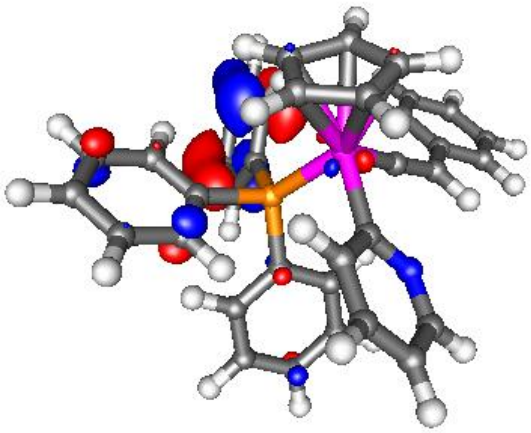	

Glossary and Structure Nomenclature

AMLA – Amphiphilic Metal Ligand Activation

COSMO – Conductor-Like Screening Model

Cp – Cyclopentadiene Ring

DCM – Dichloromethane

DFT – Density Functional Theory

DPPB – 1,2-*bis*(diphenylphosphino)butane

DPPE – *Bis*(diphenylphosphino)ethane

DRC – Dynamic Reaction Coordinate

ECP – Effective Core Potential

ESI-MS – Electrospray Ionization – Mass Spectrometry

GTO – Gaussian Type Orbital

HOMO – Highest Occupied Molecular Orbital

HF – Hartree-Fock

KS – Kohn-Sham

LCAO – Linear Combination of Atomic Orbitals

*LP/LP** - Lone Pair/Lone Pair Acceptor

LUMO – Lowest Unoccupied Molecular Orbital

MO – Molecular Orbital

NBO – Natural Bond Orbital

NRT – Natural Resonance Theory

PES – Potential Energy Surface

SCF – Self Consistent Field

STO – Slater Type Orbital

TDI – Turnover Determining Intermediate

TDTS – Turnover Determining Transition State

TOF – Turnover Frequency

TS – Transition State

WBI – Wiberg Bond Indices

ZPE – Zero Point Energy

In order to distinguish between isomers of certain states within the thesis, several shorthand notations have been used.

/cis, */trans* – This is used in octahedral *bis*-phosphine systems (in chapter 2), and denotes that the phosphines are *cis* or *trans* to one another.

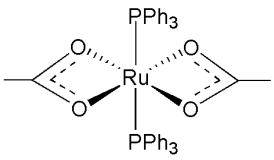

101/trans

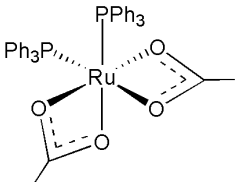

101/cis

/cis', */cis''* – Additionally when in the *cis* isomer, the free coordination site for the alkyne can be found *trans* to either the acetate (**cis'**) or phosphorous (**cis''**) ligand respectively. This nomenclature is used in chapter 2.

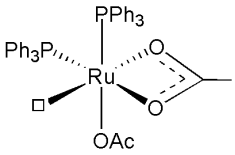

A1/cis'

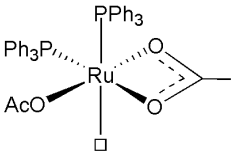

A1/cis''

/trans-ac, */trans-sty*, */trans-CO* – Used in the instances where a secondary active site is created. This site can either be *trans* to the acetate, β-styryl acetate or carbonyl group respectively. This is seen in chapter 4.

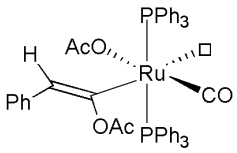

/trans-sty

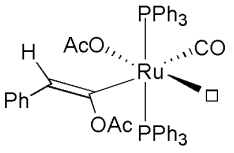

/trans-ac

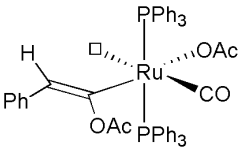

/trans-CO

/a, */b* – This is used with acetate and pyridine-based molecules. The nitrogen atom side of a pyridine or free arm of the acetate is shown to be facing toward (**a**) or away (**b**) from the substrate-binding site of the organometallic complex respectively. This is seen in chapters 2, 3, 4 and 5.

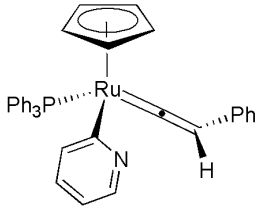

N15/a/x

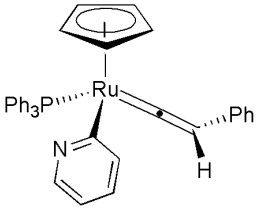

N15/b/x

/x, /y – This denotes that the alkyne-vinylidene proton is facing toward (**x**), or away (**y**) from the 'active' ligand (either a κ^1-acetate or pyridine group) when coordinated to the metal centre. This nomenclature is used throughout chapters 2, 3, 4 and 5.

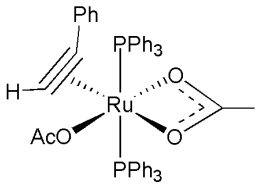

A2/trans/x

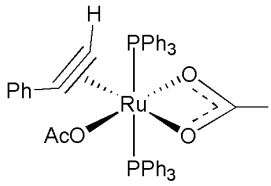

A2/trans/y

/m, /n – When a secondary coordination site is created (for example, addition of a second alkyne) the proton will face toward (**m**) or away (**n**) from the primary active site. This is seen in chapter 4.

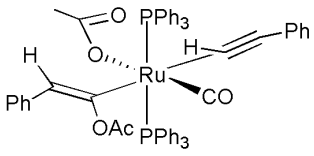

E10/trans-sty/m

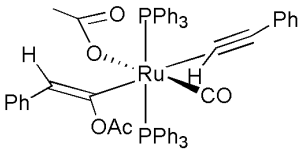

E10/trans-sty/n

/c, /d – Once again upon creation of a secondary vacant coordination site, an additional active ligand (for example, a second acetate group) can either be facing towards (**c**) or away (**d**) from the primary active site respectively. This nomenclature is used in chapter 4.

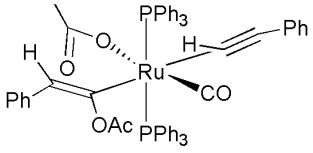

E10/trans-sty/c

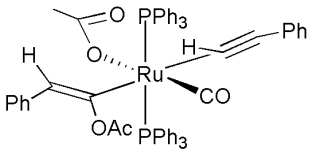

E10/trans-sty/d

/p, /q – When an unsymmetrical substrate is used (e.g. 3-methylpyridine in section 5.2.12) the sterically bulky side is furthest away from (**p**) or closest to (**q**) the other substrate respectively.

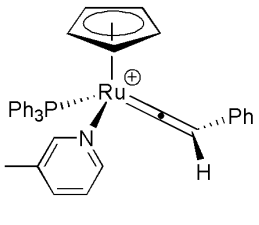

Q1/p/x

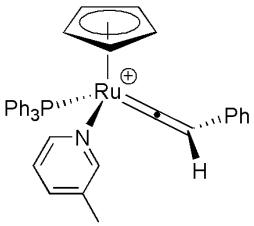

Q1/q/x

With respect to the overall naming scheme, experimentally observed complexes are given numbers, with the first number indicating the chapter where the complex was first seen (e.g. **201** in chapter 2). Theoretically observed complexes are assigned a letter dependant on their substituents (for example **A** and **C** differ in coordinated phosphine ligands). Geometries, vibrational frequencies, and spreadsheets for all systems can be located on the supplementary information disk.

References

1. D. Upper, *J. Appl. Behav. Anal.*, 1974, **7**, 497.
2. R. J. Bartlett, I. V. Schweigert and V. F. Lotrich, *Journal of Molecular Structure: THEOCHEM*, 2006, **771**, 1-8.
3. C. J. Cramer, *Essentials of Computational Chemistry Theories and Models*, Second edn., John Wiley & Sons, Ltd, 2006.
4. W. K. M. C. Holthausen, *A Chemist's Guide to Density Functional Theory*, Second edn., Wiley-VCH, 2008.
5. R. A. Millikan, *Physl. Rev.*, 1914, **4**, 73-75.
6. J. C. Maxwell, *On Physical Lines of Force*, 1861.
7. A. Einstein, *Ann. Phys. (Berlin)*, 1905, **322**, 132-148.
8. C. J. Davisson, *Bell System Tech J.*, 1928, **7**, 90-105.
9. http://www.nobelprize.org/nobel_prizes/physics/laureates/1937/, *The Nobel Prize in Physics 1937*
10. L. d. Broglie, *Ann. Phys. (Paris)*, 1925, **10**, 22-128.
11. G. Herzberg, *Atomic Spectra and Atomic Structure*, Prentice-Hall, 1937.
12. E. Rutherford, *Philos. Mag.*, 1911, **21**, 669-688.
13. N. Bohr, *Philos. Mag.*, 1913, **26**, 1-25.
14. N. Bohr, *Philos. Mag.*, 1913, **26**, 476-502.
15. W. Wilson, *Philos. Mag.*, 1915, **29**, 795-802.
16. E. Schrödinger, *Physl. Rev.*, 1926, **28**, 1049-1070.
17. http://www.nobelprize.org/nobel_prizes/physics/laureates/1954/born-lecture.html, *The Nobel Prize in Physics 1954 - Lecture by Max Born*.
18. D. O. Hayward, *Quantum Mechanics for Chemists*, Royal Society of Chemistry, 2002.
19. M. Born and R. Oppenheimer, *Ann. Phys. (Berlin)*, 1927, **389**, 457-484.
20. D. R. Hartree, *Math Proc. Cambridge*, 1928, **24**, 89-110.
21. W. Gerlach and O. Stern, *Z. Phys.*, 1922, **9**, 353-355.
22. W. Heisenberg, *Z. Phys.*, 1927, **43**, 172-198.
23. J. C. Slater, *Physl. Rev.*, 1929, **34**, 1293-1322.
24. J. C. Slater, *Physl. Rev.*, 1930, **36**, 57-64.
25. S. F. Boys, *Proc. R. Soc. London, Ser. A*, 1950, **200**, 542-554.
26. L. H. Thomas, *Math Proc. Cambridge*, 1927, **23**, 542-548.
27. E. Fermi, *Rend. Accad. Lincei.*, 1927, **6**, 602.
28. P. Hohenberg and W. Kohn, *Physl. Rev.*, 1964, **136**, B864-B871.
29. W. Kohn and L. J. Sham, *Physl. Rev.*, 1965, **140**, A1133-A1138.
30. J. P. Perdew, *Phys. Rev. B*, 1986, **33**, 8822-8824.
31. A. D. Becke, *Phys. Rev. A*, 1988, **38**, 3098-3100.
32. J. P. Perdew, K. Burke and M. Ernzerhof, *Phys. Rev. Lett.*, 1996, **77**, 3865-3868.
33. C. Adamo, M. Cossi and V. Barone, *THEOCHEM*, 1999, **493**, 145-157.

34. C. Adamo and V. Barone, *J. Chem. Phys.*, 1999, **110**, 6158-6170.
35. M. Ernzerhof and G. E. Scuseria, *J. Chem. Phys.*, 1999, **110**, 5029-5036.
36. J. C. Slater, *Physl. Rev.*, 1951, **81**, 385-390.
37. J. P. Perdew, J. A. Chevary, S. H. Vosko, K. A. Jackson, M. R. Pederson, D. J. Singh and C. Fiolhais, *Phys. Rev. B*, 1992, **46**, 6671-6687.
38. M. D. T. W. G. Frenking, in *Computational Organometallic Chemistry*, ed. T. R. Cundari, Marcel Dekker, 2001.
39. *TURBOMOLE User's Manual (Version 6.4)*, TURBOMOLE GmbH, 2012.
40. P. Deglmann, F. Furche and R. Ahlrichs, *Chem. Phys. Lett.*, 2002, **362**, 511-518.
41. J. M. Haile, *Molecular Dynamics Simulation*, Wiley-Interscience, 1992.
42. J. Tomasi, B. Mennucci and R. Cammi, *Chem. Rev. (Washington, DC, U. S.)*, 2005, **105**, 2999-3094.
43. J. Tomasi and M. Persico, *Chem. Rev. (Washington, DC, U. S.)*, 1994, **94**, 2027-2094.
44. A. Klamt and G. Schüürmann, *J. Chem. Soc., Perkin Trans. 2*, 1993, **2**, 799-805.
45. A. Klamt, *J. Phys. Chem.*, 1995, **99**, 2224-2235.
46. F. W. Sears, M. W. Zemansky and H. D. Young, *University Physics, 6th Edition*, Addison-Wesley, 1982.
47. J. P. Perdew and K. Schmidt, *AIP Conf. Proc.*, 2001, **577**, 1-20.
48. J. P. Perdew, A. Ruzsinszky, J. Tao, V. N. Staroverov, G. E. Scuseria and G. I. Csonka, *J. Chem. Phys.*, 2005, **123**, 062201-062209.
49. Y. Zhao and D. G. Truhlar, *Acc. Chem. Res.*, 2008, **41**, 157-167.
50. *Faraday Discuss.*, 2003, **124**, 92.
51. D. A. Pantazis, J. E. McGrady, F. Maseras and M. Etienne, *J. Chem. Theory Comput.*, 2007, **3**, 1329-1336.
52. M. P. Waller, H. Braun, N. Hojdis and M. Bühl, *J. Chem. Theory Comput.*, 2007, **3**, 2234-2242.
53. M. Bühl, C. Reimann, D. A. Pantazis, T. Bredow and F. Neese, *J. Chem. Theory Comput.*, 2008, **4**, 1449-1459.
54. M. J. Cowley, J. M. Lynam and J. M. Slattery, *Dalton Trans.*, 2008, 4552-4554.
55. S. Grimme, *J. Comput. Chem.*, 2006, **27**, 1787-1799.
56. S. Kozuch and S. Shaik, *Accounts of Chemical Research*, 2011, **44**, 101-110.
57. A. A. C. Braga, G. Ujaque and F. Maseras, *Organometallics*, 2006, **25**, 3647-3658.
58. J. Moellmann and S. Grimme, *Organometallics*, 2013, **In Press**.
59. E. D. Glendening, J. K. Badenhoop, A. E. Reed, J. E. Carpenter, J. A. Bohmann, C. M. Morales and F. Weinhold, Theoretical Chemistry Institute, University of Wisconsin, Madison, WI, 2009.
60. F. Weinhold and C. R. Landis, *Chem. Educ. Res. Pract.*, 2001, **2**, 91-104.
61. F. L. Weinhold, C. R., *Discovering Chemistry With Natural Bond Orbitals*, Wiley, 2012.
62. G. N. Lewis, *J. Am. Chem. Soc.*, 1916, **38**, 762-785.
63. E. D. Glendening and F. Weinhold, *J. Comp. Chem.*, 1998, **19**, 593-609.

64. E. D. Glendening and F. Weinhold, *J. Comp. Chem.*, 1998, **19**, 610-627.
65. E. D. Glendening, J. K. Badenhoop and F. Weinhold, *J. Comp. Chem.*, 1998, **19**, 628-646.
66. K. J. Laidler, *Pure Appl. Chem.*, 1996, **68**, 149-192.
67. W. C. M. Lewis, *J. Chem. Soc.*, 1918, **113**, 471-492.
68. C. R. R. Marcelin, *Hebd. Seances Acad. Sco.*, 1914, **158**, 116.
69. K. J. Laidler and M. C. King, *J. Phys. Chem.*, 1983, **87**, 2657-2664.
70. P. A. J. D. Paula, *Physical Chemistry*, seventh edn., Oxford University Press, 2006.
71. S. Kozuch, C. Amatore, A. Jutand and S. Shaik, *Organometallics*, 2005, **24**, 2319-2330.
72. S. Kozuch and S. Shaik, *J. Am. Chem. Soc.*, 2006, **128**, 3355-3365.
73. S. K. S. Shaik, *Acc. Chem. Res.*, 2011, **44**, 101-110.
74. S. Kozuch, *Wiley Interdisciplinary Reviews: Computational Molecular Science*, 2012, **2**, 795-815.
75. S. Kozuch and J. M. L. Martin, *ChemPhysChem*, 2011, **12**, 1413-1418.
76. S. C. Pan, *Beilstein J. Org. Chem.*, 2012, **8**, 1374-1384.
77. P. Knochel, K. Karaghiosoff and S. Manolikakes, in *Frustrated Lewis Pairs II*, eds. G. Erker and D. W. Stephan, Springer Berlin Heidelberg, 2013, vol. 334, pp. 171-190.
78. A. E. Shilov and G. B. Shul'pin, *Chem. Rev. (Washington, DC, U. S.)*, 1997, **97**, 2879-2932.
79. R. H. Crabtree, *J. Chem. Soc., Dalton Trans.*, 2001, 2437-2450.
80. R. G. Bergman, *Nature*, 2007, **446**, 391-393.
81. D. Balcells, E. Clot and O. Eisenstein, *Chem. Rev. (Washington, DC, U. S.)*, 2010, **110**, 749-823.
82. P. B. Arockiam, C. Bruneau and P. H. Dixneuf, *Chem. Rev. (Washington, DC, U. S.)*, 2012, **112**, 5879-5918.
83. S. R. Klei, K. L. Tan, J. T. Golden, Cathleen M. Yung, R. K. Thalji, K. A. Ahrendt, J. A. Ellman, T. D. Tilley and R. G. Bergman, *Carbon-Hydrogen Bond Activation by Iridium and Rhodium Complexes: Catalytic Hydrogen/Deuterium Exchange and Carbon-Carbon Bond-Forming Reactions*, ACS, 2004.
84. J. Chatt and J. M. Davidson, *J. Chem. Soc. (Resumed)*, 1965, 843-855.
85. A. E. Shilov, *Activation of Saturated Hydrocarbons by Transition Metal Complexes*, Riedel, 1994.
86. A. E. Shilov and G. B. Shul'pin, *Activation and Catalytic Reactions of Saturated Hydrocarbons in the Presence of Metal Complexes*, Kluwer, 2000.
87. A. H. Janowicz and R. G. Bergman, *J. Am. Chem. Soc.*, 1982, **104**, 352-354.
88. R. G. Bergman, *J. Organomet. Chem.*, 1990, **400**, 273-282.
89. D. Lapointe and K. Fagnou, *Chem. Lett.*, 2010, **39**, 1118-1126.
90. A. J. Canty and G. van Koten, *Acc. Chem. Res.*, 1995, **28**, 406-413.
91. L. Ackermann, *Chem. Rev. (Washington, DC, U. S.)*, 2011, **111**, 1315-1345.

92. Y. Boutadla, D. L. Davies, S. A. Macgregor and A. I. Poblador-Bahamonde, *Dalton Trans.*, 2009, 5820-5831.
93. J. Oxgaard, W. J. Tenn, R. J. Nielsen, R. A. Periana and W. A. Goddard, *Organometallics*, 2007, **26**, 1565-1567.
94. R.-Z. Liao, J.-G. Yu and F. Himo, *Proc. Natl. Acad. Sci. U.S.A.*, 2010, **107**, 22523-22527.
95. A. D. Ryabov, I. K. Sakodinskaya and A. K. Yatsimirsky, *Dalton Trans.*, 1985, 2629.
96. A. D. Ryabov, *Chem. Rev.*, 1990, 403.
97. D. L. Davies, S. M. A. Donald and S. A. Macgregor, *J. Am. Chem. Soc.*, 2005, **127**, 13754-13755.
98. Y. Boutadla, D. L. Davies, S. A. Macgregor and A. I. Poblador-Bahamonde, *Dalton Trans.*, 2009, **0**, 5887-5893.
99. M. Lavin, E. M. Holt and R. H. Crabtree, *Organometallics*, 1989, **8**, 99-104.
100. A. Vigalok, O. Uzan, L. J. W. Shimon, Y. Ben-David, J. M. L. Martin and D. Milstein, *J. Am. Chem. Soc.*, 1998, **120**, 12539.
101. M. Gómez, J. Granell and M. Martinez, *Organometallics*, 1997, **16**, 2539-2546.
102. M. Gómez, J. Granell and M. Martinez, *J. Chem. Soc., Dalton Trans.*, 1998, **0**, 37-44.
103. D. L. Davies, O. Al-Duaij, J. Fawcett, M. Giardiello, S. T. Hilton and D. R. Russell, *Dalton Trans.*, 2003, **0**, 4132-4138.
104. D. L. Davies, S. M. A. Donald, O. Al-Duaij, S. A. Macgregor and M. Pölleth, *J. Am. Chem. Soc.*, 2006, **128**, 4210-4211.
105. L. Li, W. W. Brennessel and W. D. Jones, *Organometallics*, 2009, **28**, 3492-3500.
106. Y. Boutadla, O. Al-Duaij, D. L. Davies, G. A. Griffith and K. Singh, *Organometallics*, 2008, **28**, 433-440.
107. D. L. Davies, S. A. Macgregor and A. I. Poblador-Bahamonde, *Dalton Trans.*, 2010, **39**, 10520-10527.
108. W. B. Cross, E. G. Hope, Y.-H. Lin, S. A. Macgregor, K. Singh, G. A. Solan and N. Yahya, *Chem. Commun. (Cambridge, U. K.)*, 2013, **49**, 1918-1920.
109. M. Lafrance, C. N. Rowley, T. K. Woo and K. Fagnou, *J. Am. Chem. Soc.*, 2006, **128**, 8754-8756.
110. M. Lafrance and K. Fagnou, *J. Am. Chem. Soc.*, 2006, **128**, 16496-16497.
111. D. García-Cuadrado, A. A. C. Braga, F. Maseras and A. M. Echavarren, *J. Am. Chem. Soc.*, 2006, **128**, 1066-1067.
112. S. Pascual, P. de Mendoza and A. M. Echavarren, *Org. Biomol. Chem.*, 2007, **5**, 2727-2734.
113. D. García-Cuadrado, P. de Mendoza, A. A. C. Braga, F. Maseras and A. M. Echavarren, *J. Am. Chem. Soc.*, 2007, **129**, 6880-6886.
114. S. Pascual, P. de Mendoza, A. A. C. Braga, F. Maseras and A. M. Echavarren, *Tetrahedron*, 2008, **64**, 6021-6029.
115. S. I. Gorelsky, D. Lapointe and K. Fagnou, *J. Am. Chem. Soc.*, 2008, **130**, 10848.

116. O. René and K. Fagnou, *Org. Lett.*, 2010, **12**, 2116-2119.
117. L.-C. Campeau, D. R. Stuart and K. Fagnou, *Aldrichim. Acta*, 2007, 35.
118. M. Lafrance, D. Lapointe and K. Fagnou, *Tetrahedron*, 2008, **64**, 6015-6020.
119. H.-Y. Sun, S. I. Gorelsky, D. R. Stuart, L.-C. Campeau and K. Fagnou, *J. Org. Chem.*, 2010, **75**, 8180-8189.
120. D. J. Schipper, L.-C. Campeau and K. Fagnou, *Tetrahedron*, 2009, **65**, 3155-3164.
121. L.-C. Campeau, D. J. Schipper and K. Fagnou, *J. Am. Chem. Soc.*, 2008, **130**, 3266-3267.
122. L.-C. Campeau, D. R. Stuart, J.-P. Leclerc, M. g. Bertrand-Laperle, E. Villemure, H.-Y. Sun, S. Lasserre, N. Guimond, M. Lecavallier and K. Fagnou, *J. Am. Chem. Soc.*, 2009, **131**, 3291-3306.
123. B. t. Liégault, D. Lapointe, L. Caron, A. Vlassova and K. Fagnou, *J. Org. Chem.*, 2009, **74**, 1826-1834.
124. B. Liégault, I. Petrov, S. I. Gorelsky and K. Fagnou, *J. Org. Chem.*, 2010, **75**, 1047-1060.
125. M. Lafrance, S. I. Gorelsky and K. Fagnou, *J. Am. Chem. Soc.*, 2007, **129**, 14570-14571.
126. S. Rousseaux, S. I. Gorelsky, B. K. W. Chung and K. Fagnou, *J. Am. Chem. Soc.*, 2010, **132**, 10692-10705.
127. S. Rousseaux, M. Davi, J. Sofack-Kreutzer, C. Pierre, C. E. Kefalidis, E. Clot, K. Fagnou and O. Baudoin, *J. Am. Chem. Soc.*, 2010, **132**, 10706-10716.
128. S. Winstein and T. G. Traylor, *J. Am. Chem. Soc.*, 1955, **77**, 3747-3752.
129. C. W. Fung, M. Khorramdel-Vahed, R. J. Ranson and R. M. G. Roberts, *J. Chem. Soc., Perkin Trans. 2*, 1980, 267.
130. M. I. Bruce, *Chem. Rev. (Washington, DC, U. S.)*, 1991, **91**, 197-257.
131. R. F. C. B. F. Eastwood, *Synlett*, 1999, **1**, 9-20.
132. O. S. Mills and A. D. Redhouse, *Chem. Commun. (London)*, 1966, **0**, 444-445.
133. O. S. Mills and A. D. Redhouse, *Journal of the Chemical Society A: Inorganic, Physical, Theoretical*, 1968, **0**, 1282-1292.
134. R. B. King and M. S. Saran, *J. Chem. Soc., Chem. Commun.*, 1972, **0**, 1053-1054.
135. R. B. King, *Ann. N. Y. Acad. Sci.*, 1974, **239**, 171.
136. R. M. Kirchner and J. A. Ibers, *Inorg. Chem.*, 1974, **13**, 1667-1673.
137. M. Bruce and R. Wallis, *Aust. J. Chem.*, 1979, **32**, 1471-1485.
138. C. Bruneau and P. H. Dixneuf, *Metal Vinylidenes and Allenylidenes in Catalysis*, Wiley, 2008.
139. W. Kirmse, *Carbene Chemistry*, Academic Press, 1964.
140. R. H. Crabtree, *The Organometallic Chemistry of the Transition Metals*, fifth edn., Wiley, 2009.
141. R. Breslow, *J. Am. Chem. Soc.*, 1957, **79**, 1762-1763.
142. R. Gleiter and R. Hoffmann, *J. Am. Chem. Soc.*, 1968, **90**, 5457-5460.

143. E. O. Fischer and A. Maasböl, *Angew. Chem., Int. Ed. Engl.*, 1964, **3**, 580-581.
144. D. J. Cardin, B. Cetinkaya and M. F. Lappert, *Chem. Rev. (Washington, DC, U. S.)*, 1972, **72**, 545-574.
145. B. M. Novak and R. H. Grubbs, *J. Am. Chem. Soc.*, 1988, **110**, 7542-7543.
146. P. Schwab, M. B. France, J. W. Ziller and R. H. Grubbs, *Angew. Chem., Int. Ed. Engl.*, 1995, **34**, 2039-2041.
147. J. S. Kingsbury, J. P. A. Harrity, P. J. Bonitatebus and A. H. Hoveyda, *J. Am. Chem. Soc.*, 1999, **121**, 791-799.
148. G. C. Vougioukalakis and R. H. Grubbs, *Chem. Rev. (Washington, DC, U. S.)*, 2009, **110**, 1746-1787.
149. R. R. Schrock, J. S. Murdzek, G. C. Bazan, J. Robbins, M. DiMare and M. O'Regan, *J. Am. Chem. Soc.*, 1990, **112**, 3875-3886.
150. G. C. Bazan, J. H. Oskam, H. N. Cho, L. Y. Park and R. R. Schrock, *J. Am. Chem. Soc.*, 1991, **113**, 6899-6907.
151. D. H. McConville, J. R. Wolf and R. R. Schrock, *J. Am. Chem. Soc.*, 1993, **115**, 4413-4414.
152. R. R. Schrock and A. H. Hoveyda, *Angew. Chem., Int. Ed.*, 2003, **42**, 4592-4633.
153. http://www.nobelprize.org/nobel_prizes/chemistry/laureates/2005/, *The Nobel Prize in Chemistry 2005*
154. H. W. Wanzlick, *Angew. Chem., Int. Ed. Engl.*, 1962, **1**, 75-80.
155. H. W. Wanzlick and H. J. Schönherr, *Angew. Chem., Int. Ed. Engl.*, 1968, **7**, 141-142.
156. A. J. Arduengo, R. L. Harlow and M. Kline, *J. Am. Chem. Soc.*, 1991, **113**, 361-363.
157. W. A. Herrmann and C. Köcher, *Angew. Chem., Int. Ed. Engl.*, 1997, **36**, 2162-2187.
158. J. Hartwig, *Organotransition Metal Chemistry - From Bonding to Catalysis*, University Science Books, 2010.
159. D. C. Miller and R. J. Angelici, *Organometallics*, 1991, **10**, 79-89.
160. H. Katayama, K. Onitsuka and F. Ozawa, *Organometallics*, 1996, **15**, 4642-4645.
161. C. Löwe, H.-U. Hund and H. Berke, *J. Organomet. Chem.*, 1989, **371**, 311-319.
162. Y. Chen, D. M. Jonas, J. L. Kinsey and R. W. Field, *J. Chem. Phys.*, 1989, **91**, 3976-3987.
163. K. M. Ervin, J. Ho and W. C. Lineberger, *J. Chem. Phys.*, 1989, **91**, 5974-5992.
164. M. M. Gallo, T. P. Hamilton and H. F. Schaefer, *J. Am. Chem. Soc.*, 1990, **112**, 8714-8719.
165. J. H. Jensen, K. Morokuma and M. S. Gordon, *J. Chem. Phys.*, 1994, **100**, 1981-1987.
166. M. Oliván, E. Clot, O. Eisenstein and K. G. Caulton, *Organometallics*, 1998, **17**, 3091-3100.
167. Y. Wakatsuki, *J. Organomet. Chem.*, 2004, **689**, 4092-4109.
168. J. M. Lynam, *Chem. Eur. J.*, 2010, **16**, 8238-8247.
169. J. Silvestre and R. Hoffmann, *Helv. Chim. Acta*, 1985, **68**, 1461-1506.
170. F. De Angelis, A. Sgamellotti and N. Re, *Organometallics*, 2002, **21**, 2715-2723.

171. D. B. Grotjahn, X. Zeng, A. L. Cooksy, W. S. Kassel, A. G. DiPasquale, L. N. Zakharov and A. L. Rheingold, *Organometallics*, 2007, **26**, 3385-3402.
172. Y. Wakatsuki, N. Koga, H. Yamazaki and K. Morokuma, *J. Am. Chem. Soc.*, 1994, **116**, 8105-8111.
173. T.A. Stephenson and G. Wilkinson, *J. Inorg. Nucl. Chem.*, 1966, **28**, 945-956.
174. S. J. La Placa and J. A. Ibers, *Inorg. Chem.*, 1965, **4**, 778-783.
175. J. A. Varela and C. Saá, *Chem. Eur. J.*, 2006, **12**, 6450-6456.
176. K. Melis, P. Samulkiewicz, J. Rynkowski and F. Verpoort, *Tetrahedron Lett.*, 2002, **43**, 2713-2716.
177. M. Bassetti, S. Marini, F. Tortorella, V. Cadierno, J. Díez, M. P. Gamasa and J. Gimeno, *J. Organomet. Chem.*, 2000, **593–594**, 292-298.
178. G. Consiglio, F. Morandini, G. F. Ciani and A. Sironi, *Organometallics*, 1986, **5**, 1976-1983.
179. B. M. Trost and J. A. Flygare, *J. Org. Chem.*, 1994, **59**, 1078-1082.
180. F. E. McDonald and C. C. Schultz, *J. Am. Chem. Soc.*, 1994, **116**, 9363-9364.
181. F. E. McDonald and A. K. Chatterjee, *Tetrahedron Lett.*, 1997, **38**, 7687-7690.
182. F. E. McDonald, S. A. Burova and L. G. Huffman Jr, *Synthesis*, 2000, **2000**, 970-974.
183. B. M. Trost, G. Dyker and R. J. Kulawiec, *J. Am. Chem. Soc.*, 1990, **112**, 7809-7811.
184. B. M. Trost and R. J. Kulawiec, *J. Am. Chem. Soc.*, 1992, **114**, 5579-5584.
185. M. Tokunaga and Y. Wakatsuki, *Angew. Chem., Int. Ed.*, 1998, **37**, 2867-2869.
186. M. Murakami, M. Ubukata and Y. Ito, *Tetrahedron Lett.*, 1998, **39**, 7361-7364.
187. Y. Nishibayashi, I. Takei and M. Hidai, *Organometallics*, 1997, **16**, 3091-3093.
188. C. Bruneau and P. H. Dixneuf, *Acc. Chem. Res.*, 1999, **32**, 311-323.
189. B. M. Trost and A. McClory, *Chemistry – An Asian Journal*, 2008, **3**, 164-194.
190. C. Bruneau and P. H. Dixneuf, *Angew. Chem., Int. Ed.*, 2006, **45**, 2176-2203.
191. W. Markownikoff, *Justus Liebigs Annalen der Chemie*, 1870, **153**, 228-259.
192. P. Hughes, *J. Chem. Educ.*, 2006, **83**, 1152.
193. F. Alonso, I. P. Beletskaya and M. Yus, *Chem. Rev. (Washington, DC, U. S.)*, 2004, **104**, 3079-3160.
194. V. Cadierno, J. Francos and J. Gimeno, *Organometallics*, 2011, **30**, 852-862.
195. M. Neveux, C. Bruneau and P. H. Dixneuf, *J. Chem. Soc., Perkin Trans. 1*, 1991, 1197-1199.
196. R. Mahé, P. H. Dixneuf and S. Lécolier, *Tetrahedron Lett.*, 1986, **27**, 6333-6336.
197. C. Ruppin and P. H. Dixneuf, *Tetrahedron Lett.*, 1986, **27**, 6323-6324.
198. H. Doucet, B. Martin-Vaca, C. Bruneau and P. H. Dixneuf, *J. Org. Chem.*, 1995, **60**, 7247-7255.
199. H. Doucet, J. Hofer, C. Bruneau and P. H. Dixneuf, *J. Chem. Soc., Chem. Commun.*, 1993, 850-851.
200. L. J. Goossen, J. Paetzold and D. Koley, *Chem. Commun. (Cambridge, U. K.)*, 2003, 706-707.

201. C. S. Yi and R. Gao, *Organometallics*, 2009, **28**, 6585-6592.
202. M. I. Bruce, *Chem. Rev. (Washington, DC, U. S.)*, 1998, **98**, 2797-2858.
203. H. D. Hartzler, *J. Am. Chem. Soc.*, 1961, **83**, 4990-4996.
204. M. Asay, B. Donnadieu, W. W. Schoeller and G. Bertrand, *Angew. Chem., Int. Ed.*, 2009, **48**, 4796-4799.
205. E. O. Fischer, H.-J. Kalder, A. Frank, F. H. Köhler and G. Huttner, *Angew. Chem., Int. Ed. Engl.*, 1976, **15**, 623-624.
206. H. Berke, *Angew. Chem., Int. Ed. Engl.*, 1976, **15**, 624-624.
207. J. P. Selegue, *Organometallics*, 1982, **1**, 217-218.
208. E. Bustelo and P. H. Dixneuf, *Adv. Synth. Catal.*, 2005, **347**, 393-397.
209. S. Datta, C.-L. Chang, K.-L. Yeh and R.-S. Liu, *J. Am. Chem. Soc.*, 2003, **125**, 9294-9295.
210. B. M. Trost and J. A. Flygare, *J. Am. Chem. Soc.*, 1992, **114**, 5476-5477.
211. T. Suzuki, M. Tokunaga and Y. Wakatsuki, *Tetrahedron Lett.*, 2002, **43**, 7531-7533.
212. K. Fukamizu, Y. Miyake and Y. Nishibayashi, *J. Am. Chem. Soc.*, 2008, **130**, 10498-10499.
213. J. M. Lynam, C. E. Welby and A. C. Whitwood, *Organometallics*, 2009, **28**, 1320-1328.
214. D. G. Johnson, J. M. Lynam, J. M. Slattery and C. E. Welby, *Dalton Trans.*, 2010, **39**, 10432-10441.
215. C. E. Welby, University of York, 2011.
216. R. W. Mitchell, A. Spencer and G. Wilkinson, *J. Chem. Soc. Dalton Trans.*, 1973, 846.
217. J. D. Gilbert and G. Wilkinson, *J. Chem. Soc.*, 1969, 1749.
218. R. S. Berry, *J. Chem. Physics*, 1960, **32**, 933-938.
219. E. Smith, University of York, 2014.
220. D. Astruc, *New J. Chem.*, 2005, **29**, 42-56.
221. E. Álvarez, Y. A. Hernández, J. López-Serrano, C. Maya, M. Paneque, A. Petronilho, M. L. Poveda, V. Salazar, F. Vattier and E. Carmona, *Angew. Chem., Int. Ed.*, 2010, **49**, 3496-3499.
222. G. Herzberg, *Molecular Spectra & Molecular Structure Vol II – Infrared and Raman Spectra of Polyatomic Molecules*, Kreiger Publishing Company, 1991 (reprint of 1945 ed.).
223. J. A. Cabeza, I. del Río, J. M. Fernández-Colinas, E. Pérez-Carreño, M. G. Sánchez-Vega and D. Vázquez-García, *Organometallics*, 2009, **28**, 1832-1837.
224. M. R. Churchill, C. H. Lake, F. J. Safarowic, D. S. Parfitt, L. R. Nevinger and J. B. Keister, *Organometallics*, 1993, **12**, 671-679.
225. M. I. Bruce, B. C. Hall, N. N. Zaitseva, B. W. Skelton and A. H. White, *J. Organomet. Chem.*, 1996, **522**, 307-310.
226. D. Touchard, P. Haquette, S. Guesmi, L. Le Pichon, A. Daridor, L. Toupet and P. H. Dixneuf, *Organometallics*, 1997, **16**, 3640-3648.
227. J. M. Galbraith and H. F. Schaefer Iii, *J. Chem. Phys.*, 1996, **105**, 862-864.

228. T. Grabarkiewicz, P. Grobelny, M. Hoffmann and J. Mielcarek, *Org. Biomol. Chem.*, 2006, **4**, 4299-4306.
229. F. Jensen, *J. Chem. Theory Comput.*, 2010, **6**, 2726-2735.
230. A. Spencer and G. Wilkinson, *J. Chem. Soc., Dalton Trans.*, 1974, **0**, 786-792.
231. S. D. Robinson and M. F. Uttley, *J. Chem. Soc., Chem. Commun.*, 1972, **0**, 1047b-1048.
232. S. D. Robinson and M. F. Uttley, *J. Chem. Soc., Dalton Trans.*, 1973, **0**, 1912-1920.
233. A. Dobson, S. D. Robinson and M. F. Uttley, *J. Chem. Soc., Dalton Trans.*, 1975, **0**, 370-377.
234. C. J. Creswell, A. Dobson, D. S. Moore and S. D. Robinson, *Inorg. Chem.*, 1979, **18**, 2055-2059.
235. S. Y. Yang, T. B. Wen, G. Jia and Z. Lin, *Organometallics*, 2000, **19**, 5477-5483.
236. R. N. Perutz and S. Sabo-Etienne, *Angew. Chem., Int. Ed.*, 2007, **46**, 2578-2592.
237. J. S. Carey, D. Laffan, C. Thomson and M. T. Williams, *Org. Biomol. Chem.*, 2006, **4**, 2337-2347.
238. M. C. Bagley, C. Glover and E. A. Merritt, *Synlett*, 2007, **2007**, 2459-2482.
239. J. A. Joule and K. Mills, *Heterocyclic Chemistry*, fifth edn., Blackwell Publishing, 2010.
240. S. Shimizu, N. Watanabe, T. Kataoka, T. Shoji, N. Abe, S. Morishita and H. Ichimura, in *Ullmann's Encyclopedia of Industrial Chemistry*, Wiley-VCH Verlag GmbH & Co. KGaA, 2000.
241. D. E. Pearson, W. W. Hargrove, J. K. T. Chow and B. R. Suthers, *J. Org. Chem.*, 1961, **26**, 789-792.
242. H. J. den hertog, L. van der Does and C. A. Landheer, *Recueil des Travaux Chimiques des Pays-Bas*, 1962, **81**, 864-870.
243. M. M. Boudakian, D. F. Gavin and R. J. Polak, *J. Heterocycl. Chem.*, 1967, **4**, 377-380.
244. M. M. Boudakian, *J. Heterocycl. Chem.*, 1967, **4**, 381-384.
245. M. T. DuPriest, C. L. Schmidt, D. Kuzmich and S. B. Williams, *J. Org. Chem.*, 1986, **51**, 2021-2023.
246. G. A. Molander and M. R. Rivero, *Org. Lett.*, 2001, **4**, 107-109.
247. S. L. Jain and B. Sain, *Chem. Commun. (Cambridge, U. K.)*, 2002, 1040-1041.
248. J. Meisenheimer, *Ber. Dtsch. Chem. Ges.*, 1926, **59**, 1848-1853.
249. E. Ochiai and D. U. Mizoguchi, *Aromatic amine oxides*, Elsevier Amsterdam, 1967.
250. A. Albini and S. Pietra, CRC Press (Boca Raton), 1990.
251. T. Kato and H. Yamanaka, *J. Org. Chem.*, 1965, **30**, 910-913.
252. R. M. Kellogg and T. J. Van Bergen, *J. Org. Chem.*, 1971, **36**, 1705-1708.
253. H. Andersson, F. Almqvist and R. Olsson, *Org. Lett.*, 2007, **9**, 1335-1337.
254. J. A. Bull, J. J. Mousseau, G. Pelletier and A. B. Charette, *Chem. Rev. (Washington, DC, U. S.)*, 2012, **112**, 2642-2713.

255. L.-C. Campeau, S. Rousseaux and K. Fagnou, *J. Am. Chem. Soc.*, 2005, **127**, 18020-18021.
256. J.-P. Leclerc and K. Fagnou, *Angew. Chem., Int. Ed.*, 2006, **45**, 7781-7786.
257. K. S. Kanyiva, Y. Nakao and T. Hiyama, *Angew. Chem., Int. Ed.*, 2007, **46**, 8872-8874.
258. H. Vorbrüggen and K. Krolikiewcz, *Tetrahedron Lett.*, 1983, **24**, 889-890.
259. E. J. Moore, W. R. Pretzer, T. J. O'Connell, J. Harris, L. LaBounty, L. Chou and S. S. Grimmer, *J. Am. Chem. Soc.*, 1992, **114**, 5888-5890.
260. T. Kawashima, T. Takao and H. Suzuki, *J. Am. Chem. Soc.*, 2007, **129**, 11006-11007.
261. P. Wen, Y. Li, K. Zhou, C. Ma, X. Lan, C. Ma and G. Huang, *Adv. Synth. Catal.*, 2012, **354**, 2135-2140.
262. J. C. Lewis, R. G. Bergman and J. A. Ellman, *J. Am. Chem. Soc.*, 2007, **129**, 5332-5333.
263. A. M. Berman, J. C. Lewis, R. G. Bergman and J. A. Ellman, *J. Am. Chem. Soc.*, 2008, **130**, 14926-14927.
264. B. M. Trost, *Acc. Chem. Res.*, 2002, **35**, 695-705.
265. M. Murakami and S. Hori, *J. Am. Chem. Soc.*, 2003, **125**, 4720-4721.
266. R. E. Shepherd and H. Taube, *Inorg. Chem.*, 1973, **12**, 1392-1401.
267. D. Lavorato, J. K. Terlouw, T. K. Dargel, W. Koch, G. A. McGibbon and H. Schwarz, *J. Am. Chem. Soc.*, 1996, **118**, 11898-11904.
268. D. Lavorato, J. Terlouw, G. McGibbon, T. Dargel, W. Koch and H. Schwarz, *Int. J. Mass Spectrom.*, 1998, **179–180**, 7-14.
269. P. Dyson and D. Ll. Hammick, *J. Chem. Soc. (Resumed)*, 1937, 1724-1725.
270. B. Crociani, F. di Bianca, A. Giovenco and A. Scrivanti, *J. Organomet. Chem.*, 1983, **251**, 393-411.
271. B. Crociani, F. Di Bianca, A. Giovenco and A. Scrivanti, *J. Organomet. Chem.*, 1984, **269**, 295-304.
272. E. Alvarez, S. Conejero, M. Paneque, A. Petronilho, M. L. Poveda, O. Serrano and E. Carmona, *J. Am. Chem. Soc.*, 2006, **128**, 13060-13061.
273. E. Álvarez, S. Conejero, P. Lara, J. A. López, M. Paneque, A. Petronilho, M. L. Poveda, D. del Río, O. Serrano and E. Carmona, *J. Am. Chem. Soc.*, 2007, **129**, 14130-14131.
274. S. Conejero, P. Lara, M. Paneque, A. Petronilho, M. L. Poveda, O. Serrano, F. Vattier, E. Álvarez, C. Maya, V. Salazar and E. Carmona, *Angew. Chem., Int. Ed.*, 2008, **47**, 4380-4383.
275. Y. A. Hernández, J. López-Serrano, M. Paneque, M. L. Poveda, F. Vattier, V. Salazar, E. Álvarez and E. Carmona, *Chem. Eur. J.*, 2011, **17**, 9302-9305.
276. S. Conejero, J. López-Serrano, M. Paneque, A. Petronilho, M. L. Poveda, F. Vattier, E. Álvarez and E. Carmona, *Chem. Eur. J.*, 2012, **18**, 4644-4664.
277. M. A. Esteruelas, F. J. Fernández-Alvarez and E. Oñate, *J. Am. Chem. Soc.*, 2006, **128**, 13044-13045.

278. M. A. Esteruelas, F. J. Fernández-Alvarez and E. Oñate, *Organometallics*, 2007, **26**, 5239-5245.
279. M. A. Esteruelas, F. J. Fernández-Alvarez, M. Oliván and E. Oñate, *Organometallics*, 2009, **28**, 2276-2284.
280. M. A. Esteruelas, F. J. Fernández-Alvarez and E. Oñate, *Organometallics*, 2008, **27**, 6236-6244.
281. K. L. Tan, R. G. Bergman and J. A. Ellman, *J. Am. Chem. Soc.*, 2001, **123**, 2685-2686.
282. K. L. Tan, R. G. Bergman and J. A. Ellman, *J. Am. Chem. Soc.*, 2002, **124**, 13964-13965.
283. J. C. Lewis, R. G. Bergman and J. A. Ellman, *Acc. Chem. Res.*, 2008, **41**, 1013-1025.
284. D. A. Colby, A. S. Tsai, R. G. Bergman and J. A. Ellman, *Acc. Chem. Res.*, 2012, **45**, 814-825.
285. S. H. Wiedemann, J. C. Lewis, J. A. Ellman and R. G. Bergman, *J. Am. Chem. Soc.*, 2006, **128**, 2452-2462.
286. N. S. Mistry, 2013.
287. K. Mauthner, K. M. Soldouzi, K. Mereiter, R. Schmid and K. Kirchner, *Organometallics*, 1999, **18**, 4681-4683.
288. E. Becker, E. Rüba, K. Mereiter, R. Schmid and K. Kirchner, *Organometallics*, 2001, **20**, 3851-3853.
289. E. Rüba, K. Mereiter, R. Schmid, V. N. Sapunov, K. Kirchner, H. Schottenberger, M. J. Calhorda and L. F. Veiros, *Chem. Eur. J.*, 2002, **8**, 3948-3961.
290. E. Becker, V. Stingl, K. Mereiter and K. Kirchner, *Organometallics*, 2006, **25**, 4166-4169.
291. K. Kirchner, *Monatshefte für Chemie - Chemical Monthly*, 2008, **139**, 337-348.
292. C. A. Tolman, *Chem. Rev. (Washington, DC, U. S.)*, 1977, **77**, 313-348.
293. L. Hintermann, L. Xiao, A. l. Labonne and U. Englert, *Organometallics*, 2009, **28**, 5739-5748.
294. K. P. Jensen, B. O. Roos and U. Ryde, *J. Chem. Phys.*, 2007, **126**, 014103-014114.
295. S. Bajo, M. A. Esteruelas, A. M. López and E. Oñate, *Organometallics*, 2012, **31**, 8618-8626.
296. D. G. Johnson, J. M. Lynam, N. S. Mistry, J. M. Slattery, R. J. Thatcher and A. C. Whitwood, *J. Am. Chem. Soc.*, 2013, **135**, 2222-2234.
297. R. J. Thatcher, D. G. Johnson, J. M. Slattery and R. E. Douthwaite, *Chem. Eur. J.*, 2012, **18**, 4329-4336.
298. R. Ahlrichs, M. Bär, M. Häser, H. Horn and C. Kölmel, *Chem. Phys. Lett.*, 1989, **162**, 165-169.
299. M. v. Arnim and R. Ahlrichs, *J. Chem. Phys.*, 1999, **111**, 9183-9190.
300. P. Császár and P. Pulay, *J. Mol. Struct.*, 1984, **114**, 31-34.
301. P. Deglmann and F. Furche, *J. Chem. Phys.*, 2002, **117**, 9535-9538.
302. T. Koga and H. Kobayashi, *J. Chem. Phys.*, 1985, **82**, 1437-1439.

303. P. Pulay, *Chem. Phys. Lett.*, 1980, **73**, 393-398.
304. O. Treutler and R. Ahlrichs, *J. Chem. Phys.*, 1995, **102**, 346-354.
305. *TURBOMOLE User's Manual (Version 5.10)*, TURBOMOLE GmbH, 2012.
306. A. Schäfer, H. Horn and R. Ahlrichs, *J. Chem. Phys.*, 1992, **97**, 2571-2577.
307. K. Eichkorn, O. Treutler, H. Öhm, M. Häser and R. Ahlrichs, *Chem. Phys. Lett.*, 1995, **242**, 652-660.
308. K. Eichkorn, F. Weigend, O. Treutler and R. Ahlrichs, *Theo. Chem. Acc.*, 1997, **97**, 119-124.
309. D. Andrae, U. Häußermann, M. Dolg, H. Stoll and H. Preuß, *Theor. Chim. Acta.*, 1990, **77**, 123-141.
310. F. Weigend, M. Häser, H. Patzelt and R. Ahlrichs, *Chem. Phys. Lett.*, 1998, **294**, 143-152.
311. F. Weigend and R. Ahlrichs, *Phys. Chem. Chem. Phys.*, 2005, **7**, 3297-3305.
312. F. Weigend, *Phys. Chem. Chem. Phys.*, 2006, **8**, 1057-1065.
313. K. Fukui, *Acc. Chem. Res.*, 1981, **14**, 363-368.
314. *CRC handbook of chemistry and physics*, Chemical Rubber Company, 2010/2011.
315. C. Caleman, P. J. v. Maaren, M. Hong, J. S. Hub, L. T. Costa and D. v. d. Spoel, *J. Chem. Theory Comput.*, 2011, **8**, 61-74.
316. M. J. Frisch, G. W. Trucks, H. B. Schlegel, G. E. Scuseria, M. A. Robb, J. R. Cheeseman, G. Scalmani, V. Barone, B. Mennucci, G. A. Petersson, H. Nakatsuji, M. Caricato, X. Li, H. P. Hratchian, A. F. Izmaylov, J. Bloino, G. Zheng, J. L. Sonnenberg, M. Hada, M. Ehara, K. Toyota, R. Fukuda, J. Hasegawa, M. Ishida, T. Nakajima, Y. Honda, O. Kitao, H. Nakai, T. Vreven, J. J. A. Montgomery, J. E. Peralta, F. Ogliaro, M. Bearpark, J. J. Heyd, E. Brothers, K. N. Kudin, V. N. Staroverov, R. Kobayashi, J. Normand, K. Raghavachari, A. Rendell, J. C. Burant, S. S. Iyengar, J. Tomasi, M. Cossi, N. Rega, J. M. Millam, M. Klene, J. E. Knox, J. B. Cross, V. Bakken, C. Adamo, J. Jaramillo, R. Gomperts, R. E. Stratmann, O. Yazyev, A. J. Austin, R. Cammi, C. Pomelli, J. W. Ochterski, R. L. Martin, K. Morokuma, V. G. Zakrzewski, G. A. Voth, P. Salvador, J. J. Dannenberg, S. Dapprich, A. D. Daniels, Ö. Farkas, J. B. Foresman, J. V. Ortiz, J. Cioslowski and D. J. Fox, Gaussian Inc., Wallingford, CT, 2009.